

---

## Assessment of Numerical Simulations for High Reynolds Flows Around the Pump Tower of a LNG membrane Tank on a Floating Structure

**Auteur :** Sajib, Md Kawsar

**Promoteur(s) :** Rigo, Philippe

**Faculté :** Faculté des Sciences appliquées

**Diplôme :** Master : ingénieur civil mécanicien, à finalité spécialisée en "Advanced Ship Design"

**Année académique :** 2022-2023

**URI/URL :** <http://hdl.handle.net/2268.2/18236>

---

*Avertissement à l'attention des usagers :*

*Tous les documents placés en accès ouvert sur le site le site MatheO sont protégés par le droit d'auteur. Conformément aux principes énoncés par la "Budapest Open Access Initiative"(BOAI, 2002), l'utilisateur du site peut lire, télécharger, copier, transmettre, imprimer, chercher ou faire un lien vers le texte intégral de ces documents, les disséquer pour les indexer, s'en servir de données pour un logiciel, ou s'en servir à toute autre fin légale (ou prévue par la réglementation relative au droit d'auteur). Toute utilisation du document à des fins commerciales est strictement interdite.*

*Par ailleurs, l'utilisateur s'engage à respecter les droits moraux de l'auteur, principalement le droit à l'intégrité de l'oeuvre et le droit de paternité et ce dans toute utilisation que l'utilisateur entreprend. Ainsi, à titre d'exemple, lorsqu'il reproduira un document par extrait ou dans son intégralité, l'utilisateur citera de manière complète les sources telles que mentionnées ci-dessus. Toute utilisation non explicitement autorisée ci-avant (telle que par exemple, la modification du document ou son résumé) nécessite l'autorisation préalable et expresse des auteurs ou de leurs ayants droit.*

---



Traditio et Innovatio



Zachodniopomorski  
Uniwersytet  
Technologiczny  
w Szczecinie



With the support of the  
Erasmus+ Programme  
of the European Union



# Assessment of Numerical Simulations for High Reynolds Flows Around the Pump Tower of a LNG Membrane Tank on a Floating Structure

A Thesis Presented for the Degree of  
Master of Science

Submitted on 21 August 2023, by  
[SAJIB, MD KAWSAR](#) | [Street No. 1 Rue de la Noë](#),  
| ZIP: 44300 | Town: Nantes  
Student ID No: 220468V

## First Reviewer:

[Dr. Eng. Florin Păcuraru](#)

Affiliation : Vice Deans,  
Head of work at [Facultatea  
de Arhitectură Navală](#)

Street No. Domneasca St. 47

ZIP City: 800008 Galati

Country: [Romania](#)

## Supervisors:

Scientific supervisor - [ECN](#):  
[Dr. Emmanuel Guilmineau](#),

Internship supervisor - [GTT](#):  
[Dr. Laurent Brosset](#)

**Contact person:** - [Prof. Dr.  
Lionel Gentaz](#)

Country: [France](#)





## **DEDICATION**

*With deep gratitude, I humbly dedicate my master's thesis to my beloved family, whose unwavering support and love have been invaluable throughout my academic journey. I have been empowered and motivated to overcome challenges and strive for excellence thanks to their encouragement and understanding. I am deeply grateful for the unfaltering backing of my mother. She has always been there for me, providing constant encouragement and motivation as I pursue my academic goals. I am extremely thankful for the chance to dedicate this work to my beloved Mehrun, Fatiha, Safura, and Ruman. In the depths of life's challenges, my thoughts became engulfed by them, and I hold onto the hope that one day they will stumble upon these words and realize the profound impact they had on me. I am tremendously thankful for my amazing EMSHIP cohort. Their constant backing has made this journey substantially less challenging than it would have been otherwise. Finally, I am overwhelmed with gratitude as I devote my work to the countless sleepless nights I have spent, tirelessly and passionately, wrestling with the challenges.*

**CONTENTS**

Dedication . . . . . 2

Nomenclature . . . . . 16

Declaration of Authorship . . . . . 17

Abstract . . . . . 18

1 Introduction . . . . . 19

    1.1 Research objectives . . . . . 26

    1.2 Outline . . . . . 26

2 Geometry . . . . . 27

3 Numerical framework . . . . . 30

    3.1  $k-\epsilon$  . . . . . 31

    3.2  $k-\omega$  . . . . . 32

    3.3  $k-\omega$  SST Menter . . . . . 33

    3.4 Hybrid URANS-LES . . . . . 35

        3.4.1 Improved delayed detached eddy simulation (IDDES) . . . . . 36

    3.5 Near wall treatment . . . . . 37

    3.6 Volume of fluid method (VOF) . . . . . 39

4 Methodology . . . . . 40

    4.1 Geometry preparation and domain setup . . . . . 43

    4.2 Boundary and initial conditions . . . . . 44

    4.3 Mesh generation . . . . . 45

    4.4 Simulation setup and solver setting . . . . . 47

    4.5 Mesh and Time step selection . . . . . 49

        4.5.1 Static Mesh . . . . . 49

4.5.2	Adaptive Refinement . . . . .	56
5	2D study of TMS - URANS $k-\omega$ SST . . . . .	67
5.1	TMS - Orientation: $30^\circ$ . . . . .	68
5.2	Comparison of 2D TMS simulation with single cylinder simulation . . . . .	76
5.2.1	Orientation: $30^\circ$ . . . . .	79
5.3	Mask Effect . . . . .	85
6	3D study of TMS . . . . .	90
6.1	Simplified 3D study - without free surface . . . . .	92
6.1.1	URANS - $k-\omega$ SST . . . . .	92
6.1.2	Hybrid URANS-LES . . . . .	99
6.1.3	Improved delayed detached eddy simulation (IDDES) . . . . .	100
6.2	R1 configuration with free surface - $30^\circ$ orientation . . . . .	105
6.2.1	URANS - $k-\omega$ SST . . . . .	105
7	Conclusion . . . . .	113
	Acknowledgement . . . . .	116
	References . . . . .	117
1	Appendices . . . . .	123
1.1	Reynolds Stress Models (RSM) . . . . .	123
1.2	Explicit Algebraic Stress Model (EASM) . . . . .	123
1.2.1	DDES . . . . .	124
1.3	Appendix : Data compilation: Single cylinder . . . . .	126
1.4	Appendix : 2D URANS $k-\omega$ SST - Six orientations . . . . .	130
1.4.1	Orientation: $0^\circ$ . . . . .	130
1.4.2	Orientation: $60^\circ$ . . . . .	136

1.4.3	Orientation: $90^\circ$ . . . . .	143
1.4.4	Orientation: $120^\circ$ . . . . .	149
1.4.5	Orientation: $180^\circ$ . . . . .	154
1.4.6	Orientation: $270^\circ$ . . . . .	160
1.5	Delayed detached eddy simulation (DDES) . . . . .	169

## LIST OF FIGURES

1	Pump tower of LNG membrane tank (technology NO96) located at aft bulkhead Figure courtesy : <a href="#">Kimmoun et al. (2020)</a> . . . . .	27
2	Tripod mast structure (TMS) - R1 and R2 configuration: Gray and Merun plane are the indications of free surface located at $Z = 5.514\text{m}$ from bottom . . . . .	28
3	Seven orientations of TMS (Counter-clockwise rotation) . . . . .	29
4	Demonstration of near-wall treatment Figure courtesy: <a href="#">Bengt et al. (2012)</a> <a href="#">Toni et al. (2018)</a> . . . . .	38
5	(a) Tandem (b) Side-by-side (c) Staggered Figure courtesy <a href="#">Sumner et al. (2010)</a>	41
6	Edge and surface capturing process in HEXPRESS: Domain creation for the TMS - R1 configuration . . . . .	44
7	2D domain for single cylinder . . . . .	44
8	Meshing step in HEXPRESS mesh wizard . . . . .	47
9	Initial coarse mesh : $Re = 110\text{k}$ . . . . .	50
10	Box1 : $Re = 110\text{k}$ . . . . .	51
11	Box2 : $Re = 110\text{k}$ . . . . .	52
12	O-type at $Re = 140\text{k}$ : Coarse mesh, $y+$ , evolution of avg. $F_x$ (note that $C_d = 2F_x$ when single cylinder case is simplified), and avg. $F_y$ (note that $C_l = 2F_y$ ) with corresponding $St$ number peak . . . . .	54
13	Mesh convergence study: O-type mesh . . . . .	55
14	O-type mesh distortion . . . . .	56
15	AGR : $Re = 110\text{k}$ . . . . .	58
16	AGR : $Re = 110\text{k}$ . . . . .	59
17	Mesh convergence study and comparison of number of cells : $Re = 140\text{k}$ . . . . .	60
18	Avg. coefficient of pressure, $C_P$ : Nomenclature . . . . .	61
19	Avg. coefficient of pressure, $C_P$ : $Re = 140\text{k}$ . . . . .	62

20	Distribution of avg. coefficient of friction, $C_f$ around the first half of the single cylinder . . . . .	64
21	Distribution of avg. coefficient of pressure, $C_p$ around the cylinder . . . . .	65
22	TMS: 30° . . . . .	67
23	Evolution of avg. coefficient of drag, $C_d$ . . . . .	68
24	Post-processing results, $\Delta t^* = 0.0050$ : 2D 30° orientation . . . . .	70
25	Number of cells: 3D URANS $k-\omega$ SST, $Tr = D/5$ (Mirror boundary condition in span-wise direction) . . . . .	70
26	Mesh: New approach (1) associated with box and AGR . . . . .	71
27	Avg. coefficient drag, $C_d$ : New approach with box+AGR vs Previous mesh . . . . .	72
28	Evolution of avg. coefficient of drag, $C_d$ : New approach vs Previous mesh . . . . .	73
29	Evolution of avg. coefficient of drag, $C_d$ . . . . .	73
30	Comparison of avg. coefficient of drag, $C_d$ : Previous mesh vs New mesh . . . . .	74
31	Post-processing results, $\Delta t^* = 0.0025$ New mesh : 2D 30° orientation . . . . .	75
32	Flow patterns : (a) Single bluff body (b) Synchronize vortex shedding (SVS) (c) Shear layer reattachment (SLR) (d) Vortex impingement (VI) (e) Extended, reattachment, and co-shedding regime for two cylinders in tandem arrangement Figure courtesy: <a href="#">Sumner et al. (2010)</a> . . . . .	77
33	The boundaries of wake and proximity interference Figure courtesy: <a href="#">Sumner et al. (2010)</a> . . . . .	78
34	Velocity contour : Orientation 30 ° . . . . .	79
35	Avg. coefficient of pressure, $C_p$ : Orientation 30 ° . . . . .	80
36	Contour of avg. coefficient of pressure, $C_p$ : Orientation 30 ° . . . . .	81
37	Vortex length : Cylinder E vs Single cylinder . . . . .	81
38	Vortex length : Cylinder F vs Single cylinder . . . . .	81
39	Avg. coefficient of pressure, $C_p$ : Cylinder Dps vs Single cylinder . . . . .	82

40	Vortex length : Cylinder Dps vs Single cylinder . . . . .	83
41	Avg. coefficient of pressure, $C_p$ : Orientation $30^\circ$ . . . . .	83
42	Vortex length : Cylinder Dsb vs Single cylinder . . . . .	84
43	Vortex length : Cylinder R vs Single cylinder . . . . .	84
44	Comparison of avg. coefficient of drag, $C_d$ and avg. coefficient of lift, $C_l$ : 2D current study : URANS - $k-\omega$ SST for all the seven orientations . . . . .	85
45	Comparison of avg. coefficient of drag, $C_d$ and lift, $C_l$ : 2D current vs 3D previous study R1 configuration with free surface <a href="#">Queutey et al. (2022)</a> : URANS - $k-\omega$ SST . . . . .	86
46	Comparison of avg. coefficient of drag, $C_d$ and lift, $C_l$ : 2D current vs 3D previous study R1 configuration with free surface <a href="#">Queutey et al. (2022)</a> : URANS - $k-\omega$ SST . . . . .	87
47	FFT analysis of 2D TMS $30^\circ$ orientation: Dimensional vs Dimensionless forms	89
48	3D domain - $30^\circ$ orientation : Simplified without free surface vs R1 configuration with free surface . . . . .	90
49	Specification of boundary condition - $30^\circ$ orientation : Simplified without free surface vs R1 configuration with free surface . . . . .	91
50	Mesh : Simplified case without free surface - Coarse vs Fine - $30^\circ$ orientation .	93
51	Evolution of avg. coefficient of drag, $C_d$ and lift, $C_l$ : 3D URANS - $k-\omega$ SST - $30^\circ$ orientations . . . . .	94
52	Comparison of avg. coefficient of drag, $C_d$ : 2D vs 3D URANS $k-\omega$ SST . . . .	95
53	3D effect: Simplified 3D without free surface - URANS $k-\omega$ SST - $30^\circ$ - First column: instantaneous velocity profile in the spanwise direction upstream, Second column: instantaneous velocity contour, Third column: instantaneous velocity profile in the spanwise direction middle of two cylinders . . . . .	96
54	Instantaneous velocity contour : 2D vs Slices in simplified 3D case - $30^\circ$ orientation	97
55	3D effect simplified case without free surface: URANS $k-\omega$ SST - Slices at X .	97
56	$Q^*$ criterion : URANS $k-\omega$ SST - Simplified 3D case without free surface . . .	98

57	Mesh : Simplified 3D without free surface IDDES - 30° orientation . . . . .	100
58	Evolution of avg. coefficient of drag, Cd and lift, Cl : Simplified 3D without free surface IDDES - 30° orientation . . . . .	100
59	3D effect: Simplified 3D without free surface - IDDES - 30° - First column: avg. velocity profile in the spanwise direction upstream, Second column: avg. velocity contour, Third column: avg. velocity profile in the spanwise direction middle of two cylinders . . . . .	101
60	Slice extracted from center to center of E-Dps in XZ plane : Avg. velocity magnitude vs Instantaneous velocity : Simplified 3D without free surface IDDES	102
61	Average (left) and instantaneous velocity contour (right) : 2D vs Slices in simplified 3D without free surface IDDES - 30° orientation . . . . .	103
62	Average (left) and instantaneous velocity contour (right) : 2D vs Slices in simplified 3D without free surface IDDES - 30° orientation . . . . .	104
63	Q* criterion : IDDES . . . . .	105
64	Mesh of R1 configuration with free surface - 30° orientation . . . . .	105
65	AGR refinement box : R1 configuration with free surface - 30° orientation . . .	106
66	Evolution of avg. coefficient of drag, Cd and lift, Cl : R1 configuration with free surface - 30° orientation . . . . .	107
67	3D effect: R1 configuration with free surface - URANS k- $\omega$ SST - 30° orientation - First row (average mass fraction, $\alpha$ , Second row, average velocity contour, Third row, average velocity profile in the spanwise direction (upstream and middle of two cylinders) . . . . .	108
68	Average (left) and instantaneous velocity contour (right) : 2D vs Slices in R1 with free surface 3D case URANS k- $\omega$ SST - 30° orientation . . . . .	109
69	Average (left) and instantaneous velocity contour (right) : 2D vs Slices in R1 configuration with free surface 3D case URANS k- $\omega$ SST - 30° orientation . . .	110
70	Comparison of avg. coefficient of drag, Cd : 2D, 3D URANS k- $\omega$ SST, IDDES, without free surface and 3D URANS k- $\omega$ SST with free surface . . . . .	111
71	Free surface : R1 configuration with free surface - 30° orientation . . . . .	111



72	Evolution of avg. coefficient of drag, $C_d$ for single cylinder from sub-critical to postcritical flow regime: EASM and RSM . . . . .	124
73	Avg. coefficient of drag, $C_d$ : Ranging from $10^4$ to $10^7$ : Experiment & Simulation	126
74	Avg. coefficient of drag, $C_d$ : Ranging from $10^4$ to $10^7$ : Experiment vs ISIS-CFD	127
75	Avg. coefficient of drag, $C_d$ : Ranging from $10^4$ to $10^7$ : Simulation vs ISIS-CFD	127
76	Avg. coefficient of base pressure, $C_{pb}$ : Ranging from $10^4$ to $10^7$ : Experiment, Simulation vs ISIS-CFD . . . . .	128
77	Strouhal number, $S_t$ : Ranging from $10^4$ to $10^7$ . . . . .	128
78	Theta separation, $\theta_{sep}$ : Ranging from $10^4$ to $10^7$ : Experiment, Simulation vs ISIS-CFD . . . . .	129
79	Post-processing results, $\Delta t^* = 0.0025$ New mesh : 2D $0^\circ$ orientation . . . . .	130
80	Velocity contour : Orientation $0^\circ$ . . . . .	130
81	Avg. coefficient of pressure, $C_p$ : Orientation $0^\circ$ . . . . .	132
82	Contour of avg. coefficient of pressure, $C_p$ : Orientation $0^\circ$ . . . . .	132
83	Vortex length : Cylinder E vs Single cylinder : Orientation $0^\circ$ . . . . .	132
84	Vortex length : Cylinder F vs Single cylinder : Orientation $0^\circ$ . . . . .	133
85	Avg. coefficient of pressure, $C_p$ : Orientation $0^\circ$ . . . . .	134
86	Vortex length : Cylinder Dsb vs Single cylinder : Orientation $0^\circ$ . . . . .	134
87	Vortex length : Cylinder R vs Single cylinder : Orientation $0^\circ$ . . . . .	134
88	$C_p$ : Cylinder Dps vs Single cylinder . . . . .	135
89	Vortex length : Cylinder Dps vs Single cylinder . . . . .	135
90	Post-processing results, $\Delta t^* = 0.0025$ New mesh : 2D $60^\circ$ orientation . . . . .	136
91	Velocity contour : Orientation $60^\circ$ . . . . .	137
92	Avg. coefficient of pressure, $C_p$ : Orientation $60^\circ$ . . . . .	138
93	Contour of avg. coefficient of pressure, $C_p$ : Orientation $60^\circ$ . . . . .	138

94	Vortex length : Cylinder E vs Single cylinder . . . . .	139
95	Vortex length : Cylinder F vs Single cylinder . . . . .	139
96	Avg. coefficient of pressure, $C_p$ : Orientation $60^\circ$ . . . . .	140
97	Vortex length : Cylinder Dsb vs Single cylinder . . . . .	140
98	Vortex length : Cylinder R vs Single cylinder . . . . .	141
99	$C_p$ : Cylinder Dps vs Single cylinder . . . . .	141
100	Vortex length : Cylinder Dps vs Single cylinder . . . . .	142
101	Post-processing results, $\Delta t^* = 0.0025$ New mesh : 2D $90^\circ$ orientation . . . . .	143
102	Velocity contour : Orientation $90^\circ$ . . . . .	143
103	Avg. coefficient of pressure, $C_p$ : Orientation $90^\circ$ . . . . .	144
104	Contour avg. coefficient of pressure, $C_p$ : Orientation $90^\circ$ . . . . .	145
105	Vortex length : Cylinder E vs Single cylinder . . . . .	145
106	Vortex length : Cylinder F vs Single cylinder . . . . .	146
107	Avg. coefficient of pressure, $C_p$ : Orientation $90^\circ$ . . . . .	146
108	Vortex length : Cylinder Dsb vs Single cylinder . . . . .	147
109	Vortex length : Cylinder R vs Single cylinder . . . . .	147
110	$C_p$ : Cylinder Dps vs SC . . . . .	148
111	Vortex length : Cylinder Dps vs Single cylinder . . . . .	148
112	Post-processing results, $\Delta t^* = 0.0025$ New mesh : 2D $120^\circ$ orientation . . . . .	149
113	Velocity contour : Orientation $120^\circ$ . . . . .	149
114	Avg. coefficient of pressure, $C_p$ : Orientation $120^\circ$ . . . . .	150
115	Contour avg. coefficient of pressure, $C_p$ : Orientation $120^\circ$ . . . . .	150
116	Vortex length : Cylinder E vs Single cylinder . . . . .	151
117	Vortex length : Cylinder F vs Single cylinder . . . . .	151

118	Avg. coefficient of pressure, $C_p$ : Orientation $120^\circ$ . . . . .	152
119	Vortex length : Cylinder Dsb vs Single cylinder . . . . .	152
120	Vortex length : Cylinder R vs Single cylinder . . . . .	152
121	$C_p$ : Cylinder Dps vs Single cylinder . . . . .	153
122	Vortex length : Cylinder Dps vs Single cylinder . . . . .	153
123	Post-processing results, $\Delta t^* = 0.0025$ New mesh : 2D $180^\circ$ orientation . . . . .	154
124	Velocity contour : Orientation $180^\circ$ . . . . .	155
125	Avg. coefficient of pressure, $C_p$ : Orientation $180^\circ$ . . . . .	155
126	Contour of avg. coefficient of pressure, $C_p$ : Orientation $180^\circ$ . . . . .	156
127	Vortex length : Cylinder E vs Single cylinder . . . . .	156
128	Vortex length : Cylinder F vs Single cylinder . . . . .	157
129	Avg. coefficient of pressure, $C_p$ : Orientation $180^\circ$ . . . . .	157
130	Vortex length : Cylinder Dsb vs Single cylinder . . . . .	157
131	Vortex length : Cylinder R vs Single cylinder . . . . .	158
132	$C_p$ : Cylinder Dps vs Single cylinder . . . . .	158
133	Vortex length : Cylinder Dps vs Single cylinder . . . . .	159
134	Post-processing results, $\Delta t^* = 0.0025$ New mesh : 2D $270^\circ$ orientation . . . . .	160
135	Velocity contour : Orientation $270^\circ$ . . . . .	160
136	Contour of avg. coefficient of pressure, $C_p$ : Orientation $270^\circ$ . . . . .	161
137	Contour avg. coefficient of pressure, $C_p$ : Orientation $270^\circ$ . . . . .	162
138	Vortex length : Cylinder E vs Single cylinder . . . . .	162
139	Vortex length : Cylinder F vs Single cylinder . . . . .	163
140	Avg. coefficient of pressure, $C_p$ : Orientation $270^\circ$ . . . . .	163
141	Vortex length : Cylinder Dsb vs Single cylinder . . . . .	164

142	Vortex length : Cylinder R vs Single cylinder . . . . .	164
143	Cp: Cylinder Dps vs Single cylinder . . . . .	165
144	Vortex length : Cylinder Dps vs Single cylinder . . . . .	165
145	Evolution of avg. coefficient of drag, Cd : Seven orientations . . . . .	166
146	Evolution of avg. coefficient of lift, Cl : Seven orientations . . . . .	167
147	Avg. tangential wall shear stress (WSSx) vs $\theta$ : Seven orientations . . . . .	168
148	DDES simulation: Excessive mesh refinement . . . . .	169
149	Evolution of avg. Cd, and Cl: DDES simulation . . . . .	169

## LIST OF TABLES

1	Dimension and location of individual members of tripod mast . . . . .	28
2	Reynolds and Froude number for each in TMS cylinder during operation . . . . .	40
3	Flow Regimes based on Re numbers . . . . .	40
4	Reynolds number range for Single cylinder simulation . . . . .	41
5	Domain specification : Rectangular and O-type (unit in m) . . . . .	43
6	Mesh wizard setup in HEXPRESS . . . . .	46
7	Simulation setup and solver setting . . . . .	48
8	Mesh information : Coarse . . . . .	49
9	Mesh information : Refinement box 01 . . . . .	51
10	Mesh information : Refinement box 02 . . . . .	53
11	Mesh information : O-type . . . . .	53
12	Hydrodynamic parameters : O-type Mesh . . . . .	54
13	Adaptive grid refinement settings . . . . .	57
14	Single cylinder simulation at subcritical Re (140k) with a range of time steps and threshold values . . . . .	61
15	Previous study : Re = 140k . . . . .	62
16	Single cylinder simulation from subcritical to post-critical range ( $Tr = D/10$ unless specified) . . . . .	66
17	Dimensional time step, $\Delta T$ calculation . . . . .	67
18	Changes in simulation setup and solver setting for 2D 30° TMS simulation (here, $D = 0.61$ m, diameter of cylinder E) . . . . .	68
19	Comparison of avg. coefficient drag, $Cd$ : $\Delta t^* = 0.0050$ vs $0.0025$ . . . . .	69
20	Mesh properties : Approach 1 (Here, $D = 0.2$ , Diameter of cylinder R) . . . . .	71
21	Mesh properties : Approach 2 (Here, $D = 0.2$ , Diameter of cylinder R) . . . . .	72

22	Comparison of avg. coefficient drag, $C_d$ : Previous mesh vs New mesh . . . . .	74
23	Hydrodynamic parameters: $30^\circ$ orientation . . . . .	84
24	Cylinders relative distance and incident angle : $30^\circ$ orientation . . . . .	84
25	Mask effect: 2D URANS $k-\omega$ SST - All orientations . . . . .	85
26	Avg. coefficient of drag, $C_d$ law utilized by GTT . . . . .	87
27	Strouhal number in drag, $St_{Cd}$ and lift $St_{Cl}$ directions for cylinders of all orientations. . . . .	88
28	Strouhal number in drag, $St_{Cd}$ and lift $St_{Cl}$ for single cylinders. . . . .	88
29	Avg. coefficient of drag, $C_d$ : 2D vs 3D URANS $k-\omega$ SST - $30^\circ$ orientations . .	95
30	Comparison of avg. coefficient of drag, $C_d$ : Simplified case (2D URANS $k-\omega$ SST, 3D URANS $k-\omega$ SST, IDDES without free surface) vs 3D URANS $k-\omega$ SST (with free surface) . . . . .	110
31	Hydrodynamic parameters: $0^\circ$ orientation . . . . .	135
32	Cylinders relative distance and incident angle : $0^\circ$ orientation . . . . .	136
33	Hydrodynamic parameters: $60^\circ$ orientation . . . . .	142
34	Cylinders relative distance and incident angle : $60^\circ$ orientation . . . . .	142
35	Hydrodynamic parameters: $90^\circ$ orientation . . . . .	148
36	Cylinders relative distance and incident angle : $90^\circ$ orientation . . . . .	148
37	Hydrodynamic parameters: $120^\circ$ orientation . . . . .	153
38	Cylinders relative distance and incident angle : $120^\circ$ orientation . . . . .	154
39	Hydrodynamic parameters: $180^\circ$ orientation . . . . .	159
40	Cylinders relative distance and incident angle : $180^\circ$ orientation . . . . .	159
41	Hydrodynamic parameters: $270^\circ$ orientation . . . . .	165
42	Cylinders relative distance and incident angle : $270^\circ$ orientation . . . . .	166

## NOMENCLATURE

$AR$	aspect (slenderness) ratio	$C_d$	mean drag coefficient
$C_l$	mean lift coefficient	$C_p$	mean pressure coefficient
$f$	vortex shedding frequency (Hz)	$C_{pb}$	mean base pressure coefficient
$G$	gap width (m)	$D$	cylinder diameter (m)
$L$	center to center longitudinal spacing (m)	$H$	cylinder height (m)
$T/D$	transverse pitch ratio	$T$	center to center transverse spacing (m)
$l_f$	vortex formation length	$L/D$	longitudinal pitch ratio
$P/D$	pitch ratio	$P$	center to center spacing (pitch) (m)
$S_t$	Strouhal number	$Re$	Reynolds number
$X$	streamwise coordinate (m)	$U$	free stream velocity
$Z$	vertical coordinate (m)	$Y$	cross-stream coordinate (m)
$\mu$	dynamic viscosity (pa.s)	$\alpha$	incident angle ( $^\circ$ )
$\theta_{sep}$	flow separation angle ( $^\circ$ )	$\rho$	density ( $\text{kg}/\text{m}^3$ )
$\Delta T$	dimensional time step (s)	$C_f$	skin friction coefficient
$SBB$	single bluff body	$\Delta t^*$	dimensionless time step
$TMS$	tripod mast structure	$SLR$	shear layer reattachment
$\alpha$	average mass fraction	$SC$	single cylinder

## **DECLARATION OF AUTHORSHIP**

I declare that this thesis and the work presented in it are my own and have been generated by me as the result of my own original research.

Where I have consulted the published work of others, this is always clearly attributed.

Where I have quoted from the work of others, the source is always given. With the exception of such quotations, this thesis is entirely my own work.

I have acknowledged all main sources of help.

Where the thesis is based on work done by myself jointly with others, I have made clear exactly what was done by others and what I have contributed myself.

This thesis contains no material that has been submitted previously, in whole or in part, for the award of any other academic degree or diploma.

I cede copyright of the thesis in favour of the Ecole Centrale de Nantes.



## ABSTRACT

Gaztransport Technigaz (GTT), a French naval engineering company, focuses on producing cryogenic membrane containment systems for storing and transporting LNG (liquefied natural gas). The Morison equation is used to determine hydrodynamic loads on the tubular Tripod mast structure (TMS). The fact that Morison equation cannot exhibit a mask effect, therefore GTT aims to evaluate the design phase using high-fidelity ISIS-CFD simulation. The previous study utilized a  $k-\omega$  SST turbulence model to forecast unsteady dynamics, suggesting a better temporal and spatial resolution could improve unsteady dynamics prediction. The first stage of the present study involved simulations of a single cylinder at different Reynolds numbers, spanning from sub-critical ( $O(10^4)$ ) to postcritical ( $O(10^7)$ ) flow regimes, to determine optimal temporal and spatial resolution. Two-dimensional simulations of TMS were performed using the resolutions from the first phase. 3D simulations were conducted using URANS  $k-\omega$  SST and hybrid RANS-LES (IDDES) turbulence models, simplifying the 3D case to assess the 3D effect in the spanwise direction. The final phase involved 3D simulation with a free surface using the URANS  $k-\omega$  SST turbulence model. The present investigation relating to single cylinders showed satisfactory agreement with the existing numerical studies documented in the literature over the whole spectrum of flow regimes. The results indicated that the eddy viscosity-based turbulence model is unable to accurately predict the coefficient of drag in the sub-critical to critical flow regime seen in the experiment, mostly owing to inherent limitations. Nevertheless, the research exhibited a high level of conformity with the experimental findings from the super-critical flow regime. The two-dimensional investigation of TMS showed promising results in comparison to the preceding 3D study, therefore highlighting the impact of enhanced temporal and spatial resolution. The present study conducted an in-depth examination of the 3D effects in the spanwise direction. This investigation revealed the presence of 3D effect which was absent in the two-dimensional (2D) study. The 3D hybrid RANS-LES demonstrated a successful capture of a wide range of the Kolmogorov turbulence spectrum. The presence of the free surface effect was evident when compared to the simpler 3D case. The mask effect was observed across all situations (involving both 2D and 3D cases) and utilizing various turbulence models. The investigation showed that URANS ( $k-\omega$  SST) turbulence model has the capability to accurately represent the unsteady dynamic of the flow, as long as appropriate temporal and spatial resolutions are maintained. The computing cost of 2D flow simulations was lower compared to 3D simulations, however, it could provide accurate predictions of hydrodynamic parameters. The hybrid RANS-LES approach should be evaluated using the identified temporal and spatial resolution for each orientation.

# 1 INTRODUCTION

Circular cylinders are categorized as semi-aerodynamic bodies, in contrast to aerodynamic bodies like airfoils, and non-aerodynamic forms with sharp edges like squares. Aerodynamic bodies are designed to prevent flow separation, whereas non-aerodynamic bodies exhibit fixed separations at specific corners. The location of separation on semi-aerodynamic bodies is subjected to variation based on factors such as free-stream velocity, flow profile, turbulence at free-stream, geometry, and surface roughness of the bodies [Niemann et al. \(1990\)](#). Researchers face challenges in understanding the flow around circular cylinders due to their complexity and transient wake. The flow dynamics surrounding a circular cylinder provide a complex and visually captivating phenomenon [Rajani et al. \(2012\)](#). The study of the flow of an incompressible fluid around a circular cylinder aims to assess structural loading caused by vortex shedding, potentially reducing device efficiency and requiring higher resolution in design and development solutions [Stringer et al. \(2014\)](#). Furthermore, it is of utmost significance in engineering applications spanning from the utilization of heat exchangers to the assessment of wind loads on bridges, offshore structures, chimneys, nuclear powerplant, cooling systems, electronic chips, air ventilation of pipelines, and the load assessment on the pump towers within LNG tanks on floating structures. [Niemann et al. \(1990\)](#), [Prafull et al. \(2022\)](#) [Kimmoun et al. \(2020\)](#).

Numerous renowned researchers have extensively experimented to study the flow around cylinders, including [Tritton \(1959\)](#), [Roshko \(1955\)](#), and [Achenbach \(1968\)](#), among many others. The classification of flow by regimes of vortex shedding with Reynolds number ( $Re$ ) was one of the main findings of those works. With the development of numerical modeling, the complexity of the turbulent wake has undergone several new discoveries. Numerous scholars have improved the flow regimes around cylinders as the Reynolds number rises, most notably [Zdravkovich \(1990\)](#), who identified 15 different ranges [Stringer et al. \(2014\)](#). Recently [Rodriguez et al. \(2017\)](#) restated from [Achenbach \(1971\)](#) that, there are four main flow regimes: sub-critical with laminar separation, critical with a rapid decrease in drag coefficient, and an asymmetric laminar separation bubble (LSB), supercritical with a plateau in drag and two symmetric LSBs followed by turbulent separation, and transcritical with purely turbulent separation. The detailed explanation of the four regimes states, (1) Within the subcritical range, the boundary layer maintains a laminar flow pattern over its whole circumference until the occurrence of separation. Laminar separation is seen to transpire at an angular distance denoted as  $\phi_s$ , which typically ranges between 70 and 80 ° from the stagnation point. The drag coefficient has a relatively weak dependence on the Reynolds number. (2) The critical regime refers to a transitional region that exists between laminar and turbulent separation. The occurrence of a typical reduction in  $C_d$  to a minimal value at the critical Reynolds number, denoted as  $Re_{crit}$ , is seen where the pri-

mary laminar separation is observed. At critical Re number, the turbulent boundary layer has the ability to maintain the adverse pressure gradient over extended distances, resulting in the downstream displacement of the separation point. This phenomenon results in an elevation in the base pressure exerted on the rear side of the cylinder, hence leading to a decrease in drag. The manifestation of the phenomenon commonly referred to as the 'Drag Crisis' [Rajani et al. \(2012\)](#). Directly next to it, there is an abrupt shift towards turbulent conditions in the free shear layer, subsequently leading to turbulent reattachment. Ultimately, a turbulent separation ensues. The area defined by the laminar separation and turbulent reattachment is commonly referred to as the "separation bubble". (3) The presence of a bubble on a smooth surface may be observed throughout a broad range of Reynolds numbers, extending up to 1.5M ( $1.5 \times 10^6$ ). The current phase of flow is commonly referred to as the supercritical stage. The observed phenomenon is distinguished by a consistently low drag coefficient, which exhibits separation occurring at around  $\phi_s = 140^\circ$  on a smooth surface. (4) In the transcritical regime, the bubble ceases to exist and the separation becomes turbulent. In the study conducted by [Roshko \(1961\)](#), the change of the transition point from laminar to turbulent boundary layer flow has occurred in an upstream direction and is in close proximity to the stagnation point, namely at a stagnation angle of  $\phi_t = 20^\circ$ . The separation of the boundary layer occurs at lower angles, namely  $\phi_s = 110^\circ$  on a smooth surface, as a result of increased friction loss. Consequently, the drag experienced is greater in comparison to the supercritical range. The presence of turbulence in free streams has a significant impact on transitional phenomena, such as mean drag, Strouhal number, and mean pressure distribution. The phenomenon induces random variations in the aerodynamic forces of lift, drag, and local pressure, thereby impacting the spanwise relation of vortex shedding. When analyzing structures subjected to atmospheric turbulence, it is imperative to incorporate these effects into the estimation of the average and fluctuating forces [Niemann et al. \(1990\)](#).

Numerous research ([Zdravkovich \(1990\)](#), [Achenbach \(1968\)](#), and [Roshko \(1961\)](#)) have provided empirical evidence indicating a drop in the drag coefficient within the Subcritical Reynolds number range, from around 1.2 to approximately 0.3 in the Supercritical flow domain. According to [Bearman et al. \(1969\)](#), a decrease in drag is followed by a rise in shedding frequency, and vice versa. Based on the obtained measurements, it is worth noting that when the Reynolds number is increased to  $Re > 3.4M$  ( $3.4 \times 10^6$ ), there is a steady enhancement in the drag coefficient, eventually reaching about 0.7. As the Reynolds number (Re) approaches a magnitude of 10M ( $10^7$ ), the transition to turbulence is observed to occur in greater proximity to the front stagnation point. Consequently, a state of complete turbulence is observed both in the vicinity of the cylinder and within the wake area [Rajani et al. \(2012\)](#). An experimental study was conducted by [Jones et al. \(1969\)](#) using a wind tunnel to examine the aerodynamic forces acting on a stationary and oscillating circular cylinder in two-dimensional flow. The Reynolds numbers considered

ranged from 360k ( $0.36 \times 10^6$ ) to 18.70M ( $18.70 \times 10^6$ ). The static-pressure distribution remains consistent above a Reynolds number of 8M ( $8 \times 10^6$ ), the mean drag coefficient is roughly 0.54, and the Strouhal number is approximately 0.3. The  $C_d$  experiences a slight decrease to 0.52 at a Reynolds number of 10M ( $10^7$ ). The Reynolds number equal to 17.82M ( $17.82 \times 10^6$ ), falls within the range associated with primarily turbulent flow. The observed distributions exhibit a higher degree of symmetry compared to those observed at Reynolds numbers below 6M ( $6 \times 10^6$ ). The range of Reynolds numbers spanning from 8.27M ( $8.27 \times 10^6$ ) to 18.70M ( $18.70 \times 10^6$ ), the impact of elevating the Reynolds number on the pressure distribution was found to be minimal, with the exception of a marginal augmentation in the magnitude of negative pressure peaks. In the range of Reynolds numbers ranging from 8M ( $8 \times 10^6$ ) to 17M ( $17 \times 10^6$ ), it has been observed that the Strouhal number remains rather constant, with an approximate value of 0.3.

Prior research conducted by [Roshko \(1954, 1955\)](#) and [Eppler \(1954\)](#) has provided evidence supporting the effectiveness of employing a free-streamline flow model to depict the mean flow in the vicinity of the cylinder. In this particular model, a fixed wake width, denoted as  $d_w$ , is considered in relation to the diameter of the cylinder, represented as  $d$ . The subcritical zone is seen when the separation occurs at the front of the cylinder, and the rate of change of the width with respect to the distance along the cylinder,  $d_w/d$ , is more than 1. Conversely, for supercritical and transcritical flow, the separation occurs at the rear of the cylinder and  $d_w/d$ , is less than 1. The asymptotic behavior of flow as the Reynolds number approaches infinity remains unresolved. The impact of augmenting Reynolds number beyond transcritical  $Re$  value is unlikely, as boundary-layer transitions on cylinders can only proceed continuously. This factor may affect the separation point location, but it is unlikely to cause immediate or significant changes. The influence of Reynolds number on flow characteristics in the wake region remains a subject of inquiry [Roshko \(1961\)](#).

Flow around a circular cylinder involves three transitions: near wake, along free shear layers, and along boundary layers. These transitions are sensitive to disturbances like free stream turbulence and surface roughness, which can cause obliteration of some flow regimes and move the transition state to lower Reynolds numbers. The first transition state manifests when the orderly vortices undergo a change from laminar to turbulent flow as a consequence of three-dimensional perturbations occurring further downstream. The second transition is observed in free-shear layers, where it migrates in the upstream direction towards the separation point as the Reynolds number increases. The third transition pertaining to separation, observed in the context of spheres and cylinders, exerts the most significant influence on the drag force. The occurrence of the fourth transition state is observed in boundary layers that are located at a considerable distance from the separation point. The ultimate turbulent condition of fluid motion is reached when the free shear, wake, and boundary layers have all transitioned into a completely turbu-

lent state. The post-critical phase proposed by Batchelor (1956) is a theoretical concept, but, in practice, actual flows at high Reynolds numbers will introduce additional influencing parameters before the Reynolds number approaches infinity. Hence, the applicability of computation of flow when  $Re \rightarrow \infty$  to wind and oceanic engineering structures remains questionable and this specific state is somewhat unknown and requires further examination Zdravkovich (1990).

The organization of numerous cylinders in a cross-flow configuration introduces complexities in the interactions between shear layers, vortices, and wakes, as compared to the flow over a single cylinder. The primary configurations of twin cylinders in cross-flow consist of three arrangements: (1) Tandem, (2) Side-by-side and (3) Staggered. When the spacing between cylinders is sufficiently large, the flow of fluid across the circular cylinder is considered two-dimensional. The primary factors that influence the flow behavior are the spacing between the cylinders, the orientation of the circular cylinders in relation to the incoming fluid flow, and the fluid velocity Sumner et al. (2010). Researchers tend to prioritize the examination of tandem and side-by-side arrangements over staggered ones. However, in the context of engineering applications, it holds more practical significance. The geometric characteristics of various configurations are determined by the longitudinal (L) and transverse (T), and pitch (P) spacing as seen in Figure 5. These distances are commonly expressed in a non-dimensional manner, using either transverse (T/D) or longitudinal (L/D), pitch ratios (P/D). In the case of tandem, side-by-side, and staggered arrangements, several researchers have opted to employ the gap width, denoted as G, as a substitute for both transverse and longitudinal spacing Prafull et al. (2022). The parameter denoted as the stagger or incident angle ( $\alpha$ ) is employed to describe the geometric configuration of a staggered arrangement. Researchers have categorized fluid dynamics in the wake of numerous cylinders into four zones based on interference. Various methodologies, such as theoretical analysis, experimental investigation, and numerical simulation, can be employed to understand fluid dynamics within the wake interference zone. (1) Proximity interference occurs when interference phenomena are found in close proximity, with a large incident angle of  $\alpha$ . In the side-by-side arrangement, weak flow results in a single bluff body (SBB) and vortex street, with a broad and narrow street within the intermediate range of  $\alpha$  and P Wang et al. (2005). (2) Wake interference is a phenomenon observed in tandem configurations with multiple cylinders, where one cylinder is partially or fully submerged in the wake generated by the others. The upstream cylinder functions independently, while the downstream cylinder is affected by the upstream cylinder's effects Sumner et al. (2010), Zdravkovich (1987), and Zdravkovich (1984). (3) Wake and proximity interference occurs in tandem and staggered arrangements with narrow separation, affecting the wake region of the upstream cylinder affected by the downstream cylinder. Various flow topologies can be observed in this situation Prafull et al. (2022). (4) Absence of interference: In the event that the distance between the cylinders is substantial, it may be inferred

that there will be no occurrence of interference between them under any circumstances [Sumner et al. \(2010\)](#). Numerical simulations are a recent approach to studying flow patterns in cylinders, but their effectiveness is lower compared to experimental methods due to the complex nature of the flow. Experimental studies often focus on the subcritical region, with Reynolds numbers between 300 and 140k. The study conducted by [Hu et al. \(2019\)](#) demonstrated that the influence of the length-to-diameter ratio ( $L/D$ ) on the Strouhal number ( $St$ ) for high Reynolds numbers equal to 3M exhibits a stepwise increase at  $L/D = 3.5$ . When the  $L/D$  ratio exceeds 3.5, the  $St$  value is seen to be higher for a Reynolds number of 3M compared to a Reynolds number of 22k. The supercritical regime is characterized by a higher  $St$  value. According to the numerical study of [Kitagawa et al. \(2008\)](#), it was shown that for  $L/D$  values less than 3, there is a decrease in  $St$  as the  $L/D$  number grows. Cylinders have the potential to exhibit the characteristics of a single bluff body (SBB) when positioned in close proximity, resulting in intricate wake flow patterns and interactions with vortex streets [Prafull et al. \(2022\)](#). To enhance comprehension of the distinctive frequency of wake, an examination is conducted on the spectral response of the  $C_d$  signal. Additionally, the unique patterns of  $C_d$ , which are attributed to various wake topologies, result in the division of the drag signal into  $C_d$ -narrow wake and  $C_d$ -wide wake. The wide wake (WW) promotes lower frequencies in contrast to the narrow wake (NW) [Thiago et al. \(2022\)](#). The impact of the Reynolds number is somewhat less pronounced in the case of the tandem configuration. There exist three distinct flow patterns that may be observed in side-by-side arrangements. These patterns are categorized as follows: (1) Single bluff body (SBB) behavior at a Low pitch ratio (2) Biased flow pattern, and (3) Parallel vortex street, which is observed in arrangements with high pitch ratios [Prafull et al. \(2022\)](#).

Variations in experimental published results can be attributed to secondary differences between experimental facilities. Parameters like free-stream turbulence, surface finish, aspect ratio, end constraints, and wind tunnel blockage significantly affect flow patterns. Turbulence intensity affects force coefficients similarly to the Reynolds number. At large turbulence intensities, pressure distribution asymmetry results in a mean lift force, which can be in either direction [West et al. \(1993\)](#).

The numerical modeling of flow around a circular cylinder in the drag-crisis zone poses significant challenges for turbulence models due to the occurrence of laminar-turbulent transition and variable-locus separation in the boundary layer. There has been a scarcity of research discoveries in recent years pertaining to the time-dependent numerical modeling of three-dimensional flow around a circular cylinder. Those researches are conducted by [Tamura et al. \(1990\)](#), [Karniadakis et al. \(1992\)](#), [Mittal et al. \(1997\)](#), [Mittal et al. \(2001\)](#), [Kakuda et al. \(2006\)](#), and [Rajani et al. \(2009\)](#). In addition, a significant portion of these complex three-dimensional flow computations are limited to the laminar flow domain, particularly at exceedingly low Reynolds numbers rang-



ing from 200 to 300. To provide an accurate representation of the flow scenario, it is crucial to effectively replicate the phenomena of transition and turbulence when the Reynolds number rises [Rajani et al. \(2012\)](#).

The high Reynolds number  $k-\epsilon$  model is widely used in commercial CFD codes, but it has several shortcomings, particularly in the subcritical flow regime, where a drag crisis occurs. The Shear Stress Transport turbulence model (SST) was developed by [Menter \(1994\)](#) and uses a  $k-\omega$  model for near-wall turbulence and  $k-\epsilon$  outside the boundary layer. It is chosen for the study due to its availability in both solvers and its preference for high shear conditions over alternative mainstream models [Stringer et al. \(2014\)](#). [Franke et al. \(1989\)](#) and [Tutar et al. \(2001\)](#) evaluated [Cantwell et al. \(1983\)](#) experiments at  $Re = 140k$  ( $1.4 \times 10^5$ ), using URANS with the standard high Reynolds number  $k-\epsilon$  model and non-linear  $k-\epsilon$  models. Both studies found that  $k-\epsilon$  models inaccurately predicted flows with strong anisotropic turbulence. [Catalano et al. \(2003\)](#) studied drag coefficients, pressure distribution, and Strouhal number for Reynolds numbers 1M ( $1 \times 10^6$ ), 2M ( $2 \times 10^6$ ), and 4M ( $4 \times 10^6$ ), and Strouhal number for  $Re = 1M$  using URANS with the standard high Reynolds number model. Results were satisfactory with experimental data [Ong et al. \(2009\)](#). [Ong et al. \(2009\)](#) evaluated the  $k-\epsilon$  transport model at critical and supercritical  $Re$  values of 1M ( $1.0 \times 10^6$ ) and 3.6M ( $3.6 \times 10^6$ ). They found that force and shedding frequencies fell within known limits, but pressure distribution and shear stress showed some divergence [Stringer et al. \(2014\)](#). The impact of turbulence models on the calculated mean drag coefficient appears to be insignificant until the Reynolds number ( $Re$ ) surpasses 69K ( $6.9 \times 10^4$ ). Nevertheless, it has been shown that there is a significant reduction in drag when the Reynolds number surpasses 69k. The use of the SA model in computational analysis reveals a notable reduction in performance at a Reynolds number of 100k ( $10^5$ ). Consequently, this results in a substantial underestimating of the drag coefficient,  $C_d$  when compared to the empirical data. Nevertheless, it is worth mentioning that there is a significant reduction in the drag coefficient,  $C_d$  at a Reynolds number of 140k, occurring slightly earlier than what is observed in the experimental data [Rajani et al. \(2012\)](#). The URANS outcomes were unable to anticipate the occurrence of the drag crisis, may be attributed to their limited capability in forecasting the transition of the boundary layer [Vaz et al. \(2007\)](#), [Ye et al. \(2017\)](#). Several investigations have been conducted with hybrid RANS-LES simulations, as documented by [Moussaed et al. \(2014\)](#), [Lakshmipathy et al. \(2010\)](#), and [Pereira et al. \(2018\)](#).

Recent years have shown a growing interest in hybrid RANS-LES approaches for high-fidelity simulations of massively separated flows. These models aim to overcome the limitations of RANS and the computational cost of Large Eddy Simulation (LES), which is too demanding for practical use. However, many industrial applications have too large Reynolds numbers making hybrid RANS-LES models or wall-modeled LES approaches mandatory. The RANS equations

are active near solid walls, while LES is used in separated flow regions where larger eddies can be resolved. The hybrid RANS/LES approach combines the most favorable aspects of RANS and LES, aiming to reduce near-wall grid resolution [Bassi et al. \(2012\)](#). The RANS approach is limited in accuracy for more complex flows, such as bluff-body flow separation. The superior performance of LES stems from the capability to explicitly resolve larger scales of turbulence, which significantly contribute to the transport of mass, momentum, and energy in the flow. The impact of laminar or turbulent states in upstream regions on massive separation in downstream regions remains unclear. Current numerical methods, like DNS and DLES, face challenges in modeling transitions and massive separations [Guangxing et al. \(2020\)](#). Transcritical flow regimes are more forgiving due to narrower wake and less intense vortex shedding [Michael et al. \(2015\)](#). [Catalano et al. \(2003\)](#) and [Singh et al. \(2005\)](#) reported few numerical results for (for  $Re > 1M$ ). They applied 3D Large Eddy Simulation (LES), for  $500k < Re < 4M$ . [Singh et al. \(2005\)](#) conducted studies using a 2D LES method for flow rates  $100 < Re < 10M$ . They found that the LES method was more accurate than URANS at  $Re \sim 1M$ . However, they noted that the LES results became less accurate at higher Reynolds numbers due to insufficient grid resolution [Ong et al. \(2009\)](#). [Catalano et al. \(2003\)](#) conducted an additional investigation on Large Eddy Simulation (LES), focusing on Reynolds numbers of 500k and 1M. The findings of this study demonstrated promising outcomes in the accurate estimation of the local pressure coefficient. Nonetheless, the skin-friction distribution estimated exhibited similarities to the differences seen in the study conducted by [Travin et al. \(2000\)](#). [Singh et al. \(2005\)](#) conducted two-dimensional simulations without a subgrid-scale (SGS) model. The drag coefficients are significantly overestimated in both the sub-critical and super-critical regimes. The utilization of the G4 mesh, which consists of 1.7 million cells, results in somewhat reduced values for  $C_d$  and  $C_{pb}$ . This suggests that there may be an influence of grid size on the accuracy of the simulations. Several investigations have observed that grid refinement leads to a reduction in  $C_d$  [Travin et al. \(2000\)](#), [Moussaed et al. \(2014\)](#), [Lo et al. \(2005\)](#), and [Breuer et al. \(2000\)](#). Based on the aforementioned analysis, it can be inferred that the SA-DDES hybrid RANS model is unable to accurately simulate the drag crisis due to its deficiency in incorporating a mechanism for laminar-turbulent transition. RANS-LES hybrid models effectively capture the turbulent flow field to a greater extent compared to RANS models. However, it is important to note that this holds true only in cases when the flow field is genuinely turbulent, without the presence of complicating factors such as laminar-turbulent transition. The notion is optimistic, given that hybrid models are often regarded as the prospective approach for turbulence modeling in the context of actual engineering flows. However, this also implies the need of ensuring that hybrid models possess the capability to effectively manage the transition from laminar to turbulent flow, in order to establish their reliability as instruments for conducting such simulations [Athkuri et al. \(2023\)](#).



## 1.1 Research Objectives

The tubes and other components of the *Tripod mast* (see Figure 2) are subjected to hydrodynamic loads induced by waves generated by liquefied natural gas (LNG) and inertial loads associated with the movements of the floating structure. The hydrodynamic loads under concern are evaluated at GTT using the Morison formula, which involves a localized calculation of the fluid's relative velocities and accelerations in respect to the ship's reference point. The estimation is achieved by the utilization of numerical simulation, employing the incompressible Navier-Stokes solver called DIVA3D. The simulations proceed without taking into account the presence of the mast. GTT has utilized the Morison formula as a means of estimating forces during the design process. However, GTT seeks to improve the approach by utilizing high-fidelity ISIS-CFD simulations to account for the existence of the mast [Queutey et al. \(2022\)](#). In accordance with the suggestions put out by prior research on 3D RANS, (1) It is essential to conduct a more comprehensive investigation to find out improved temporal and spatial resolution (2) It is advised to conduct a research utilizing hybrid RANS-LES turbulence model. Hence, the present work aims to investigate for achieving improved temporal and spatial resolution. Subsequently, RANSE simulations will be conducted for different orientations of TMS. Finally, the hybrid RANS-LES turbulence model will be subjected to testing.

## 1.2 Outline

[Chapter 1](#) demonstrates the literature review and the potential research gap which will be performed in the current study. [Chapter 2](#) provides a geometric description of the *Tripod mast structure (TMS)* that is installed in the LNG membrane tank, which has been designed by *Gaz Transport and Technigaz (GTT)*. The turbulence models are discussed in detail in [Chapter 3](#). [Chapter 4](#) discusses the various steps involved in the simulation process, starting from geometry preparation and extending to the imposition of boundary conditions, mesh generation, simulation, and solver settings. This chapter also covers the topics of mesh and time step selection, which will be utilized in later sections. The chapter is of profound importance as it provides a detailed description of the domain and the types of mesh selection. In [Chapter 5](#), the TMS simulation will be conducted in two dimensions, exploring various orientations. In this chapter, issues related to the chosen spatial resolution from [Chapter 4](#) will be discussed. An alternative solution will be proposed to carry out 3D studies. Furthermore, it describes the masking effect for each cylinder in different orientations. [Chapter 6](#) studies the 3D simulations, which take into account the applicable spatial resolution derived from 2D simulations. This will compare various turbulence models using different geometrical approaches. The [Chapter 7](#) section will offer final remarks, while the [Appendices 1](#), will provide additional details about the studies.

## 2 GEOMETRY

Floating structures, such as LNG carriers, FLNG (Floating Liquefied Natural Gas) units, FSRU (Floating Storage Regasification Units), LFS (LNG Fueled Ships), and LBV (LNG Bunker Vessels), employ LNG membrane tanks. These tanks store liquefied gas in a state of close thermodynamic equilibrium at a temperature of  $-162^{\circ}$  under atmospheric conditions. The volumetric capacity of liquefied natural gas (LNG) tanks exhibits variation across various types of floating constructions. The range of storage capacity of a tank varies from a few thousand cubic meters for small-scale applications like Liquefied Natural Gas Fuel Systems (LFS) to  $55,000 \text{ m}^3$  for the biggest Liquefied Natural Gas (LNG) carriers. The tanks possess a prismatic form which is designed by GTT, characterized by smaller chamfers at the bottom section and greater chamfers at the top section. The tanks exhibit a susceptibility to the phenomenon of liquefied natural gas (LNG) sloshing. There is no additional structure inside the tank except the pump towers. The pump tower has a tubular configuration, characterized by a vertically oriented construction composed of stainless steel. The primary purpose of the construction is to facilitate the transfer of liquefied natural gas (LNG) by means of the two pumps situated at the base of the structure. [Kimmoun et al. \(2020\)](#).

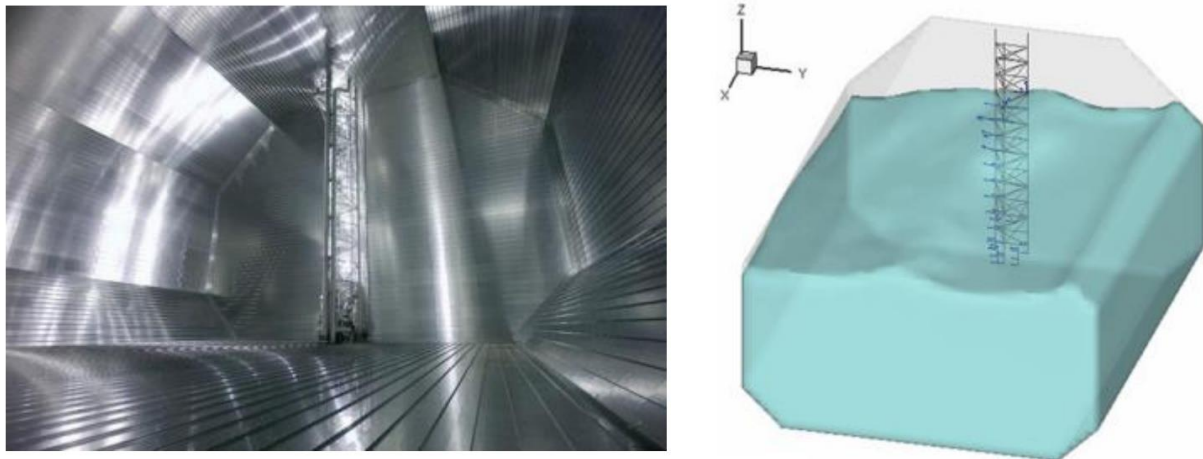


Figure 1: Pump tower of LNG membrane tank (technology NO96) located at aft bulkhead  
Figure courtesy :[Kimmoun et al. \(2020\)](#)

The picture presented in Figure 1 illustrates the structure of the LNG membrane tank, which consists of five vertical pipes arranged in a specific configuration. These pipes are referred to collectively as the "Tripod mast structure (TMS)," with the emergency pipe (E) and filling pipe (F) positioned closely together at the front. Additionally, there are two discharge pipes (Dps, Dsb) located on the port and starboard sides at the rear. Lastly, the radar pipe (R) is situated in close proximity to the port-side discharge pipe. The interconnection between these separate pipes is achieved by the utilization of struts, which are cylindrical pieces functioning as trusses

to guarantee the structural integrity of the entire configuration. The CAD shape of the TMS positioned at the center of the tank's rear is seen in Figure 2. The support provided for the TMS (It is called TMS since emergency (E) and discharge pipes (Dps, and Dsb) are considered to be the main pipes) is facilitated by the 'Pump Tower Base Support, commonly abbreviated as PTBS.

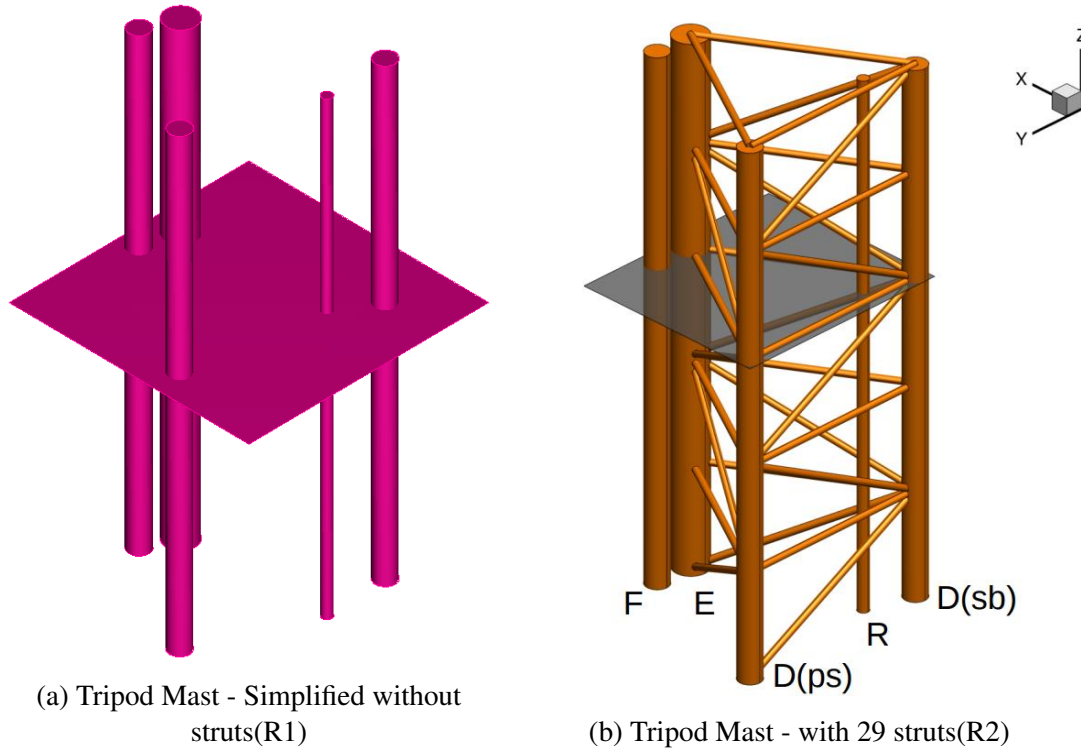


Figure 2: Tripod mast structure (TMS) - R1 and R2 configuration: Gray and Merun plane are the indications of free surface located at  $Z = 5.514\text{m}$  from bottom  
Figure courtesy for R2 configuration [Queutey et al. \(2022\)](#)

Table 1 presents the dimensions and positions of the constituent elements of the TMS at an orientation of  $0^\circ$  [Queutey et al. \(2022\)](#). The appropriate alignment may be achieved by rotating the structure around the central point located at coordinates  $(X,Y) = (0,0)$ .

Table 1: Dimension and location of individual members of tripod mast

Name of the Pipe	Short Form	Diameter, D	X	Y	Zmin	Zmax
		[m]	[m]	[m]	[m]	[m]
Emergency	E	0.610	+2.0104	0.000	0.120	9.187
Discharge Portside	Dps	0.410	-0.9896	+1.750	0.628	9.187
Discharge Starboard	Dsb	0.410	-0.9896	-1.750	0.628	9.187
Filling	F	0.410	+2.0104	+0.710	0.200	9.187
Radar	R	0.200	-0.7396	-0.900	0.120	9.187
Strut		0.115				

To facilitate the flow simulation of TMS, the struts are often disregarded to save computational expense. The configuration without struts is called R1 configuration and with the struts is called R2 configuration (see Figure 2b). The flow can emerge from any direction to the TMS in the

operation. However, to test the TMS in a wave canal or conduct a simulation, it is arranged in a total of seven orientations ranging from  $0^\circ$  to  $270^\circ$ . The pivot point location is at  $(X,Y) = (2.4104, 0)$ . The seven orientations are  $0^\circ, 30^\circ, 60^\circ, 90^\circ, 120^\circ, 180^\circ,$  and  $270^\circ$ . Figure 3 depicts the seven orientations of TMS.

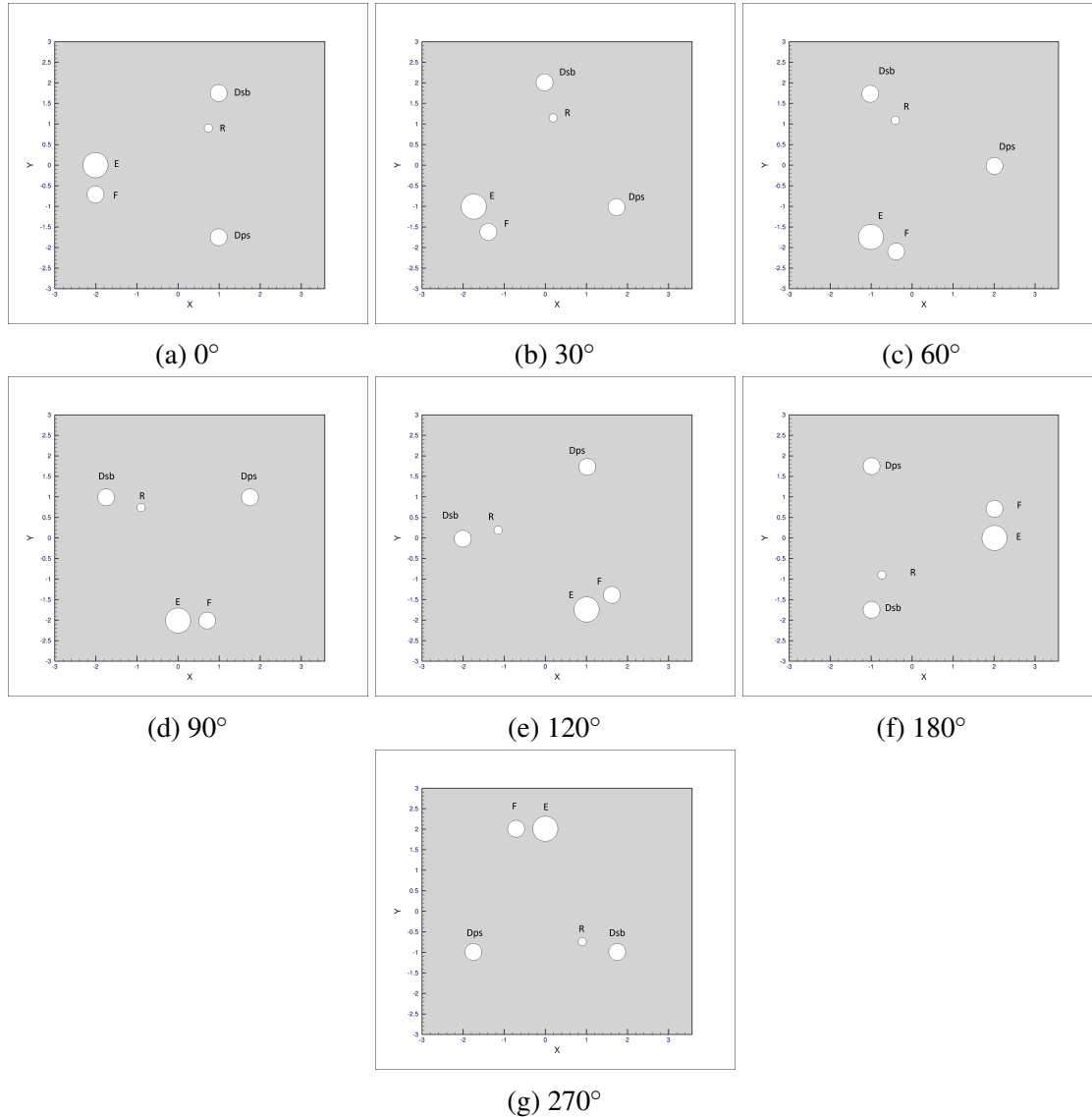


Figure 3: Seven orientations of TMS (Counter-clockwise rotation)

### 3 NUMERICAL FRAMEWORK

The majority of fluid flows seen in both natural phenomena and technical applications exhibit turbulent behavior, including those specifically related to the field of hydrodynamics. Turbulent flows exhibit chaotic behavior and encompass a broad spectrum of length and velocity scales. Resolving turbulence comprehensively in both temporal and spatial domains is computationally challenging due to its inherently chaotic characteristics. Nevertheless, in several engineering applications, achieving a precise resolution of turbulent flow is deemed unnecessary. Instead, statistical turbulence modeling may be employed to reduce the computational demands of the simulation. There are several methodologies available for turbulence modeling, and the selection of a suitable model for each simulation scenario is crucial [Toni et al. \(2018\)](#). Prior to delving into the various turbulence models, it is vital to introduce the Navier-Stokes equations, which serve as the fundamental equations regulating fluid flows. The continuity and momentum equations for incompressible flows influenced by gravity are expressed as stated:

$$\frac{\partial U_j}{\partial x_j} = 0 \quad (1)$$

$$\frac{\partial U_i}{\partial t} + U_j \frac{\partial U_i}{\partial x_j} = -\frac{1}{\rho} \frac{\partial P}{\partial x_i} + \nu \frac{\partial^2 U_i}{\partial x_j \partial x_j} + g_i \quad (2)$$

The fundamental concept behind the RANS equations is the segregation of turbulent velocity fluctuations from the average flow velocity. The RANS equations are derived by initially applying Reynolds decomposition to align the instantaneous flow variables into their respective mean and fluctuation components. The velocity and pressure variables are utilized in the continuity and momentum equations.

$$U_i = \langle U_i \rangle + u_i \quad (3)$$

$$P = \langle P \rangle + p \quad (4)$$

Subsequently, the decomposed variables are employed as substitutions in the continuity equation 1 and momentum equation 2. The subsequent step involves the temporal averaging of the Navier-Stokes equations, resulting in the derivation of the Reynolds-averaged Navier-Stokes (RANS) equations, which may be mathematically expressed as:

$$\begin{aligned} \frac{\partial \langle U_i \rangle}{\partial x_i} &= 0 \\ \frac{\partial \langle U_i \rangle}{\partial x_t} + \langle U_j \rangle \frac{\partial \langle U_i \rangle}{\partial x_j} &= -\frac{1}{\rho} \frac{\partial}{\partial x_j} \left\{ \langle P \rangle \delta_{ij} + \mu \left( \frac{\partial \langle U_i \rangle}{\partial x_j} + \frac{\partial \langle U_j \rangle}{\partial x_i} \right) - \rho \langle u_i u_j \rangle \right\} + g_i \end{aligned} \quad (5)$$

The primary distinction between the Navier-Stokes equations in their original form and the Reynolds-averaged Navier-Stokes (RANS) equations lies in the inclusion of the Reynolds stress factor  $-\rho \langle u_i u_j \rangle$ . The quantity denotes the mean momentum flux resulting from fluctuations in velocity and therefore needs modeling in order to achieve the closure of the equation set. The primary aim of many turbulence models based on Reynolds-Averaged Navier-Stokes (RANS) equations is to accurately represent the Reynolds stress term [Bengt et al. \(2012\)](#). Turbulence models that rely on the Boussinesq approximation are widely utilized in engineering applications. The hypothesis of turbulent viscosity was first proposed by Boussinesq in 1877 and displays an analogy to the stress-rate-of-strain relationship observed in Newtonian fluids [Eric et al. \(2010\)](#). Based on the theories, there exists a relationship.

$$-\langle u_i u_j \rangle = \nu_T \left( \frac{\partial \langle U_i \rangle}{\partial x_j} + \frac{\partial \langle U_j \rangle}{\partial x_i} \right) - \frac{2}{3} k \delta_{ij} \quad (6)$$

The underlying concept of this approximation is to represent the Reynolds stress term by employing a turbulent eddy viscosity denoted as  $\nu_T$ . Multiple models are employed to ascertain the turbulent viscosity, which exhibits spatial and temporal variability. Two-equation models, such as the  $k$ - $\epsilon$  and  $k$ - $\omega$  models, are widely utilized in engineering simulations. The local turbulent viscosity is determined by the utilization of two supplementary transport equations, one pertaining to the turbulent length scales and the other to the turbulent velocity scales. The  $k$ - $\omega$  model has been seen to have favorable performance in the vicinity of the wall, but the  $k$ - $\epsilon$  model is better suited for flows located at greater distances from the wall. The shear stress transfer (SST)  $k$ - $\omega$  model, as proposed by [Menter \(1994\)](#), successfully integrates both of these approaches. The categorization of turbulence models may be determined based on the number of equations they introduce into the system. Several often used models include:

- Zero Equation Model: The Mixing Length model
- One Equation Model: Spalart-Allmaras
- Two Equation Models: The  $k$ - $\epsilon$  model, the  $k$ - $\omega$  model, and Shear Stress Transport (SST) model
- Seven Equation Model: Reynolds Stress Model [Hatlevik et al. \(2018\)](#)

### 3.1 $k$ - $\epsilon$

The  $k$ - $\epsilon$  model, as described by [Versteeg and Malalasekera \(1995\)](#), incorporates the influence of turbulent transport and diffusion resulting from the formation and dissipation of turbulence.

Two more model equations are incorporated into the system, namely one for the turbulent kinetic energy, denoted as  $k$ , and another for the rate of viscous dissipation, represented as  $\epsilon$ . The equations for the  $k$ - $\epsilon$  model are provided below for the case of incompressible flow.

$$\begin{aligned} \frac{\partial k}{\partial t} + \langle U_j \rangle \frac{\partial k}{\partial x_j} &= -\frac{\partial}{\partial x_j} \left( \frac{1}{2} \langle u_i u_j u_k \rangle + \frac{1}{\rho} \langle u_j p \rangle - \nu \frac{\partial k}{\partial x_j} \right) - \langle u_i u_j \rangle \frac{\partial \langle u_i \rangle}{\partial x_j} - \epsilon \\ \frac{\partial \epsilon}{\partial t} + \langle u_j \rangle \frac{\partial \epsilon}{\partial x_j} &= \frac{\partial}{\partial x_j} \left( \frac{\nu_T}{\sigma_\epsilon} \frac{\partial \epsilon}{\partial x_j} \right) + C_{\epsilon 1} \frac{\epsilon}{k} \nu_T \left( \frac{\partial \langle u_i \rangle}{\partial x_j} + \frac{\partial \langle u_j \rangle}{\partial x_i} \right) \frac{\partial \langle u_i \rangle}{\partial x_j} - C_{\epsilon 2} \frac{\epsilon^2}{k} \end{aligned} \quad (7)$$

The expression for the turbulent viscosity is formulated as:

$$\nu_T = C_\mu k^2 / \epsilon \quad (8)$$

The symbol  $C_\mu$  represents a constant in the model. The  $k$ - $\epsilon$  turbulence model is formed by the equation for  $k$  and  $\epsilon$ , together with the definition of  $\nu_T$ . The  $k$ - $\epsilon$  model has four components, whereby two model equations are solved to determine the values of  $k$  and  $\epsilon$ . The turbulent viscosity may be mathematically expressed as  $\nu_T = C_\mu k^2 / \epsilon$ . The Reynolds stresses are determined based on the turbulent-viscosity hypothesis, and then, the Reynolds equations are solved to get  $\langle U_i \rangle$  and  $\langle P \rangle$ . The model equations for the  $k$ - $\epsilon$  turbulence model often employ standard values for the model constants.

$$C_\mu = 0.09, C_{\epsilon 1} = 1.44, C_{\epsilon 2} = 1.92, \sigma_k = 1.0, \sigma_\epsilon = 1.0 \quad (9)$$

### 3.2 $k$ - $\omega$

The  $k$ - $\omega$  model, proposed by [D. C. Wilcox \(1988\)](#), introduces two additional equations to the existing system, in a manner similar to the  $k$ - $\epsilon$  model. However, instead of including the viscous dissipation rate  $\epsilon$ , the  $k$ - $\omega$  model utilizes the vorticity rate  $\omega$ . The variable denoted as  $\omega$  is often known in academic literature as a specific dissipation rate. Moreover, the eddy viscosity is formulated in relation to the variables  $k$  and  $\omega$ . Similar to the  $k$ - $\epsilon$  model, this model assumes isotropic viscosity, which leads to limitations in accurately predicting the anisotropy of normal stresses and accounting for the effects of streamlined curvature. Nevertheless, the model demonstrates more accuracy in handling adverse pressure gradients, making it more suitable for resolving flows that involve wall effects [Hatlevik et al. \(2018\)](#).



### 3.3 $k$ - $\omega$ SST Menter

The entirety of the material has been sourced from the *Turbulence Modeling Resource* authored by the Langley Research Center [Rumsey et al. \(2023\)](#).

The first model, known as the baseline (BSL) model, employs Wilcox's original  $k$ - $\omega$  model inside the inner area of the boundary layer. It then transitions to the conventional  $k$ - $\epsilon$  model in the outside area and in free shear flows. The performance of this model has similarities to the Wilcox model, while effectively mitigating the severe freestream sensitivity characteristic of the latter. The second model is derived by adjusting the eddy-viscosity definition in the BSL model to incorporate the influence of the transit of the principal turbulent shear stress. The shear-stress transport model referred known as the "SST model" in the literature [Menter \(1994\)](#), demonstrates significant advancements in accurately forecasting adverse pressure gradient flows. Linear models commonly employ the Boussinesq assumption as the constitutive relation.

$$\tau_{ij} = 2\mu_t \left( S_{ij} - \frac{1}{3} \frac{\partial u_k}{\partial x_k} \delta_{ij} \right) - \frac{2}{3} \rho k \delta_{ij} \quad (10)$$

The present model has a high degree of similarity to the Menter baseline model. There exists a constant, denoted as  $\sigma_{k1}$ , which distinguishes itself from the equation representing turbulent eddy viscosity. The presented model is a two-equation system, expressed in conservation form.

$$\begin{aligned} \frac{\partial \rho k}{\partial t} + \frac{\partial \rho u_j k}{\partial x_j} &= P - \beta^* \rho \omega k + \frac{\partial \left[ (\mu + \sigma_k \mu_t) \frac{\partial k}{\partial x_j} \right]}{\partial x_j} \\ \frac{\partial \rho \omega}{\partial t} + \frac{\partial \rho u_j \omega}{\partial x_j} &= \frac{\gamma}{\nu_t} P - \beta \rho \omega^2 + \frac{\partial}{\partial x_j} \left[ (\mu + \sigma_\omega \mu_t) \frac{\partial \omega}{\partial x_j} \right] + 2(1 - F_1) \frac{\rho \sigma_{\omega 2}}{\omega} \frac{\partial k}{\partial x_j} \frac{\partial \omega}{\partial x_j} \end{aligned} \quad (11)$$

It is important to acknowledge that the reference use the Lagrangian derivative, which differs from the correct formulation of these equations as presented by the author and other sources. The equations presented above have been formulated in a manner that adheres to the principles of conservation, as demonstrated in references such as [D. C. Wilcox \(2006\)](#), [Menter et al. \(2003\)](#), and [Menter \(1992\)](#).

$$\begin{aligned} P &= \tau_{ij} \frac{\partial u_i}{\partial x_j} \\ \tau_{ij} &= \mu_t \left( 2S_{ij} - \frac{2}{3} \frac{\partial u_k}{\partial x_k} \delta_{ij} \right) - \frac{2}{3} \rho k \delta_{ij} \\ S_{ij} &= \frac{1}{2} \left( \frac{\partial u_i}{\partial x_j} + \frac{\partial u_j}{\partial x_i} \right) \end{aligned} \quad (12)$$



The computation of the turbulent eddy viscosity is derived from:

$$\mu_t = \frac{\rho a_1 k}{\max(a_1 \omega, \Omega F_2)} \quad (13)$$

Each constant in the set is a combination of an inner constant (1) and an outer constant (2), which are blended together using the following process:

$$\phi = F_1 \phi_1 + (1 - F_1) \phi_2 \quad (14)$$

The symbol  $\phi_1$  denotes the value of constant 1, whereas  $\phi_2$  indicates the value of constant 2. Additional functions are provided by:

$$\begin{aligned} F_1 &= \tanh(\arg_1^4) \\ \arg_1 &= \min \left[ \max \left( \frac{\sqrt{k}}{\beta^* \omega d}, \frac{500\nu}{d^2 \omega} \right) \frac{4\rho\sigma_{\omega 2} k}{CD_{k\omega} d^2} \right] \\ CD_{k\omega} &= \max \left( 2\rho\sigma_{\omega 2} \frac{1}{\omega} \frac{\partial k}{\partial x_j} \frac{\partial \omega}{\partial x_j}, 10^{-20} \right) \\ F_2 &= \tanh(\arg_2^2) \\ \arg_2 &= \max \left( 2 \frac{\sqrt{k}}{\beta^* \omega d}, \frac{500\nu}{d^2 \omega} \right) \end{aligned} \quad (15)$$

where  $\rho$  represents the density,  $\nu_t = \mu_t / \rho$  denotes the turbulent kinematic viscosity and  $\mu$  represents the molecular dynamic viscosity.  $d$  represents the distance between the field point and the closest wall, and  $\Omega = 2W_{ij}W_{ij}$  is the magnitude of vorticity.

$$W_{ij} = \frac{1}{2} \left( \frac{\partial u_i}{\partial x_j} - \frac{\partial u_j}{\partial x_i} \right) \quad (16)$$

It is commonly advised to utilize a production limiter [Menter \(1993\)](#). In the given reference, the variable P in the k-equation is substituted with

$$\min(P, 20\beta^* \rho \omega k)$$

The boundary requirements prescribed in the original source are as follows:

$$\begin{aligned}
\frac{U_\infty}{L} &< \omega_{farfield} < 10 \frac{U_\infty}{L} \\
\frac{10^{-5} U_\infty^2}{Re_L} &< k_{farfield} < \frac{0.1 U_\infty^2}{Re_L} \\
\omega_{wall} &= 10 \frac{6\nu}{\beta_1 (\Delta d_1)^2} \\
k_{wall} &= 0
\end{aligned} \tag{17}$$

The ' $L$ ' represents the approximate length of the computational domain, and the sum of the two far-field values should result in a freestream turbulent viscosity ranging from  $10^{-5}$  and  $10^{-2}$  times the freestream laminar viscosity.

The constants are:

$$\begin{aligned}
\gamma_1 &= \frac{\beta_1}{\beta^*} - \frac{\sigma_{\omega 1} \kappa^2}{\sqrt{\beta^*}} \\
\gamma_2 &= \frac{\beta_2}{\beta^*} - \frac{\sigma_{\omega 2} \kappa^2}{\sqrt{\beta^*}} \\
\sigma_{k1} &= 0.85, \sigma_{\omega 1} = 0.5, \beta_1 = 0.075 \\
\sigma_{k2} &= 1.0, \sigma_{\omega 2} = 0.856, \beta_2 = 0.0828 \\
\beta^* &= 0.09, \kappa = 0.41, a_1 = 0.31
\end{aligned} \tag{18}$$

### 3.4 Hybrid URANS-LES

*The entire document for the current section of hybrid URANS-LES has been taken from [Gritskevich et al. \(2012\)](#).*

The preference for hybrid and/or zonal RANS-LES models is increasing industrial simulations for high-Reynolds numbers since significant expenses are associated with traditional Large Eddy Simulation (LES). A limited quantity of model formulations are now employed in industrial computational fluid dynamics (CFD) and are broadly classified as follows.

- Improved Unsteady RANS (URANS)
- Detached Eddy Simulation (DES)
- Wall Modeled LES (WMLES)
- Zonal (or embedded) LES models

Although the initial DES model is characterized by its simplicity and straightforwardness, it remains one of the most challenging models to employ in intricate applications. The user must possess not just a rudimentary comprehension of the model's behavior but also adhere to detailed

grid creation requirements in order to prevent encountering undefined simulation behavior that is in between RANS and LES. Moreover, there exist multiple versions of the DES model.

- Delayed Detached Eddy Simulation (DDES)
- Improved Delayed Detached Eddy Simulation (IDDES)

### 3.4.1 Improved delayed detached eddy simulation (IDDES)

The IDDES approach is an advancement over the DDES concept. The IDDES technique proposes a hybrid model that combines DDES with Wall-Modeled LES (WMLES) for improved accuracy in computational fluid dynamics simulations. The length scale  $l_{DDES}$  is substituted with the length scale  $l_{IDDES}$ .

$$\begin{aligned}
 l_{IDDES} &= \tilde{f}_d \cdot (1 + f_e) \cdot l_{RANSE} + (1 - \tilde{f}_d) \cdot l_{LES} \\
 l_{LES} &= C_{DES} \Delta \\
 l_{RANSE} &= \frac{\sqrt{k}}{C_\mu \omega} \\
 C_{DES} &= C_{DES1} \cdot F_1 + C_{DES2} \cdot (1 - F_1)
 \end{aligned} \tag{19}$$

The length-scale  $\Delta$  of the LES is defined as:

$$\Delta = \min \{ C_\omega \max [d_\omega, h_{max}], h_{max} \} \tag{20}$$

The term  $h_{max}$  represents the maximum edge length of the cell. The computation of the empiric blending function  $\tilde{f}_d$  in the given context involves the utilization of the following relations.

$$\begin{aligned}
 \tilde{f}_d &= \max \{ (1 - f_{dt}), f_b \} \\
 f_{dt} &= 1 - \tanh \left[ (C_{dt1} \cdot r_{dt})^{C_{dt2}} \right] \\
 r_{dt} &= \frac{\nu_t}{\kappa^2 d_\omega^2 \sqrt{0.5 (S^2 + \Omega^2)}} & f_b &= \min \{ 2 \exp(-9\alpha^2), 1.0 \} \\
 \alpha &= 0.25 - \frac{d_\omega}{h_{max}}
 \end{aligned} \tag{21}$$

In the initial model formulation, the elevating function  $f_e$  in equation 22 is expressed as follows:

$$\begin{aligned}
f_e &= f_{e2} \cdot \max((f_{e1} - 1.0), 0.0) \\
f_{e1} &= \begin{cases} 2 \cdot \exp(-11.09 \cdot \alpha^2), & \alpha \geq 0 \\ 2 \cdot \exp(-9.0 \cdot \alpha^2), & \alpha < 0 \end{cases} \\
f_{e2} &= 1.0 - \max(f_t - f_l) \\
f_t &= \tanh((C_t^2 \cdot r_{dt})^3) \\
f_l &= \tanh((C_l^2 \cdot r_{dl})^{10}) \\
r_{dl} &= \frac{\nu}{\kappa^2 d_\omega^2 \sqrt{0.5(S^2 + \Omega^2)}}
\end{aligned} \tag{22}$$

In the simplified form of the IDDES, the function  $f_e$  in Equation 19 is assigned a value of zero. Therefore, the IDDES length scale may be expressed as follows.

$$l_{IDDES} = \tilde{f}_d \cdot l_{RANSE} + (1 - \tilde{f}_d) \cdot l_{LES} \tag{23}$$

In addition to the model constants presented in Equations 20 and 21, the model incorporates the introduction of the following constants.

$$C_\omega = 0.15, C_{dt1} = 20, C_{dt2} = 3, C_l = 5.0, C_t = 1.87 \tag{24}$$

### 3.5 Near Wall Treatment

In the field of hydrodynamics, as well as in numerous other computational fluid dynamics (CFD) applications, the consideration of near-wall treatment is crucial for the accurate determination of wall shear stresses and the assessment of turbulence effects within the boundary layer. Nevertheless, the flow variables exhibit significant gradients within this rather narrow region, necessitating the utilization of an exceedingly refined mesh to accurately capture the flow phenomena. In an alternative approach, wall functions may be employed to approximate the velocities within the first cell next to the wall. By employing this approach, the development of a significantly fine mesh on the wall may be prevented. Nevertheless, wall functions may not be appropriate for every circumstance. The boundary layer is characterized by a gradual rise in flow velocity from a value of zero at the wall to the velocity of the free stream. The nature of the boundary layer, whether it is turbulent or laminar, is dependent upon the Reynolds number. In the case of flow with high Reynolds numbers, the boundary layer is turbulent in nature. Accurate resolution or modeling of a turbulent boundary layer is frequently necessary since it entails more shear stresses on the wall compared to laminar boundary layers. The turbulent boundary layer is

commonly divided into three distinct layers, as seen in Figure 4a.

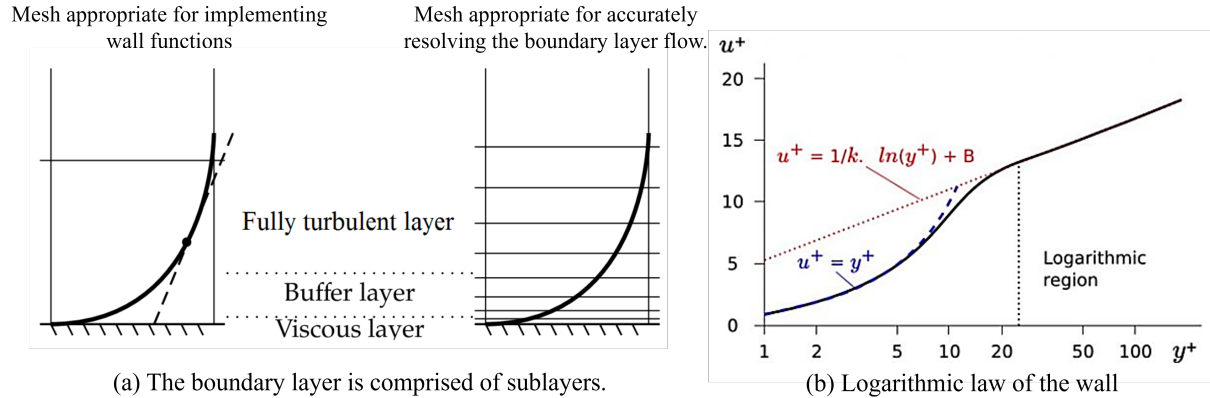


Figure 4: Demonstration of near-wall treatment  
Figure courtesy: Bengt et al. (2012) Toni et al. (2018)

Nondimensional wall variables are commonly utilized to represent the velocities and distances inside the boundary layer. It is presupposed that the reader holds familiarity with the nondimensional  $y^+$  variable, which serves as a means to articulate the distance from the wall. The region known as the viscous layer, with a  $0 < y^+ < 5$ , is the layer in closest proximity to the wall. As its name suggests, this layer is characterized by the prevalence of viscous stress. The buffer layer, characterized by a range of  $5 < y^+ < 30$ , serves as an intermediary zone connecting the viscous and completely turbulent layers. Within this area, the turbulent viscous and stresses are roughly equivalent. In the regime of complete turbulence, characterized by  $y^+ > 30$ , the influence of viscous stresses can be considered insignificant. As previously stated, there exist two primary methodologies for addressing near-wall treatment: employing wall functions resolving the near-wall region by utilizing a highly refined mesh (also called low Reynolds approach - LRN). The estimation of flow variables in the first cell next to the wall is performed using wall functions, which utilize empirical formulae derived from the logarithmic law of the wall. This concept is depicted in Figure 4b. The wall functions are based on the assumption that the velocity distribution within the viscous layer is linearly dependent on  $y^+$ . Conversely, within the totally turbulent layer, the velocity distribution is characterized by a logarithmic profile (log law layer). The velocity tends to approach the log law profile in the buffer layer. Nonetheless, accurately determining the flow variables inside this region is difficult. The optimal location for the first cell point is in proximity to the lower limit of the totally turbulent zone, often ranging from  $30 < y^+ < 100$ , with the specific range being dependent upon the Reynolds number. It is advisable to avoid the range of  $5 < y^+ < 30$  due to the inherent uncertainty associated with the buffer layer. Despite the wall function technique has demonstrated significant efficacy, there exist certain scenarios where its application is not advised. The accuracy of wall functions is dubious when applied to flows that involve significant pressure gradients and flow separation, as

these functions are primarily created for flows across flat plates. In such instances, it is advisable to employ a refined mesh (LRN approach) for the purpose of resolving the boundary layer [Bengt et al. \(2012\)](#).

### 3.6 Volume Of Fluid Method (VOF)

The Volume of Fluid (VOF) method is used to capture the free surface. The approach is utilized to solve an additional transport Equation 27 for a scalar function  $\alpha$ , which is normalized to a value of 1. This variable represents the relative concentration of air in relation to water at every location within the computational domain. The URANS equations are employed to solve for a fluid mixture of water and air, whereby the properties of the mixture are established using the scalar function  $\alpha$ :

$$\rho = (1 - \alpha)\rho_w + \alpha\rho_A \quad (25)$$

$$\mu = (1 - \alpha)\mu_w + \alpha\mu_A \quad (26)$$

The local value of  $\alpha$  at each time step is determined by solving the following equation:

$$\frac{\partial \alpha}{\partial t} + \nabla \cdot (\alpha U) + \nabla \cdot [\alpha(1 - \alpha)U_r] = 0 \quad (27)$$

The term  $U_r$  in Equation 27 represents the relative velocity between water and air. The tuning of  $U_r$  is achieved by the parameter  $C_f$  in the following manner:

$$U_r = n_f \min\left[C_f \frac{\phi}{S_f}, \max\left(\frac{\phi}{S_f}\right)\right] \quad (28)$$

Note that,  $\nabla \cdot [\alpha(1 - \alpha)U_r]$  is termed as artificial compression (AC) which becomes active when  $\alpha \neq 0$  and  $\alpha \neq 1$ . The tuning of the AC is strategically performed to enhance the compression of the free surface, hence minimizing the occurrence of interface smearing commonly observed in the use of surface capture methods for the prediction of free surface flows [Hirt et al. \(1981\)](#).

## 4 METHODOLOGY

This section provides an overview of the numerical framework employed in the present investigation. Given that data on the flow across single cylinders, tandem, and side-by-side arrangements at various Reynolds numbers can be found in existing literature, it is advisable to conduct these basic scenarios with identical circumstances in order to assess the credibility of the current study. In addition, the TMS (Tripod mast structure) developed by GTT has many cylinders with varying orientations, resulting in the inclusion of diverse flow fields. To facilitate the comparison and comprehension of flow fields, it is essential to have a reference dataset that enables the analysis of changes in these flow fields. The Re number varies for each cylinder in TMS due to the different diameter sizes. Table 2 depicts the cylinder name with the corresponding Reynolds and Froude number.

Table 2: Reynolds and Froude number for each in TMS cylinder during operation

	<b>Diameter, D</b>	<b>Re</b>	<b>Fr</b>
	[m]	[-]	[-]
<b>R</b>	0.2	8.28E+06	8.567
<b>E</b>	0.61	2.52E+07	4.905
<b>Dps</b>	0.41	1.70E+07	5.983
<b>Dsb</b>	0.41	1.70E+07	5.983
<b>F</b>	0.41	1.70E+07	5.983

The functioning of the TMS may be observed to occur within the post-critical flow regime when compared with Table 3 from [Stringer et al. \(2014\)](#). Nevertheless, the literature mostly contains extensive data for the sub-critical flow, with only a limited amount of information accessible for the transcritical flow. However, the tandem and side-by-side arrangements (see Figure 5) frequently encountered in the literature demonstrate a notable degree of specialization and simplicity. For example, these configurations frequently make the assumption of equal cylinder diameters and function throughout the sub-critical range of Reynolds numbers. Therefore, the utilization of these configurations for simulations may not result in significant findings for the present investigation. Therefore, in order to ascertain the temporal and spatial resolution, a sequence of simulations will be performed on the flow around a single cylinder, encompassing a spectrum of Reynolds values spanning from sub-critical to post-critical.

Table 3: Flow Regimes based on Re numbers

<b>Re Range</b>	<b>Flow Regime</b>
Re < 1	Creeping flow
3-5 < Re < 30-40	Steady separation (Foppl Vortices)
30-40 < Re < 150-300	Laminar periodic shedding
150-200 < Re < 1.4x10 <sup>5</sup>	Subcritical
1.4x10 <sup>5</sup> < Re < 1x10 <sup>6</sup>	Critical
1x10 <sup>6</sup> < Re < 5x10 <sup>6</sup>	Supercritical
5x10 <sup>6</sup> < Re < 8x10 <sup>6</sup>	Transcritical
8x10 <sup>6</sup> < Re	Postcritical

When a pair of circular cylinders are placed in a tandem arrangement with parallel alignment to the mean flow, the downstream cylinder will be shielded from the incoming flow by the cylinder directly upstream (see Figure 5a). In terms of side-by-side placing (see Figure 5b), with their axes perpendicular to the mean flow, the wakes generated by each cylinder interact with one another on both sides of the gap between them. The most intricate configuration combining two circular cylinders may be observed in Figure 5c, where a staggered arrangement is depicted. The staggered pair of cylinders is governed by two variables: the non-dimensional center-to-center pitch ratio ( $P/D$ ), and the angle of incidence,  $\alpha$ . In an alternative perspective, several scholars have characterized the configuration of the cylinders by employing the longitudinal pitch ratio ( $L/D$ ) and the transverse pitch ratio ( $T/D$ ) [Prafull et al. \(2022\)](#) [Sumner et al. \(2010\)](#) also stated in section 1.

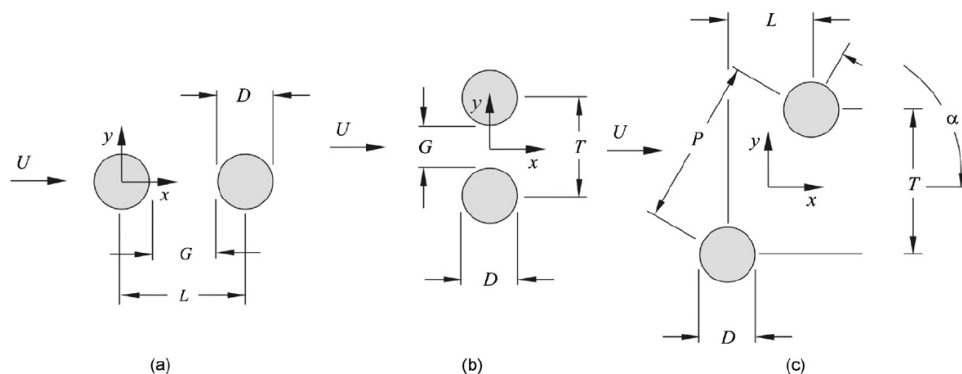


Figure 5: (a) Tandem (b) Side-by-side (c) Staggered  
Figure courtesy [Sumner et al. \(2010\)](#)

The current investigation will commence by conducting simulations using single cylinder with the Reynolds numbers specified in Table 4.

Table 4: Reynolds number range for Single cylinder simulation

Re	Short form	Flow Regime
$1.0 \times 10^5$	100k	Sub-critical
$1.4 \times 10^5$	140k	
$8.5 \times 10^5$	850k	Critical
$3.6 \times 10^6$	3.6M	Super-critical
$8.27 \times 10^6$	8.27M	Post-critical
$8.4 \times 10^6$	8.4M	
$1 \times 10^7$	10M	
$1.7 \times 10^7$	17M	
$2.5 \times 10^7$	25M	

Since the data in the dimensionless form provides significant insights, therefore the dimension and flow properties for a single cylinder have been selected in a way to get an advantage in post-processing. Some essential dimensionless numbers are avg. coefficient of drag,  $C_d$ , avg.



coefficient of lift,  $C_l$ , avg. coefficient of pressure,  $C_P$ , avg. skin friction coefficient,  $C_f$ , RMS drag,  $Cd_{RMS}$ , RMS lift,  $Cl_{RMS}$  and Reynolds number,  $Re$ , Strouhal number,  $St$ , Time step,  $\Delta t^*$  which can be written as,

$$C_d = \frac{F_x}{\frac{1}{2}\rho AU^2} \quad (29)$$

$$Cd_{RMS} = \frac{\sqrt{\frac{1}{n}(F_{x1}^2 + F_{x2}^2 + \dots + F_{xn}^2)}}{0.5\rho U^2 D} \quad (30)$$

$$C_l = \frac{F_y}{\frac{1}{2}\rho AU^2} \quad (31)$$

$$Cl_{RMS} = \frac{\sqrt{\frac{1}{n}(F_{y1}^2 + F_{y2}^2 + \dots + F_{yn}^2)}}{0.5\rho U^2 D} \quad (32)$$

$$C_P = \frac{P - P_\infty}{\frac{1}{2}\rho_\infty U^2} \quad (33)$$

$$C_f = \frac{\tau_{wall}}{1/2\rho U^2} \sqrt{Re} \quad (34)$$

$$Re = \frac{\rho U D}{\mu} \quad (35)$$

$$St = \frac{f D}{U} \quad (36)$$

$$\Delta t^* = \Delta T U / D \quad (37)$$

where,

$F_x$  = Evolution of drag force or force induced in the x-direction w.r.t time [ $N$ ]

$F_y$  = Evolution of lift force or force induced in the y-direction w.r.t time [ $N$ ]

$A$  = Projected area of the geometry towards flow [ $m^2$ ]

$D$  = Diameter of the cylinder [ $m$ ]

$\rho$  = Density of the fluid [ $kg/m^3$ ]

$\rho_\infty$  = Density at far field [ $kg/m^3$ ]

$P$  = Pressure on the body [ $Pa$ ]

$P_\infty$  = Pressure at far field [ $Pa$ ]

$U$  = Inlet velocity [ $m/s$ ]

$\mu$  = Dynamic viscosity [ $Pa.s$ ]

$n$  = Number of data points

$f$  = Shedding frequency [ $Hz$ ]

$\Delta T$  = Time step with dimension [ $s$ ]

$\tau_{wall}$  = Tangential wall shear stress [ $N/m^2$ ]

## 4.1 Geometry Preparation And Domain Setup

The CAD geometry for the single cylinder has been generated in HEXPRESS 11.1-6 (FineMarine11.2) as a parasolid file format  $.x_t$ . The cylinder's center is positioned at the coordinates  $(X, Y) = (0,0)$ . A specific vertical dimension is provided for the extrusion in the Z-axis. However, the height has been suppressed during the meshing process due to the consideration of the 2D simulation. The cylinder's diameter (D) is defined as unity (1 m). The domain construction has been carried out using the identical HEXPRESS environment. The shape of the domain for a single cylinder is influenced by the prior research conducted by other researchers as documented in the existing literature. The two primary types of domains commonly employed for studying the flow through a single cylinder are **Rectangular** and **O-type** domains. Figure 7a and 7b depict both domains, respectively. In the case of domains, locations are determined according to the following convention in Table 5 (here, D (m) is the diameter of the cylinder):

Table 5: Domain specification : Rectangular and O-type (unit in m)

<b>Rectangular type</b>	
Inlet (X)	-20D upstream
Outlet(X)	+40D downstream
Side by side(Y)	-20D to +20D
<b>O-type</b>	
Domain diameter	40D
Inlet (X)	-20D upstream
Outlet(X)	+20D downstream

The domain selection is conducted with the objective of minimizing the blockage ratio (BR) and disregarding any far-field disturbance that may have an impact on the simulation. The blockage ratio is commonly described as a ratio of the structure's projected area in the direction of flow to the cross-sectional area of the surrounding domain. HEXPRESS utilizes '**Faceting settings**' to accurately capture the edge and surface of the geometry. These settings are separated into numerous options that enable the creation of a domain with adequate precision. In the present investigation, the curve resolution and surface resolution have been both set to 0.1. Additional information about domain settings may be accessed in the FineMarine documentation guide [FineMarine \(2023\)](#). The picture presented in Figure 6 illustrates the process of capturing the edge and surface geometry during the development of a domain. It should be noted that the original TMS has been shown in order to provide a more comprehensive explanation of the argument behind domain creation.

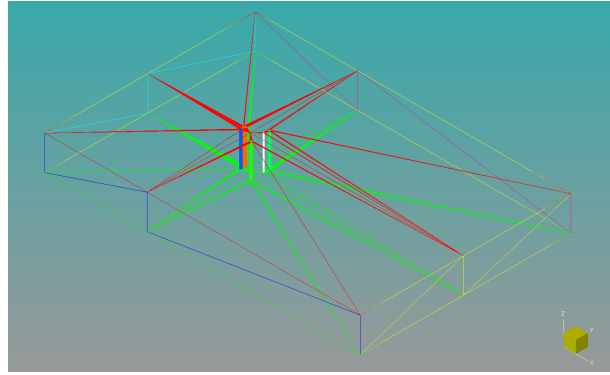


Figure 6: Edge and surface capturing process in HEXPRESS: Domain creation for the TMS - R1 configuration

## 4.2 Boundary And Initial Conditions

During the simulation, No-slip boundary condition is applied to the cylindrical geometry for both types of domain (Rectangular and O-type). For the rectangular domain, a far-field boundary condition has been applied to the inlet and both sides of the domain with a unit velocity (1 m/s) in the X-direction (referred to as  $v_x$ ). The outlet boundary condition is set to the prescribed pressure. The O-type domain is given a cut right through the center of the geometry (e.g. X, Y = 0,0), therefore, it has only two edges complying inlet (arc: X,Y = 0, -20 ; -20, 0 ; 0, +20) and outlet (arc: X,Y = 0, -20 ; +20, 0 ; 0, +20). The inlet is set to far-field boundary condition (with velocity,  $V_x = 1$  m/s) and the outlet is set to prescribed pressure identical to the rectangular domain. Since, the simulation is set up in 2D, the spanwise axis are set to mirror boundary condition automatically by FineMarine. Figure 7 explains the above statement visually.

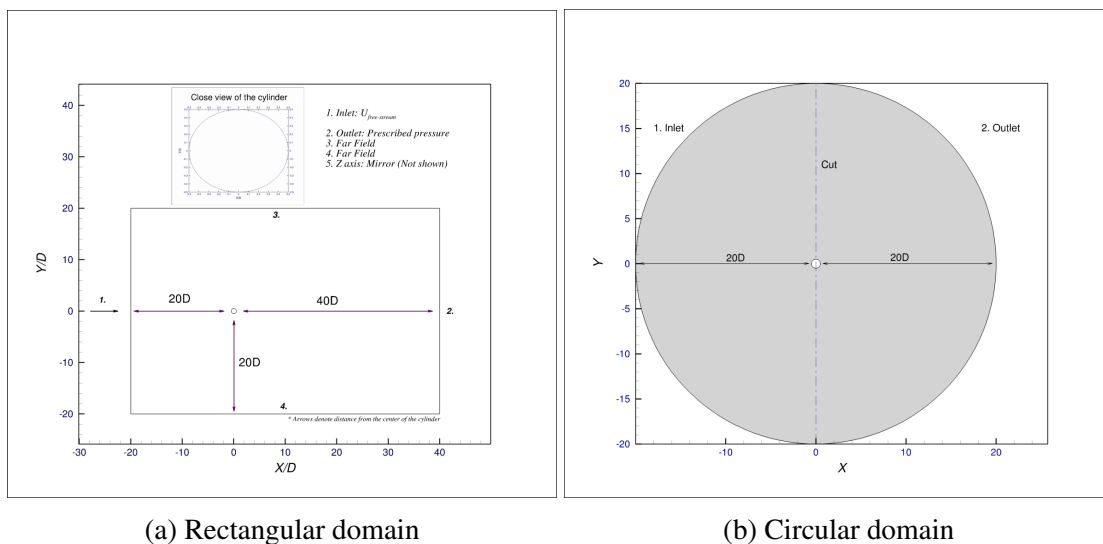


Figure 7: 2D domain for single cylinder

### 4.3 Mesh Generation

To generate mesh, the HEXPRESS mesh wizard has been utilized. The wizard has five steps to accomplish the grid generation process. They are as follows:

#### ***-Initial mesh***

The HEXPRESS mesh creation technique starts by establishing an initial mesh that includes the entirety of the computational domain. An initial geometric configuration is automatically suggested, which corresponds to an isotropic partitioning of the boundary box of the computational area. The box is either rectangular or cylindrical. The section titled *Subdivide the domain bounding box* focuses on the subdivision of rectangular boxes, whereas the section titled *Create cylindrical mesh* pertains to the creation of initial cylindrical boxes. In addition, the user has the capability to import their own unstructured mesh.

#### ***-Adapt to geometry***

The mesh creation step in HEXPRESS is considered to be of utmost importance in terms of user engagement. The HEXPRESS calculated mesh is directly determined by the parameter input. The adaption phase consists of two primary acts, namely refining, and trimming. During the process of refinement, cells undergo a gradual subdivision in order to meet specific geometrical requirements. The process of trimming involves the removal of cells that either intersect or are located outside of the given geometry. The HEXPRESS algorithm automatically identifies and locates the cells present inside the computational domain. In the concluding phase of the process, a lattice structure comprising all internal cells is generated.

#### ***-Snap to geometry***

In order to produce a high-quality mesh that conforms well to the body, the completely automated meshing process incorporates the insertion of a staircase mesh onto the surface. To assure the connectivity of mesh vertices to corners and edges, lower-dimensional geometric characteristics are recovered through the utilization of sophisticated algorithms. The addition of buffer insertion layers facilitates the creation of a mesh that fits the contours of the body. The mesh is then rendered smooth by the displacement of points located on its surface as well as within its volume.

#### ***-Optimize***

The resulting mesh formed following the snapping process may exhibit suboptimal cell quality in the vicinity of corners and curves, with certain cells being concave or possessing negative volumes. HEXPRESS provides techniques that facilitate the conversion of concave cells into convex cells and enhance orthogonality. The presence of convex cells is of utmost importance in ensuring the stability and robustness of flow solvers. It is advisable to refrain from utilizing negative cells, and HEXPRESS generates a mesh that is devoid of such cells.

**-Viscous layer**

The HEXPRESS method is a precise approach that effectively resolves boundary layers by employing cells with high aspect ratios. This methodology utilizes a series of subdivisions and an inflation algorithm to enhance resilience, speed, and mesh quality in viscous layers. Further information can be found in FineMarine documentation [FineMarine \(2023\)](#). Figure 8 shows all the meshing steps in detail. Table 6 demonstrates a primary mesh wizard setup for the simulation. However, this is not the final setup. The adjustments have been implemented to address various circumstances; yet, it provides readers and future researchers with a general grasp of the meshing setup.

Table 6: Mesh wizard setup in HEXPRESS

<b>Initial Mesh Parameters</b>		<b>Snap to geometry</b>	
Subdivide the domain bounding box	yes	Advanced	enabled
x axis	24	Global parameters	
y axis	16	Insert buffer on faces not used for trimming	no
Nb of cells	384	Improve mesh quality near concave corners	no
Create cylindrical mesh		Freeze faces not used for trimming	no
Import a mesh file		Curve snapping	
<b>Adapt to geometry</b>		Snapping option	
Global		<i>Must be captured</i>	yes
Max number of refinement	6	<i>Must be skipped</i>	no
Advanced		<i>Can be skipped</i>	no
Enable refinement	yes	Buffer insertion	
Enable trimming	yes	Buffer insertion layer type	
Refinement diffusion	4	<i>Type 1</i>	
Number of cells in gap	7	<i>Type 2</i>	yes
Minimum cell size	0	<b>Optimize</b>	enabled
Maximum cell size	1.00E+20	Enable optimization	yes
Prevent refinement of the exterior cell	no	Advanced	
Impose isotropic refinement	yes	Relax geometry to eliminate invalid cells	no
Apply trimming by distance	no	Max nb of external loops	4
		Max nb of invalid cells	100
Curve refinement	not active	Max nb of final optimization iterations	7
Surface refinement		Percentage of vertices to optimize during final optimization	3
Mirror	not active	Max nb of orthogonality optimization iterations	5
External	not active	Minimal orthogonality threshold	5
Cylinder	active	<b>Viscous layer</b>	
Refinement		Global	
<i>Max number of refinement</i>	1000	Global parameters	
Adaptation criteria		First layer thickness	default
<i>Distance</i>	no	Stretching ratio	default
<i>Curvature</i>	yes	Apply to active surface	
<i>Target cell sizes</i>	yes	Control parameters	
x axis	0	Fixed first layer thickness method	yes
y axis	0	<i>Inflate viscous layers</i>	yes
Advanced		Fixed nb of layers	no
<i>Maximum aspect ratio</i>	2	Floating number of layers	yes
<i>Curvature ref factor(R/C)</i>	3.5	<i>Minimum number of layers</i>	default
<i>Anisotropic extent</i>	85	<i>Maximum number of layers</i>	default
<i>Refinement diffusion</i>	Global	Variable first layer thickness method	no
Box refinement	not active	Advanced	
During box creation → Box size (corner to corner)		Inflation factor	2
Refinement		<i>Snap new surface vertices</i>	no
<i>Max nb of refinement</i>		<i>Use smarter inflation method</i>	yes
Target cell sizes		Surface	
x axis		cylinder	active
Y axis		Parameters	
Advanced		<i>First layer thickness</i>	compute
<i>Refinement diffusion</i>		<i>Stretching ratio</i>	1.1
Trimming		<i>Number of layers</i>	
MIR	not used for trimming		
EXT	not used for trimming		

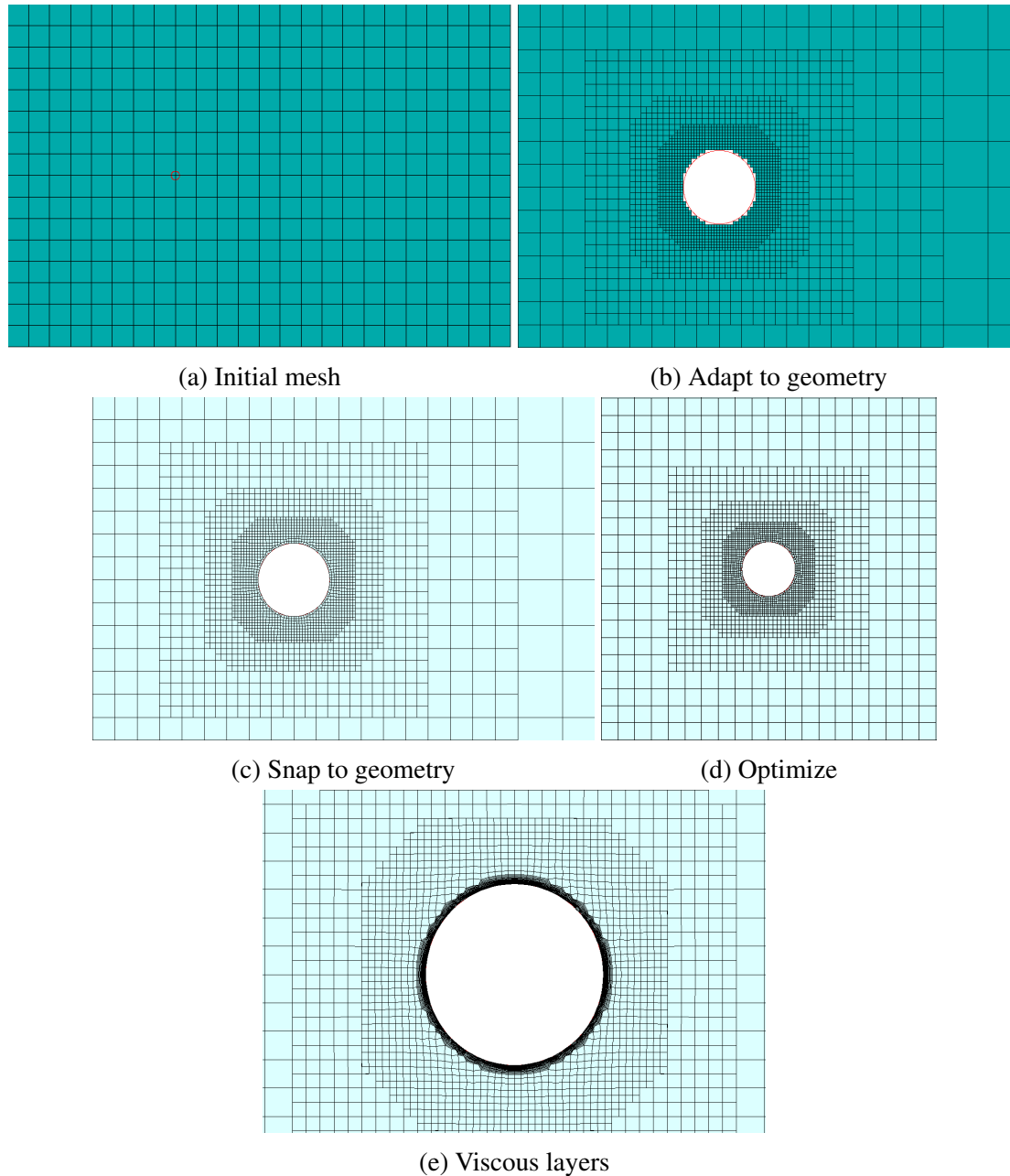


Figure 8: Meshing step in HEXPRESS mesh wizard

#### 4.4 Simulation Setup And Solver Setting

The settings of the solver are specified in the Computations of FineMarine ISIS-CFD solver. The parameters are divided into as follows;

-Physical configuration

Additional models

-Numerical parameters

## -Computation control

These options are further subdivided. The settings are mentioned in Table 7. The number of time step and time step ( $\Delta T$ ) values are not presented since a range of dimensional time step values (unit in s) has been taken into consideration for finding out a better temporal resolution. It will be discussed in the further sections. The diameter  $D$  of the cylinder, density  $\rho$  of the fluid, and the inlet velocity  $U$  are taken as unity. So that the Reynolds number of the flow changes inversely proportional to the dynamic viscosity of the fluid. Therefore, it is not registered in Table 7 for the time being. It is important to mention that, the temporal and spatial discretization scheme in FineMarine is second-order upwind.

Table 7: Simulation setup and solver setting

<b>Physical configuration</b>	
General parameters	
Flow type	Unsteady
Fluid-1 properties	
Name	LNG
Dynamic viscosity [pa.s]	
Density[kg/m <sup>3</sup> ]	1
Flow model	
Regime/Turbulence model	K-omega (SST Menter)
Reference length[m]	1
Reference velocity[m/s]	1
<i>Turbulence</i>	
From turbulence level initialization	no
Turbulent kinetic energy[m <sup>2</sup> /s <sup>2</sup> ]	default(9.091e-09)
Turbulent dissipation[m <sup>2</sup> /s <sup>3</sup> ]	default(8.182e-10)
<b>Numerical parameters</b>	
<i>Turbulence</i>	
Discretization scheme	AVLSMART
<i>Momentum</i>	
Discretization scheme	AVLSMART
<b>Computation control</b>	
Time step	
Number of time step	
Time step law	uniform
Time step value[s]	
General parameters	
<i>Max nb of non-linear iteration</i>	20
<i>Convergence criteria</i>	2
<i>Save solution every</i>	500
Pressure solver parameters	
<i>solver method</i>	Dynamic switch
PCGSTAB_MB	
BoomerAMG	

## 4.5 Mesh And Time Step Selection

### 4.5.1 Static Mesh

#### Initial coarse mesh

Initially, a coarse mesh has been taken into consideration to run the simulation at sub-critical Re number 110k ( $1.1 \times 10^5$ ). As mentioned earlier the size of the domain in the longitudinal direction is  $-20D$  to  $+40D$  and in the transverse direction  $-20D$  to  $+20D$ . The number of cells in the X-direction is set to 24, and in the Y-direction 16. Therefore, before any refinement and addition of a viscous layer total number of cells is 384. The refinement diffusion has been used equal to 4 which can be seen from Figure 9a and found in Table 6 highlighted in gray, the final total number of cells after refinement and the inclusion of viscous layer is equal to 8464. The minimum cell size is found to be  $0.039D$  in both X and Y directions respectively. Table 8 records the mesh information.

Table 8: Mesh information : Coarse

Number of cell in , X	-	24
Number of cell in , Y	-	16
Total number of cells	-	8464
Minimum cell size in , X	m	$0.039D$
Minimum cell size in , Y	m	$0.039D$
Time step, $\Delta T$	s	0.001

Figure 9 shows the  $y+$  value, avg. coefficient of drag,  $C_d$ , and avg. coefficient of lift,  $C_l$ . The  $y+$  value has been restricted to 0.2 during the simulation setup. However,  $y+$  is directly proportional to the wall shear stress ( $WSS_x$ ) therefore, it can not be exactly maintained without running a simulation. Since  $y+$  has been calculated before running the simulation using flat plate theory, a little deviation can be seen. Although it is less than 1 which is set to be a primary concern. For all the simulations presented in this thesis report,  $y+$  has been seen as less than 0.5 and close to 0.2.

The  $C_d$  value has been recorded more than 1 (around 1.2) experimentally for a circular cylinder receiving a flow with Re number 110k. However, the oscillatory convergence is showing a value around 0.4715. Therefore, it can be said that the flow has converged into a pseudo-stable point which was also reported in a previous study by [Queutey et al. \(2022\)](#).

The mesh is constructed symmetrically in the transverse direction, also the geometry is a simple circular cylinder therefore, the average lift coefficient,  $C_l$  is expected to be zero. However, it is evident that the simulation produces a positive lift with a numeric value of 0.03579 in Figure 9d which is not physical.

Considering the discrepancy in the result compared to the experimental one, it has been decided to refine the mesh imposing box around the cylinder. Two approaches have been taken into



consideration namely **Box 01** and **Box 02**, which are described in this section.

### Coarse Mesh: $Re = 110K$

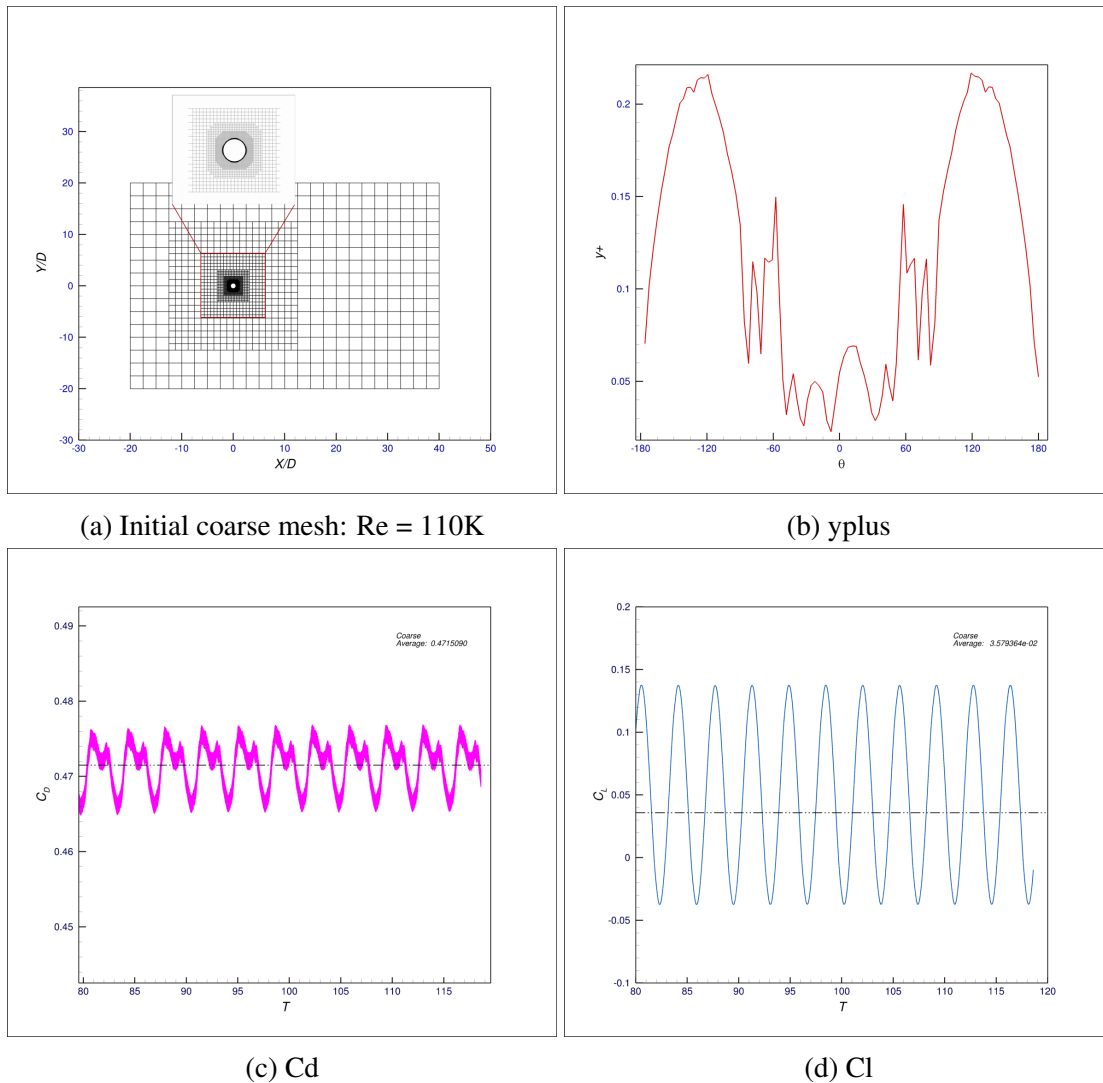


Figure 9: Initial coarse mesh :  $Re = 110k$

### Refinement Box: 01

A box of equal longitudinal and transverse length  $-5D$  to  $+5D$  has been taken into consideration. Refinement has been used (refinement diffusion 4) and can be seen from Figure 10a. The far field after  $20D$  is not refined since it is not necessary to consider enough refinement length in the longitudinal direction. The mesh is created symmetrically in the transverse direction so that there is no influence of mesh symmetry on the average lift coefficient. Figure 10b shows a tremendous fluctuation in  $y^+$  value although it is restricted to  $< 1$ . The real anomaly comes from the  $C_d$  and  $C_l$  values respectively. It can be well seen that the  $C_d$  and  $C_l$  values are showing non-physical results. It is worth mentioning that the minimum cell size in the both  $X$  and  $Y$  directions is approximately  $0.005D$ . The total number of cells after the viscous layer is around  $2M$  (see

Table 9 for mesh information) which is very high in terms of a 2D single cylinder simulation. Therefore, a different approach has been taken into consideration for setting up a box.

Table 9: Mesh information : Refinement box 01

Box size in, X	m	-5D to 5D
Box size in, Y	m	-5D to 5D
Number of cell in , X	-	24
Number of cell in , Y	-	16
Total number of cells	-	2202130
Minimum cell size in , X	m	0.005D
Minimum cell size in , Y	m	0.005D
Time step, $\Delta T$	s	0.001

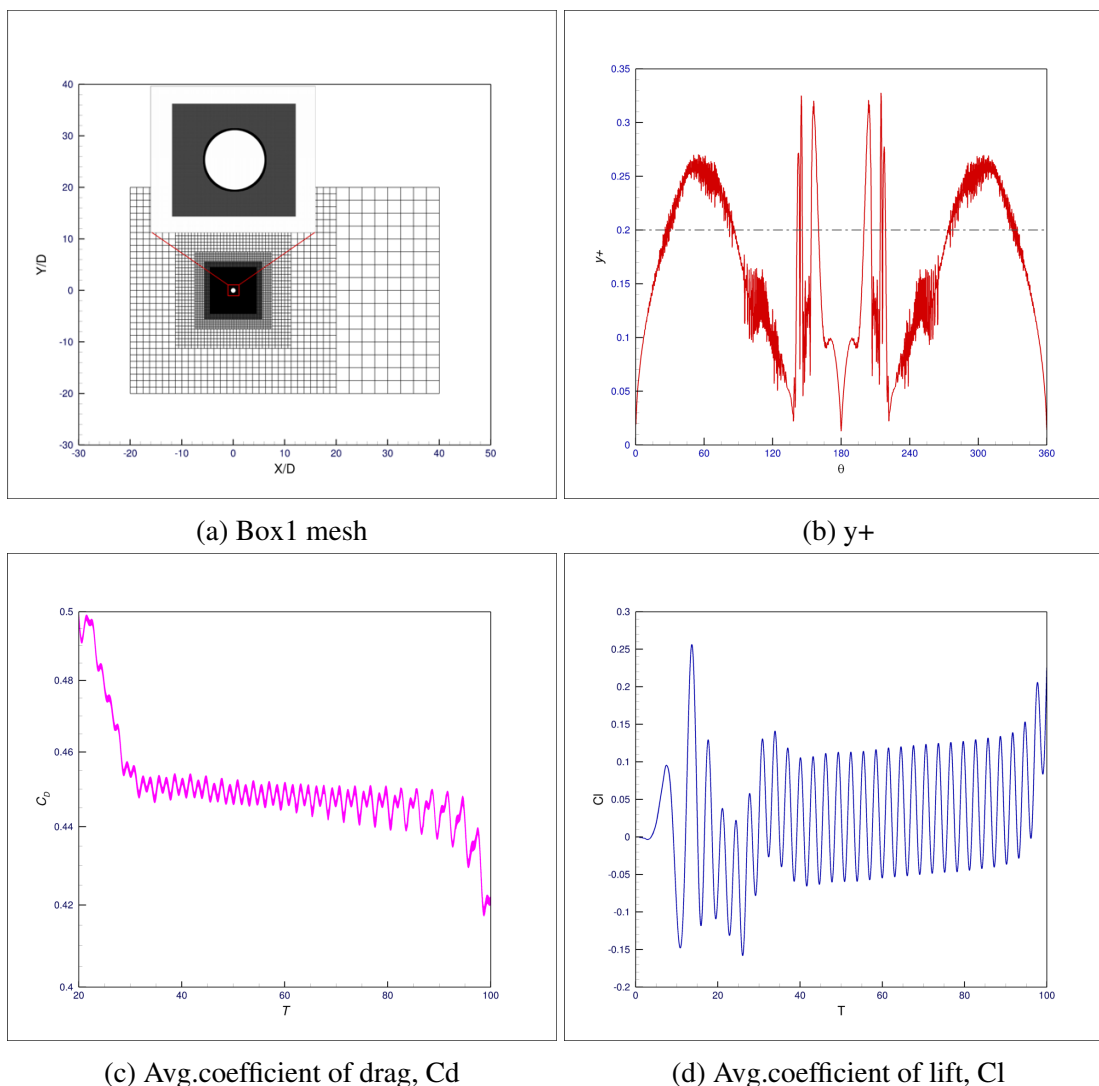


Figure 10: Box1 :  $Re = 110k$

**Refinement Box: 02**

A box has been set up which has the range  $-5D$  to  $+30D$  in the longitudinal direction, and  $-5D$  to  $5D$  in the transverse direction (see Figure 11a). The minimum cell size is  $0.04D$  m in both directions and the total number of cells (with viscous layers) is equal to 186,538 (186k) (see Table 10 for mesh information). Although the  $y^+$  is in the expected range, the evolution of  $C_d$  and  $C_l$  are showing anomalies. Furthermore, the value of  $C_d$  is stuck in a pseudo-stable point and the lift is highly positive which are not physical (see Figure 11). Therefore, a different approach should be adopted to address these matters and obtain outcomes that are physical.

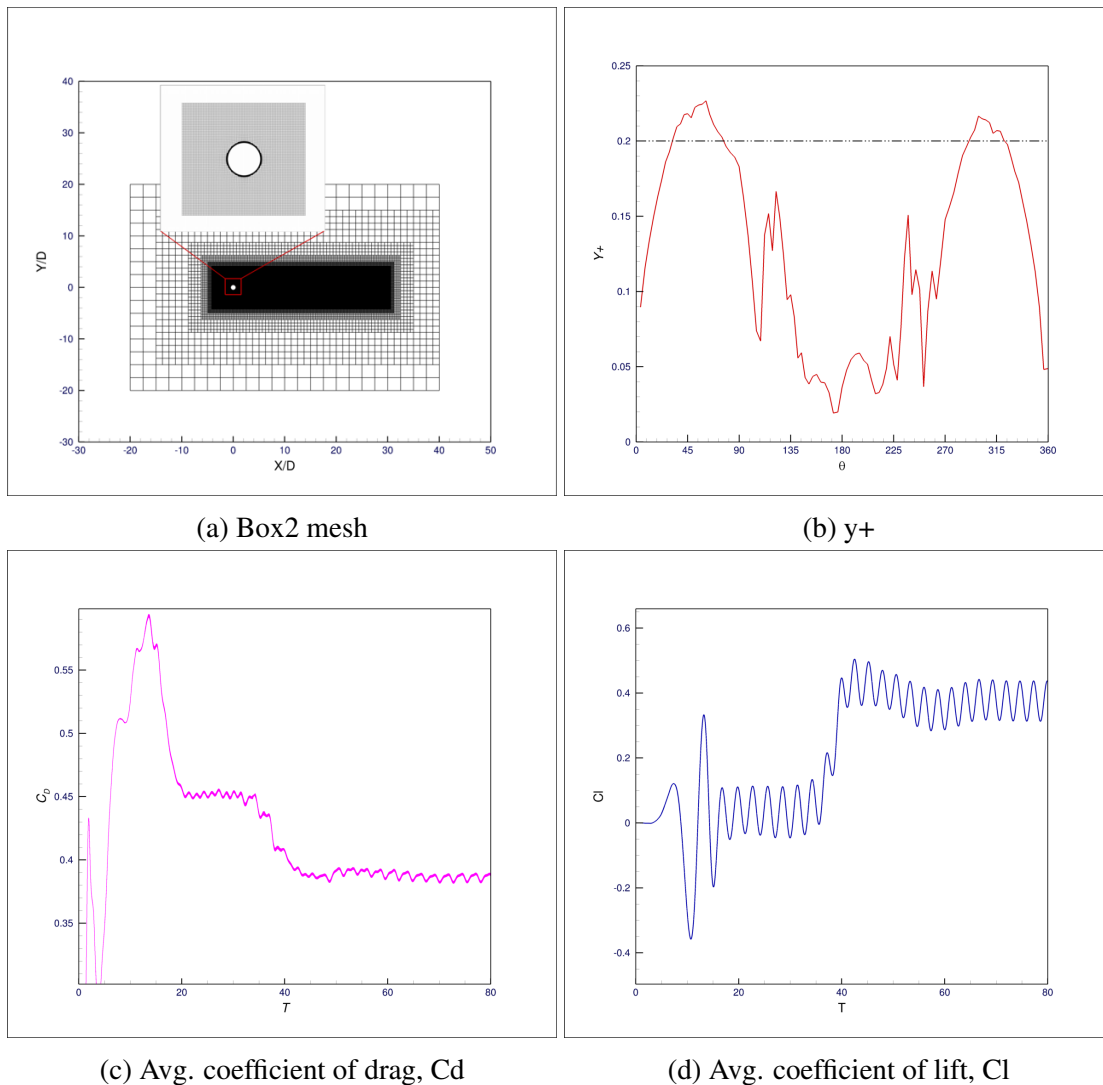
Figure 11: Box2 :  $Re = 110k$

Table 10: Mesh information : Refinement box 02

Box size in, X	m	-5D to 30D
Box size in, Y	m	-5D to 30D
Number of cell in , X	-	24
Number of cell in , Y	-	16
Total number of cells	-	186538
Minimum cell size in , X	m	0.039D
Minimum cell size in , Y	m	0.039D
Time step, $\Delta T$	s	0.001

### O-type mesh

Defining the number of cells in radial( $r$ ) and circumferential directions ( $\theta$ ), an O-type mesh has been constructed. This is another approach to constructing a static mesh for single-cylinder simulation. Three different types of mesh have been set up with two different time steps. Also, the meshes are created by multiplying a constant equal to 1.5 in both directions with the coarser one. It is worth noting that no refinement box has been considered for constructing an O-type mesh. Table 11 shows information about all three meshes in detail.

Table 11: Mesh information : O-type

		M1	M2	M3
Number of cells in Radial( $r$ ) x Circumferential direction( $\theta$ )	-	144x120	216x180	324x240
Total number of cells without viscous layers	-	17280	38880	77760
Total number of cells with viscous layers	-	21716	23880	84720
Time step, T1	s	0.05		
Time step, T2	s	0.005		

Figure 12a demonstrates the coarse mesh (M1) and corresponding outcomes after simulation such as  $y^+$ ,  $C_d$ , and  $C_l$  values. The other two meshes' pictures (M2 and M3) are not shown in the report. It seems that with the coarse O-type mesh the  $y^+$  value stays in the limit and the average lift coefficient,  $C_l$  shows zero lift with symmetry which is physical. The  $C_d$  value on the other hand shows the numeric value equivalent to 0.8280 which agrees with the numerical simulation performed by other researchers in  $Re = 140k$  ( $1.4 \times 10^5$ ) (see Table 15).  $C_d$  and  $C_l$  figures also show the shedding frequency in drag and lift directions (Figure 12). The prediction of shedding frequencies in both directions is also a piece of vital information for single-cylinder benchmark simulation. However, still, the  $C_d$  value does not correspond with the experimental value. The reason will be explained later since it depends on the physics of the flow for the specific  $Re$  number range in which flow solvers are not capable of predicting an equivalent drag as compared to the experiment.

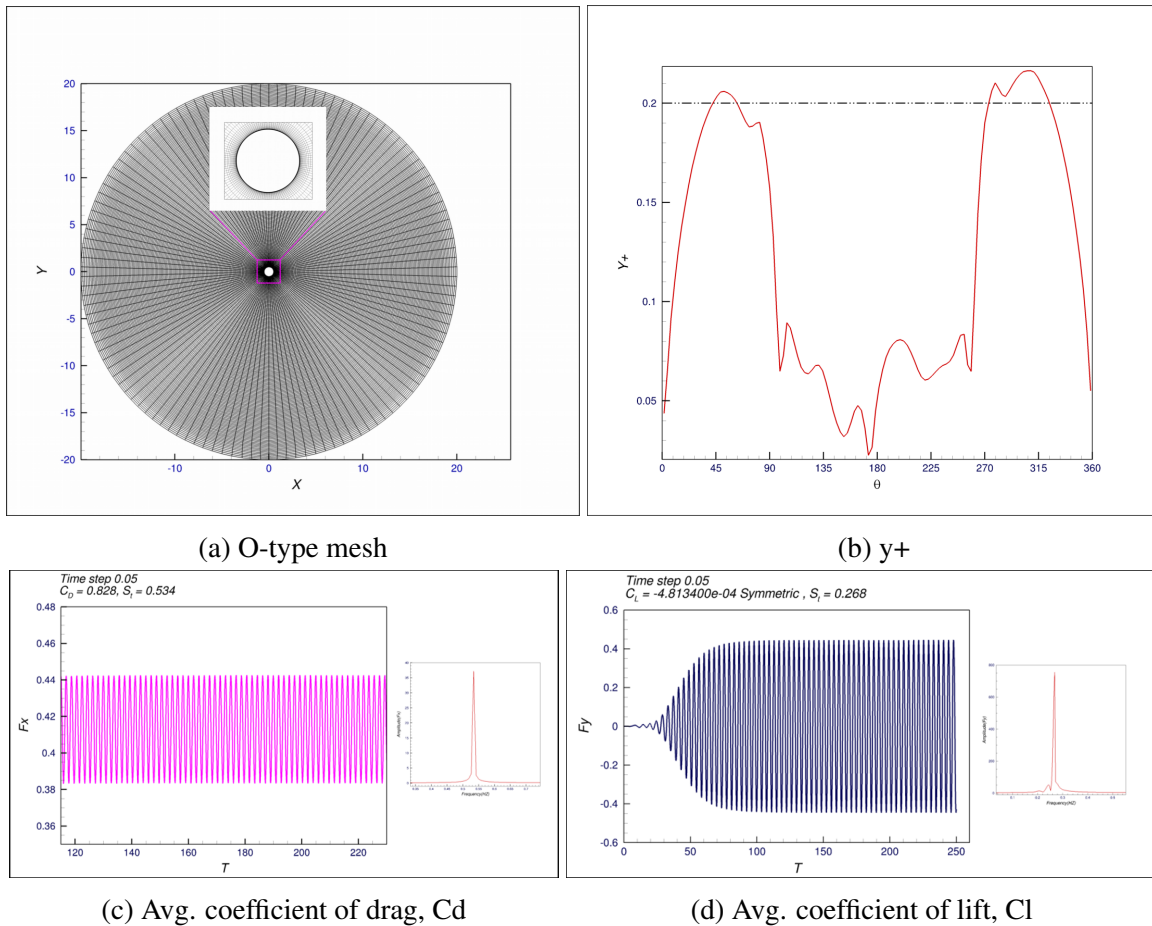


Figure 12: O-type at  $Re = 140k$  : Coarse mesh,  $y^+$ , evolution of avg.  $F_x$  (note that  $C_d = 2F_x$  when single cylinder case is simplified), and avg.  $F_y$  (note that  $C_l = 2F_y$ ) with corresponding  $St$  number peak

With the O-type mesh, simulations are conducted in sub-critical ( $140k$ ) and post-critical ( $10^7 = 10M$ )  $Re$  numbers and the outcomes are documented in Table 12.

Table 12: Hydrodynamic parameters : O-type Mesh

Re	r by $\theta$	Time step, $\Delta T$ [s]	$C_d$	$C_l$	$\theta_{sep}$ [°]	$St_{C_d}$	$St_{C_l}$	Cpb ( $\theta = 180^\circ$ )
$1.4 \times 10^5$	144x120	0.0500	0.8280	-0.0005	100.5090	0.5340	0.2680	-0.9093
		0.0050	0.7900	0.0005	98.0995	0.5100	0.2520	-0.8361
	216x180	0.0500	0.8000	0.0001	100.4030	0.5400	0.2700	-0.9461
		0.0050	0.7300	-0.0027	97.3911	0.5100	0.2600	-0.8061
10M	144x120	0.0500	0.7700	0.0083	100.2506	0.5500	0.2750	-0.8222
		0.0050	0.7020	0.0049	95.9846	0.5380	0.2580	-0.6997
	216x180	0.0500	0.5800	0.0087	120.3720	0.6000	0.3100	-0.8148
		0.0050	0.5500	-0.0075	117.8720	0.6000	0.3100	-0.7604
324x240	0.0500	0.5600	-0.0071	120.8800	0.6060	0.3140	-0.7673	
	0.0050	0.5600	0.0029	119.9140	0.6130	0.3110	-0.7706	
324x240	0.0500	0.5270	0.0042	117.4000	0.6270	0.3080	-1.2721	
	0.0050	0.5030	0.0002	116.7562	0.6380	0.3190	-0.6012	

The study with O-type mesh has given a significant insight into the single-cylinder benchmark simulation, that is, the single-cylinder simulation is highly sensitive to mesh type in terms of resolving flow parameters. It has been shown earlier that the previous mesh types (coarse mesh with and without refinement box) propose tremendous anomaly resolving flow parameters such as converging in pseudo stable point which undermines  $C_d$ , generating non-physical lift,  $C_l$  other than zero. However, with the O-type mesh, these issues are recovered. Again, the  $C_d$  value is lowered than the experiment in sub-critical Re number will be discussed later. Even though having all the positive aspects of O-type mesh, it has not been utilized in further studies to conduct TMS simulation. The reasons are as follows;

1. Mesh convergence could not be achieved even with three different arrangements and two-time steps value. Figure 13 shows the mesh convergence study for O-type mesh.

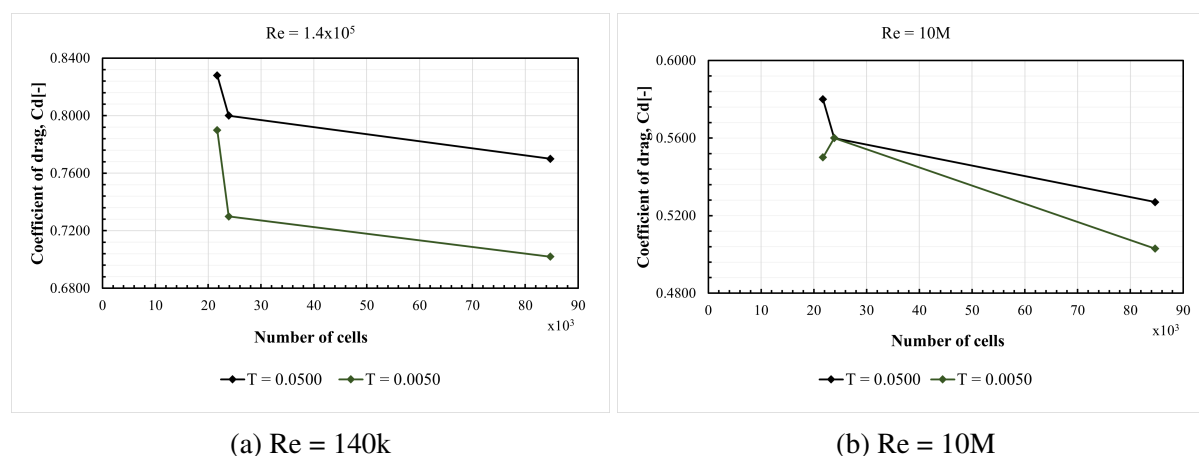


Figure 13: Mesh convergence study: O-type mesh

2. The inherent problem of creating the mesh around the cylinder. It is explained earlier about the five meshing steps of HEXPRESS in section 4.3. While using mesh wizard for a circular domain, the snapping step has shown an inability to capture the geometry even though it is a simple cylinder. After that, other meshing steps have been failed. A technique has been adopted to resolve the issue. Instead of the full domain, only half has been constructed for the meshing steps, and later on, the second half has been created by the mirroring process. In that way, a mesh distortion has been seen right through the middle cut of the flow domain. Figure 14 demonstrates the issue. Therefore, a single point may have been introduced at the middle cut which can be the cause of flow separation (can act like a corner) which is undesirable since the flow is separated on the smooth cylinder body due to the physics of the flow, not because of the geometry.

3. TMS has five cylinders and that can be quite a daunting task to ensure a good mesh around the cylinders as well as in the gap of those cylinders because gap flow will also play significant roles yielding the hydrodynamic parameters of each cylinder. Therefore, a technique has been adopted so that the above issues can be resolved.

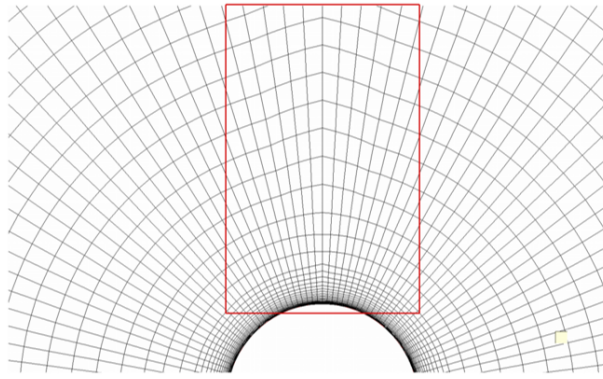


Figure 14: O-type mesh distortion

#### 4.5.2 Adaptive Refinement

The explanation about AGR has been documented from [Wackers et al. \(2022\)](#).

**Adaptive grid refinement (AGR)** is a computational technique that involves the local and automated refining of the mesh throughout a simulation, based on the specific flow needs. After a prolonged period of extensive research, the field of mesh adaptation is reaching a state of maturity, and its use in simulating intricate fluid dynamics is getting increasing traction. The determination of cell refinement in ISIS-CFD is conducted according to the following procedure. Initially, the refinement criteria  $C$ , a symmetric tensor field of dimensions  $3 \times 3$ , is calculated based on the flow solution, namely at the cell centers. The size of each hexahedral cell  $i$ , denoted as  $d_{i,j}$  ( $j = 1, 2, 3$ ), are determined by the vectors connecting the centers of opposing faces along the three cell orientations  $j$ . The objective of the grid refinement process is to approximate a given constant **threshold** parameter, denoted as  $Tr$ . Here the equation as follows ,

$$\|C_i \mathbf{d}_{i,j}\| = Tr, \forall i, j.$$

The refinement of a cell in the direction  $j$  occurs if  $\|C_i \mathbf{d}_{i,j}\|$  exceeds a threshold value denoted as  $Tr$ . Conversely, a group of cells that has been previously refined is unrefined in the direction  $j$  if  $\|C_i \mathbf{d}_{i,j}\|$  is smaller than  $Tr/d$  for all cells in the group. The constant  $d$  is selected with a value slightly more than 2 in order to avoid a scenario where cells are alternatively refined and re-refined. This choice is made as a global specification for determining the fineness of the mesh, ensuring that all cell sizes are proportionally dependent on this parameter.

The **minimum cell size** refers to the threshold below which cells are no longer subjected to further refinement. This alternative serves to mitigate the occurrence of erroneous refinement when locally significant error arise during the calculation of the refining criterion. Such errors are more likely to occur in cells with high aspect ratios, particularly in the near-wall boundary-layer mesh. Moreover, it serves to avoid the occurrence of endless fine-tuning surrounding flow singularities. Further details on AGR may be seen in [Wackers et al. \(2022\)](#). Table 13 shows the

AGR setup for the single cylinder simulation in  $Re = 110k$ , where  $D$  (m) is the unit diameter of the cylinder.

Table 13: Adaptive grid refinement settings

Refinement criterion	Flux component hessian	
	AGR1	AGR2
Refinement threshold, $Tr$	$D/5$	$D/10$
Type of refinement allowed in boundary layer	Longitudinal direction only	
Number of steps before first call to refinement procedure	10000	
Number of steps between calls to refinement procedure	10	
Minimum cell size limit for refined cells	$D/512$	

AGR has been applied to the initial coarse mesh described in Figure 9a. Figure 15a and 15b shows the formation of mesh in order to capture the flow field. The  $y+$  value is under desired limit. The avg. lift coefficient,  $Cl$  is symmetric and the average of it is close to zero which is expected by the physics of the flow. The value of avg. drag coefficient,  $Cd$  is not stuck at the pseudo stable value unlike the previous initial coarse mesh event. Therefore, AGR has the potential to resolve flow parameters which in turn agree well with the flow physics. With the change of threshold value there are substantial differences in the flow fluctuation and generation of number of cells. It can be seen from Figure 15. Therefore, a detail study is needed to select an optimum threshold value with a suitable time step. The immediate overview is devoted for the detail study of selecting suitable time step with an optimal threshold value.

#### Remarks

The application of AGR can also be extended to the O-type mesh. However, it should be noted that the challenges associated with generating the O-type mesh, as previously discussed, will not be resolved by the implementation of AGR. Therefore, the integration of AGR with O-type mesh was not performed.



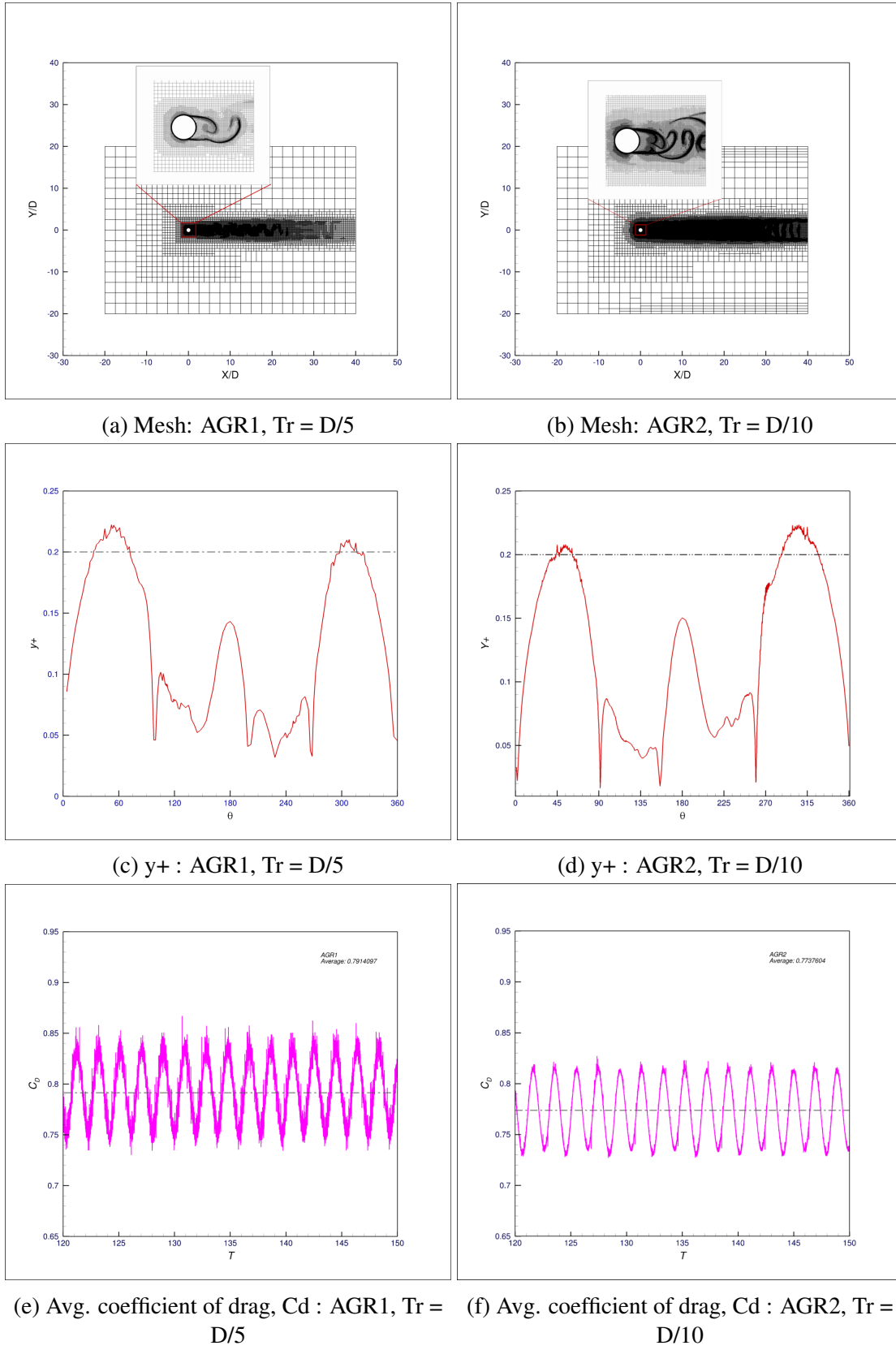
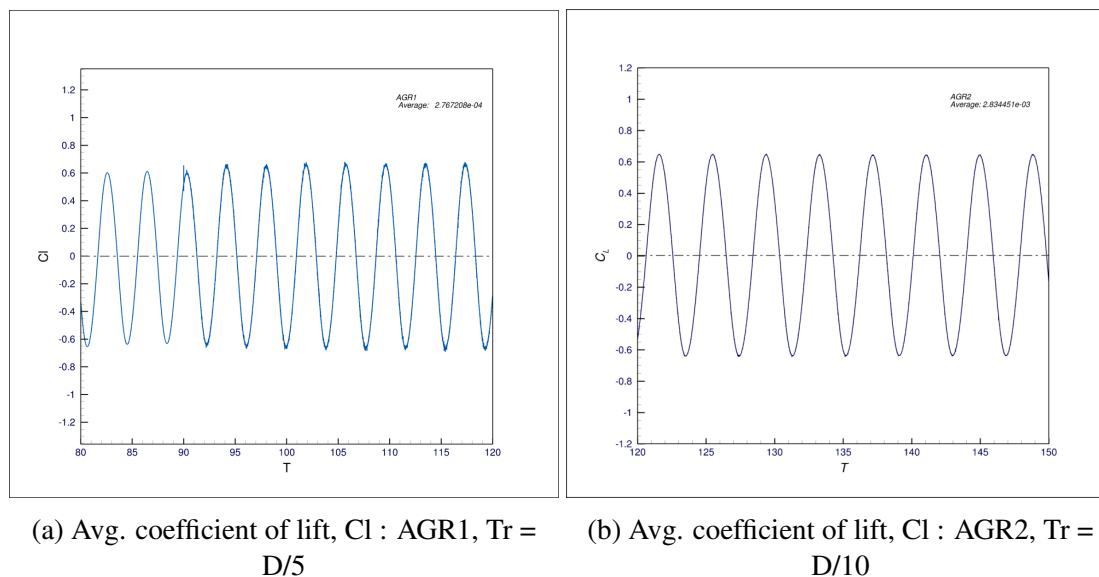
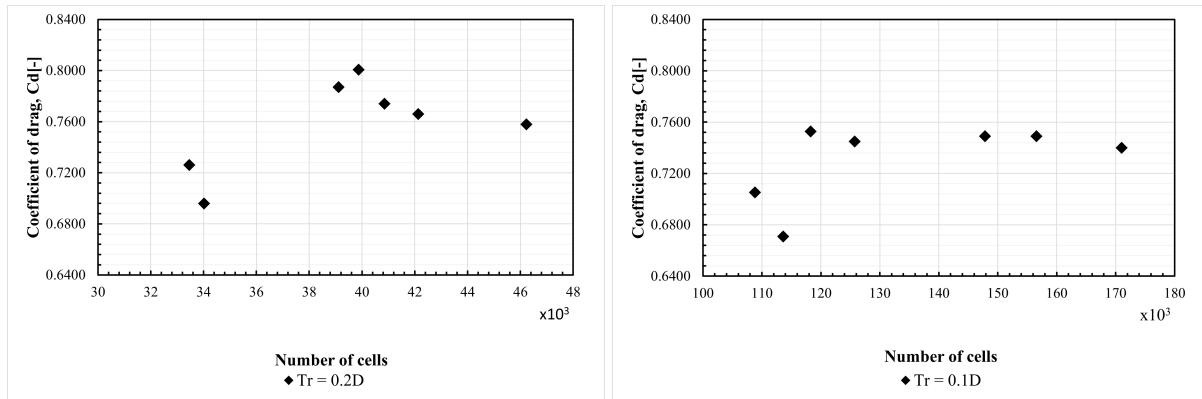


Figure 15: AGR :  $Re = 110k$

Figure 16: AGR :  $Re = 110k$ 

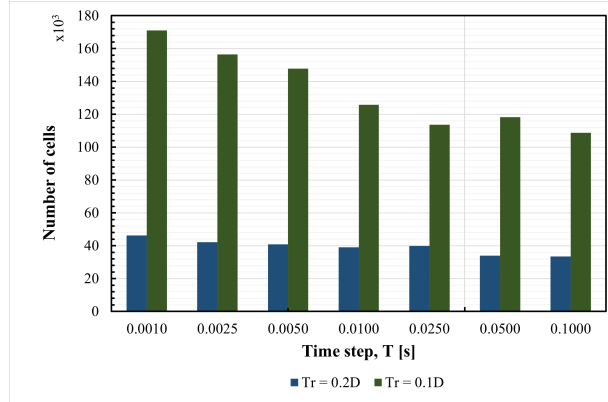
The  $Re = 140k$  is commonly investigated for fluid flow over a circular cylinder. Given the wide availability of numerical and experimental data relating to this Reynolds number, it has been decided to undertake temporal investigations employing three distinct AGR threshold limits. They are  $Tr = D/5$ ,  $D/10$ , and  $D/20$ . Other parameters remain unchanged as described in Table 13. Total seven-time steps are taken into consideration ranging from 0.1 s to 0.001 s. One important note is that the dimensionless time step is defined as  $\Delta t^* = \Delta T U / D$  where,  $\Delta T$  = time step [s],  $U$  = inlet velocity [m/s], and  $D$  = diameter (m) of the cylinder. Since  $U$  and  $D$  are taken equal to 1,  $\Delta t^* = \Delta T$  for the single cylinder simulation. Figure 17a and 17b shows the mesh convergence studies for  $D/5$ , and  $D/10$  threshold limit for all time steps. The mesh convergence could be shown for  $Tr = D/10$ , however, with  $\Delta t^* = 0.001$  s the avg. drag coefficient declined. With decreasing time steps, the number of cells is seen to increase in AGR setup which is evident in Figure 17c. The decline in  $C_d$  has been reported by [Athkuri et al. \(2023\)](#) as well with additional mesh refinement. Therefore,  $\Delta t^* = 0.0050$  and  $0.0025$  can be taken as the optimal time step obtained with  $Tr = D/10$ . Mesh convergence with  $Tr = D/5$  could not be shown. However, the  $C_d$  value and  $St$  numbers are in close proximity with the  $Tr = D/10$  results with significantly lesser cells keeping conservative results (small overestimation than  $Tr = D/10$ ). Therefore,  $Tr = D/5$  also shows a potential to conduct simulations with less expense than  $Tr = D/10$ . Table 14 shows the hydrodynamic parameters obtained from the simulation with different time steps and threshold values stated above. Note that,  $D/20$  has been set to only three-time steps ( $\Delta t^* = 0.0050$  s,  $0.0025$  s, and  $0.0010$  s) since distinct  $St$  numbers could be found with these three-time steps in a previous study conducted with  $Tr = D/5$ , and  $D/10$ . However, with  $D/20$  the simulation is seen to take excessive time than the previous two. Furthermore,

obtaining erroneous results is evident. This phenomenon may arise as a result of the excessive refinement of cells caused by a low threshold value. Therefore, studies with this threshold have been dropped. Note that, physically  $St_{Cd} = 2xSt_{Cl}$ , hence it is also necessary to obtain the same to validate the numerical simulation. The Strouhal (St) number is the indication of vortex shedding in the flow field which alters the flow pattern of other cylinders when stays in close proximity.



(a) Mesh convergence: Tr = 0.2D

(b) Mesh convergence: Tr = 0.1D



(c) Number of cell: Tr = 0.2D vs Tr = 0.1D

Figure 17: Mesh convergence study and comparison of number of cells : Re = 140k

Table 14: Single cylinder simulation at subcritical Re (140k) with a range of time steps and threshold values

Tr	Time step, $\Delta T$ [s]	$C_d$	$C_l$	$\theta_{sep}$ [°]	$St_{Cd}$	$St_{Cl}$	Cpb ( $\theta = 180^\circ$ )	Number of cells
D/5	0.1000	0.7260	0.0028	97.2278	Random	0.2440	-0.7827	33460
	0.0500	0.6960	0.0044	94.9332	Random, 0.5400	0.2720	-0.7451	34021
	0.0250	0.8007	0.0048	98.5774	0.5360	0.2680	-0.9517	39878
	0.0100	0.7870	0.0046	98.7465	0.5280	0.2620	-0.9321	39117
	0.0050	0.7740	0.0042	98.2072	0.5280	0.2580	-0.8841	40854
	0.0025	0.7660	-0.0051	97.6217	0.5201	0.2608	-0.8786	42134
	0.0010	0.7580	0.0044	97.9293	0.5290	0.2560	-0.8667	46224
D/10	0.1000	0.7053	0.7053	98.9440	Random	Random, 0.1128	-0.7809	108808
	0.0500	0.7527	-0.0094	99.0914	Random	Random, 0.1722	-0.7828	118262
	0.0250	0.6710	-0.0001	95.1964	Random, 0.5115	Random, 0.2558	-0.7369	113598
	0.0100	0.7449	0.0030	98.0893	Random, 0.5134	0.2610	-0.8448	125724
	0.0050	0.7490	0.0021	98.2949	0.5329	0.2664	-0.8698	147840
	0.0025	0.7490	-0.0004	98.2356	0.5222	0.2662	-0.8672	156546
	0.0010	0.7401	0.0012	98.7701	0.5251, 1.0501	0.2700	-0.8659	171029
D/20	0.0050	0.5965	0.0056	94.0269	0.1815, 0.3631, 0.5446	0.1815, 0.5446, 0.7261	-0.6165	500158
	0.0025	Abnormal flow		93.7882				
	0.0010	Stopped						

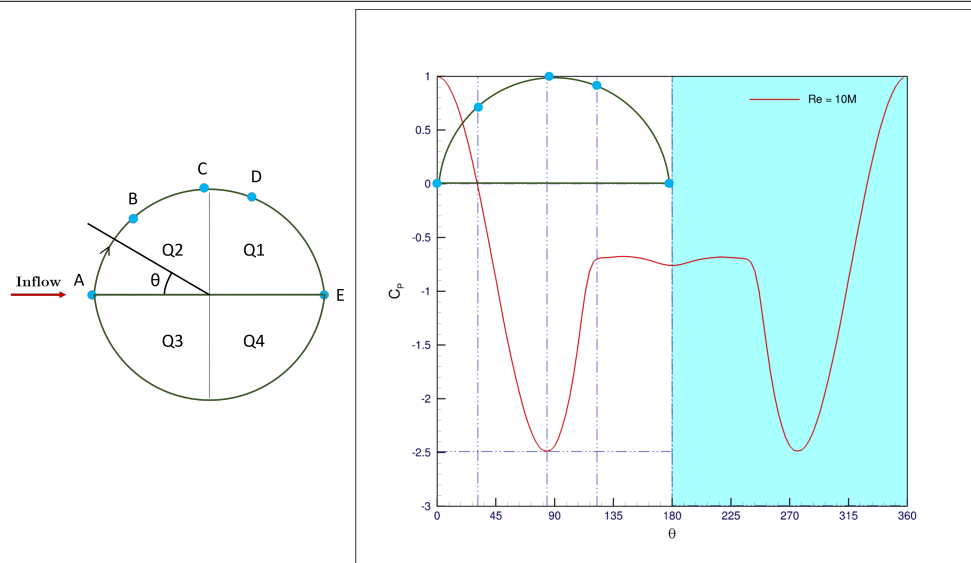


Figure 18: Avg. coefficient of pressure,  $C_P$  : Nomenclature

To understand the  $C_p$  plot around the cylinder body, Figure 18 is presented with introducing some points A to E and other nomenclatures.

- A : Stagnation point where velocity of the fluid becomes stationary, therefore,  $C_p$  is maximum with a positive value and velocity is 0 at that point.
- B : The pressure on the cylinder is equal and opposite to the free-stream pressure, therefore  $C_p = 0$ .
- C : Suction point, where  $C_p$  is maximum with a negative value.
- D : Turbulent separation point. Note that, the same point can be identified as a laminar separation point, in that case  $\theta$  lies before  $90^\circ$  can be seen only in experimental study

presented in Figure 19.

- E : Rear of the cylinder ( $\theta = 180^\circ$ ) at which avg. base pressure coefficient,  $C_{pb}$  is extracted. Note that, the journey of stagnation to rear point has been taken clockwise.
- Q1 - Q4 : Cylinder has been divided into four quadrants.
- The symmetric part has been identified with cyan color

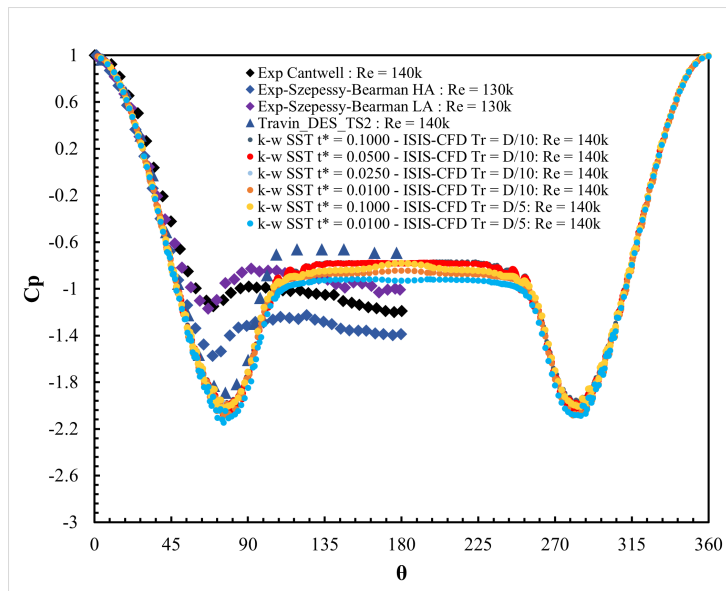


Figure 19: Avg. coefficient of pressure,  $C_P$  :  $Re = 140k$

Average coefficient of pressure,  $C_p$  around the cylinder wall is plotted and compared with the existing numerical and experimental data. The current study is showing identical trend with the numerical study, however, the suction peaks are overestimated than the other results. ISIS-CFD solver shows identical  $C_p$  plot with the numerical simulation conducted by [Travin et al. \(2000\)](#). Note that, the experimental data is recorded by the authors for the first half of the cylinder (average on time) due to the symmetry of the flow. The numerical simulation also shows the symmetry which is presented in Figure 19.

Table 15: Previous study :  $Re = 140k$

	Cd	$-C_{pb} (\theta = 180^\circ)$	$St_{Cl}$
DES (B1-4 ( <a href="#">Lo et al. (2005)</a> )))	0.62–0.704	0.83–0.91	0.287–0.305
SST DES ( <a href="#">Lakshmiathy et al. (2010)</a> ))	0.847	0.892	0.26
DES (TS 2 ( <a href="#">Travin et al. (2000)</a> )))	0.59	0.67	0.31
DES (TS 4 ( <a href="#">Travin et al. (2000)</a> )))	0.64	0.7	0.28

The previous numerical studies show variation of results among them at  $Re = 140k$  numbers in Table 15 found from [Athkuri et al. \(2023\)](#). Furthermore, Figure 73 shows the variation of Cd results both experimental and numerical among the researchers from sub-critical to post-critical flow regimes. Therefore, performing an error study is not possible since a reference can not be

fixed. It is quite evident that imposing AGR ( $Tr = D/5$ , and  $D/10$ ) with time steps ( $\Delta t^* = 0.0050$ ,  $0.0025$ ) shows nearly identical prediction of hydrodynamic parameters with the numerical study (see Table 14). Therefore,  $Tr = D/10$  and time step,  $\Delta t^* = 0.0050$  are taken as optimal temporal and spatial parameters for the simulation over a cylinder. Simulations are also conducted with range of  $Re$  number with the identical optimal temporal and spatial parameters. The skin friction,  $C_f$  and the avg. coefficient of pressure,  $C_p$  are plotted with the available numerical and experimental studies in Figure 20 and 21 respectively. Also, data has been compiled and compared for various hydrodynamic parameters from sub-critical to post-critical range for single cylinder simulation (See Figure 74 to 78 in [Appendix 1.3](#)). Now the question is, *Why does the numerical data namely hydrodynamic parameters do not correspond with the experiment presented by the other researchers in sub-critical to critical  $Re$  numbers? (see flow regime in Table 3).*

The flow around the cylinder is governed by both laminar and turbulent separation from sub-critical (laminar separation) up to critical (laminar to turbulent transition separation)  $Re$  numbers. The variation in the hydrodynamic coefficients can be ascribed to the insufficiency of eddy viscosity turbulence models when dealing with the flow that undergoes laminar to turbulent transition. The URANS findings illustrated the inability to predict accurately the occurrence of the drag crisis, mostly attributed to their inadequate capacity to forecast the transition of the boundary layer (laminar to turbulent) [Vaz et al. \(2007\)](#) [Ye et al. \(2017\)](#). It can also be observed from Figure 19, where the experimental curve shows a laminar separation occurs before  $90^\circ$  which is stated earlier. However, the numerical simulations could not predict the laminar separation, instead, it proposes a turbulent separation identical to the Figure 18 in which the  $C_p$  plot is shown for  $Re = 10M$  as a demonstration. Therefore, the eddy-viscosity solver could not predict the laminar separation. [Travin et al. \(2000\)](#) conducted simulations utilizing a hybrid RANS-LES (DES). The simulations were run under the assumption of laminar separation (LS), which considers a laminar inlet flow, and turbulent separation (TS), which assumes a turbulent inlet, for a Reynolds number ( $Re$ ) of 140k. In their study, the avg. drag coefficient and pressure coefficient for a  $Re$  of 140k, as determined by the laminar separation (LS), exhibited a closer agreement with the experimental data. However, the turbulent separation (TS) significantly underestimated the values in compared to the experiment. Therefore, the LS exists in the sub-critical region where the transition (laminar to turbulent transition separation) exists in the critical region, which exactly says why the hydrodynamic parameters found from the numerical simulation in the current study for  $Re = 110k$ ,  $140k$ , and  $850k$  show a better agreement with numerical data than the experimental ones (see Figure 74 and 78 in [Appendix 1.3](#)). It also implies that the aforementioned models are incapable of accurately representing the drag-crisis phenomenon due to their inability to mimic the shift from a laminar to a turbulent boundary layer. Table 16 records the hydrodynamic parameters for single cylinder simulation from sub-critical to post-critical flow regime. However,

since all the cylinders in TMS experience the incoming flow in a post-critical regime with an inlet velocity of 12 m/s, at which the boundary layer will be fully turbulent, therefore, the eddy-viscosity model is expected to predict the hydrodynamic parameters closer to the experimental value.

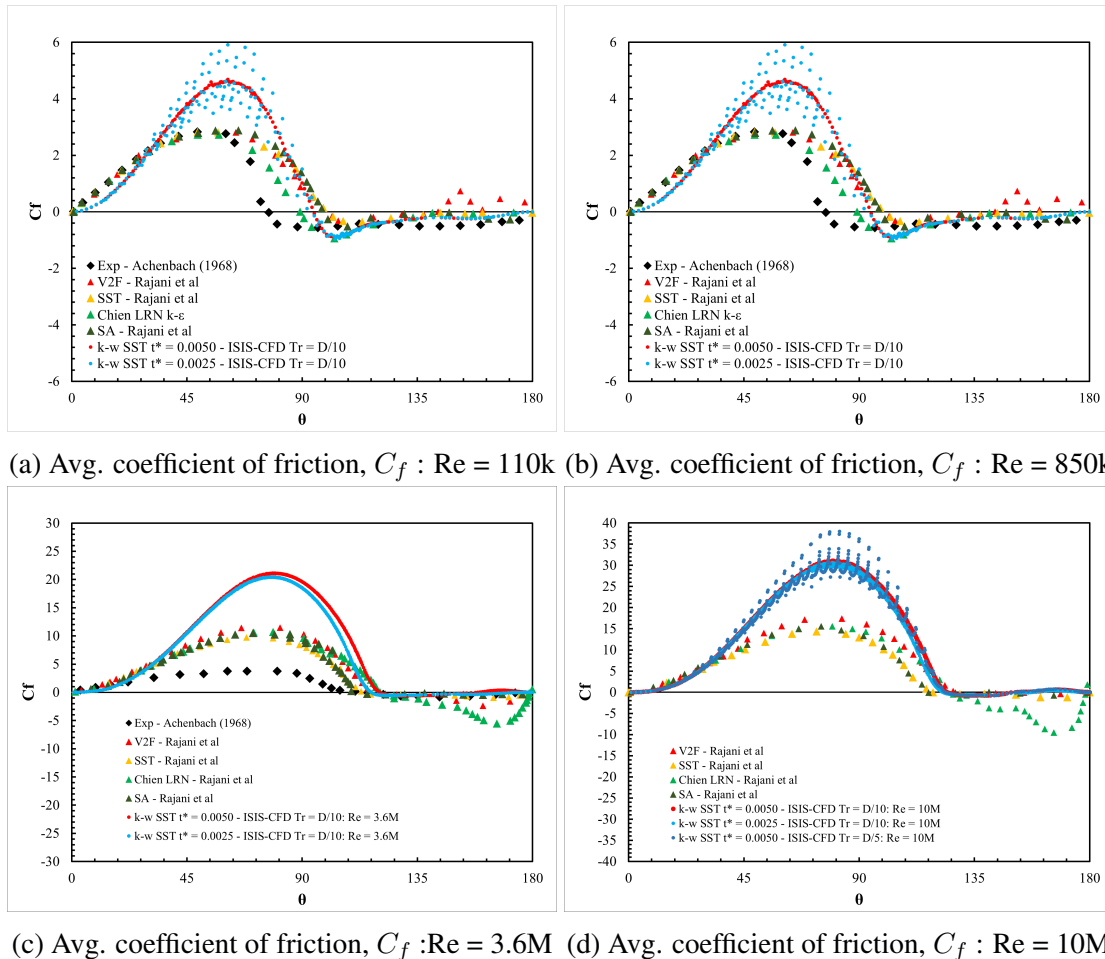


Figure 20: Distribution of avg. coefficient of friction,  $C_f$  around the first half of the single cylinder

Figure 20 shows scattered points for skin friction,  $C_f$  instead of distinct curve for particular simulations at  $Re = 110k$ ,  $850k$ , and  $10M$ . As aforementioned, any geometry is captured during the five meshing stages performed in mesh wizard. However, new points are created during the mesh refinement and unrefinement process when AGR is activated. If the option '**Project refined grid onto body surface**' is not turned on in AGR setting, the new points may lie outside of the original geometry and the effect of that can be seen in avg. skin friction coefficient,  $C_f$  and avg. coefficient of pressure,  $C_p$  plots. The setting has been turned off for those simulations, therefore a scattered  $C_f$  and  $C_p$  are observed. Therefore, it is necessary to turn on that setting when AGR is activated. However, by looking at those figures it can also be realized that the

scatter plot will provide a distinct curve if averaged. Thus, this option gives a significant insight for AGR setting in the current study which is kept in mind for later simulations as well.

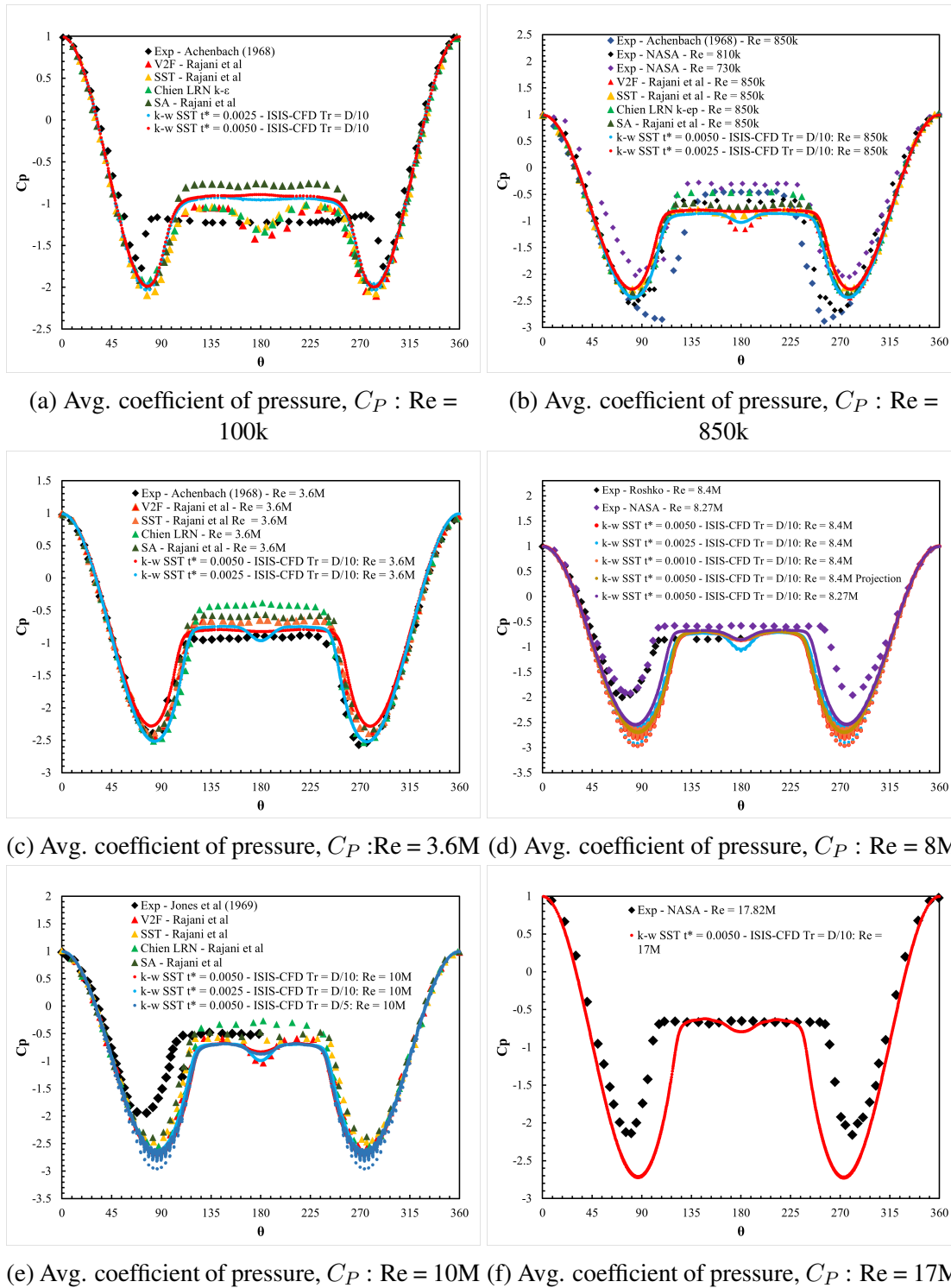


Figure 21: Distribution of avg. coefficient of pressure,  $C_p$  around the cylinder



Table 16: Single cylinder simulation from subcritical to post-critical range ( $Tr = D/10$  unless specified)

Re	Time step, $\Delta T$ [s]	$C_d$	$C_l$	$\theta_{sep}[^\circ]$	$St_{Cd}$	$St_{Cl}$	Cpb ( $\theta = 180^\circ$ )	Number of cells
110k	0.0050	0.783	-0.0058	94.4578	0.5130	0.2620	-0.8906	146849
140k	0.0050	0.7490	0.0021	98.2949	0.5329	0.2664	-0.8698	147840
850k	0.0050	0.726	0.0086	111.475	0.6015	0.3008	-1.0276	179044
3.6M	0.0050	0.674	0.0063	120.354	0.6646	0.3285	-0.9503	228114
8.27M	0.0050	0.5642	0.0007	118.9370	0.6264, 1.2528	0.3132, 0.9396	-0.8569	198372
8.4M	0.0050	0.640	-0.0021	124.237	0.6815	0.3420	-0.8656	276107
10M								
D/5	0.0050	0.6293	0.0121	123.7380	0.6809	0.3332	-0.8723	136044
D/10	0.0025	0.6151	0.0040	124.2940	0.6778	0.3389	-0.8324	287087
12M	0.0050	0.5783	0.0044	121.5100	0.6366	0.3183	-0.9352	216166
17M	0.0050	0.5541	0.0026	125.7010	0.6869, 1.3739, 2.0609, 2.7479	0.3401, 1.0271, 1.7141, 2.4010	-0.7939	294110
25M	0.0050	0.5494	-0.0014	124.0340	0.6630, 1.3260	0.33153, 0.9945	-0.9040	215864

Figure 20 and 21 demonstrate that the ISIS-CFD solver predicts the avg. skin friction coefficient,  $C_f$  and the avg. pressure coefficient,  $C_p$  distribution around the cylinder and flow separation close to the other numerical studies. Therefore, the settings obtained from the single cylinder simulations will be performed for the TMS as well. Literature shows that depending upon the evolution 30-100 dimensionless time steps are adequate to calculate the mean hydrodynamic parameters when the simulation is converged for single cylinder. In conclusion, the temporal and spatial resolution obtained from this particular section will be utilized in the subsequent section for the 2D simulation of TMS.

#### Remarks

In the single cylinder simulation, the mean of the hydrodynamic parameters was calculated by using an average time window of 100 dimensionless time steps, denoted as  $\Delta t^*$ . The simulations for the single cylinder in the present study were conducted for a total of 250 dimensionless time steps. The size of the average window has been taken from 150 to 250. According to the existing literature, it has been shown that, for a single cylinder simulation, the mean hydrodynamic parameters may be accurately calculated by employing a range of 10 to 100 dimensionless time steps  $\Delta t^*$ , depending on the extent of flow fluctuation and the convergence of the simulation.

## 5 2D STUDY OF TMS - URANS $k-\omega$ SST

Since the TMS has a total of seven orientations which was stated in section 2, initially  $30^\circ$  orientation has been chosen to conduct the 2D simulation. It is expected that the 2D  $30^\circ$  orientation simulation would provide valuable insight before proceeding with the rest of the orientations and 3D simulation. Figure 22 depicts the  $30^\circ$  orientation.

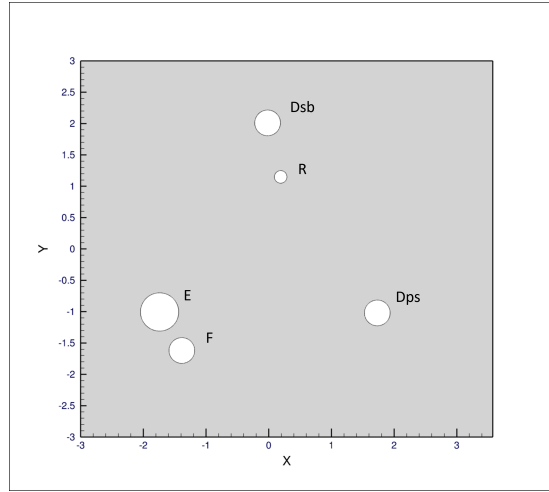


Figure 22: TMS:  $30^\circ$

In a single-cylinder simulation, the dimensional time step was equal to the dimensionless time step,  $\Delta T = \Delta t^*$  due to the unit diameter  $D(m)$  of the cylinder. However, TMS has five cylinders with three different diameters. Therefore, to relate the identical dimensionless time step  $\Delta t^*$  to the time step with dimension  $\Delta T$  a calculation is needed. Here, two extreme diameters have been taken into consideration. Cylinder E has the highest diameter  $D = 0.61$  m and cylinder R has the smallest equal to,  $D = 0.2$  m.

Table 17: Dimensional time step,  $\Delta T$  calculation

$\Delta t^* = \Delta T U / D$ [-]	Diameter, $D$ [m]	$\Delta T = D \Delta t^* / U$ [s]	Inlet velocity, $U$ [m/s]
0.0050	0.61	2.54E-04	12
0.0025		1.27E-04	
0.0010		5.08E-05	
0.0050	0.2	8.33E-05	12
0.0025		4.17E-05	
0.0010		1.67E-05	
0.0005		8.33E-06	

The time step,  $\Delta T$  which is found with cylinder R has been taken into consideration since it shows a smaller time step than what is found with cylinder E so that a better temporal resolution can be offered to all cylinders. The changes have been introduced to the previously **simulation setup and solver setting** and **AGR settings** (see Table 7 and 13) are given as follows in Table

18. Note that, the diameter,  $D = 0.61$  (cylinder E) for the simulation setup, since the highest Re number (25M) corresponds to the highest diameter of the TMS.

Table 18: Changes in simulation setup and solver setting for 2D 30° TMS simulation (here,  $D = 0.61$  m, diameter of cylinder E)

Parameters	Unit	Numeric value
Dynamic viscosity	pa.s	0.000145
Density of LNG	kg/m <sup>3</sup>	500
Reference length	m	0.61
Reference velocity	m/s	12
Time step values	s	8.33E-05, 4.17E-05, and 1.67E-05
AGR threshold, Tr	-	D/10
Minimum size limit for refined cells	m	D/512

## 5.1 TMS - Orientation: 30°

In single-cylinder simulation,  $\Delta t^* = 0.0050$ , and  $0.0025$  were found to be optimal. Here, the 2D simulation has been conducted with three dimensionless time steps,  $\Delta t^* = 0.0050$ ,  $0.0025$ , and  $0.0010$  (time with dimension,  $\Delta T = 8.33E-05$ ,  $4.17E-05$ , and  $1.67E-05$  s. Noting that, dimensional time step,  $\Delta T$  was used as input in *FineMarine*) considering identical mesh setup. The evolution of the avg. coefficient of drag,  $C_d$  for all the cylinders for the above-mentioned time steps,  $\Delta t^*$  is shown in Figure 23.

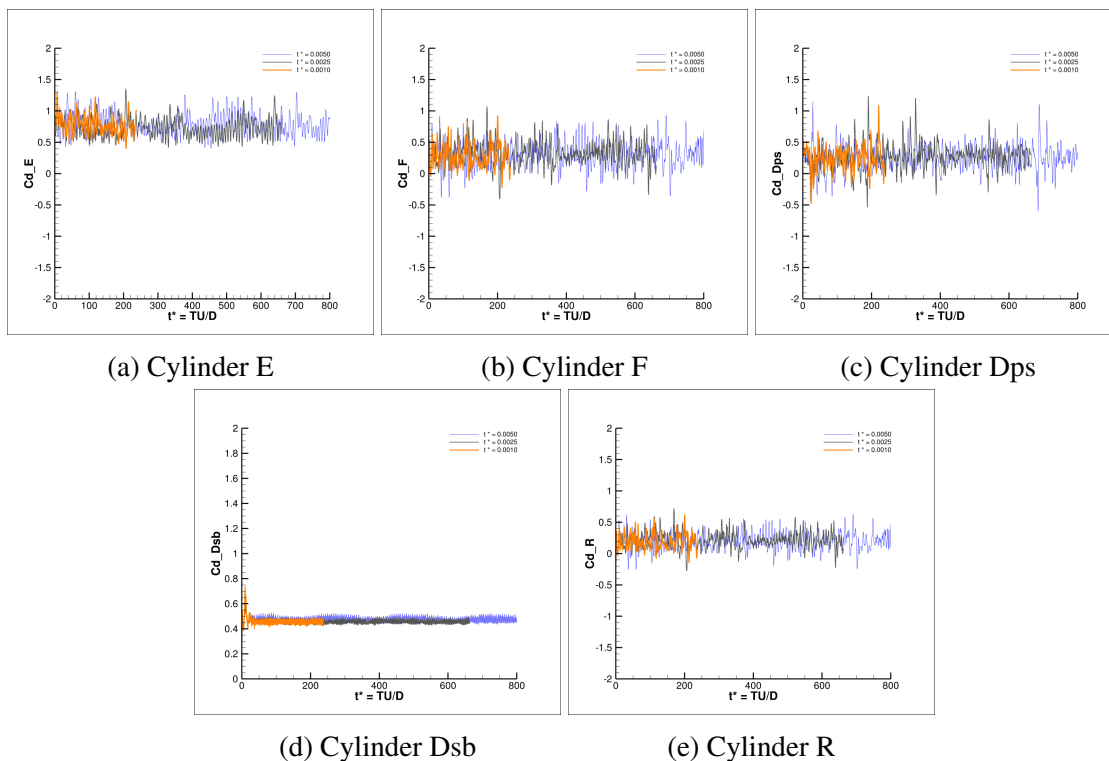


Figure 23: Evolution of avg. coefficient of drag,  $C_d$

Table 19: Comparison of avg. coefficient drag,  $C_d$  :  $\Delta t^* = 0.0050$  vs  $0.0025$ 

Cylinder name	$\Delta t^* = 0.0050$	$\Delta t^* = 0.0025$	Error [%]
	[-]	[-]	
$C_d$	E	0.7775	9.3387
	F	0.3019	-5.4881
	Dps	0.2996	7.1347
	Dsb	0.4461	-2.1992
	R	0.5795	9.0366
Number of cell	752006	732704	-
Physical Time [s]	16.9190	11.4480	-
Number of iterations	203109	274532	-

Figure 23 shows that with different time steps, there is a change in the fluctuation of the flow. However, all the time steps seem to follow an identical trend. Simulation with  $\Delta t^* = 0.0010$  was forced to stop due to high computational expense. A comparison is shown for avg. drag coefficient,  $C_d$  with  $\Delta t^* = 0.0050$ , and  $0.0025$  can be seen in Table 19. To compare,  $\Delta t^* = 0.0025$  has been set as a reference value since it shows lesser fluctuation in flow than the  $\Delta t^* = 0.0050$ . Also, it seems that the number of cells generated in  $\Delta t^* = 0.0050$  is more than  $\Delta t^* = 0.0025$ , however, it is not true and one can appreciate it by looking at the physical run time of both simulations. The error of the hydrodynamic parameters between these two simulations is calculated by maintaining the following equation.

$$Error[\%] = \frac{Value - Reference}{Reference} \times 100 \quad (38)$$

Figure 24 demonstrates the mesh formation resolving the flow, avg. coefficient of pressure,  $C_p$  contour, and the function  $F$  (function  $F$  can be denoted by the ratio of integral length to the cell edge size) for  $\Delta t^* = 0.0050$ . The detail about the function  $F$  is recorded in section 6.1.2.

With the 2D study, it was decided to run a 3D simulation with mirror boundary conditions in a span-wise direction. The identical mesh setting which was attained in 2D  $30^\circ$  applied for the 3D simulation as well. Note that, the generation of cells in the far field is not essential (see Figure 24a) from the study point of view. Therefore, to restrict the refinement in the far zone, a control box has been proposed for 3D simulation (see Figure 64a). The 2D mesh was extruded in a spanwise direction with 100 cells. The detail is discussed in the 3D URANS section. The 3D simulation showed an unfeasible event of running it further since the number of cells generated approximately 350M ( $350 \times 10^6$ ) within 4-time steps only (Total physical time = 0.291655 s). The simulation was performed in 600 cores in **French national computer**. Again, the threshold value for 3D simulation was minimized and set to  $Tr = D/5$ , to check the generation of the number of cells. It is found that the cell number has increased exponentially and eventually reached 325M within 4-time steps (see Figure 25).

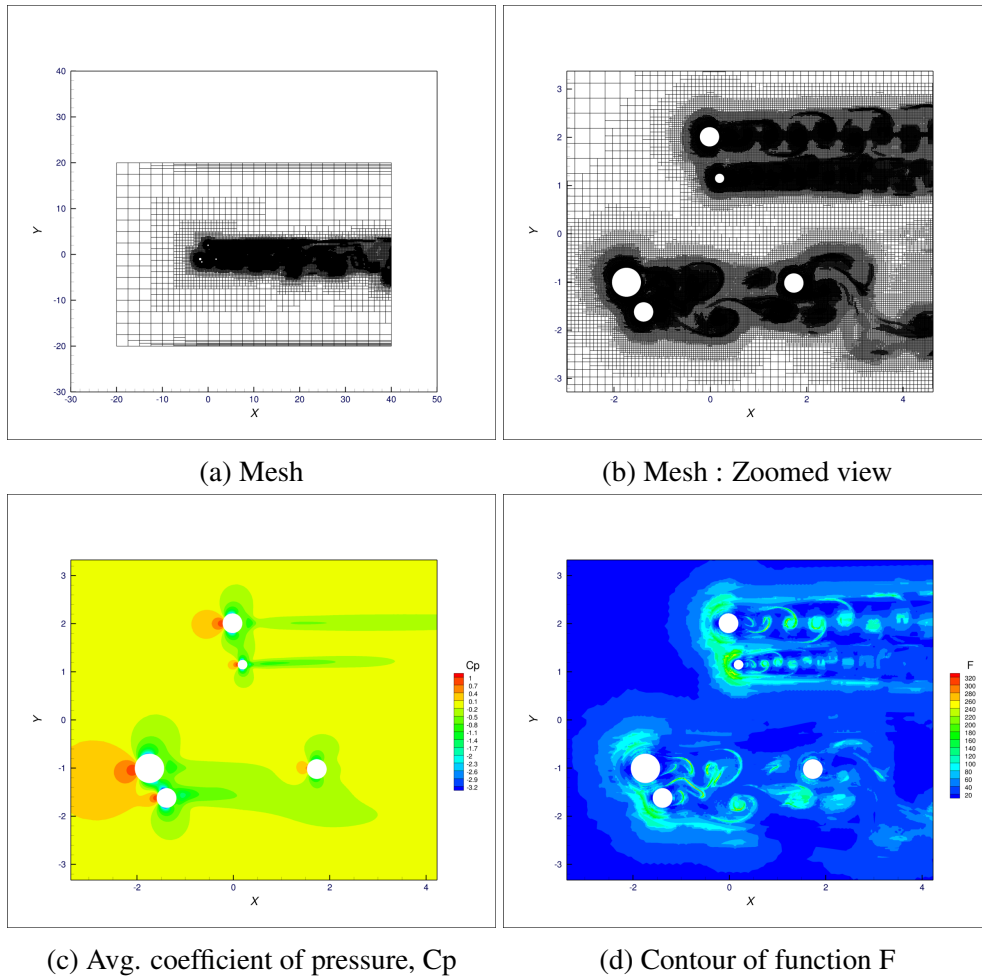


Figure 24: Post-processing results,  $\Delta t^* = 0.0050$  : 2D  $30^\circ$  orientation

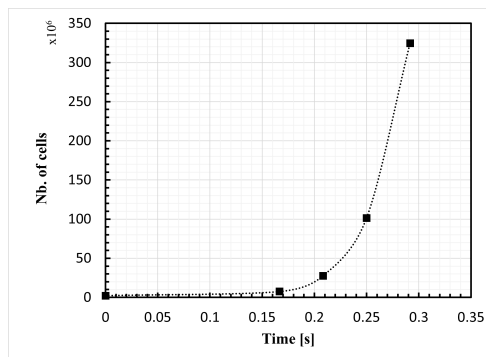


Figure 25: Number of cells: 3D URANS  $k-\omega$  SST,  $Tr = D/5$  (Mirror boundary condition in span-wise direction)

Due to the large number of cells, the simulation was stopped. Therefore, a new study was needed with a different mesh for 2D TMS cases, so that the 3D simulation can be performed. Two different approaches have been taken into consideration to change the mesh.

## Approach 1

Table 20: Mesh properties : Approach 1 (Here,  $D = 0.2$ , Diameter of cylinder  $R$ )

<b>Approach 1</b>	
Number of cells in, X	72
Number of cells in, Y	24
Refinement threshold, Tr	$D/5$
Minimum cell size limit for refined cells	$0.06D$
Local Refinement	
Sector	
Sector radius	$10D$
Sector centre (X,Y)	(0,0)
Box	
Box size in the longitudinal direction (X)	0 to $60D$
Box size in the transverse direction (Y)	$-20D$ to $20D$
Minimum cell size in (Sector + Box), X by Y	$0.1310D$ by $0.2595D$

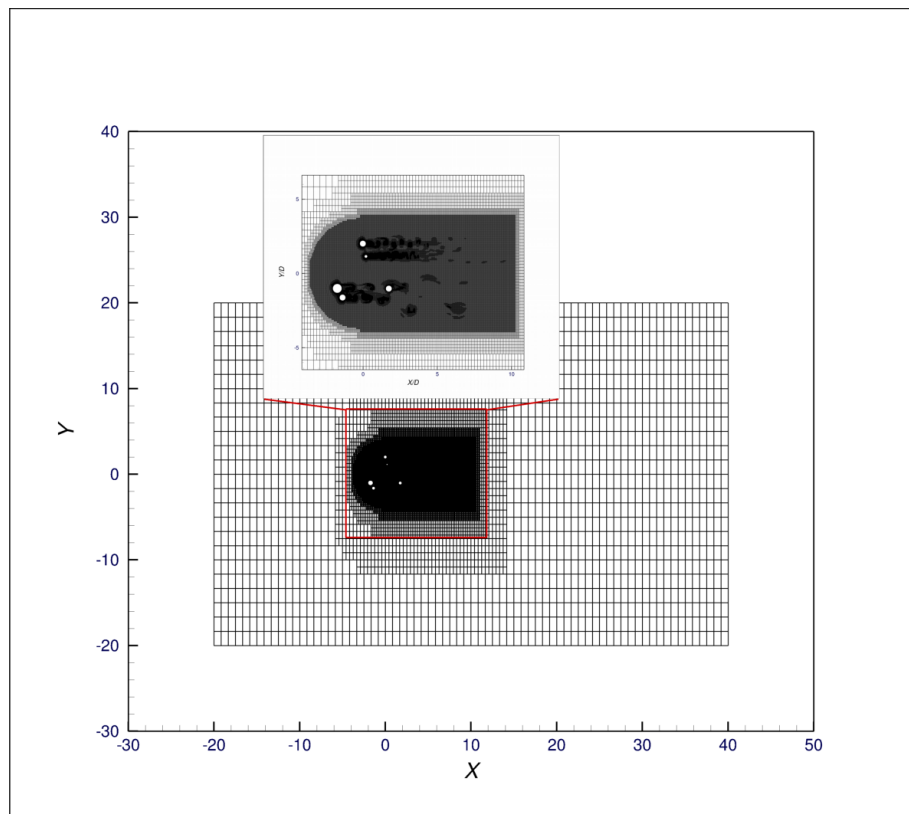


Figure 26: Mesh: New approach (1) associated with box and AGR

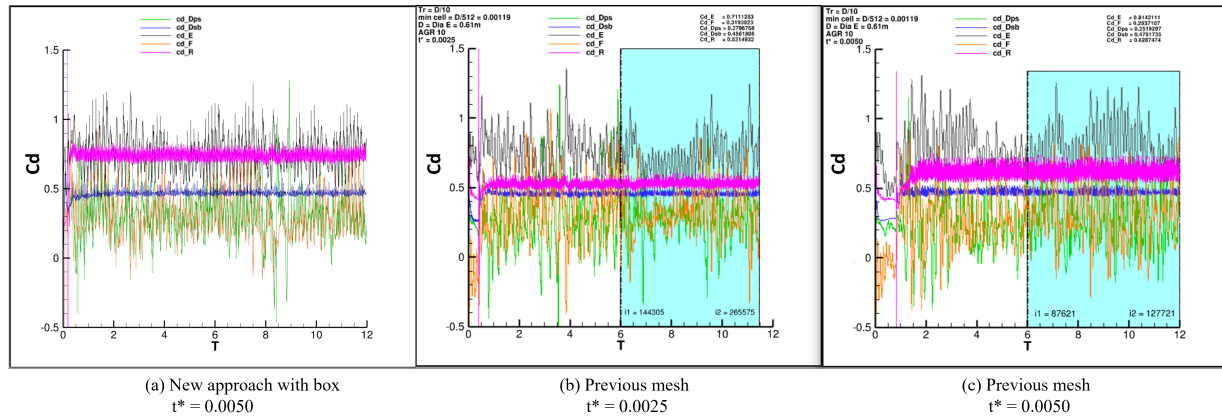


Figure 27: Avg. coefficient drag, Cd : New approach with box+AGR vs Previous mesh

The utilization of the diameter of cylinder R in the mesh setup (see Table 20) has shown remarkable effectiveness in the present investigation. This method inspired a sense of optimism as it demonstrated the potential to reduce cell production and yield comparable values of Cd when compared to the previous mesh architecture. Despite the study demonstrating promising potential in forecasting almost equal values of Cd, it was ultimately disregarded due to its inaccurate prediction (e.g. over prediction) of Cd for cylinder R compared to the prior study (see Figure 27). It should be noted that the simulation was conducted with a time step of  $\Delta t^* = 0.0050$ , and the average time window is visually represented in the color cyan. The selection of the mesh involves maintaining a high average window in response to the presence of significant flow fluctuations. In this study, the average window for approach 1 & 2 was set to  $T = 6$  s of the total physical time. This corresponds to about  $t^* = 72000$  dimensionless time units for a time step of  $\Delta t^* = 0.0050$ , and  $t^* = 144000$  for  $\Delta t^* = 0.0025$ .

**Approach 2**

After getting insight from approach 1, it was determined that conducting a simulation with the initial coarse mesh using the identical AGR settings (which includes the diameter of the cylinder R) would be appropriate. At this stage, the introduction of a box was not implemented. Table 21 demonstrates the mesh settings for approach 2. The simulation was run with a time step  $\Delta t^* = 0.0050$ . The comparison of the Cd evolution of the current setting with the previous mesh can be seen in Figure 28.

Table 21: Mesh properties : Approach 2 (Here, D = 0.2, Diameter of cylinder R)

<b>Approach 2</b>	
Number of cell in , X	24
Number of cell in , Y	16
Refinement threshold, Tr	D/5
Minimum cell size limit for refined cells	0.06D

The formation depicted in Figure 28 demonstrates that this technique has successfully achieved

a comparable evolution to that of the prior mesh. Consequently, a study was undertaken utilizing approach 2, whereby three distinct time intervals, denoted as  $\Delta t^* = 0.0050, 0.0025,$  and  $0.0010,$  were considered. The evolution of  $C_d$  with approach 2 can be seen in Figure 29.

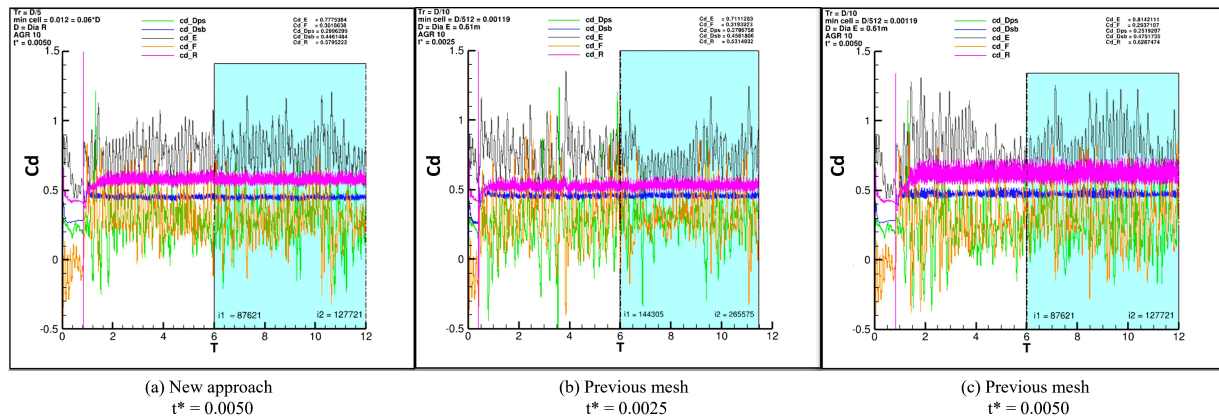


Figure 28: Evolution of avg. coefficient of drag,  $C_d$  : New approach vs Previous mesh

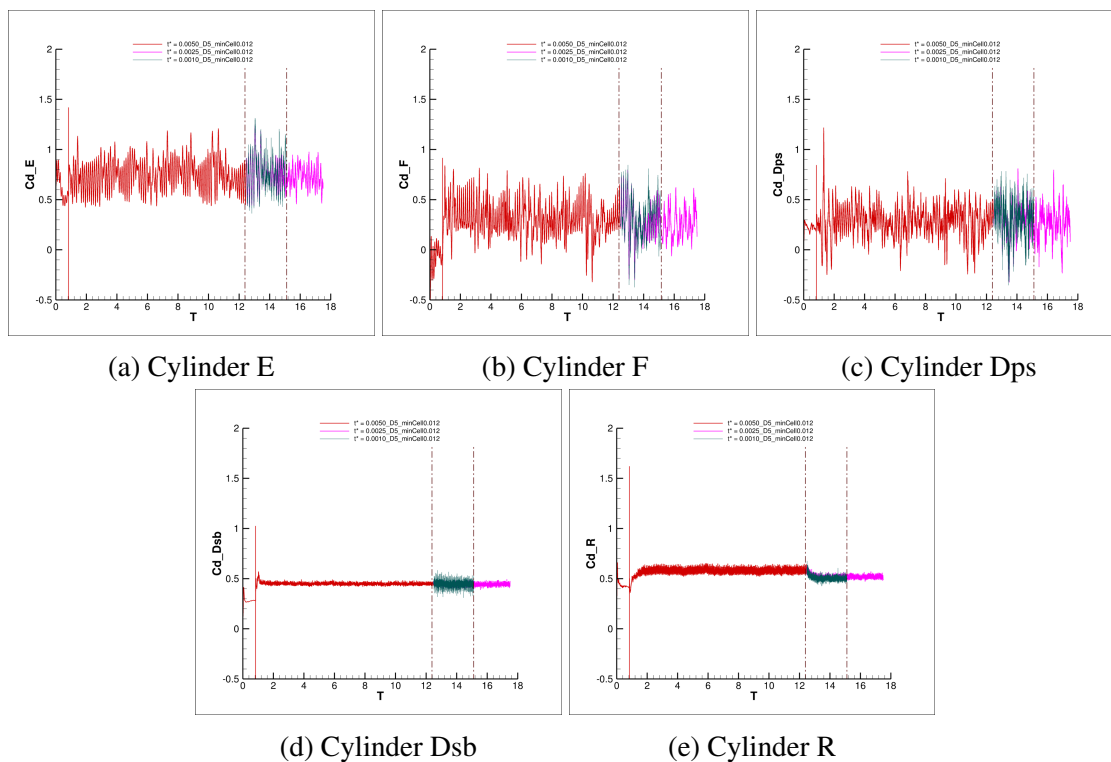


Figure 29: Evolution of avg. coefficient of drag,  $C_d$



Table 22: Comparison of avg. coefficient drag, Cd : Previous mesh vs New mesh

Cylinder name	$\Delta t^* = 0.0025$		$\Delta t^* = 0.0050$		$\Delta t^* = 0.0025$		$\Delta t^* = 0.0010$	
	Reference	New mesh (NM)	Error[%]	NM	Error[%]	NM	Error[%]	
Cd	E	0.7111	0.8142	14.4957	0.7230	1.6754	0.7621	7.1689
	F	0.3194	0.2937	8.0408	0.2593	18.8201	0.2891	9.4902
	Dps	0.2797	0.2519	9.9208	0.2668	4.6184	0.2788	0.3269
	Dsb	0.4562	0.4752	4.1635	0.4410	3.3282	0.4400	3.5392
	R	0.5315	0.6287	18.2983	0.5156	2.9815	0.4962	6.6458

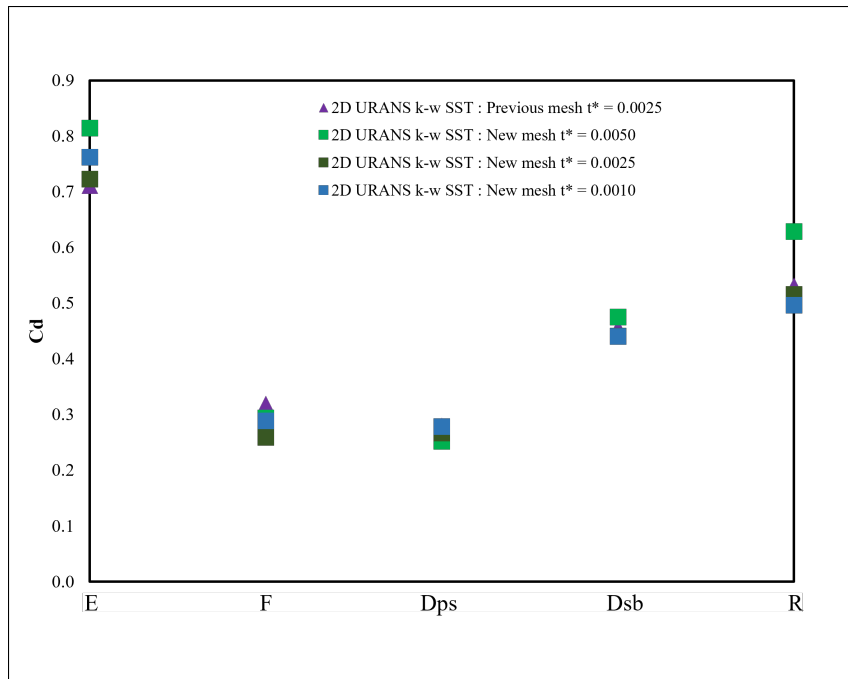


Figure 30: Comparison of avg. coefficient of drag, Cd : Previous mesh vs New mesh

In order to optimize computing efficiency, simulations were conducted for time steps of  $\Delta t^* = 0.0025$  and  $0.0010$ , starting from an initial time step of  $\Delta t^* = 0.0050$ . The initial vertical line depicted in Figure 29 signifies the point at which the simulations were restarted. Both simulations were terminated after an identical pattern had been detected and no more alterations were identified. The last iteration for  $\Delta t^* = 0.0010$ , at which the simulation was halted, is indicated by the second vertical line, the simulation with a time step of  $\Delta t^* = 0.0025$  exhibited progress more than double than  $\Delta t^* = 0.0010$ .

The comparison of the Cd values between the previous and the new mesh for each cylinder is seen in Figure 30. The error analysis was conducted and the results are presented in Table 22. The selection has been made to employ the new mesh with a time step of  $\Delta t^* = 0.0025$  for the purpose of conducting 3D studies and the rest of the 2D studies of other orientations. The cylinder F exhibits a higher degree of fluctuation in its Cd value compared to the previous mesh study, with a decrease from 0.32 to 0.26. On the other hand, the remaining cylinders have a margin of error of less than 5%. Furthermore, when considering a time step of  $\Delta t^* = 0.0010$ , it

can be shown that the error for cylinder F is around 9.5%. In consideration of the computational time constraints, a decision has been made to reach a compromise with respect to cylinder F. It is important to acknowledge that the prior mesh, with a time step of  $\Delta t^* = 0.0050$ , resulted in the generation of around 750,000 cells for a 2D 30° orientation. In contrast, the new mesh with a time step of  $\Delta t^* = 0.0025$  produced only 110,000 cells, which is almost one-seventh in the number of cells compared to the previous mesh. Figure 31 shows the post-processing outcome from the new mesh. The computational gain may be observed by examining Figure 24 and Figure 31. The post-processing outcome and the evolution of  $C_d$  and  $C_l$  for other orientations can be seen in [Appendix 1.4](#). Note that, to calculate mean hydrodynamic parameters (such as  $C_d$ , and  $C_l$ ) around 100 dimensionless time steps have been taken (keeping that the simulation is converged) for the averaging window depicted with color cyan.

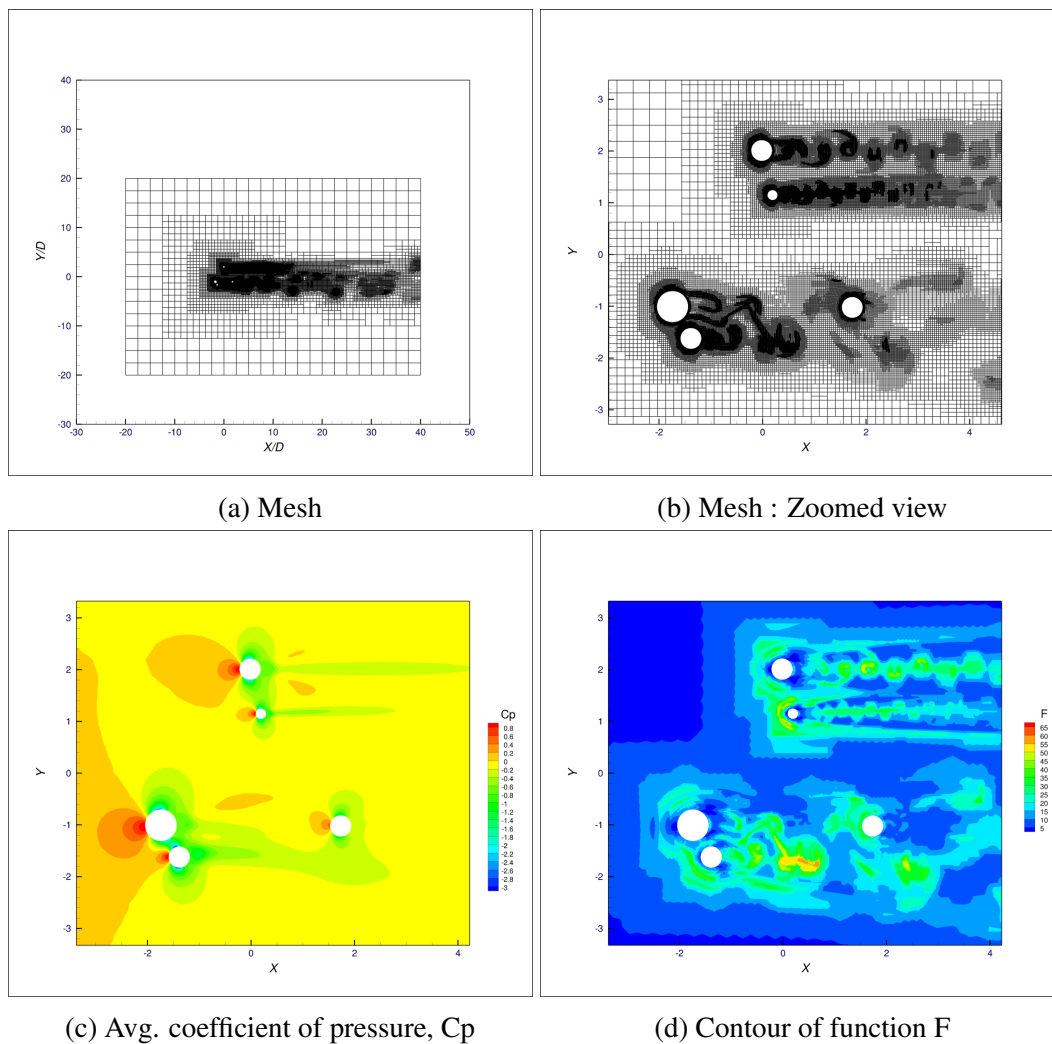


Figure 31: Post-processing results,  $\Delta t^* = 0.0025$  New mesh : 2D 30° orientation

## 5.2 Comparison Of 2D TMS Simulation With Single Cylinder Simulation

In a side-by-side arrangement, the wakes generated by the two cylinders mutually interact. According to [Bearman et al. \(1969\)](#), when cylinders are positioned in close proximity, they might exhibit characteristics similar to a **Single Bluff Body (SBB)**, a phenomenon referred to as '**Base Bleed**', in which, fluid with higher momentum enters the near-wake through the gap, resulting in an increase in base pressure, a decrease in drag for both cylinders and an extension of the vortex formation zone in the streamwise direction. Although it is probable for the vortex streets of adjoining cylinders to **synchronize**, the presence of a significant distance between the cylinders can result in their behavior resembling that of two separate bluff bodies. Once the cylinders are placed at points in between the aforementioned extremes, complex interactions occur in the wake and vortex street, resulting in a flow pattern that is **asymmetric or biased**. The flow pattern under consideration has the potential to display bi-stable characteristics [Spivack et al. \(1946\)](#) [Ishigai et al. \(1972\)](#). The manifestation of this behavior is contingent upon the specific experimental conditions and the Reynolds number, as well as a range of P/D (pitch ratios). The presence of a biased gap flow between the two cylinders gives rise to a flow pattern that is asymmetric in nature. When the flow exhibits bias towards a particular cylinder, it results in a smaller near-wake with increased frequency in vortex shedding, as well as an observed increase in the avg. drag coefficient. The second cylinder displays contrasting characteristics [Sumner et al. \(2010\)](#) [Prafull et al. \(2022\)](#).

The flow conditions of the incoming stream, specifically the incident vorticity field, are altered by the wake produced by the cylinders located upstream in a tandem arrangement. Conversely, the wake dynamics and vortex creation region of the upstream cylinder are influenced by the presence of the downstream cylinder [Lin et al. \(2002\)](#). Due to the phenomenon of mutual interference, it is seen that the cylinder located upstream can function as a source of **turbulence generator**, while the cylinder positioned downstream can serve as a **drag-reduction** device or '**wake stabilizer**' [Lee et al. \(1997\)](#).

Furthermore, the numerical simulations conducted by [Meneghini et al. \(2001\)](#) demonstrate the occurrence of vortex impingement leads in an **amalgamation** process. This process involves the merging of vortices from the upstream cylinder with those created by the downstream cylinder. The incident vortices undergo significant deformation as they circulate across the downstream cylinder [Lin et al. \(2002\)](#), resulting in the formation of Karman vortices in close proximity to the base of the downstream cylinder [Sumner et al. \(2010\)](#). In comparison to the extended-body and reattachment regimes, the Karman vortices that are shed from the downstream cylinder exhibit reduced strength but increased size [Zhou et al. \(2006\)](#).

Based on the categorization proposed by [Zdravkovich \(1987\)](#), the flow patterns seen in tandem

arrangements exhibit three distinct forms of wake interference behavior.:

1. **Single bluff-body (SBB)**, also recognized as the extended-body regime occurs when the two cylinders are in close proximity and may be treated as a single structure. This behavior is observed particularly at lower  $P/D$  values.
2. **Shear layer reattachment (SLR)**, also known as the re-attachment regime, involves the reattachment of free shear layers which are separated from the upstream cylinder onto the surface of the downstream cylinder. This process can result in the formation of vortices in the gap between the cylinders, particularly at intermediate  $P/D$  ratios.
3. **Co-shedding regime**, the phenomenon of Karman vortex shedding from each cylinder at greater  $P/D$  ratios [Xu et al. \(2004\)](#) [Zhou et al. \(2006\)](#).

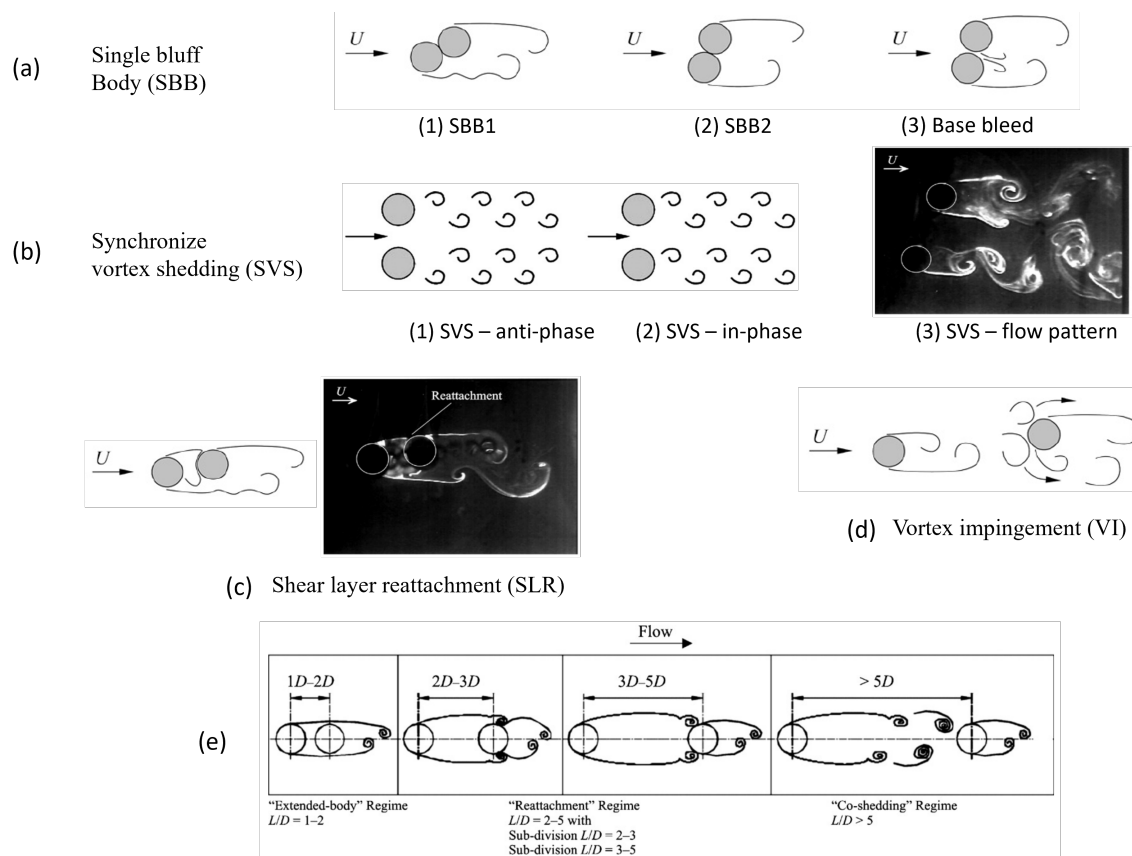


Figure 32: Flow patterns : (a) Single bluff body (b) Synchronize vortex shedding (SVS) (c) Shear layer reattachment (SLR) (d) Vortex impingement (VI) (e) Extended, reattachment, and co-shedding regime for two cylinders in tandem arrangement

Figure courtesy:[Sumner et al. \(2010\)](#)

The flow field exhibits a great degree of complexity since the interaction between cylinders determines the characteristics of the wake. The phenomenon of vortex shedding from the upstream cylinder is inhibited when the cylinders are in close proximity to each other. As the distance between the cylinders is increased, a range of flow patterns are seen. Initially, the shear

layer upstream reattaches to the downstream cylinder, and subsequently, vortex shedding is re-established behind the upstream cylinder. Upon the occurrence of this phenomenon, the wake's impact on the body downstream results in the generation of significant unstable forces and the emission of strong radiated noise. This state is commonly referred to as the co-shedding or critical regime [Weinmann et al. \(2014\)](#).

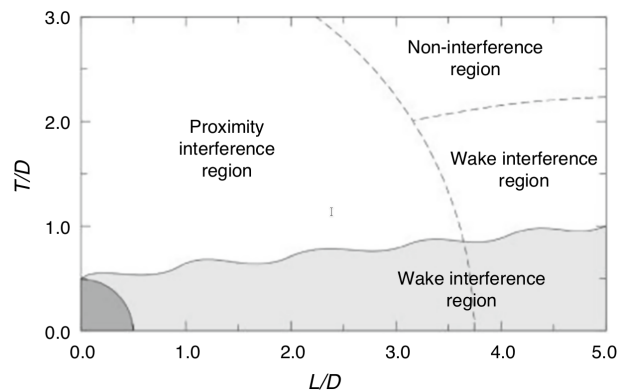


Figure 33: The boundaries of wake and proximity interference  
Figure courtesy: [Sumner et al. \(2010\)](#)

The flow pattern characterized by specific terminology has been identified in Figure 32. Moreover, the boundaries of wake and proximity interference can be seen in Figure 33. Nevertheless, the Reynolds number ( $Re$ ) range utilized in the investigation was inside the lower subcritical range, as indicated by the accompanying research. Given the absence of comparable research within the post-critical domain, the study has been advanced utilizing the aforementioned concepts.

#### Remarks

**St numbers** for each cylinder of **2D TMS** and **Single cylinder** with different  $Re$  numbers are documented in Table 27 and 28 respectively.

### 5.2.1 Orientation: 30°

#### Remarks

- Avg. coefficient of drag,  $C_d$ , Avg. coefficient of lift  $C_l$ , RMS of drag coefficient,  $Cd_{RMS}$ , RMS of lift coefficient,  $Cl_{RMS}$ , Base pressure coefficient,  $C_{pb}$  ( $\theta = 180^\circ$ ), Flow separation,  $\theta_{sep}$ , Vortex length of 2D TMS and single cylinder are shown in Table 23.
- The incident angle,  $\alpha$ , Pitch distance, P/D are shown in Table 24.

*The conclusion of each orientation description is where you'll find all the tables. To avoid repetitive descriptions, **Readers** are urged to have a look at them as they go through the description.*

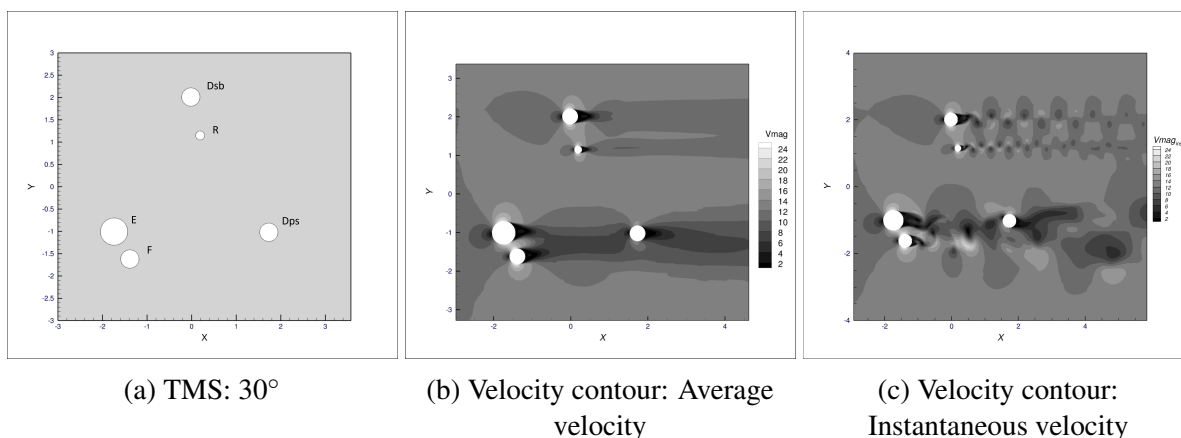


Figure 34: Velocity contour : Orientation 30°

#### Cylinder E-F

-The arrangement is staggered, with a pitch distance  $P/D = 1.164$  and a large incidence angle  $\alpha = -60^\circ$ . Flow pattern that is similar to SVS (Synchronized vortex shedding) and the shedding from both cylinders meets and keeps shedding together. However, the synchronization took place in the anti-phase (see Figure 34c and 32). There is evidence of proximity interference since two cylinders are close to one another but none is immersed in the wake of the other.

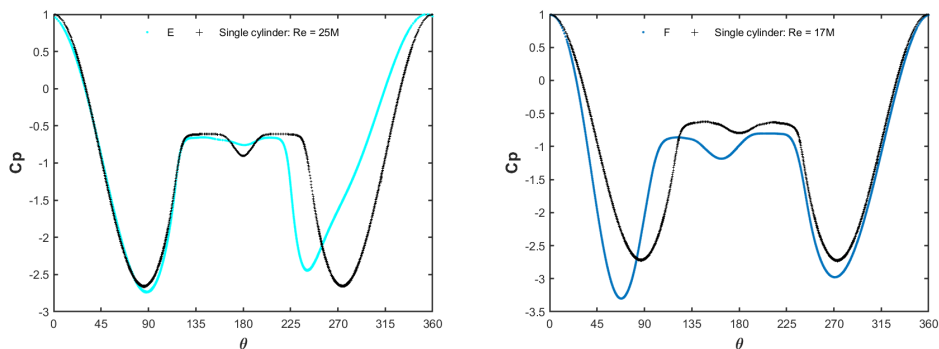
-Vortex shedding may be seen in the gap between the E-F and Dps cylinders. Due to the staggered arrangement of E-F, the gap also exhibits a complex flow pattern. Furthermore, the shedding in the gap is not suppressed due to the large P/D distance between cylinders E and Dps (see Figure 34c). The interaction of E-F cylinders results in a higher  $C_d$  for cylinder E and a lower  $C_d$  for cylinder F than the single cylinder (SC). The interaction causes an opposite lift to each other, as evidenced by the  $C_l$  values. The pattern is also visible for the  $Cd_{RMS}$  and  $Cl_{RMS}$  readings. For cylinder E,  $Cd_{RMS}$  increases while  $Cl_{RMS}$  decreases as compared to the SC. However, for cylinder F, the opposite is true. Unlike the SC, a lift is found in both cylinders E and F due to

non-symmetric flow behavior.

-During FFT (Fast Fourier Transform) analysis, various peaks have been identified for both E and F cylinders showing various  $St$  numbers in both directions ( $Drag = St_{Cd}$  and  $Lift = St_{Cl}$ ). It is expected because the flow is complex and vortex shedding does not produce a unique  $St$  number. As a result, several  $St$  numbers are seen. FFT analysis revealed two peaks in the SC cylinder as well. The dominating peak, on the other hand, was chosen as the primary  $St$  number, which is smaller than unity and follows the equation  $St_{Cd} = 2 \times St_{Cl}$ . Furthermore, for E-F cylinders, the  $St$  number with the largest peak value has been determined to be less than the SC in both directions. Again, it has been cut in 50% for cylinder E in the drag direction compared to SC. With the  $St$  numbers, more analysis can be proposed. However, it is recommended that readers glance at the Table 27 dedicated to  $St$  number to get a better comprehension.

-The  $C_p$  plot for cylinder E is not symmetric such as SC. If the cylinder is divided into four quadrants (see Figure 18), the interaction with cylinder F causes a shift in  $C_p$  for cylinder E in the third and fourth quadrants. Suction point modifications may be detected in the shifted region where it moved to the left-upward than the SC. Furthermore, due to changes in the dip size, the  $C_{pb}$  value at  $180^\circ$  has been changed. Because cylinder F is smaller than cylinder E, the shift of  $C_p$  is considerably more prominent than in cylinder E. The minimal avg. base pressure coefficient,  $C_{pb}$  is no longer at  $180^\circ$ . As expected, the shift in the suction point of the first and second quadrants is prominent for cylinder F. As a result, the influence of this interaction can be seen in the pressure coefficient plot when compared to the SC simulation (see Figure 35).

-The flow separation is more advanced in Dps than in SC. The separation point for the SC was found at approximately  $125.7010^\circ$ , where it occurred for Dps at  $118.2188^\circ$ . Vortex length increases for both cylinders when compared to the SC simulation which is demonstrated by Figure 38. Cylinder E has a narrower tilted vortex, but cylinder F has a larger wake with asymmetric vortex development.



(a)  $C_p$ : Cylinder E vs Single cylinder

(b)  $C_p$ : Cylinder F vs Single cylinder

Figure 35: Avg. coefficient of pressure,  $C_p$  : Orientation  $30^\circ$



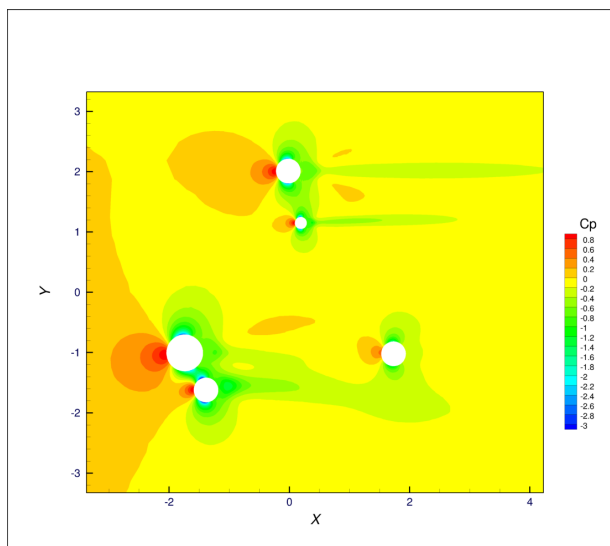
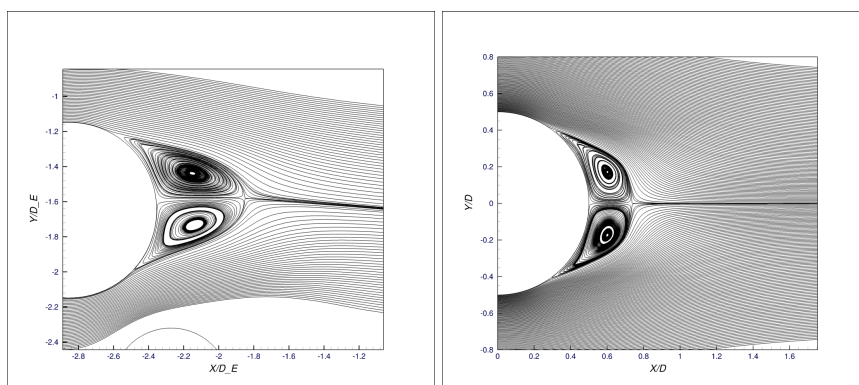


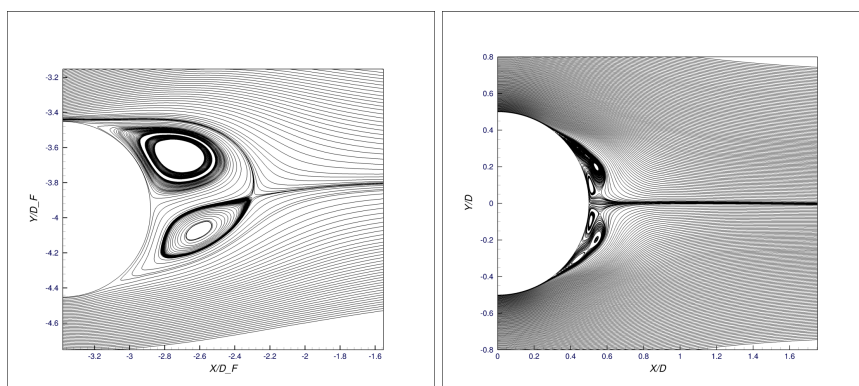
Figure 36: Contour of avg. coefficient of pressure,  $C_p$  : Orientation  $30^\circ$



(a) Vortex length: Cylinder E

(b) Vortex length:  $Re = 25M$

Figure 37: Vortex length : Cylinder E vs Single cylinder



(a) Vortex length: Cylinder F

(b) Vortex length:  $Re = 17M$

Figure 38: Vortex length : Cylinder F vs Single cylinder



## Cylinder Dps

-The structure of the reattachment regime in front of the cylinder is altered, in contrast to the conventional tandem layout typically observed in [Zhou et al. \(2006\)](#). It is also clear that the reattachment happens at the cylinder's forebody (first half) or leading surface. It should be noted that the pitch distance,  $P/D = 5.69$  with incident angle  $\alpha = 0$ .

-A strong Karman vortex can be detected downstream of the Dps cylinder, and a wake interference effect can be identified due to the existence of the E-F cylinder upstream.

-The drag of the Dps cylinder is lower than that of the SC because it functions as a drag reduction device, as previously indicated. In addition, the incoming turbulence from E-F cylinders generates uneven flow conditions, which can be seen as a higher  $C_l$  value than the SC. The rise in  $C_l$  for the Dps cylinder is one order of magnitude greater than the SC. The flow unsteadiness of the Dps cylinder, however, is minimized. It can be noticed by comparing the  $C_{d_{RMS}}$  and  $C_{l_{RMS}}$  values, which are lower than the SC simulation (see Table 23).

-The Dps cylinder has a different St number in the drag and lift directions than the SC. As the incoming flow was influenced by the upstream cylinders, no distinct value of the St number is seen.

-The variations in the Cp distribution found in Figure 39 are more noticeable than the expected SC simulation due to the strong wake interference generated by E-F cylinders. The stagnation point has a 50% lower value than the SC. A flat distribution at  $\theta = 180^\circ$  can be seen. Furthermore, the Cp<sub>b</sub> value increases in the Dps cylinder more than in the SC. The  $C_d$  modifications are closely related to the Cp<sub>b</sub> variations indicated by [Roshko \(1961\)](#).

-The flow separation is more advanced in Dps than in SC. The separation point for the SC turned out to be about  $125.7010^\circ$ , whereas the Dps occurred around  $118.2188^\circ$ . Vortex length increases in comparison to the SC with an asymmetric vortex generation (see Figure 40).

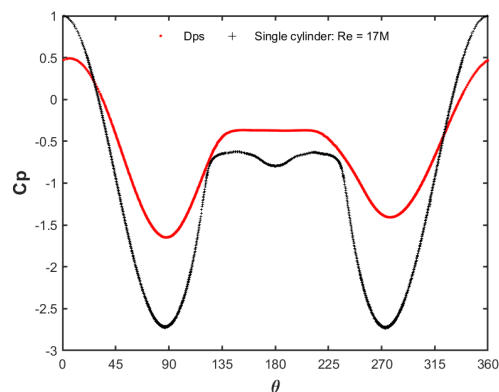
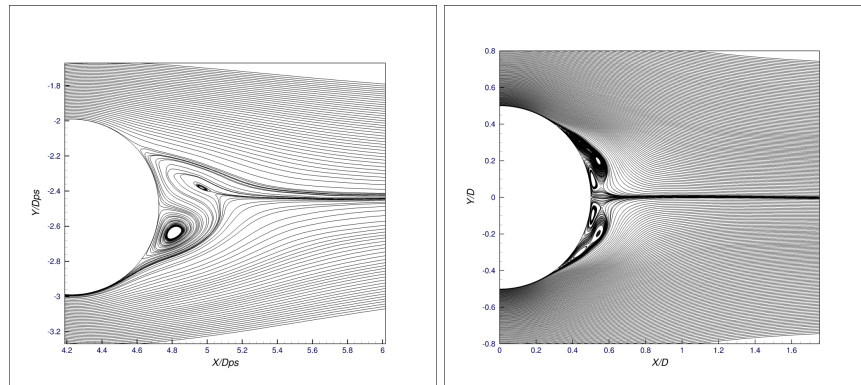


Figure 39: Avg. coefficient of pressure, Cp: Cylinder Dps vs Single cylinder

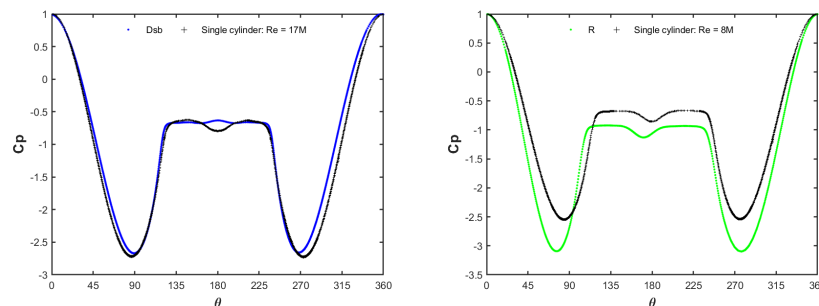


(a) Vortex length: Cylinder Dps      (b) Vortex length: Re = 17M

Figure 40: Vortex length : Cylinder Dps vs Single cylinder

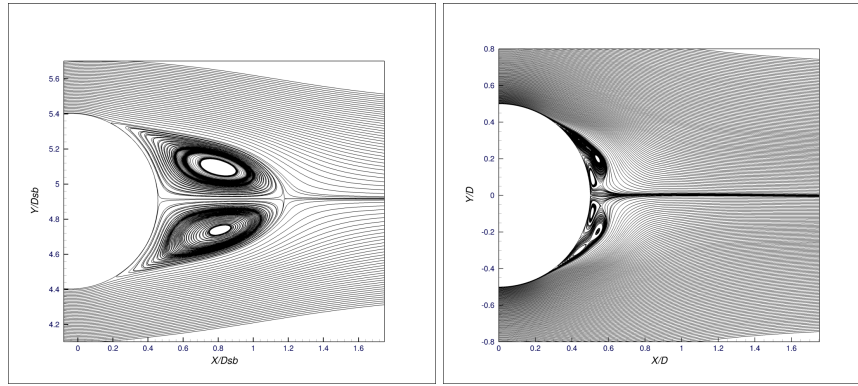
**Cylinder Dsb - R**

- The staggered arrangement with a pitch distance,  $P/D = 2.16$  and incident angle  $\alpha = -76^\circ$  shows the vortex street synchronization in an anti-phase state
- There is evidence of proximity interference. The instant velocity contour in Figure 34c reveals a unique vortex street, resulting in two distinct Strouhal numbers in the lift direction for both cylinders. The  $St_{Cl}$  values for both cylinders are close to the SC simulation.
- When assessed with SC, the changes in  $C_d$  in cylinder Dsb are larger than in cylinder R. The same scenario applies to the  $C_{d_{RMS}}$  value. Because of the proximity interference between these two cylinders, the avg. lift coefficient  $C_l$  for Dsb and R has been increased in comparison to the SC. However,  $C_{l_{RMS}}$  shows a reduction in the unsteadiness of lift (see Table 23).
- Since R is a small cylinder that is dominated by the Dsb, the change in  $C_p$  around the cylinder is greater for R than Dsb. When  $C_p$  is compared to the SC, the dip for the cylinder Dsb is found to be concave upward (see Figure 41a).
- The flow separation is advanced for both cylinders. The vortex lengths for both cylinders have increased more than the SC and the vortex symmetry is sustained (see Figure 42).



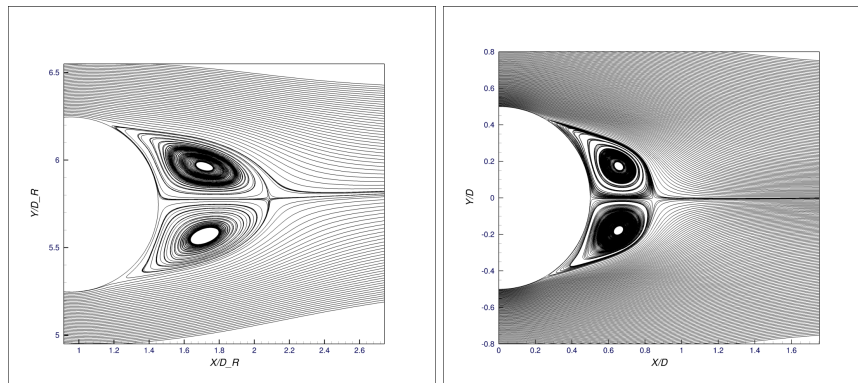
(a) Cp: Cylinder Dsb vs Single cylinder      (b) Cp: Cylinder R vs Single cylinder

Figure 41: Avg. coefficient of pressure,  $C_p$  : Orientation  $30^\circ$



(a) Vortex length: Cylinder Dsb (b) Vortex length: Re = 17M

Figure 42: Vortex length : Cylinder Dsb vs Single cylinder



(a) Vortex length: Cylinder R (b) Vortex length: Re = 8M

Figure 43: Vortex length : Cylinder R vs Single cylinder

Table 23: Hydrodynamic parameters: 30 ° orientation

Re	Cylinder	$C_d$	$C_l$	$C_{d_{RMS}}$	$C_{l_{RMS}}$	$C_{pb} (\theta = 180^\circ)$	$\theta_{sep} [^\circ]$	Vortex length
25M	E	0.723	0.3053	0.7315	0.3667	-0.6132	120.5114	0.5400
	Single cylinder (SC)	0.5494	-0.0014	0.5508	0.5775	-0.9040	124.0340	0.2392
17M	F	0.2593	-0.1185	0.2963	0.6543	-0.9392	141.6233	0.5915
	Dps	0.2668	0.0337	0.3061	0.4454	-0.3233	118.2188	0.3905
	Dsb	0.441	0.0264	0.4411	0.1252	-0.5578	107.5224	0.7564
8M	SC	0.5541	0.0026	0.5866	0.6470	-0.7939	125.7010	0.0951
	R	0.5156	-0.0138	0.5159	0.27	-0.7796	117.6524	0.6688
	SC	0.5642	0.0007	0.5653	0.5260	-0.8569	118.9370	0.3417

Table 24: Cylinders relative distance and incident angle : 30 ° orientation

	30 °	Unit	E-F	Dsb-R	E-Dps
Pitch distance, P	m		0.7100	0.8860	3.4731
L	m		0.3550	0.2085	0.0000
T	m		0.6149	0.8611	0.0000
$\alpha$	°		-60.0000	-76.0000	0.0000
P/D	-		1.1639	2.1609	5.6936
L/D	-		0.5819	0.5085	
T/D	-		1.0080	2.1002	

### 5.3 Mask Effect

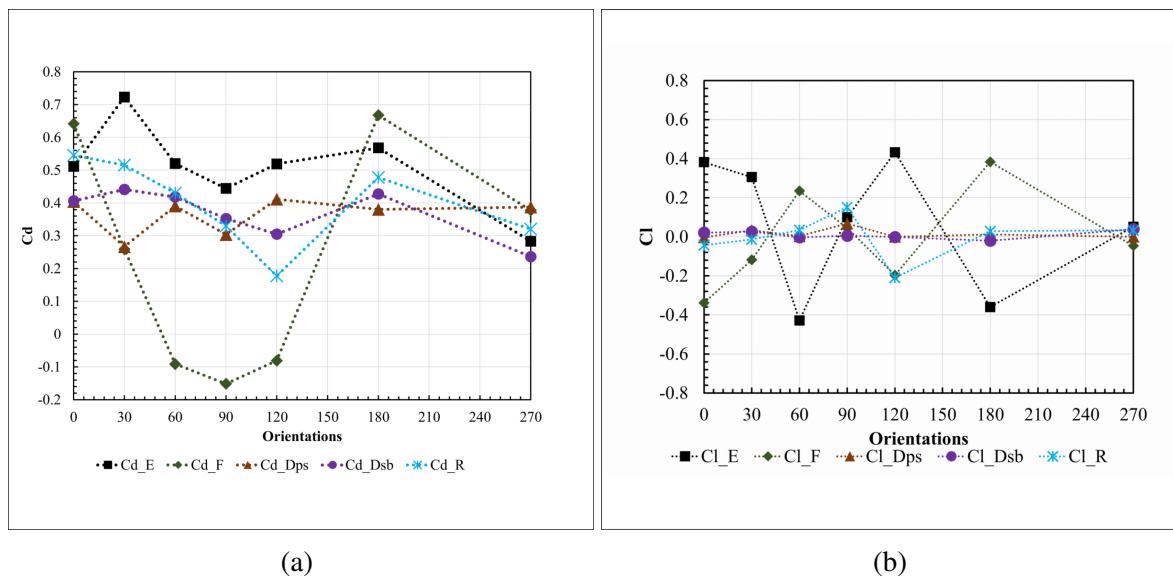
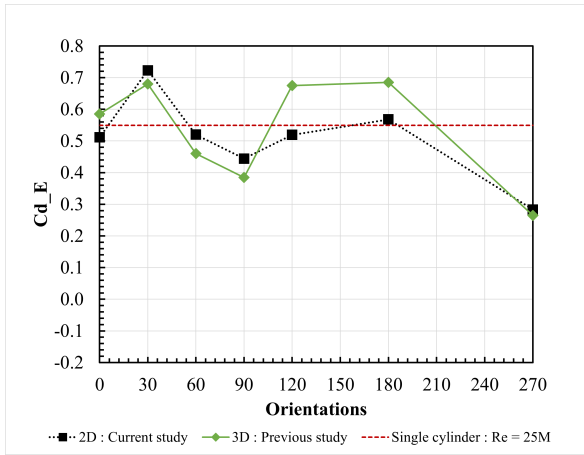


Figure 44: Comparison of avg. coefficient of drag,  $C_d$  and avg. coefficient of lift,  $C_l$  : 2D current study : URANS -  $k-\omega$  SST for all the seven orientations

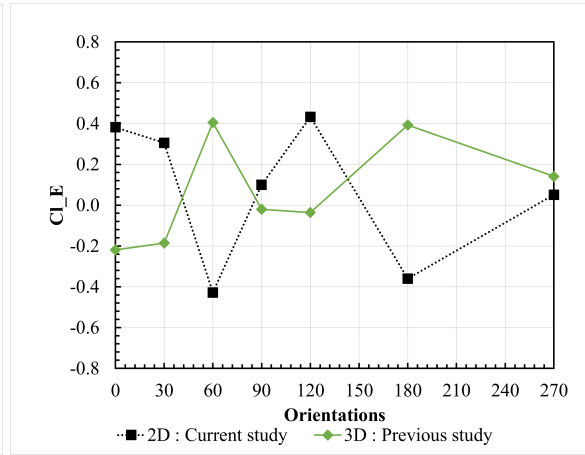
Table 25: Mask effect: 2D URANS  $k-\omega$  SST - All orientations

Cylinder name	Mask effect [%] for avg. coefficient of drag, $C_d$						
	0°	30°	60°	90°	120°	180°	270°
E	-6.9150	<b>31.6171</b>	-5.3529	-19.1430	-5.4708	<b>3.4019</b>	-48.4263
F	<b>15.8283</b>	-53.2066	-116.4577	-127.3292	-114.5845	<b>20.4982</b>	-31.8285
Dps	-27.0261	-51.8572	-29.4505	-45.1679	-25.7032	-31.3397	-30.0340
Dsb	-26.7053	-20.4119	-24.5665	-36.4035	-44.9928	-22.8851	-57.3631
R	-3.2750	-8.5991	-23.7848	-41.6106	-68.5452	-15.3016	-43.2172

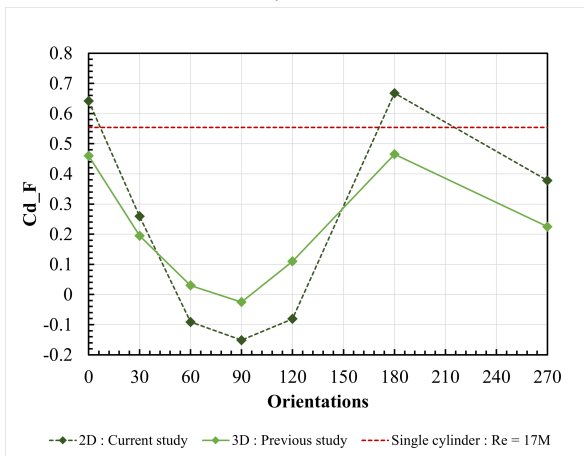
Figure 44 shows the avg. coefficient of drag,  $C_d$ , and lift,  $C_l$  for all the TMS orientations from 0° to 270°. Figure 45 & 46 demonstrate the mask effect due to complex interaction among cylinders when compared to the single cylinder. The value of the avg. drag coefficient for a single cylinder has been shown in the red dotted line. For a single cylinder, the lift is always close to zero, therefore it is not shown in the plot. Furthermore, the mask effect is not calculated with  $C_l$ , since dividing any number with a value close to zero significantly increases the outcome. The trend of avg.lift coefficient,  $C_l$  seems reversed than the previous 3D study for R1 configuration with free surface which was performed at ECN by [Queutey et al. \(2022\)](#). This is due to the definition of the flow domain. In the current study, the incoming flow has been set to start from -X to +X direction, while the previous study has done the opposite. Table 25 documents the percentage of mask effect. The drag of the cylinders for all orientations has reduced except for four instances which are colored blue for the readers.



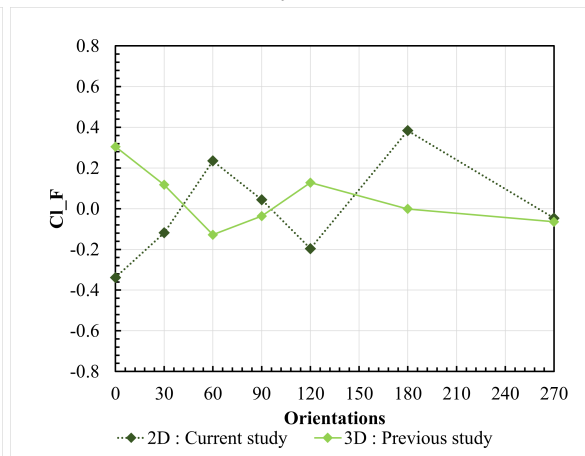
(a) Cylinder E



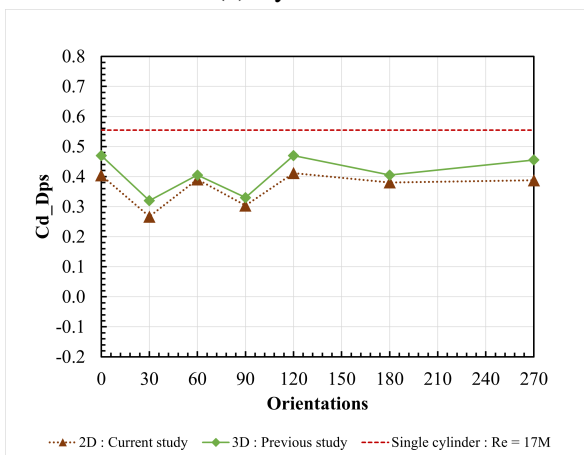
(b) Cylinder E



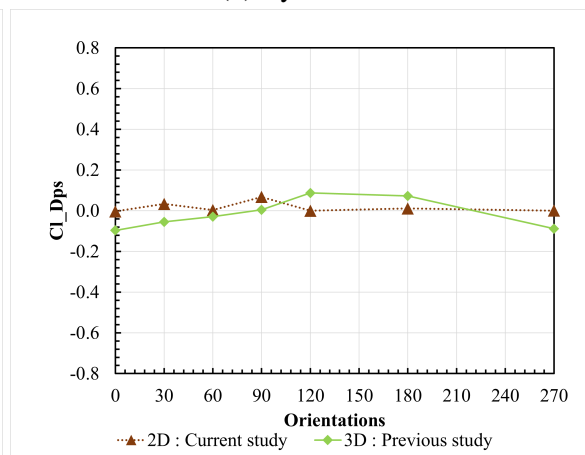
(c) Cylinder F



(d) Cylinder F



(e) Cylinder Dps



(f) Cylinder Dps

Figure 45: Comparison of avg. coefficient of drag,  $C_d$  and lift,  $C_l$  : 2D current vs 3D previous study R1 configuration with free surface [Queutey et al. \(2022\)](#): URANS -  $k-\omega$  SST

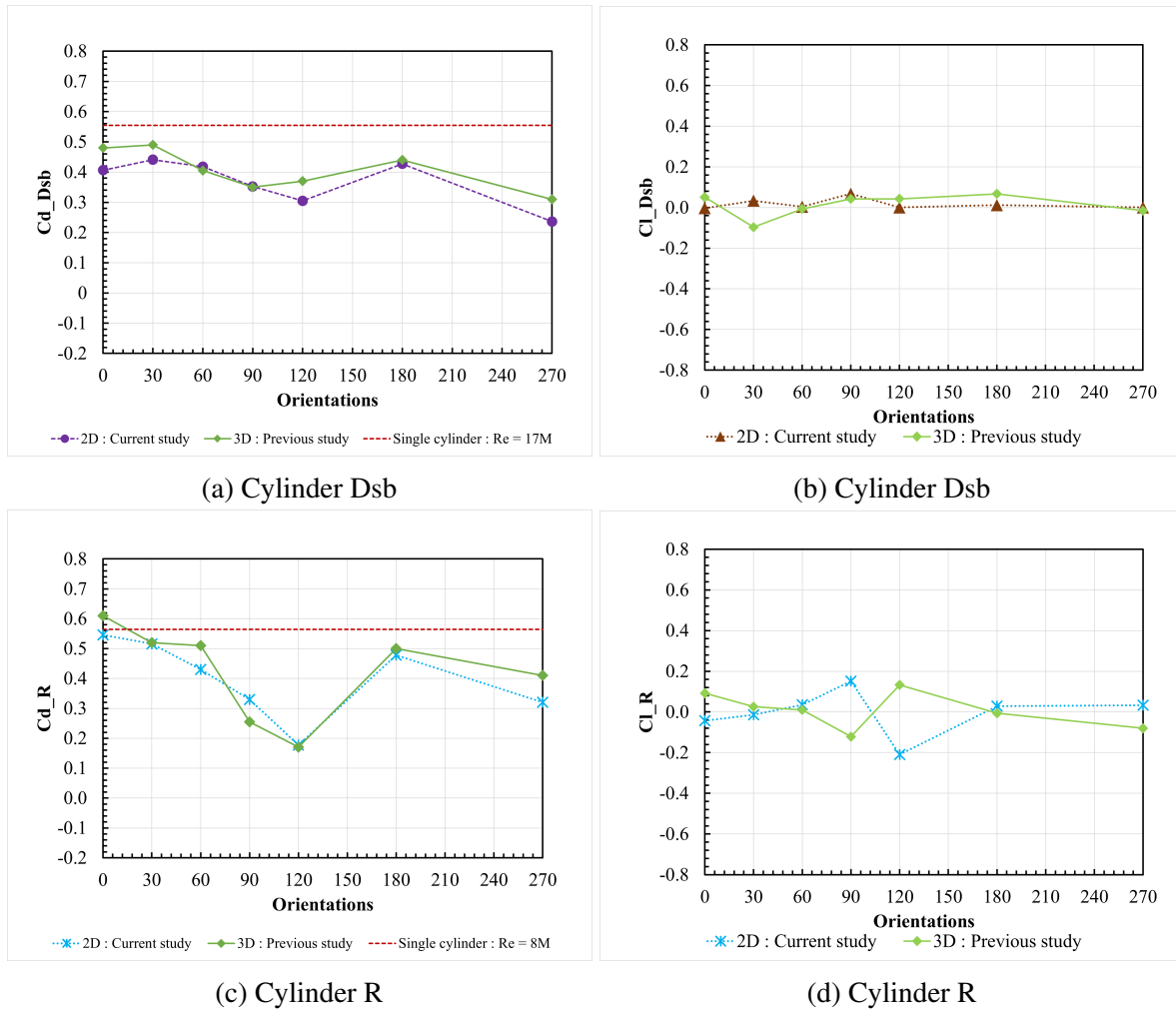


Figure 46: Comparison of avg. coefficient of drag,  $C_d$  and lift,  $C_l$  : 2D current vs 3D previous study R1 configuration with free surface [Queutey et al. \(2022\)](#): URANS -  $k-\omega$  SST

Note that, although the trend in the current 2D and previous 3D URANSE studies are similar, however, the difference may come from (1) possible 3D effect and (2) Insufficient temporal and spatial resolution of the previous 3D study. One of the primary recommendations from the previous study was to conduct a separate temporal and spatial resolution which are achieved and shown in the earlier stages. In this context, GTT employs a fixed avg. coefficient of drag,  $C_d$  equal to 0.7 after the Reynolds number ( $Re$ ) above the critical  $Re$  threshold (see Table 64a).

Table 26: Avg. coefficient of drag,  $C_d$  law utilized by GTT

Range of $Re$ number	Avg. coefficient of drag, $C_d$
$Re < 10^4$	$\log(C_d) = -0.01 \log(Re)^3 + 0.158 \log(Re)^2 + 0.682 \log(Re) + 0.935$
$10^4 < Re < 10^5$	$C_d = 1.2$
$10^5 < Re < 10^6$	$C_d = 1.2 + 0.25[\sin(\pi(0.61 - 0.11Re10^{-5})) - 1]$
$Re > 10^6$	$C_d = 0.7$

However, the avg. drag coefficient,  $C_d$  at a  $Re$  of 10M ( $10^7$ ) is dependent upon the surface smoothness of the cylinders. [Jones et al. \(1969\)](#) discovered that at a  $Re = 10M$ , the avg. drag

coefficient,  $C_d$  was determined to be 0.52. Conversely, Roshko (1961) reported a value of 0.7 for  $C_d$  in his experimental study. According to Jones et al. (1969), the disparity in drag seen between Roshko's cylinder and his might plausibly be ascribed to disparities in surface roughness between the two cylinders. The cylinder, as developed by Roshko, featured a sandblasted surface finish that exhibited a roughness height measuring 200 micro inches (equivalent to 5.08 micrometers). As a consequence, there was an observed increase in the roughness factor, which is quantified as the ratio of the roughness height to the diameter of the cylinder, about six times greater than that of the Jones et al. (1969)'s cylinder. The simulation conducted using ISIS-CFD revealed an estimated value of 0.62, which falls within the range of the two experimental results. It should be noted that the cylinder used in the simulation does not incorporate any roughness factor.

Table 27: Strouhal number in drag,  $St_{Cd}$  and lift  $St_{Cl}$  directions for cylinders of all orientations.

Orientation	$St_{Cd}$					$St_{Cl}$				
	Dps	Dsb	F	E	R	Dps	Dsb	F	E	R
0°	0.1638	0.1638	0.1638	0.1219	0.0799	0.1638	0.1638	0.1638	0.2438	0.3676
	0.1966	0.3604	0.3441	0.2438	0.1678	0.3604	0.3604	0.3441	0.5119	
	0.3441	0.7045	0.5079	0.5119	0.3676					
	0.5243	0.7537	0.6717	0.7557	0.7353					
	0.7209									
	82.0013	82.0013	82.0013	122.0019	40.0006	82.0013	82.0013	82.0013	122.0019	40.0806
	164.0026	164.0026	164.0026	244.0039	80.0013	164.0026	164.0026	164.0026	244.0039	80.0892
	246.0039	246.0039	246.0039	366.0058	120.0019	246.0039	246.0039	246.0039	365.7621	120.0898
	328.0052	328.0052	328.0052	488.0078	160.0026	328.0052	328.0052	328.0052	487.7640	160.0905
	410.0065	410.0065	410.0065	610.0097	200.0032	410.0065	410.0065	410.0065	609.7660	199.9233
30°	0.1020		0.1020	0.1518	0.1825	0.1020	0.3741	0.1190	0.1771	0.3318
	0.1701	0.3741	0.2211	0.2783	0.3318	0.1871		0.1871	0.2783	
	0.2211	0.7482	0.3401	0.3289	0.6719	0.2211		0.2211	0.3289	
						0.2721		0.2721	0.4301	
60°	0.7344	0.4006	0.2504	0.3725	0.1140	0.3672	0.4006	0.2504	0.3725	0.1954
		0.6342	0.5174	0.7698	0.1954			0.5174	0.7698	0.3094
		0.8012	0.7678	0.3094	0.6106				0.5060	0.6072
90°	0.3507	0.3507	Random	Random	0.1711	0.2028	0.3548	0.0845	0.1257	0.1731
	Random	0.7181			0.3503	Random		0.1183	0.1760	0.3462
120°	0.3701	0.2524	0.2524	0.3755	0.1395	0.3701	0.2524	0.2524	0.3755	0.1723
	0.7403	0.6561	0.5047	0.7509	0.1723		0.3533	0.5047	0.7509	0.3201
180			0.7571	0.3201	0.6401		0.6561			
	0.0840	0.0840	0.0840	0.1250	0.1803	0.3528	0.3696	0.0840	0.1250	0.1803
	0.1680	0.1680	0.1680	0.2500	0.3196		0.6552	0.2520	0.2500	0.3196
	0.3528	0.3696	Random	0.3749	0.6474			0.3360	0.4999	
270	0.7056	0.6552	0.4999					0.4368		
	0.0998	0.3660	0.2329	0.1237	0.1785	0.3660	0.3660	0.0998	0.1485	0.1785
	0.3660	0.7153	0.4658	0.3465				Random	0.1980	0.3489
	0.7153		0.6930					0.2475		

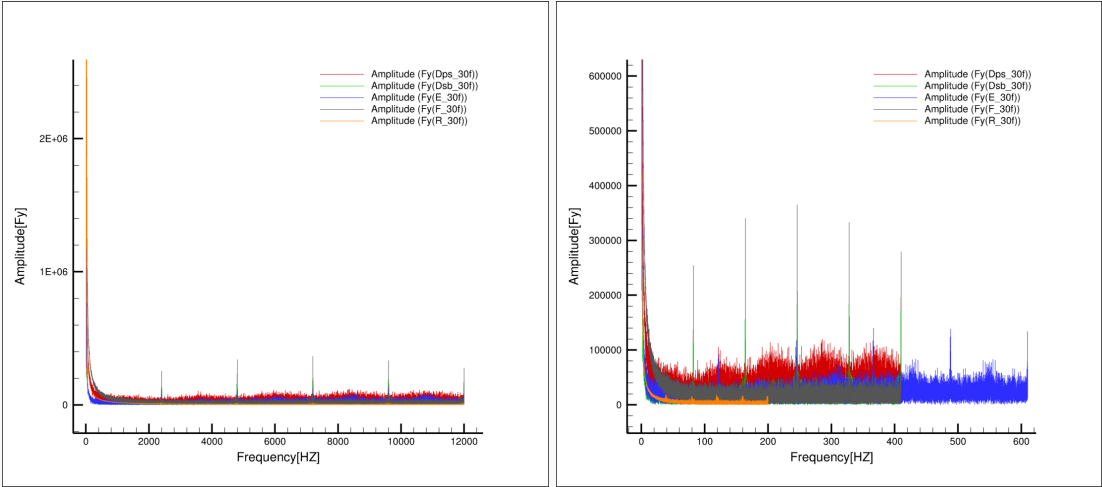
Table 28: Strouhal number in drag,  $St_{Cd}$  and lift  $St_{Cl}$  for single cylinders.

Re	$St_{Cd}$	$St_{Cl}$
25M	0.6630, 1.3260	0.3315, 0.9945
17M	0.6869, 1.3739,	0.3401, 1.0271,
	2.0609, 2.7479	1.7141, 2.4010
8M	0.6264, 1.2528	0.3132, 0.9396



Remarks

- Dominant peak values are colored red for the St numbers presented in Table 27.
- The first St number is the dominant one for the single cylinder simulation presented in Table 28.
- There is a small light blue colored box presented in Table 27 for 0° orientation. Basically, five peaks have been identified for all the cylinders during FFT analysis (see Figure 47). Their positions are identical (happens at the same frequency, f (Hz)) before the dimensionless form ( $St = fD/U$ ). Note that, the diameter, D represents the individual diameter of each cylinder. These five peaks can be seen for all other orientations as well, therefore, not tabulated to avoid repetition. The reason for these peaks is not known for the time being. Nevertheless, it is possible that the cylinders have shared frequencies, as evidenced by the presence of five distinct peaks..



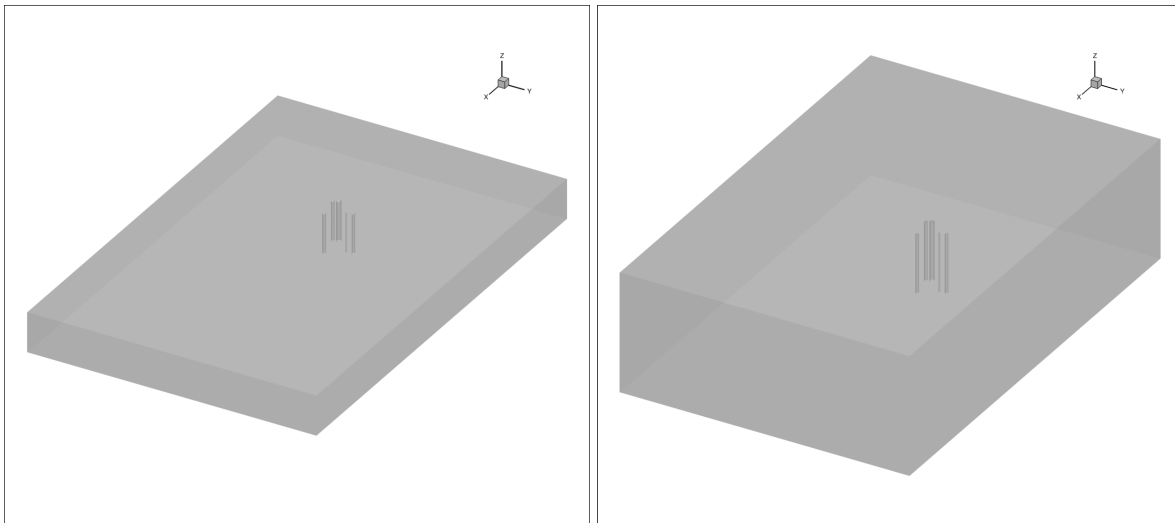
(a) Dimensional form in X-axis: Frequency, f (Hz) = 1/T      (b) Dimensionless form in X-axis: Strouhal, St = fD/U

Figure 47: FFT analysis of 2D TMS 30° orientation: Dimensional vs Dimensionless forms



## 6 3D STUDY OF TMS

This part will conduct 3D simulations on the TMS orientation at an angle of  $30^\circ$ , after the consultation with GTT. The simulation will be executed without the inclusion of struts due to the considerable computational resources required [Queutey et al. \(2022\)](#). Hence, the examination will be done undertaking the geometry without struts, namely the R1 configuration, as seen in Figure 2. It is noteworthy that the 3D configuration will be subject to a particular treatment. The study will commence taking into account mirror boundary conditions in the spanwise direction. This approach aims to reduce computing costs and get insights into potential 3D effects, thereby resulting in a simplified case. The subsequent phase of the study will involve an examination of 3D simulations that closely resemble the tripod mast structure (TMS) (e.g. R1 configuration). The domain of the system for R1 configuration, and the simplified case, is depicted in Figure 48. The domain for both approaches exhibits equal longitudinal and transverse lengths, as established in the 2D simulations. The longitudinal length ranges from  $-20\text{m}$  to  $+40\text{m}$ , while the transverse length ranges from  $-20\text{m}$  to  $+20\text{m}$ . In the simplified arrangement, the upper wall ( $Z_{max}$ ) is positioned at a height of  $5.514\text{m}$ , which is equivalent to the height of the free surface in terms of R1 configuration. In contrast, the R1 configuration includes a top wall located  $16\text{m}$  above the bottom. In order to mitigate complexity, a value of  $0\text{ m}$  was designated as the minimum height ( $Z_{min}$ ) for all cylinders throughout the simulation. The investigation of the tip flow vortex which will be generated by the gap is not within the scope of the current research. In addition, it should be noted that the height of the cylinders in the R1 configuration is  $8.187\text{ m}$ .



(a) Simplified : Domain and cylinder height,  $Z = 5.514\text{ m}$  (equivalent to free-surface height)      (b) R1 : Domain height,  $Z_d = 16\text{ m}$ , Cylinder height,  $Z_c = 8.187\text{ m}$  (free surface at  $Z = 5.514\text{ m}$ )

Figure 48: 3D domain -  $30^\circ$  orientation : Simplified without free surface vs R1 configuration with free surface

## Boundary condition

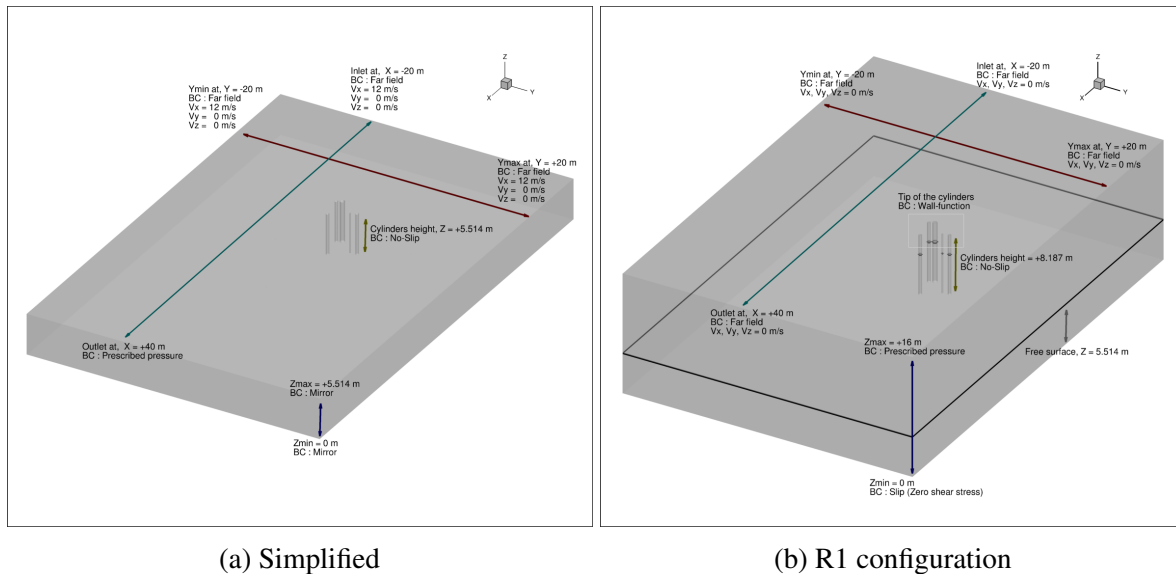


Figure 49: Specification of boundary condition - 30° orientation : Simplified without free surface vs R1 configuration with free surface

The boundary conditions imposed for the **Simplified** 3D case are as follows:

**Far field** with longitudinal velocity,  $V_x = 12$  m/s, has been imposed to inlet ( $X = -20$  m),  $Y_{min}$  ( $Y = -20$  m), and  $Y_{max}$  ( $Y = +20$  m) faces.

**Prescribed pressure** has been imposed to outlet ( $X = +40$  m).

**No-slip** to cylinders wall.

**Mirror boundary condition** has been imposed on the span-wise directions. The mirror condition postulates that both the geometry and the flow exhibit symmetry, with the velocity field being tangential to the mirror plane. In this particular scenario, the calculation can be constrained to a single half of the entire domain, resulting in significant savings of computational resources [FineMarine \(2023\)](#). The mirror boundary condition operates on the assumption that the cylinders possess an infinite length, and it calculates the flow as if the prescribed fluid domain were a single cell within the infinitely long domain.

The boundary conditions imposed for the **R1 configuration** case are as follows:

**Far field** with no velocity in any directions has been imposed to the inlet ( $X = -20$  m),  $Y_{min}$  ( $Y = -20$  m),  $Y_{max}$  ( $Y = +20$  m), and outlet ( $X = +40$  m) faces.

**Wall function** has been imposed to the cylinders tip at  $Z = 8.187$  m.

**No-slip** to cylinders wall.

**Slip (Zero shear stress)** to the  $Z_{min} = 0$  or the bottom of the domain

**Prescribed pressure** to the  $Z_{max} = 16$  m or the top of the domain.

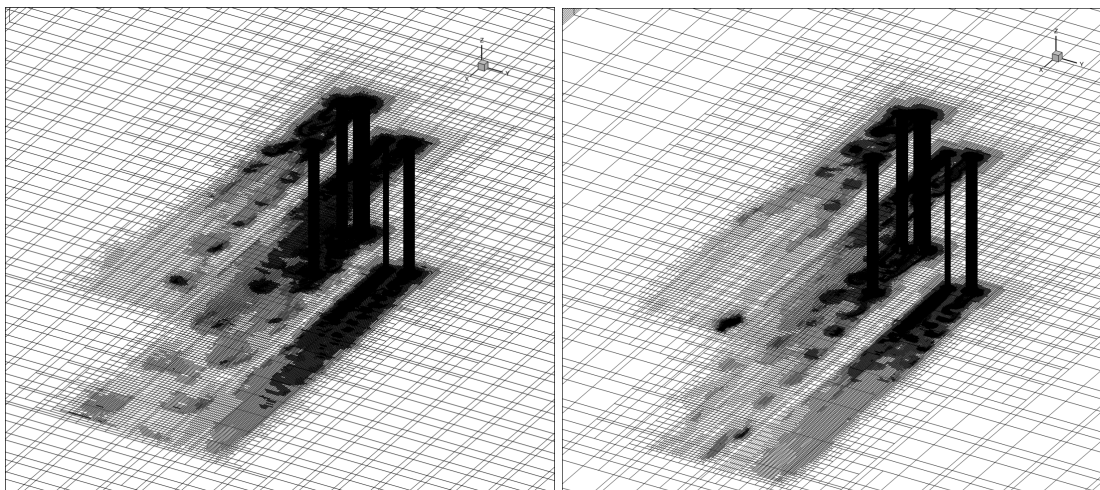
The R1 configuration, which encompasses the presence of a free surface, represents a classical

multiphase simulation case for FineMarine. In order to establish the fluid motion, it is necessary to construct a frame (accessible through the **Body definition** option) and afterward assign it an initial velocity. For the purposes of this investigation, a longitudinal velocity of 12 m/s is of particular interest. Hence, the frame operates in a manner analogous to that of a towing tank, simulating the motion of the geometry as it is towed at a certain velocity. The functionality of prescribing velocity may be found inside the **Body motion** option. It should be noted that the velocity for free surface-related simulation is provided as a ramp input in FineMarine. The current investigation employed a 1/4 sinusoidal ramp profile. The beginning time was designated as 0s, while the end time was established as 10s. The end velocity was determined to be -12 m/s. Consequently, in order to achieve this velocity at the inlet, the user must wait for a duration of 10s in physical time.

## 6.1 Simplified 3D Study - Without Free Surface

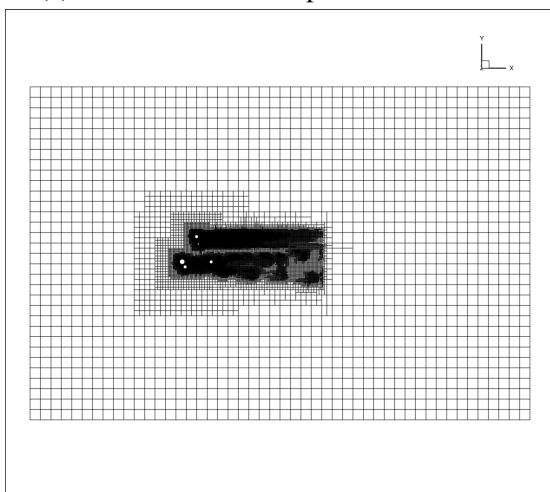
### 6.1.1 URANS - $k$ - $\omega$ SST

The mesh for the simplified three-dimensional illustration has been created by extruding a two-dimensional mesh in the span-wise ( $Z$ ) direction, using a predetermined number of cells. Two meshes were built, one with 25 cells (referred to as the coarse mesh : 0.7M cells) and another with 100 cells (referred to as the fine mesh : 1.5M cells). In contrast, the coarser mesh possessed a higher cell count in both the longitudinal and transverse directions, which was twice as much as that of the fine mesh. The simulation with a fine mesh was conducted for a duration of 240 dimensionless time steps, while the coarser simulation was extended to 260 dimensionless time steps. The mesh for both scenarios is depicted in Figure 50. The graphical representation of the changes in the avg. coefficient of drag ( $C_d$ ) and lift ( $C_l$ ) over time may be observed in Figure 51. Approximately 50 dimensionless time steps were utilized in order to compute the average hydrodynamic parameters. The observed flow variability in the coarse mesh appears to be higher compared to the finer mesh. Furthermore, the coarse mesh incorporating AGR yielded a total cell count of around 127 million, but the fine mesh exhibited a cell count of just around 40 million. The process of cell production has provided valuable insights, revealing that even when beginning from a less refined mesh, a greater number of cells may be generated compared to a finer one. This observation has a direct connection with the computation cost. It should be noted that the AGR parameters for both meshes were essentially the same as those used in the 2D study. This includes having an analogous AGR restriction box, a threshold value of  $Tr = D_E/5 = 0.122\text{m}$ , and a minimum cell size of  $0.06D_R = 0.012\text{m}$ , where  $D_E$  is equal to  $0.61\text{m}$  and  $D_R$  is equal to  $0.2\text{m}$ .

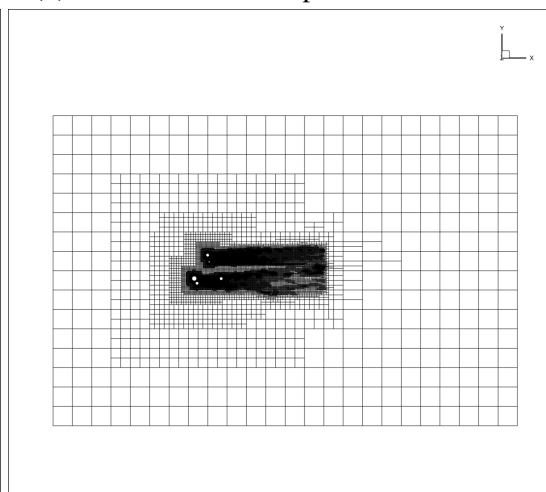


(a) Mesh : 3D view - Span-wise cell = 25

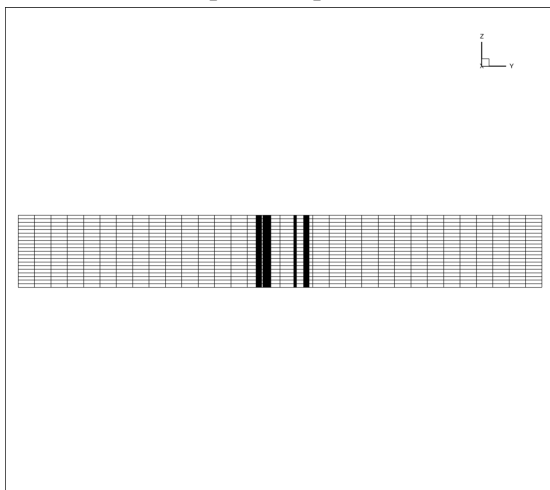
(b) Mesh : 3D view - Span-wise cell = 100



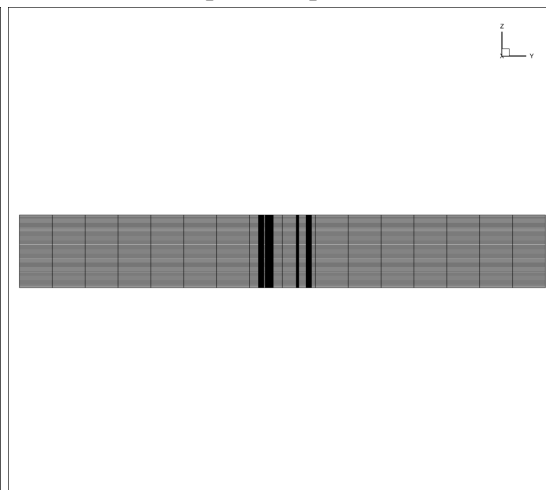
(c) Mesh : XY plane - Span-wise cell = 25



(d) Mesh : XY plane - Span-wise cell = 100



(e) Mesh : XZ plane - Span-wise cell = 25



(f) Mesh : XZ plane - Span-wise cell = 100

Figure 50: Mesh : Simplified case without free surface - Coarse vs Fine - 30° orientation

The comparison between 2D and recent 3D studies is illustrated in Figure 52. The comparative data is recorded in Table 29 as well. The agreement between the computed avg. coefficients of drag,  $C_d$ , obtained from both 2D and 3D investigations is identical, with the exception of cylinder F where a noticeable discrepancy is shown. Additionally, a little deviation is observed for cylinder Dps. Furthermore, almost equal avg. coefficients of drag ( $C_d$ ) may be seen in both three-dimensional (3D) investigations. Moreover, it is evident that cylinder F exhibits a significant decrease in  $C_d$  by about 50% in both the 3D trials, as compared to the 2D study. Hence, there is speculation regarding the potential presence of a three-dimensional phenomenon that may have led to the modification of the avg. drag coefficient. The utilization of a fine mesh case has been considered for the purpose of post-processing.

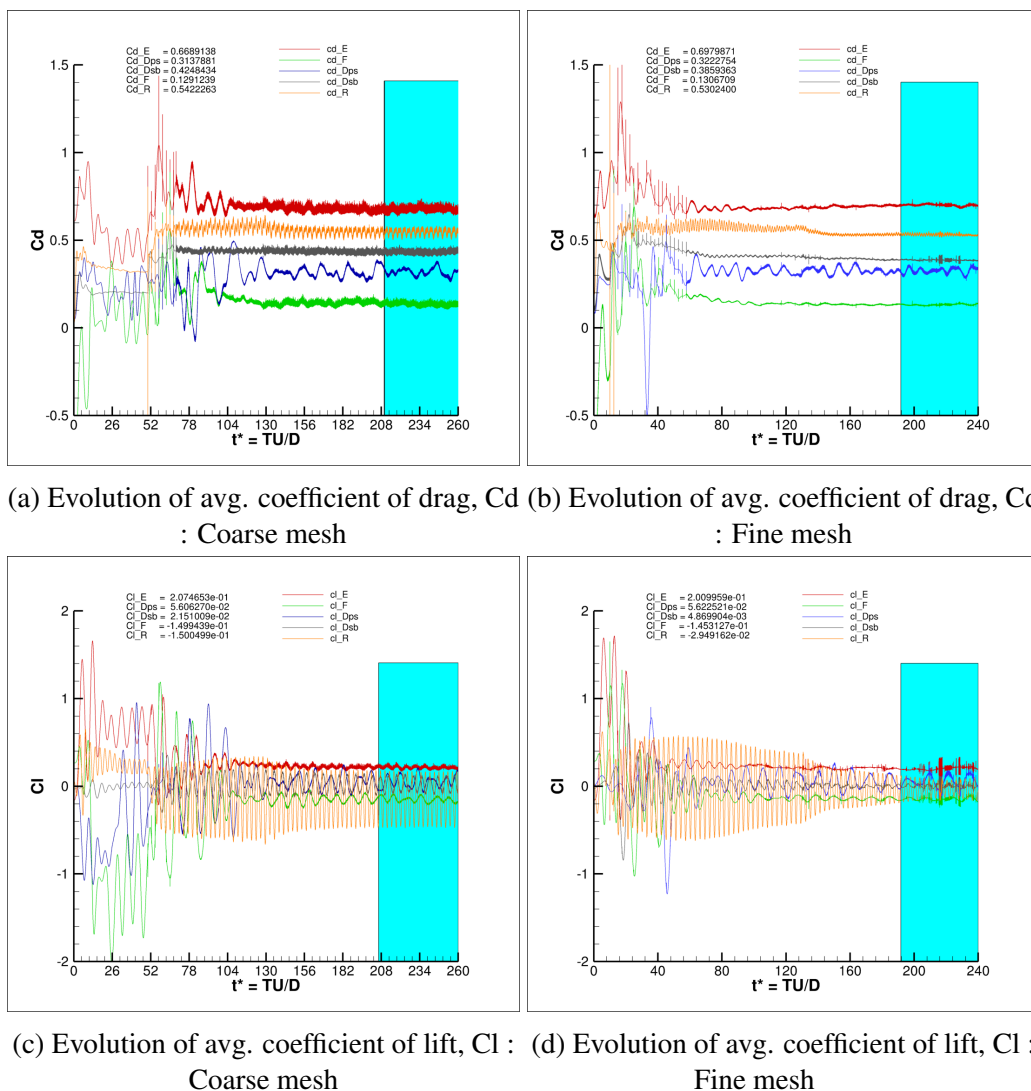
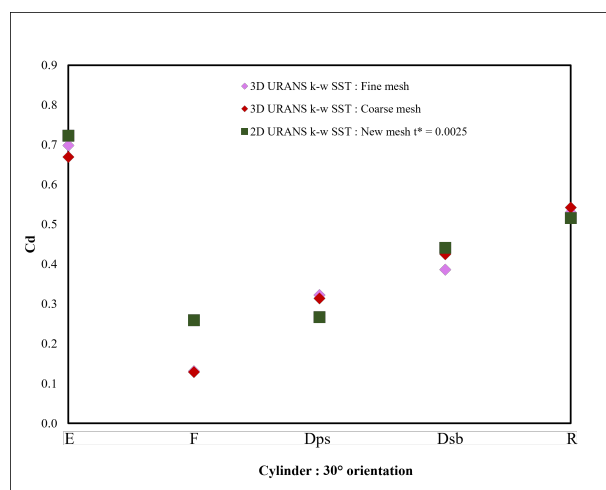


Figure 51: Evolution of avg. coefficient of drag,  $C_d$  and lift,  $C_l$  : 3D URANS -  $k-\omega$  SST -  $30^\circ$  orientations

Table 29: Avg. coefficient of drag,  $C_d$  : 2D vs 3D URANS  $k-\omega$  SST -  $30^\circ$  orientations

		$t^* = 0.0025$			
	Cylinder name	3D FineMesh	3D Coarse Mesh	2D New mesh	2D Previous mesh
Cd	E	0.6980	0.6689	0.7230	0.7111
	F	0.1307	0.1291	0.2593	0.3194
	Dps	0.3223	0.3138	0.2668	0.2797
	Dsb	0.3859	0.4248	0.4410	0.4562
	R	0.5302	0.5422	0.5156	0.5315

Figure 52: Comparison of avg. coefficient of drag,  $C_d$  : 2D vs 3D URANS  $k-\omega$  SST

To analyze the 3D effects, three cross-sectional slices inside the XZ plane are extracted. The cross-sectional slices are obtained along the center axes of the E-F, Dsb-R, and E-Dps cylinder sets. Moreover, inside each cylinder set, two lines are employed, each including 1000 data points, to extract the velocity profile in a spanwise direction at two distinct locations: the position upstream and the halfway between the two cylinders. The analysis of the instantaneous velocity profile in the spanwise direction provides useful insights into the three-dimensional effects. In the instance involving E-F and Dsb-R cylinder sets, it can be observed from Figure 53 that the magnitude of the instantaneous velocity at the midpoint of the cylinders surpasses the velocity of the incoming flow upstream. Particularly about cylinder F, it appears that the velocity has seen an approximately 1.5-fold increase compared to the upstream flow. Moreover, the velocity fluctuation may be observed in the spanwise direction, so supporting the three-dimensional effect. Cylinder Dsb-R exhibits a much less degree of fluctuation. The inability to capture span-wise fluctuations in a two-dimensional simulation is the reason for the observed changes in the avg. coefficient of drag ( $C_d$ ) and lift ( $C_l$ ) while conducting three-dimensional flow simulations for cylinders F and Dps. Moreover, the phenomenon of masking may be elucidated as the alteration of the incoming flow when a cylinder is positioned in the wake of another upstream cylinder. The presence of upstream cylinders significantly modifies the hydrodynamic characteristics by obstructing the flow. The magnitude of the impact is reliant upon the geometry (such as the

diameter of the cylinders), their proximity to each other, and the velocity of the oncoming flow. The velocity profile near the center of the E-Dps cylinders exhibits more pronounced fluctuations due to the wider distance between them in comparison to other sets. However, the flow subsequently recovers as it approaches the Dps. Hence, the three-dimensional (3D) impact is not prominently evident, despite the presence of a more noticeable fluctuation in the middle of E-Dps.

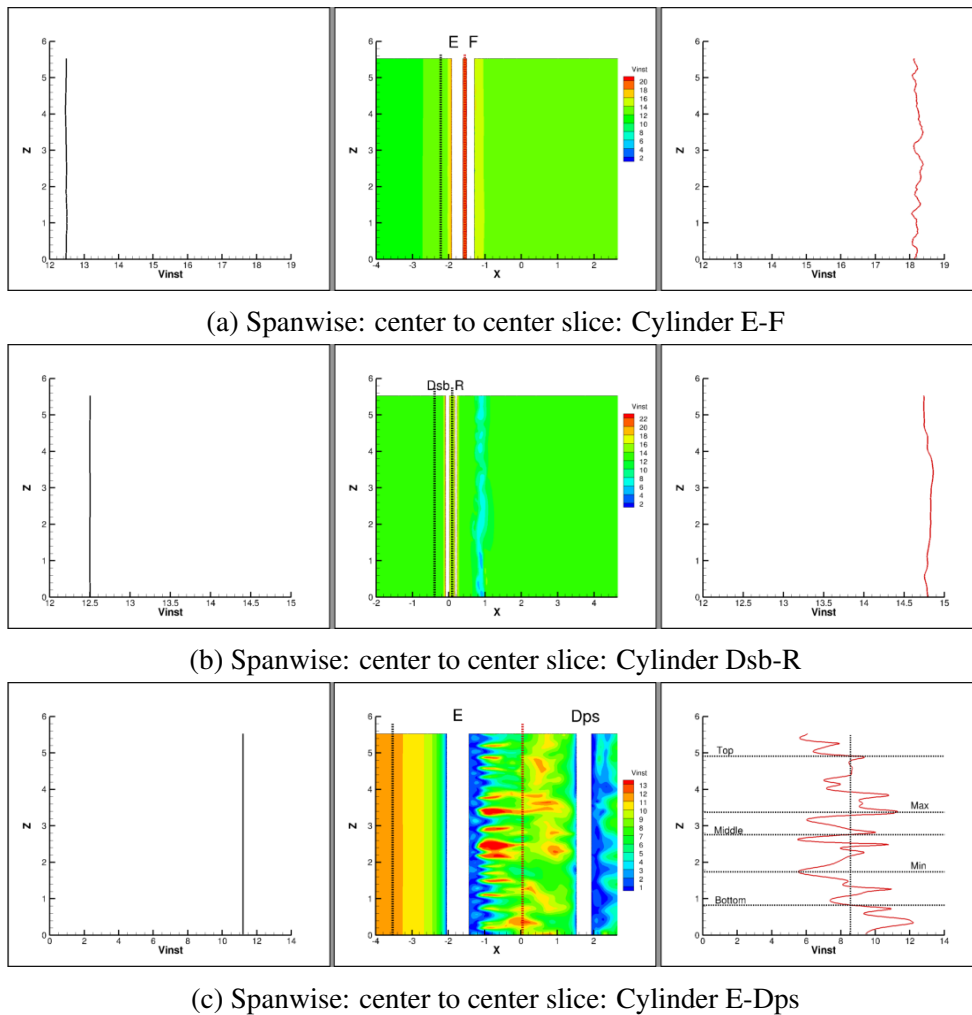


Figure 53: 3D effect: Simplified 3D without free surface - URANS  $k-\omega$  SST -  $30^\circ$  - First column: instantaneous velocity profile in the spanwise direction upstream, Second column: instantaneous velocity contour, Third column: instantaneous velocity profile in the spanwise direction middle of two cylinders

Figure 53 illustrates the various sections and their respective instantaneous velocity profiles at the upstream and middle extracted lines. Furthermore, it has been shown that the velocity at the halfway of the E-Dps cylinder is around 8 m/s, as determined using a two-dimensional simulation. Hence, a vertical line has been established in the E-Dps velocity profile that connects with the velocity along the spanwise direction at the identical magnitude. Hence, three slices are

extracted from the XY plane, namely at the top, middle, and bottom positions, while ensuring that the velocity remains consistent with the 2D simulation. Two further slices are obtained at the locations where the minimum and maximum velocities are identified. The presented Figure 54 reveals that the slices obtained from the 3D simulation exhibit distinct characteristics in terms of vortex shedding and flow pattern. A distinction may be observed when making a comparison with the two-dimensional flow, as depicted in Figure 54a.

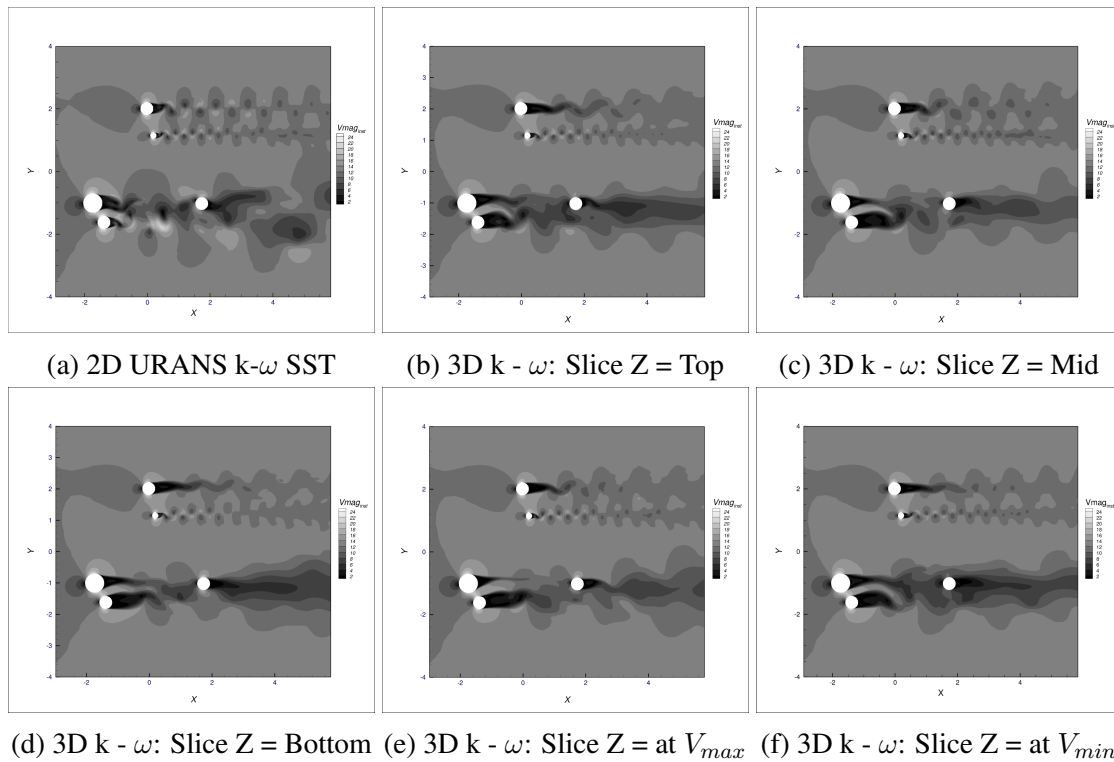


Figure 54: Instantaneous velocity contour : 2D vs Slices in simplified 3D case - 30° orientation

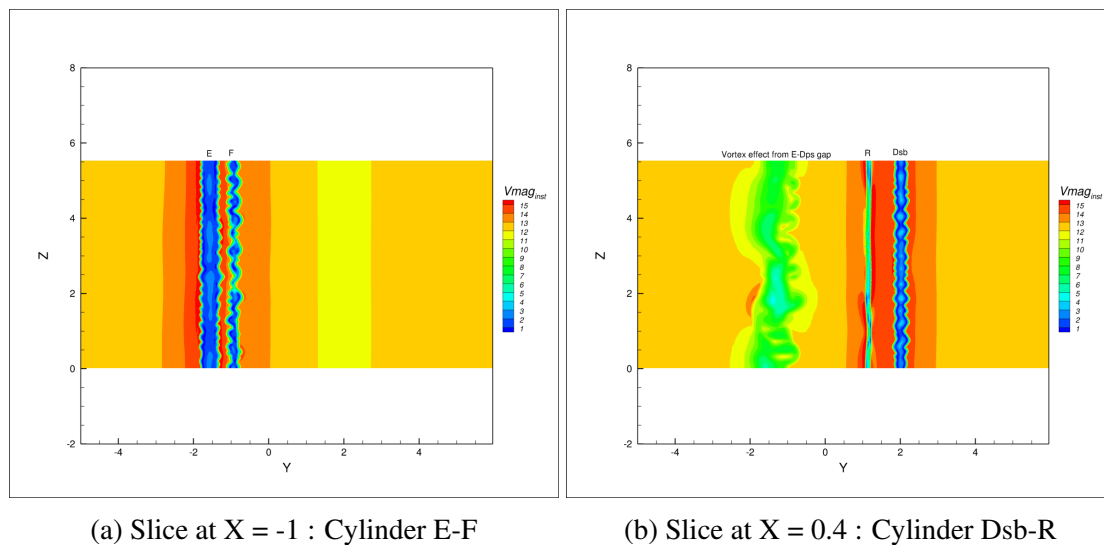
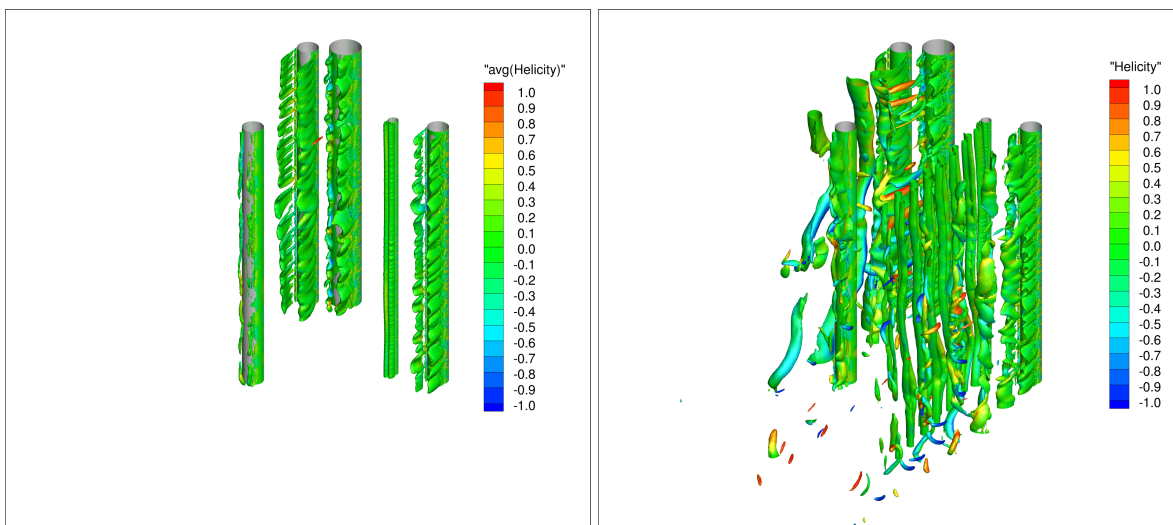


Figure 55: 3D effect simplified case without free surface: URANS k-omega SST - Slices at X



In addition, it can be shown from Figure 55 that the velocity fluctuations for cylinder F and Dsb are larger in the slices next to E-F (at  $X = -1$ ) and Dsb-R ( $X = 0.4$ ). The  $Q^*$  criteria, a dimensionless quantity defined as  $Q^* = \frac{D^2}{U^2}$ , serves as a second invariant of the velocity field. This criterion provides an improved depiction of the three-dimensional effect. The existence of E prevents from revealing of any discernible vortices for cylinder F. Moreover, the disruption of the shedding of Dps is attributed to the presence of upstream E-F cylinders. The visualization of discrete vortex shedding is facilitated by the comparatively smaller size and isolated positioning of cylinder R in relation to other cylinders. It is noteworthy that the  $Q^*$  criteria, when used with URANS, demonstrates the incomplete capture of all turbulent scales (see Figure 56b). This outcome is anticipated as the URANS approach models the Kolmogorov turbulence spectrum instead of solving it in its own mesh.



(a) Average  $Q^*$  ( $=1$ ) criterion colored with average helicity : Simplified 3D

(b) Instantaneous  $Q^*$  ( $=1$ ) criterion colored with instantaneous helicity : Simplified 3D

Figure 56:  $Q^*$  criterion : URANS  $k-\omega$  SST - Simplified 3D case without free surface

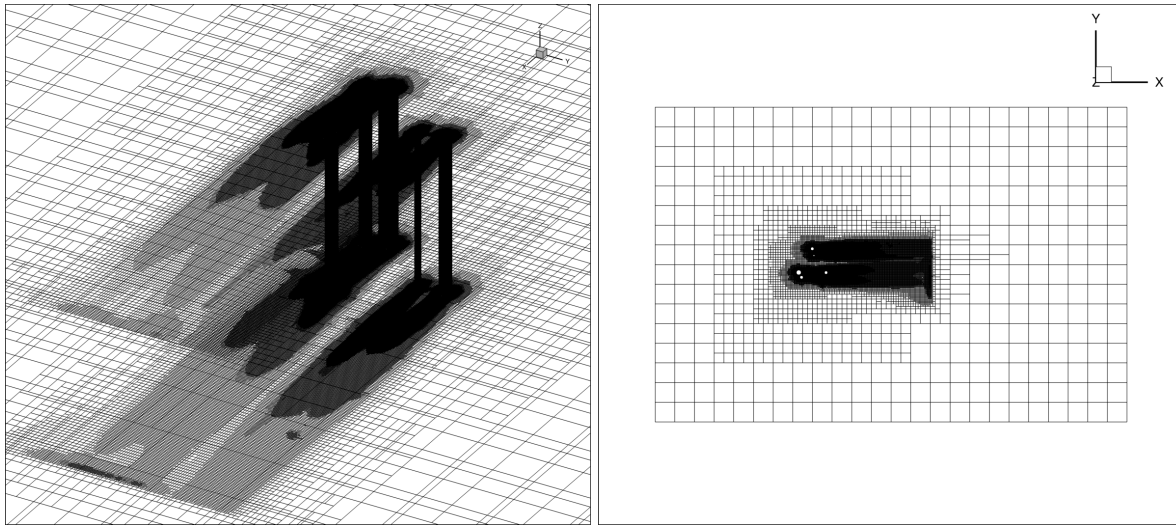
### 6.1.2 Hybrid URANS-LES

In the context of Large Eddy Simulation (LES), it is advisable to use a mesh resolution that effectively resolves 80% of the total turbulent kinetic energy (TKE) at the local level. There is a notable increase in the cell count within the mesh as compared to a simulation employing the Reynolds-averaged Navier-Stokes (RANS) method. The introduction of a hybrid RANS-LES technique can lead to a substantial decrease in mesh size. The feasibility of performing a mesh independence analysis in a Large Eddy Simulation (LES) is unfeasible due to the inherent relationship between the SGS (subgrid-scale) eddy viscosity and the cell size of the grid  $\Delta$  [Athkuri et al. \(2023\)](#). According to [Pope \(2000\)](#), it is essential that the ratio between the integral length scale  $L_o$  and the cell dimension  $\Delta$  follows the Equation 39.

$$\Delta \leq L_o/4.8 \quad (39)$$

where, the integral length scale is computed as  $L_o = \sqrt{k}/(0.09\omega)$ ,  $k$  is the turbulent kinetic energy and  $\omega$  is the specific dissipation rate. In this current study, a function,  $F$  has been created that is defined by the ratio of the integral length scale,  $L_o$  to cell size,  $\Delta$ . If the contour of function  $F$  indicates values below 5, it implies that the mesh in such regions should be further improved. The estimation of function values ranging from 5 and beyond guarantees the successful resolution of 80% of the total turbulent kinetic energy (TKE). All of the 2D simulations conducted for TMS have successfully met the specified criteria. The AGR setting ensures that the relationship is preserved in the 3D simulation as well. The hybrid RANS-LES simulation is commonly initiated from the convergent RANS/URANS simulation. Hence, the decision has been made to utilize the simplified geometry with a finer mesh to initiate a hybrid RANS-LES simulation. This choice was based on the observation that the finer mesh exhibited reduced fluctuation and required fewer cell creations in comparison to the coarser mesh. There will be a modification to the numerical scheme employed in this particular section. The turbulence and momentum discretization technique has been configured as **Blended** with a 20% upwinding level. Moreover, an option called *Additional parameters* would be switched on, with a scaling factor of 10. The hybrid RANS-LES simulation exhibits greater fluctuation compared to URANS, resulting in a rapid increase in local velocity depending upon the geometry. The increase in local velocity will necessitate a higher rate of cell production if the AGR is activated. The potential consequences of this issue include higher computational costs, simulation failure, and the generation of inaccurate or unreliable data. Given an inlet velocity of 12 m/s, it ensures that the maximum velocity within the flow domain is 120 m/s, as determined by a factor of 10.

6.1.3 Improved delayed detached eddy simulation (IDDES)

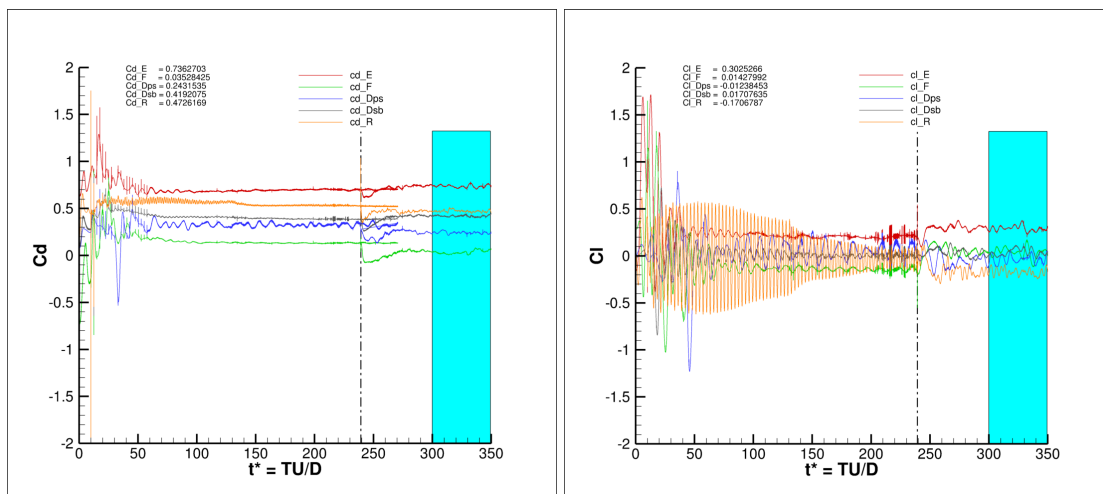


(a) Mesh XYZ : Simplified 3D without free surface - 30° orientation

(b) Mesh XY : Simplified 3D without free surface - 30° orientation

Figure 57: Mesh : Simplified 3D without free surface IDDES - 30° orientation

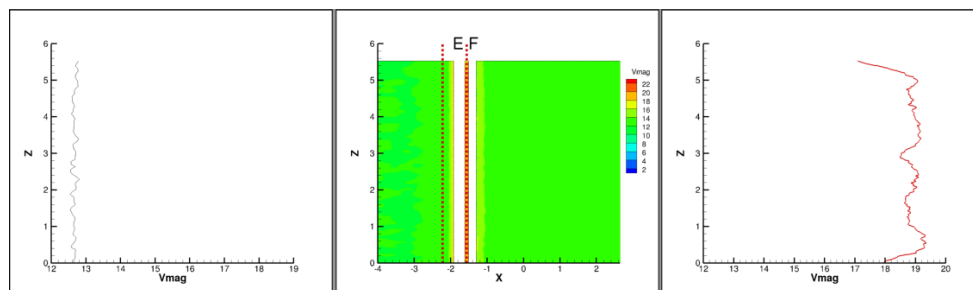
The resulting mesh in the IDDES simulation appears in Figure 57. Figure 58 illustrates the evolution of the avg. coefficient of drag, Cd, and the avg. coefficient of lift, Cl. The vertical line is the URANS simulation that has converged, utilizing the previously mentioned fine mesh. The calculation of the mean hydrodynamic parameters involved the utilization of 50 dimensionless time steps shown in color cyan.



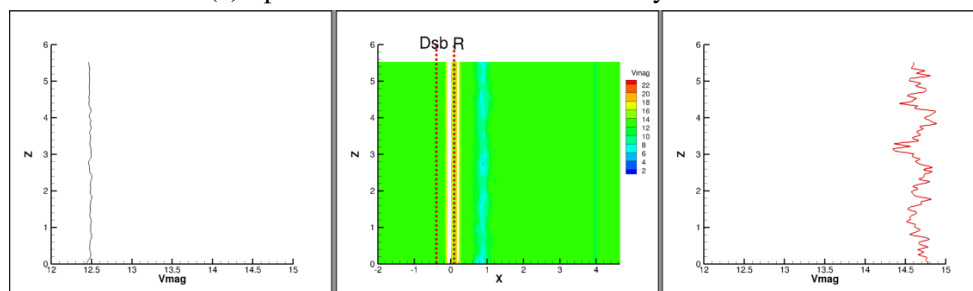
(a) Evolution of avg. coefficient of drag, Cd : Simplified 3D without free surface - 30° orientation

(b) Evolution of avg. coefficient of lift, Cl : Simplified 3D without free surface - 30° orientation

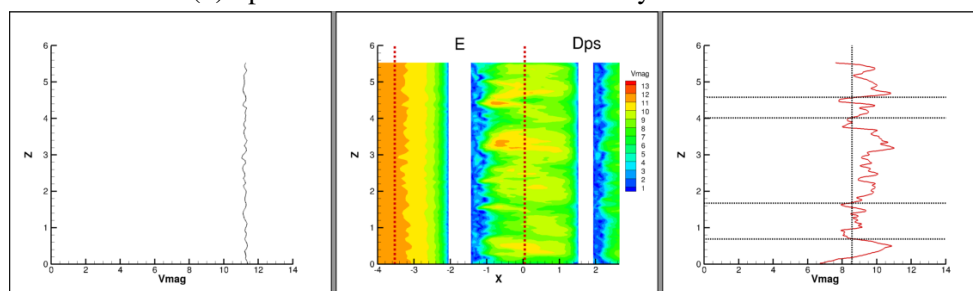
Figure 58: Evolution of avg. coefficient of drag, Cd and lift, Cl : Simplified 3D without free surface IDDES - 30° orientation



(a) Spanwise: center to center slice: Cylinder E-F



(b) Spanwise: center to center slice: Cylinder Dsb-R



(c) Spanwise: center to center slice: Cylinder E-Dps

Figure 59: 3D effect: Simplified 3D without free surface - IDDES - 30° - First column: avg. velocity profile in the spanwise direction upstream, Second column: avg. velocity contour, Third column: avg. velocity profile in the spanwise direction middle of two cylinders

After analyzing the velocity profile in the span-wise direction, as depicted in Figure 59, it becomes apparent that the IDDES simulation demonstrates a higher level of fluctuations in comparison to the URANS simulation. Additionally, Figure 60 illustrates the average and instantaneous velocity magnitude profile in the spanwise direction. In a manner analogous to the approach undertaken in URANS, several slices are extracted. The sampling technique employed ensures that the mean and instantaneous velocities at the center of the E-Dps cylinders are equivalent to those obtained by the utilization of the two-dimensional 2D URANS method. The slice positions are depicted in Figure 60.

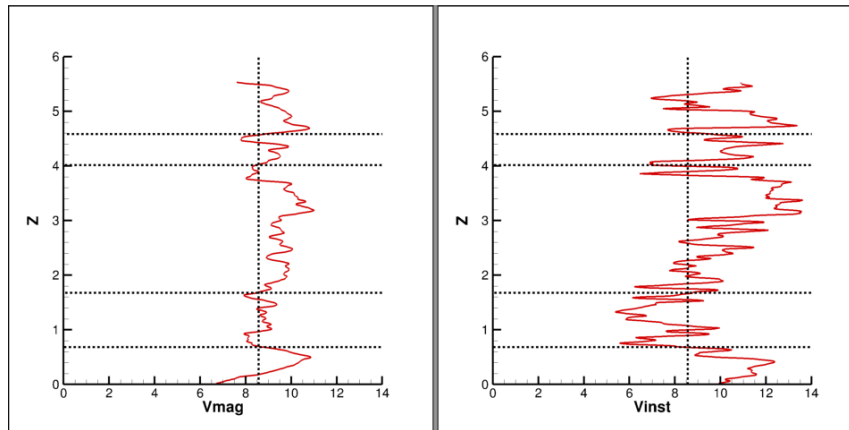


Figure 60: Slice extracted from center to center of E-Dps in XZ plane : Avg. velocity magnitude vs Instantaneous velocity : Simplified 3D without free surface IDDES

Figure 61 & 62 shows the comparison of the average and instantaneous velocity of the extracted slices (from the IDDES simulation) with the 2D URANS simulation. One important remark is that the omission of vortex stretching, a significant factor in the energy cascade process, is a limitation inherent in 2D LES simulations. The findings from [Shigehiro et al. \(1993\)](#) indicate a strong agreement between the LES results obtained through 3D computing and the experimental results. However, there are notable discrepancies between the LES results obtained through 2D calculation and both the 3D computational results and the experimental data. The utilization of a fine grid resolution, particularly in the near wall region, in two-dimensional large eddy simulation has been observed to yield a satisfactory depiction of the quasi-two-dimensional mechanisms of the flow. This is due to the direct simulation of these mechanisms, as opposed to their representation through statistical turbulence models. The 2D slices utilized in this study are derived from 3D simulations, which suggests that the limitations often associated with 2D LES simulations may not be present in the current hybrid RANS-LES 2D slices. Hence, a comparison may be formed. The extracted slices obtained from the IDDES simulation exhibit variations in flow visualization at each individual slice, so providing evidence of the three-dimensional effect. Furthermore, the alterations in wake interference for cylinder Dps resulting from the upstream E-F cylinders are clearly observable in both the average and instantaneous velocity contour for different slices. Moreover, the changes in the interaction between cylinders E-F may be observed at every cross-section. In the context of 3D simulation, the width of the cavity fluid, specifically referring to the region towards the back of the cylinder where the velocity is lower, exhibits variations across different slices, characterized by varying patterns of larger and narrower sheds. Variations in the wake width give rise to fluctuations in the avg. base pressure coefficient, denoted as  $C_{pb}$ , which is directly associated with the avg. drag coefficient,  $C_d$ , as elucidated in the context of a two-dimensional simulation.

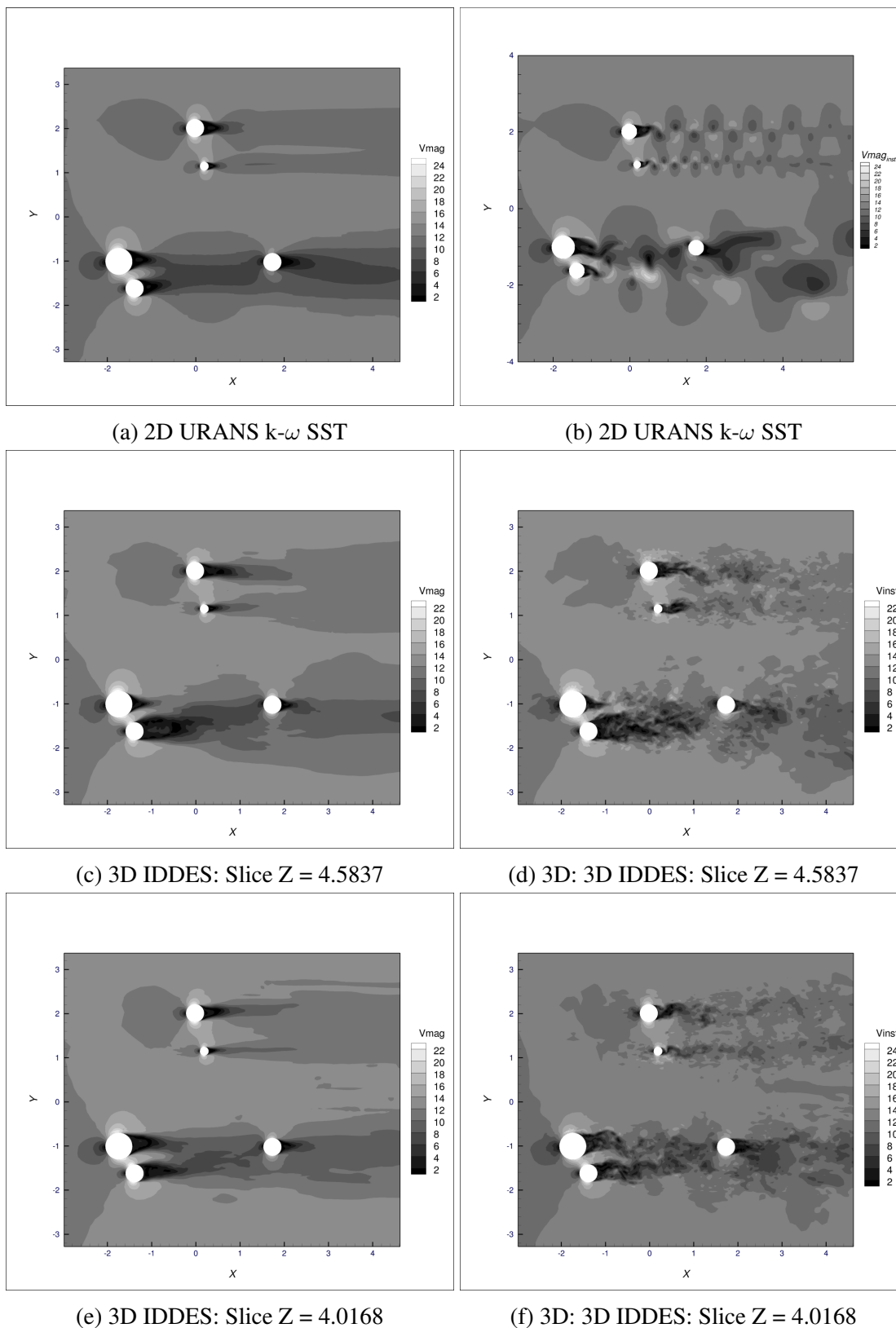


Figure 61: Average (left) and instantaneous velocity contour (right) : 2D vs Slices in simplified 3D without free surface IDDES - 30° orientation

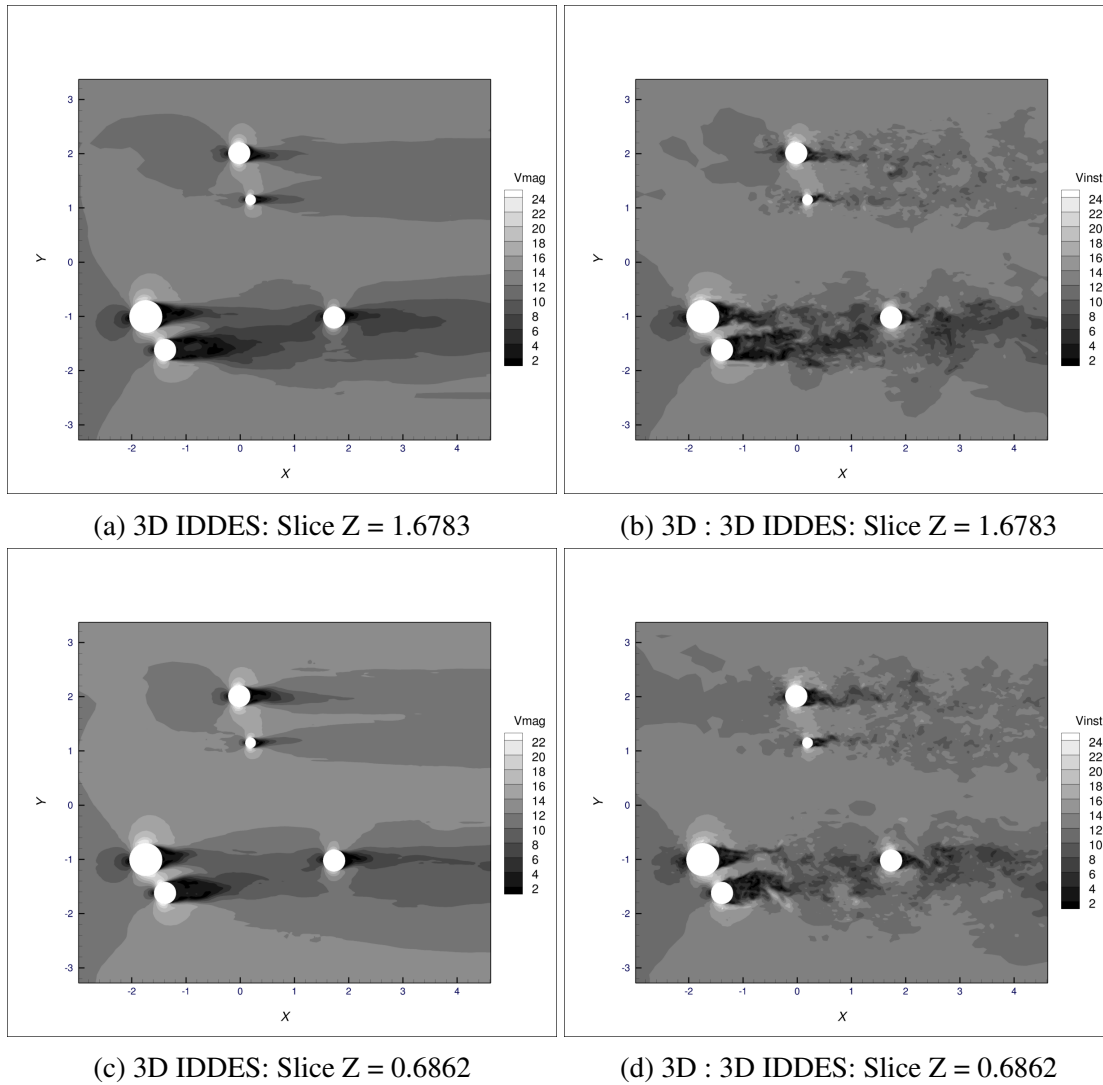
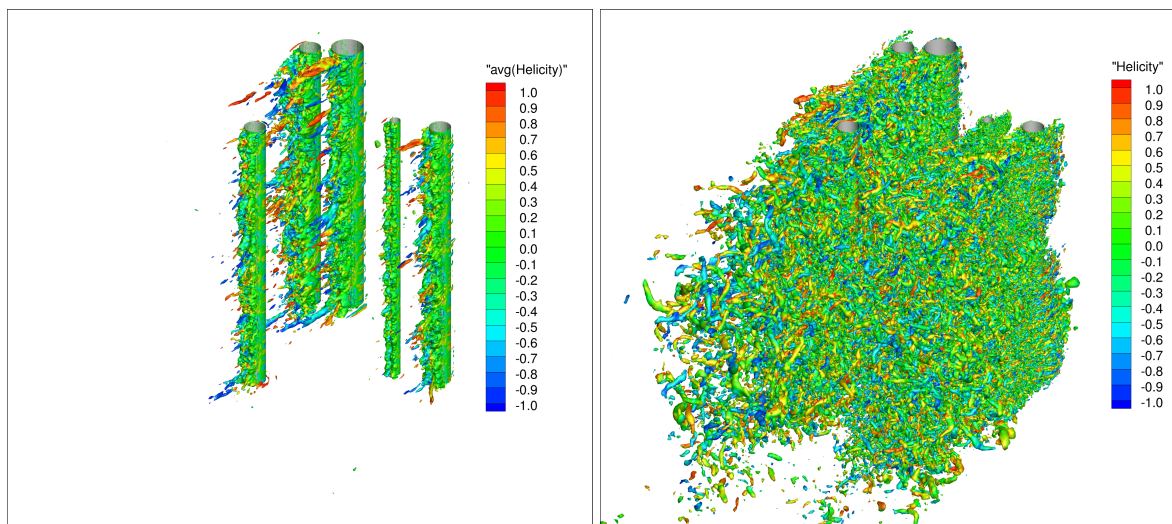


Figure 62: Average (left) and instantaneous velocity contour (right) : 2D vs Slices in simplified 3D without free surface IDDES -  $30^\circ$  orientation

The comparison between the average and instantaneous  $Q^*$  criterion in IDDES and URANS reveals a significant outcome, as seen in Figure 63b and Figure 56b, respectively. The instantaneous  $Q^*$  criteria suggest that the IDDES simulation effectively caught a broad spectrum of the Kolmogorov turbulence scale, which is resolved in its mesh, a feat that was unattainable with URANS. The results depicted in Figure 63a emphasize the necessity of further continuation of the simulation in order to enhance the visualization of the average  $Q^*$  criteria.





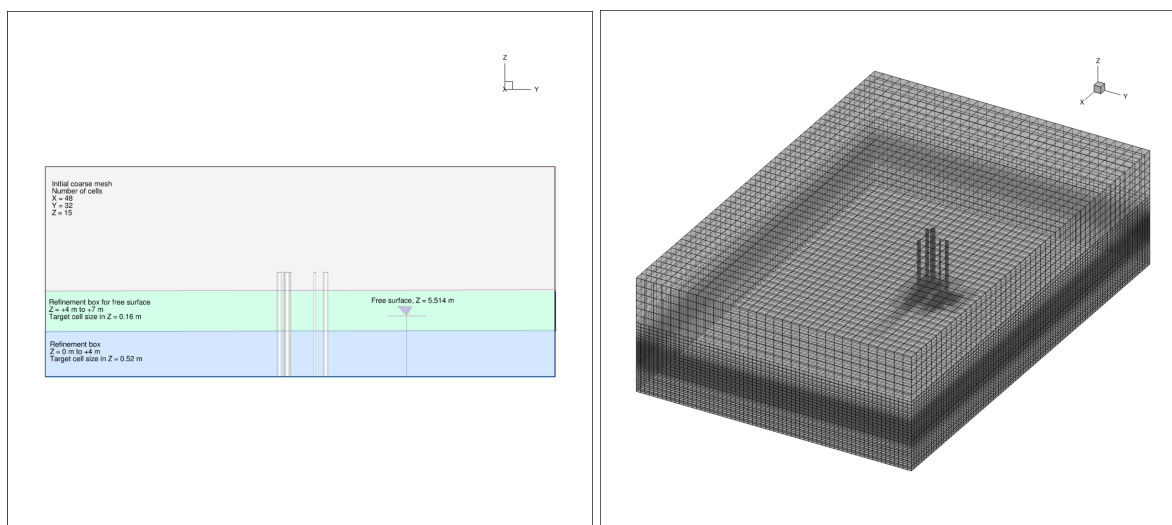
(a) Average  $Q^*$  ( $= 1$ ) criterion colored with average helicity : Simplified 3D without free surface

(b) Instantaneous  $Q^*$  ( $= 1$ ) criterion colored with instantaneous helicity : Simplified 3D without free surface

Figure 63:  $Q^*$  criterion : IDDES

## 6.2 R1 Configuration With Free Surface - 30° Orientation

### 6.2.1 URANS - $k-\omega$ SST



(a) Refinement box information

(b) Mesh

Figure 64: Mesh of R1 configuration with free surface - 30° orientation

The R1 configuration went through the meshing procedure, which involved the implementation of two refinement boxes. The initial mesh, prior to any refinement, consisted of cells arranged in  $X = 48$ ,  $Y = 32$ , and  $Z = 15$  dimensions. Given that the free surface is located at a distance of



5.514 m from the bottom, it is essential to implement a more detailed refinement in the spanwise direction, namely in the range of +4 to +7 m. The target cell size was set at 0.16 m. The second box was implemented within the range of 0 to +4 m, aligned with the existing direction. The target cell size was set at 0.52 m. The number of cells resulting from the meshing procedure was determined to be around 15M. The refinement boxes with colors and the mesh are illustrated in Figure 64. It should be noted that the mesh depicted in this context is obtained from post-processing, thereby revealing the presence of AGR activity in proximity to the cylinders. In the AGR settings, the refinement criterion type was specified as **Multisurface + flux component hessian**.

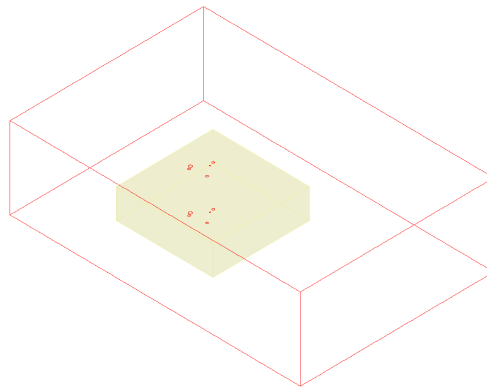
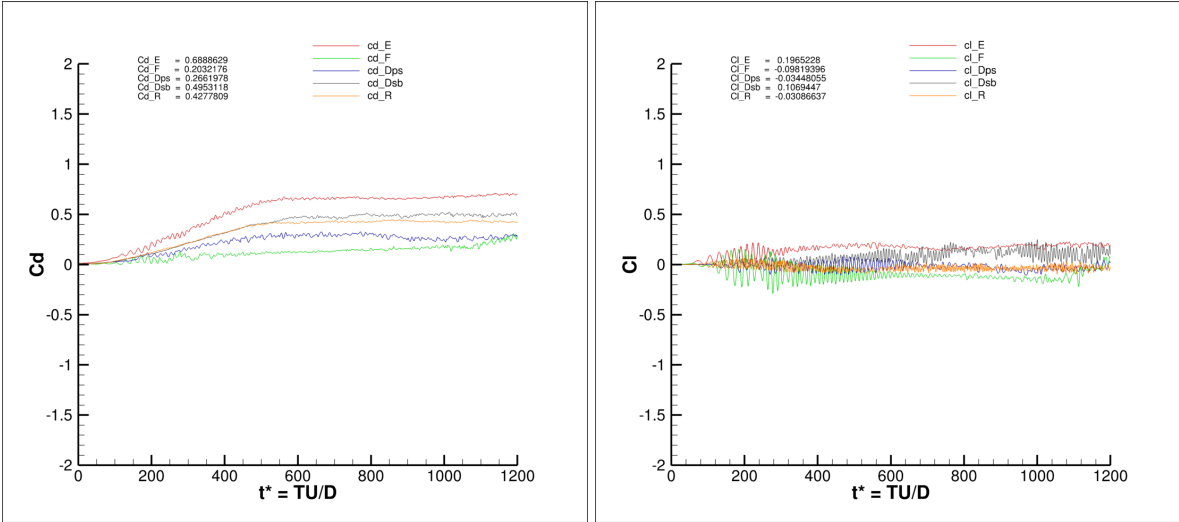


Figure 65: AGR refinement box : R1 configuration with free surface - 30° orientation

The multisurface criterion functions similarly to the flux component tensor in its ability to capture the refinement of the free surface. The threshold value,  $Tr$ , and the minimum cell size were maintained at the same values as those used in the 2D TMS simulation. The *target grid spacing normal to the free surface* was set at 0.1 m. Furthermore, an attempt has been put up to implement a box that would serve as a constraint on the AGR process. The longitudinal range (X) of the box spans from -8m to +12m, the transverse range (Y) extends from -10m to +10m, and the span-wise range (Z) reaches from 0m to +6m (see Figure 65). The simulation utilized a time step of 0.01s in order to allow the ramp input to reach a velocity of 12 m/s within a physical period of 10s (corresponding to  $t^* = 600$ ). Figure 66 illustrates the temporal evolution of the avg. coefficient of drag,  $C_d$ , and the avg. lift coefficient,  $C_l$ . The simulation was performed using the dimensionless time step until  $t^* = 1200$ , in order to assure the generation of a steady flow field suitable for activating the AGR. It should be noted that the simulation has already achieved convergence using the current time step. However, in order to more accurately capture the characteristics of a flow field, it is vital to conduct the investigation using AGR. The AGR has been successfully initiated, and the simulation is currently in progress utilizing 800 cores in the French national computer. Once the simulation will reach convergence using URANS (with the specified dimensionless time step  $\Delta t^* = 0.0025$  along with AGR), the hybrid RANS-LES

will be initiated. The current simulation is post-processed where the time step of  $\Delta T = 0.01s$ .



(a) Evolution of avg. coefficient of drag, Cd : R1 configuration with free surface - 30° orientation (b) Evolution of avg. coefficient of lift, Cl : R1 configuration with free surface - 30° orientation

Figure 66: Evolution of avg. coefficient of drag, Cd and lift, Cl : R1 configuration with free surface - 30° orientation

The visual representation in Figure 67 illustrates the average mass fraction and velocity contour in the XZ plane. The influence resulting from the presence of a free surface is clearly apparent in the mass fraction image, which depicts the occurrence of flow disruption when the fluid encounters the cylinders. The scenario shows the upward vertical movement of high-momentum fluid through the cylindrical wall. The presence of a very thin layer of fluid with high momentum can be observed at a significant distance above the free surface. The phenomenon of splashing at the free surface is more pronounced in cylinder Dps compared to other cylinders. Upon visual examination of the Dsb-R cylinder set slice, a noticeable depression in the elevation level becomes apparent immediately following the aforementioned cylinders. Nevertheless, this complex interaction occurred immediately following cylinder E-F in the direction of flow which can be seen in Figure 71. Note that, the observed slices in the XZ plane are taken from the center to the center of the cylinders. Therefore, the Dsb-R slice provides the scenario of the complex interaction between E and F. The impact resulting from the presence of E-F cylinders is also evident in the velocity contour observed in Dsb-R, where a distinct blue wake is observed above the free surface. Based on the velocity contour plot, it can be observed that the cylinders E-Dps exhibit the presence of cavity fluid, but the cylinders E-F and Dsb-R do not have similar shades of blue at their rear ends. The wake zone can only be observed by capturing a cross-sectional slice aligned with the direction of flow. In the case of E-F and Dsb-R, the slices exhibit misalignment with the direction of flow, resulting in the absence of visible shades of blue. However, readers have the option to examine the grayscale representation of the 2D slice in order to comprehend the

mentioned statement (see Figure 68 & 69).

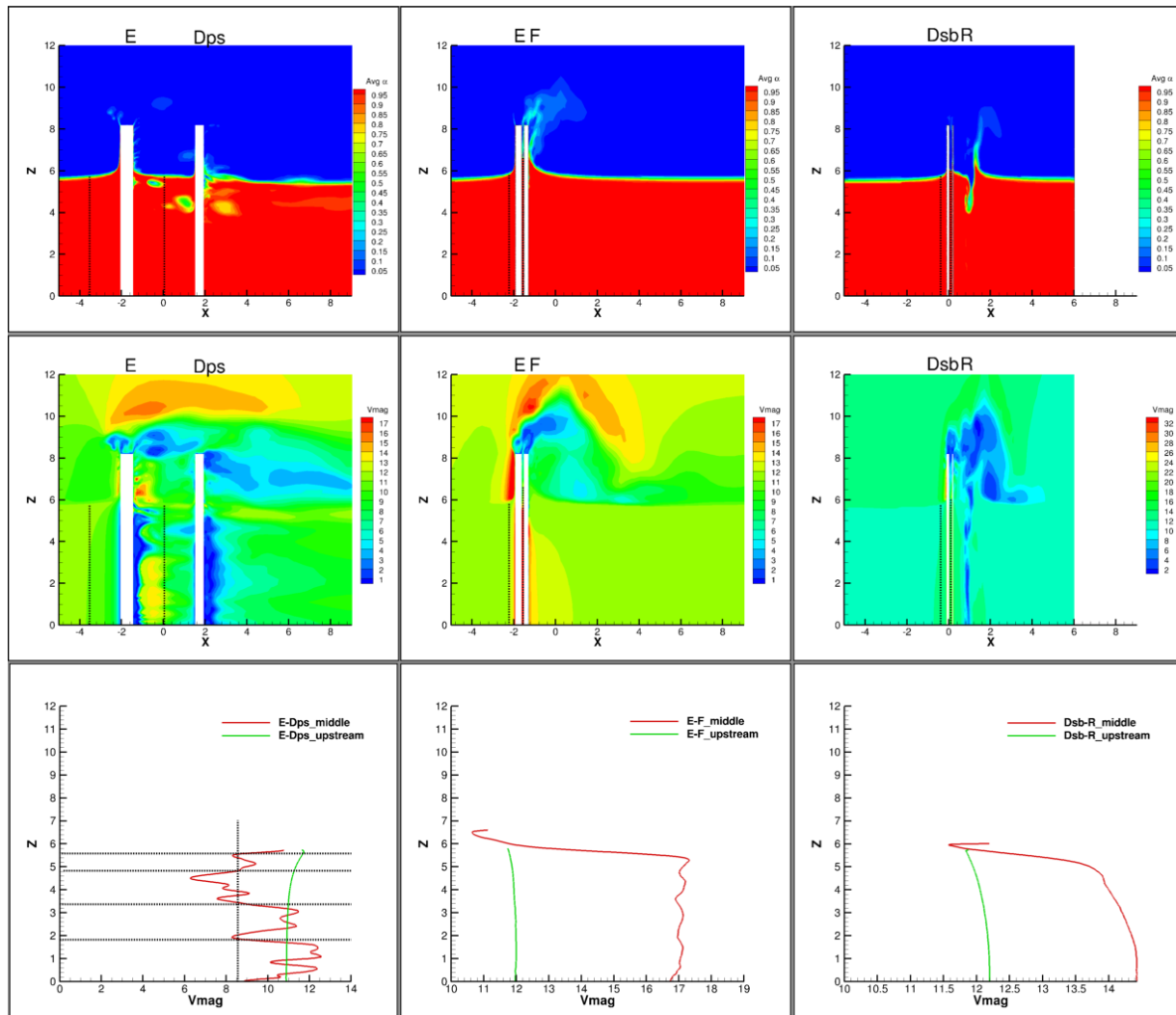


Figure 67: 3D effect: R1 configuration with free surface - URANS  $k-\omega$  SST -  $30^\circ$  orientation - First row (average mass fraction,  $\alpha$ , Second row, average velocity contour, Third row, average velocity profile in the spanwise direction (upstream and middle of two cylinders))

The visibility of the shades on all of the cylinders rear end is obvious. In addition, two vertical lines extracted for each cylinders set to extract average velocity in the spanwise direction are also illustrated in Figure 67. In line with prior investigations on two-dimensional (2D) and simplified three-dimensional (3D) analyses, the present analysis incorporating a free surface reveals the presence of velocity variations in the spanwise direction across all sets of cylinders. The region of maximum momentum within cylinder E-F, as shown in prior studies, is located in its middle. The velocity of fluid appears to decrease in the upper sections of cylinder E-F and Dsb-R sets, however, it is important to note that this relates to the velocity of air and not the LNG. In a manner similar to the simplified 3D case, cross-sectional slices in the spanwise direction are

employed to assess variations in the flow field. Four slices have been extracted and are shown in Figure 68 and Figure 68. As anticipated, variation in flow features is observable in every individual slice.

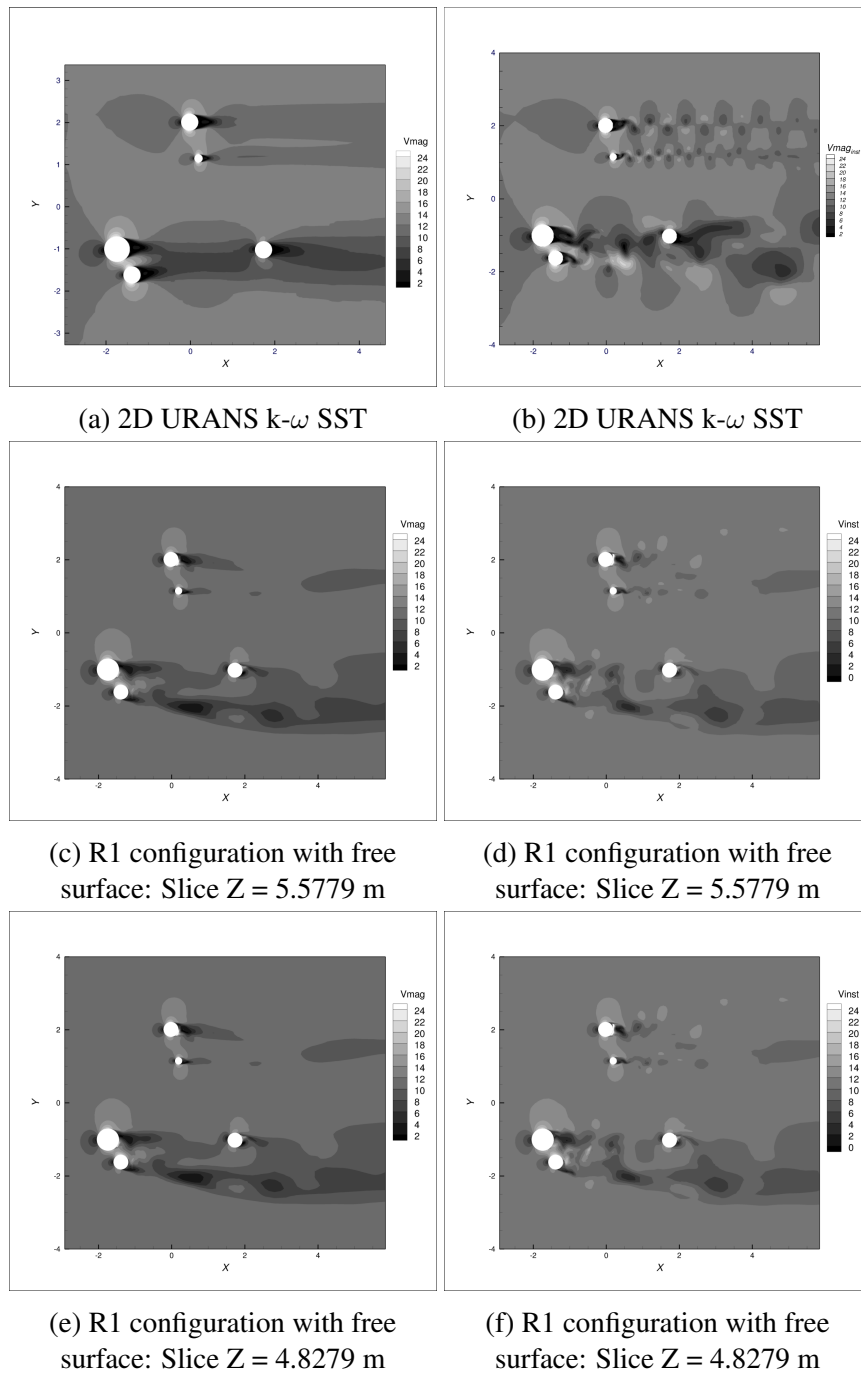


Figure 68: Average (left) and instantaneous velocity contour (right) : 2D vs Slices in R1 with free surface 3D case URANS  $k-\omega$  SST -  $30^\circ$  orientation

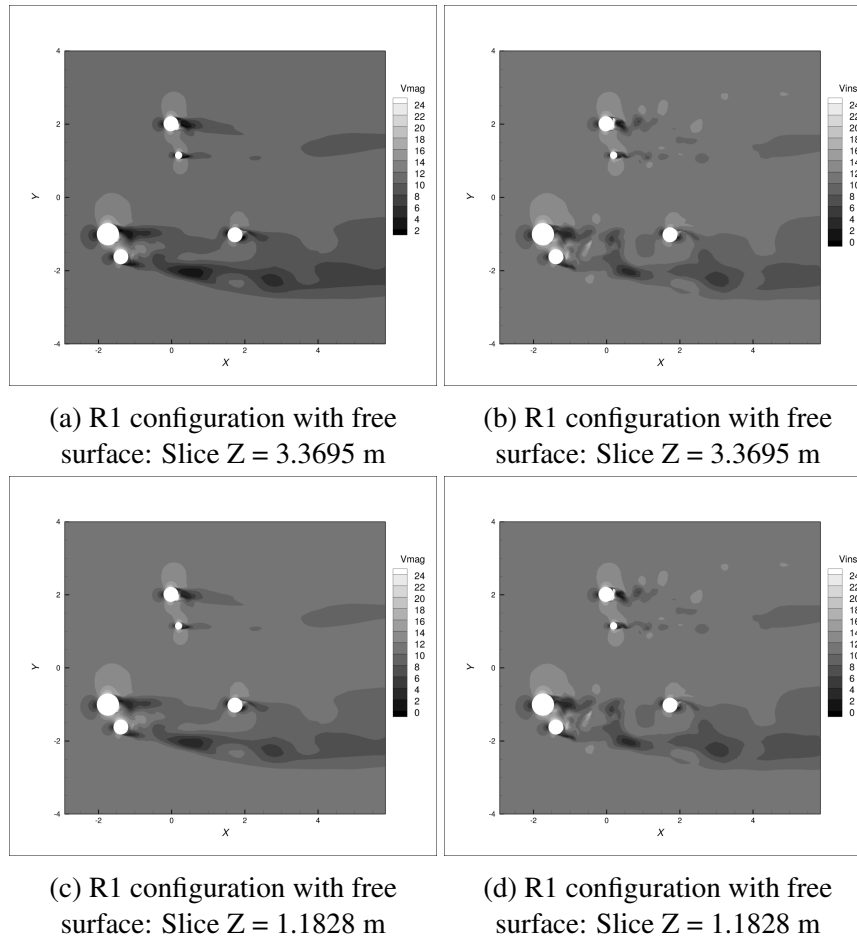


Figure 69: Average (left) and instantaneous velocity contour (right) : 2D vs Slices in R1 configuration with free surface 3D case URANS  $k-\omega$  SST -  $30^\circ$  orientation

The study presents a depiction of the comparison of the avg. drag coefficient using various approaches (2D, 3D, and 3D with free surface) and turbulence models (URANS  $k-\omega$  SST and hybrid RANS-LES). This comparison is illustrated in Figure 70 and recorded in Table 30. The complexity of the free surface can be seen in Figure 71.

Table 30: Comparison of avg. coefficient of drag,  $C_d$  : Simplified case (2D URANS  $k-\omega$  SST, 3D URANS  $k-\omega$  SST, IDDES without free surface) vs 3D URANS  $k-\omega$  SST (with free surface)

Cylinder name	URANS - $k-\omega$ SST			Hybrid RANS-LES	URANS - $k-\omega$ SST
	2D New mesh	3D Coarse mesh	3D Fine Mesh	IDDES	Free surface
E	0.7230	0.6689	0.6980	0.7363	0.6889
F	0.2593	0.1291	0.1307	0.0353	0.2032
Cd	Dps	0.2668	0.3138	0.2432	0.2662
	Dsb	0.4410	0.4248	0.4192	0.4953
	R	0.5156	0.5422	0.5302	0.4726

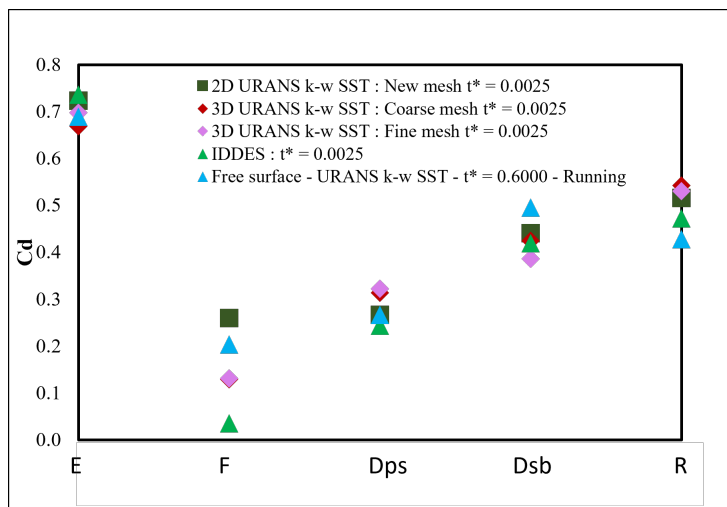


Figure 70: Comparison of avg. coefficient of drag,  $C_d$ : 2D, 3D URANS  $k-\omega$  SST, IDDES, without free surface and 3D URANS  $k-\omega$  SST with free surface

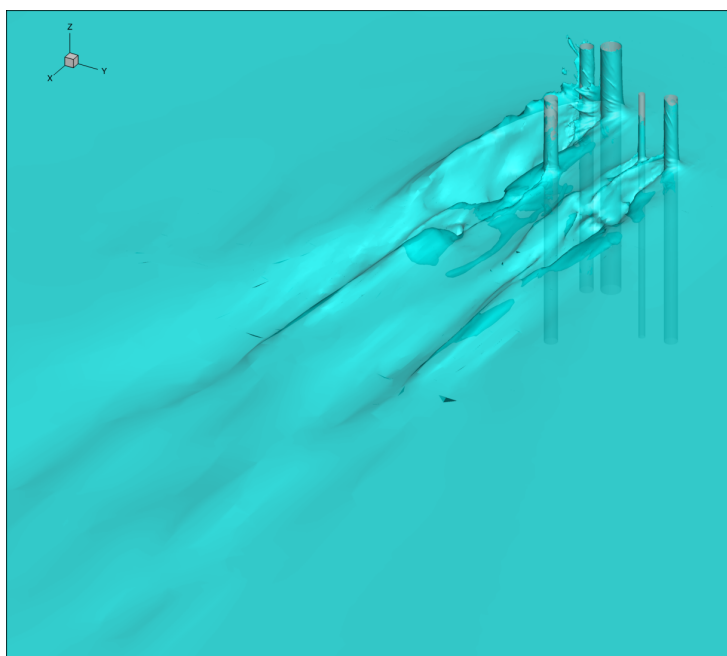


Figure 71: Free surface : R1 configuration with free surface -  $30^\circ$  orientation

The existence of cylinder E in close proximity has a significant impact on cylinder F. Hence, a modification in the flow field significantly impacts on cylinder F. It is apparent that the 2D simulation, lacking the inclusion of 3D and free surface effects, does not accurately depict reality. The implementation of a 3D mirror boundary condition resulted in a considerable reduction in the drag experienced by cylinder F. The drag encountered further decreased when simulated utilizing IDDES, a method known for its ability to accurately capture a wide range of the Kolmogorov turbulence spectrum. Additionally, the simulation incorporating the free surface offers

significant insights. Conducting an investigation on the free surface configuration with a hybrid RANS-LES approach would be of great interest, particularly focusing on cylinder F. Lastly, the elevation of the fluid level along the cylinders, when exposed to a uniform flow, suggests a strong likelihood of the occurrence of sloshing events in the presence of a wave. The integration of wave with identical geometry (R1 configuration) has the potential to serve as an intriguing direction for future research.

## 7 CONCLUSION

The present investigation was initiated with the objective of finding a better temporal and spatial resolution for simulating Tripod mast structure (TMS) in various orientations. Subsequently, conducting simulation using a hybrid RANS-LES turbulence model. In order to determine an improved temporal and spatial resolution, an extensive investigation was conducted using a single cylinder through a variety of Reynolds numbers, and the outcomes had been compared with the experimental and numerical findings found in the literature. It should be noted that the TMS functions within the post-critical flow regime ( $Re > 8M$ ). Nevertheless, due to the limited availability of experimental and numerical data, it was necessary to conduct simulations within the sub-critical region as well. Flow over a single cylinder simulation has been performed in a range spanning from sub-critical to postcritical conditions, and these results have been compared to the current data available in the literature. The sensitivity of the single-cylinder simulation to different meshing techniques has been observed. However, while conducting simulations using the eddy viscosity turbulence model, a notable discrepancy was seen in the sub-critical to the critical region in compared to the experimental findings. The absence of studies in the sub-critical to postcritical region, concerning a single cylinder, poses significant challenges in the current investigation. Consequently, a significant percentage of the present research effort has been dedicated to aligning with established academic findings and bridging gaps in regions that suffer from limited data availability. As observed before, the TMS exhibits a layout consisting of five cylinders, hence resulting in complexity within the flow field. Nevertheless, academic research is typically conducted using simpler setups, such as tandem and side-by-side arrangements using cylinders of equivalent diameters. The significance of the staggered arrangement between two cylinders was relatively limited in the aforementioned investigations; yet, from an industrial perspective, this arrangement has pronounced importance. The TMS is a combination of tandem, side-by-side, and staggered arrangements in terms of different orientations. Furthermore, researchers have extensively examined two different arrangements of cylinders within the lower subcritical ranges ( $Re = O(10^4)$ ). Therefore, the nomenclature of the flow pattern in the present work is based on these previous investigations even though the current study performs in  $Re = O(10^7)$ . The present analysis also highlights a significant disparity between scholarly research and industrial needs. The study aimed to enhance the temporal and spatial resolutions of TMS by implementing a two-dimensional (2D) simulation approach across seven different orientations. The study revealed that the spatial resolution deemed appropriate for single-cylinder simulations with the activation of AGR is not viable for 3D TMS simulation, because of the significant proliferation of cells exceeding 350M. Hence, an additional spatial resolution analysis was conducted, revealing its suitability for the 3D simulations. In order to simplify the analysis



and examine the influence of three-dimensional effects in the spanwise direction, a simplified three-dimensional model with mirror boundary condition (in the spanwise direction) was used for investigation. This scenario was simulated using the URANS  $k-\omega$  SST turbulence model. The findings derived from the simplified research yielded significant insights and consolidated information on the R1 configuration (Tripod mast structure (TMS) without struts) involving a free surface. The simulation using the hybrid RANS-LES (IDDES) was conducted on the simplified case, highlighting the importance of employing this particular turbulence model for the investigation. The improved characterization of the Kolmogorov turbulence spectrum yielded more comprehensive insights into the intricate dynamics of flow interaction between cylinders, particularly in the case of cylinder F, which was situated in close proximity to cylinder E. The R1 configuration with a free surface has been studied using the URANS  $k-\omega$  SST model (this will be continued with hybrid RANS-LES). The presence of the masking effect was evident in the study, and its estimation wasn't possible using the Morison equation. The present work introduces a unique approach by

- doing a comprehensive analysis of a single cylinder throughout a wide range of Reynolds numbers, a research endeavor that has not been previously explored in the academic literature. The study provides hydrodynamic parameters for the postcritical range that can be utilized by other researchers
- demonstrating a mesh dependency of a single cylinder in resolving flow parameters that align with the underlying physics of the flow
- the application of adaptive grid refinement (AGR) to capture the flow physics, showcasing its robustness in industrial applications compared to the conventional static mesh-based approach
- showing the efficacy of doing a two-dimensional TMS simulation that closely aligns with the findings of three-dimensional (3D) investigations
- figuring out an appropriate temporal and spatial resolution so that the continuation of the study can be carried out using URANS  $k-\omega$  SST (in 2D and 3D) and hybrid RANS-LES (3D) turbulence model with and without a free surface for different orientations

The future recommendations are as follows:

- Conducting the 3D simulation using URANS  $k-\omega$  SST and hybrid RANS-LES turbulence model with the free surface for other orientations (since the current study only performed 30° orientation)

- Incorporating wave to the study
- By conducting extensive research utilizing the aforementioned turbulence models, the position of the TMS within the LNG membrane tank can be varied across different locations to assess the corresponding variations in hydrodynamic loads for each location and orientation
- Following that, it would be possible to construct a surrogate model incorporating the result found in the previous recommendation. This surrogate model will utilize a neural-based network approach as an alternative to the conventional meshing approach.

## **ACKNOWLEDGEMENT**

I would like to express my deep appreciation to the Almighty for protecting my well-being during the completion of my master's thesis. I would like to express my sincere gratitude to my scientific supervisor, Dr. Emmanuel GUILMINEAU, for his consistent guidance and unwavering support throughout my academic journey. I am sincerely grateful to my internship supervisor Dr. Laurent BROSSET from Gaztransport & Technigaz (GTT) for his firm belief in my abilities and consistent acknowledgment of my contributions, which have been incredibly valuable to me. I would like to express my heartfelt appreciation to Dr. Nicolas COUTY for his invaluable recommendation in the study. The LHEEA laboratory and the opportunity to conduct research on the most powerful supercomputer in France, Jean Zay, are gratefully acknowledged. I would like to extend my sincere appreciation to the distinguished faculty members of the LHEEA laboratory at Ecole Centrale Nantes (ECN). Their comprehensive and engaging pedagogy in the field of hydrodynamics has greatly enhanced my understanding. Finally, I am grateful to my coordinators Professor Lionel GENTAZ and Professor Philippe RIGO for their consistent support, which greatly contributed to the successful completion of this academic endeavor.

## REFERENCES

- Achenbach, E. (1968). Distribution of local pressure and skin friction around a circular cylinder in cross-flow up to  $re = 5 \times 10^6$ . *Journal of fluid Mechanics*, 34(4), 625–639.
- Achenbach, E. (1971). Influence of surface roughness on the cross-flow around a circular cylinder. *Journal of fluid mechanics*, 46(2), 321–335.
- Athkuri, S. S. C., et al. (2023, feb). Computation of drag crisis of a circular cylinder using hybrid RANS-LES and URANS models. *Ocean Engineering*, 270, 113645. doi: 10.1016/j.oceaneng.2023.113645
- Bassi, et al. (2012, June). Hybrid rans-les and simulations with and the and discontinuous galerkin and method. In *6th european conference on computational mechanics (eccm 6) 7th european conference on computational fluid dynamics (ecfd 7)*.
- Batchelor, G. (1956). A proposal concerning laminar wakes behind bluff bodies at large reynolds number. *Journal of fluid mechanics*, 1(4), 388–398.
- Bearman, P. W., et al. (1969). On vortex shedding from a circular cylinder in the critical reynolds number regime. *Journal of Fluid Mechanics*, 37(3), 577–585.
- Bengt, A., et al. (2012). Computational fluid dynamics for engineers..
- Breuer, M., et al. (2000). A challenging test case for large eddy simulation: high reynolds number circular cylinder flow. *International journal of heat and fluid flow*, 21(5), 648–654.
- Cantwell, B., et al. (1983). An experimental study of entrainment and transport in the turbulent near wake of a circular cylinder. *Journal of fluid mechanics*, 136, 321–374.
- Catalano, P., et al. (2003). Numerical simulation of the flow around a circular cylinder at high reynolds numbers. *International journal of heat and fluid flow*, 24(4), 463–469.
- Charles, G. S., et al. (1991). Analytical methods for the development of reynolds-stress closures in turbulence. *Annu. Rev. Fluid Mech.* 1991.23 : 107-57 Copyright © 1991 by Annual Reviews Inc. All rights reserved.
- Eppler, R. (1954). Beiträge zu theorie und anwendung der unsteady strömungen. *Journal of Rational Mechanics and Analysis*, 3, 591–644.
- Eric, F., et al. (2010). Evaluation of rans turbulence models for flow problems with significant impact of boundary layers..
- FineMarine. (2023). Documentation platform. Retrieved from [https://www.cadence.com/en\\_US/home/tools/system-analysis/computational-fluid-dynamics/fidelity/marine.html](https://www.cadence.com/en_US/home/tools/system-analysis/computational-fluid-dynamics/fidelity/marine.html)
- Franke, et al. (1989). Analysis of experimental vortex-shedding data with respect to turbulence modelling. In *7th symposium on turbulent shear flows, volume 2* (Vol. 2, pp. 24–4).

- Gatski, et al. (2002). Linear and nonlinear eddy viscosity models. In B. E. Launder & N. D. Sandham (Eds.), *Closure strategies for turbulent and transitional flows* (p. 9–46). Cambridge University Press. doi: 10.1017/CBO9780511755385.003
- Gritskevich, M. S., et al. (2012). Development of ddes and iddes formulations for the k- $\omega$  shear stress transport model. *Flow turbulence and combustion*, 88, 431–449.
- Guangxing, W., et al. (2020, oct). Simultaneous simulation of transition and massive separation by RANS-LES-tr model. *Aerospace Science and Technology*, 105, 106026. doi: 10.1016/j.ast.2020.106026
- Hatlevik, A. S., et al. (2018, July). Resistance analysis of trimaran service vessel using cfd..
- Hirt, C. W., et al. (1981). Volume of fluid (vof) method for the dynamics of free boundaries. *Journal of computational physics*, 39(1), 201–225.
- Hu, X., et al. (2019). On the flow around two circular cylinders in tandem arrangement at high reynolds numbers. *Ocean Engineering*, 189, 106301.
- Ishigai, S., et al. (1972). Experimental study on structure of gas flow in tube banks with tube axes normal to flow: Part 1, karman vortex flow from two tubes at various spacings. *Bulletin of JSME*, 15(86), 949–956.
- Jones, G. W., et al. (1969). *Aerodynamic forces on a stationary and oscillating circular cylinder at high reynolds numbers* (Vol. 300). National Aeronautics and Space Administration.
- Kakuda, et al. (2006). Finite element simulation of 3d flow around a circular cylinder. *International Journal of Computational Fluid Dynamics*, 20(3-4), 193–209.
- Karniadakis, G. E., et al. (1992). Three-dimensional dynamics and transition to turbulence in the wake of bluff objects. *Journal of fluid mechanics*, 238, 1–30.
- Kimmoun, O., et al. (2020). Assessment of morison equation for non-impacting wave loads on a vertical cylinder. In *Proceedings of the thirtieth (2020) international ocean and polar engineering conference www.isope.org shanghai, china, october 11-16, 2020 copyright © 2020 by the international society of offshore and polar engineers (isope) isbn 978-1-880653-84-5; issn 1098-6189*.
- Kitagawa, et al. (2008). Numerical investigation on flow around circular cylinders in tandem arrangement at a subcritical reynolds number. *Journal of Fluids and Structures*, 24(5), 680–699.
- Lakshmipathy, S., et al. (2010). Partially averaged navier–stokes (pans) method for turbulence simulations: flow past a circular cylinder.
- Lee, T., et al. (1997). Nonintrusive measurements of the boundary layer developing on a single and two circular cylinders. *Experiments in fluids*, 23(3), 187–192.
- Lin, J.-C., et al. (2002). Flow past two cylinders in tandem: instantaneous and averaged flow structure. *Journal of Fluids and Structures*, 16(8), 1059–1071.

- Lo, et al. (2005). Numerical investigation of high reynolds number flows over square and circular cylinders. *Journal of Thermophysics and Heat Transfer*, 19(1), 72–80.
- Meneghini, J. R., et al. (2001). Numerical simulation of flow interference between two circular cylinders in tandem and side-by-side arrangements. *Journal of fluids and structures*, 15(2), 327–350.
- Menter, F. R. (1992, October). *Improved two-equation and k- omega and turbulence models for aerodynamic flows* (Tech. Rep. No. unedited). NASA.
- Menter, F. R. (1993, July). Zonal two equation k-cl, turbulence models for aerodynamic flows. 24th Fluid Dynamics Conference July 6-9, 1993 / Orlando, Florida.
- Menter, F. R. (1994, aug). Two-equation eddy-viscosity turbulence models for engineering applications. *AIAA Journal*, 32(8), 1598–1605. doi: 10.2514/3.12149
- Menter, F. R., et al. (2003). Ten years of industrial experience with the sst turbulence model. Begell House, Inc.
- Michael, S., et al. (2015, oct). Evaluation of vortex generators for separation control in a transcritical cylinder flow. *AIAA Journal*, 53(10), 2967–2977. doi: 10.2514/1.j053851
- Mittal, et al. (1997). On the inclusion of three-dimensional effects in simulations of two-dimensional bluff-body wake flows. In *Asme fluids engineering division summer meeting* (pp. 1–6).
- Mittal, et al. (2001). Computation of three-dimensional flows past circular cylinder of low aspect ratio. *Physics of Fluids*, 13(1), 177–191.
- Moussaed, C., et al. (2014). Simulation of the flow past a circular cylinder in the supercritical regime by blending rans and variational-multiscale les models. *Journal of Fluids and Structures*, 47, 114–123.
- Niemann, H., et al. (1990). A review of recent experiments on the flow past circular cylinders..
- Ong, M. C., et al. (2009, apr). Numerical simulation of flow around a smooth circular cylinder at very high reynolds numbers. *Marine Structures*, 22(2), 142–153. doi: 10.1016/j.marstruc.2008.09.001
- Pereira, et al. (2018). Simulation of the flow around a circular cylinder at re= 3900 with partially-averaged navier-stokes equations. *International Journal of Heat and Fluid Flow*, 69, 234–246.
- Pope, S. B. (2000). *Turbulent flows*. Cambridge University Press. doi: 10.1017/CBO9780511840531
- Prafull, H., et al. (2022). Analysis of flow characteristics of two circular cylinders in cross-flow with varying reynolds number: a review.. doi: .org/10.1007/s10973-021-10933-w
- Queutey, P., et al. (2022). Laboratoire lhea -umr 6598..
- Rajani, et al. (2009). Numerical simulation of laminar flow past a circular cylinder. *Applied*

- Mathematical Modelling*, 33(3), 1228–1247.
- Rajani, et al. (2012). On the reliability of eddy viscosity based turbulence models in predicting turbulent flow past a circular cylinder using urans approach..
- Rodriguez, I., et al. (2017, oct). LES-based study of the roughness effects on the wake of a circular cylinder from subcritical to transcritical reynolds numbers. *Flow, Turbulence and Combustion*, 99(3-4), 729–763. doi: 10.1007/s10494-017-9866-2
- Roshko, A. (1954). *On the drag and shedding frequency of two-dimensional bluff bodies* (Tech. Rep.).
- Roshko, A. (1955). On the wake and drag of bluff bodies. *Journal of the aeronautical sciences*, 22(2), 124–132.
- Roshko, A. (1961). Experiments on the flow past a circular cylinder at very high reynolds number..
- Rumsey, C., et al. (2023). *Turbulence modeling resource*. Retrieved from <https://turbmodels.larc.nasa.gov/sst.html>
- Shigehiro, S., et al. (1993). Numerical study on flow past 2d square cylinder by large eddy simulation: Comparison between 2d and 3d computations. *Journal of Wind Engineering and Industrial Aerodynamics*, 50, 61-68. Retrieved from <https://www.sciencedirect.com/science/article/pii/016761059390061R> doi: [https://doi.org/10.1016/0167-6105\(93\)90061-R](https://doi.org/10.1016/0167-6105(93)90061-R)
- Singh, et al. (2005). Flow past a cylinder: shear layer instability and drag crisis. *International journal for numerical methods in fluids*, 47(1), 75–98.
- Spivack, H. M., et al. (1946). Vortex frequency and flow pattern in the wake of two parallel cylinders at varied spacing normal to an air stream. *Journal of the Aeronautical Sciences*, 13(6), 289–301.
- Stringer, et al. (2014, sep). Unsteady RANS computations of flow around a circular cylinder for a wide range of reynolds numbers. *Ocean Engineering*, 87, 1–9. doi: 10.1016/j.oceaneng.2014.04.017
- Sumner, et al. (2010). Two circular cylinders in cross-flow: A review. *Journal of fluids and structures*, 26(6), 849–899.
- Tamura, T., et al. (1990). On the reliability of two-dimensional simulation for unsteady flows around a cylinder-type structure. *Journal of Wind Engineering and Industrial Aerodynamics*, 35, 275–298.
- TB, G., et al. (2000). Nonlinear eddy viscosity and algebraic stress models for solving complex turbulent flows. *Progress in Aerospace Sciences*, 36(8), 655–682.
- Thiago, G., et al. (2022). Hydrodynamic characteristics of two side-by-side cylinders at a pitch ratio of 2 at low subcritical reynolds numbers.. doi: [.org/10.3390/fluids7090287](https://doi.org/10.3390/fluids7090287)

- Toni, K., et al. (2018, September). Cfd analysis of stepped planing vessels..
- Travin, A., et al. (2000). Detached-eddy simulations past a circular cylinder. *Flow turbulence and combustion*, 63(1-4), 293–313.
- Tritton, D. J. (1959). Experiments on the flow past a circular cylinder at low reynolds numbers. *Journal of Fluid Mechanics*, 6(4), 547–567. doi: 10.1017/S0022112059000829
- Tutar, M., et al. (2001). Computational modelling of flow around a circular cylinder in sub-critical flow regime with various turbulence models. *International journal for numerical methods in fluids*, 35(7), 763–784.
- Vaz, G., et al. (2007). Viscous flow computations on a smooth cylinders: a detailed numerical study with validation. In *International conference on offshore mechanics and arctic engineering* (Vol. 4269, pp. 849–860).
- Versteeg, & Malalasekera, W. (1995). Computational fluid dynamics. *The finite volume method*, 1–26.
- Wackers, J., Deng, G., Raymond, C., Guilmineau, E., Leroyer, A., Queutey, P., & Visonneau, M. (2022). Adaptive grid refinement for ship resistance computations. *Ocean Engineering*, 250, 110969. Retrieved from <https://www.sciencedirect.com/science/article/pii/S0029801822003973> doi: <https://doi.org/10.1016/j.oceaneng.2022.110969>
- Wang, Z., et al. (2005). Vortex interactions in a two side-by-side cylinder near-wake. *International journal of heat and fluid flow*, 26(3), 362–377.
- Weinmann, et al. (2014, dec). Tandem cylinder flow and noise predictions using a hybrid RANS/LES approach. *International Journal of Heat and Fluid Flow*, 50, 263–278. doi: 10.1016/j.ijheatfluidflow.2014.08.011
- West, et al. (1993). Measurements of fluctuating pressures and forces on a circular cylinder in the reynolds number range 104 to 2.5 x 10<sup>5</sup>. *Journal of Fluids and Structures (1993)* 7, 227-244.
- Wilcox, D., et al. (2006). *Turbulence modeling for cfd* (No. vol. 1). DCW Industries. Retrieved from <https://books.google.fr/books?id=tFNNPgAACAAJ>
- Wilcox, D. C. (1988). Re-assessment of the scale-determining equation for advanced turbulence models. *AIAA journal*, 26(11), 1299–1310.
- Wilcox, D. C. (2006). *Turbulence modelling for cfd*. Birmingham Press, Inc., San Diego, California.
- Xu, G., et al. (2004). Strouhal numbers in the wake of two inline cylinders. *Experiments in Fluids*, 37, 248–256.
- Ye, H., et al. (2017). Benchmark computations for flows around a stationary cylinder with high reynolds numbers by rans-overset grid approach. *Applied Ocean Research*, 65, 315–326.



- Zdravkovich. (1984). Classification of flow-induced oscillations of two parallel circular cylinders in various arrangements. In *Asme proc. symp. flow-induced vibration* (Vol. 2, p. 1).
- Zdravkovich. (1987). The effects of interference between circular cylinders in cross flow. *Journal of fluids and structures*, 1(2), 239–261.
- Zdravkovich. (1990). Conceptual overview of laminar and turbulent flows past smooth and rough circular cylinders. In *Journal of wind engineering and industrial aerodynamics*, 33 (1990) 53-62.
- Zhou, Y., et al. (2006). Flow structure, momentum and heat transport in a two-tandem-cylinder wake. *Journal of Fluid Mechanics*, 548, 17–48.

# 1 APPENDICES

## 1.1 Reynolds Stress Models (RSM)

The utilization of Reynolds stress closures in the context of Reynolds-Averaged Navier-Stokes (RANS) equations is appealing due to their ability to obviate the requirement for an eddy viscosity. However, it should be noted that the resultant equations derived from such closures are significantly more intricate when compared to those arising from two-equation closures. In general, Reynolds stress models exhibit a higher level of superiority compared to two-equation closures. The incorporation of streamline curvature and rotation effects is achieved by directly utilizing the term  $\frac{D\rho\langle u_i u_j \rangle}{Dt}$ . The relevant information may be obtained from [Charles et al. \(1991\)](#), [Pope \(2000\)](#), and [D. Wilcox et al. \(2006\)](#). The equation governing the transfer of Reynolds stress in the  $R_{ij} - \omega$  model, specifically for the cross-correlation component  $\langle u_i u_j \rangle$ , may be expressed as follows:

$$\frac{\partial}{\partial t} (\rho \langle u_i u_j \rangle) + \frac{\partial}{\partial x_k} (\rho U_k \langle u_i u_j \rangle) = P_{ij} + \Phi_{ij} - \epsilon_{ij} + \frac{\partial}{\partial x_k} \left( C_{ijk} + \mu \frac{\partial}{\partial x} \langle u_i u_j \rangle \right) \quad (40)$$

For more information, please refer to the documentation provided by [FineMarine \(2023\)](#).

## 1.2 Explicit Algebraic Stress Model (EASM)

The quadratic Explicit Algebraic Stress Model (EASM  $\kappa - \omega$ ) considers the fluctuation of the production-to-dissipation rate ratio. The robustness of a newly implemented ASM model that utilizes the explicit solution for turbulent eddy viscosity has been observed. The validation of ship flows has been conducted at both model and full scale for several models. The RSM model has superior predictive capabilities in regions characterized by convex curvature, although limited enhancements are detected in the vicinity of concave surfaces. The Reynolds stress transport equation is as follows:

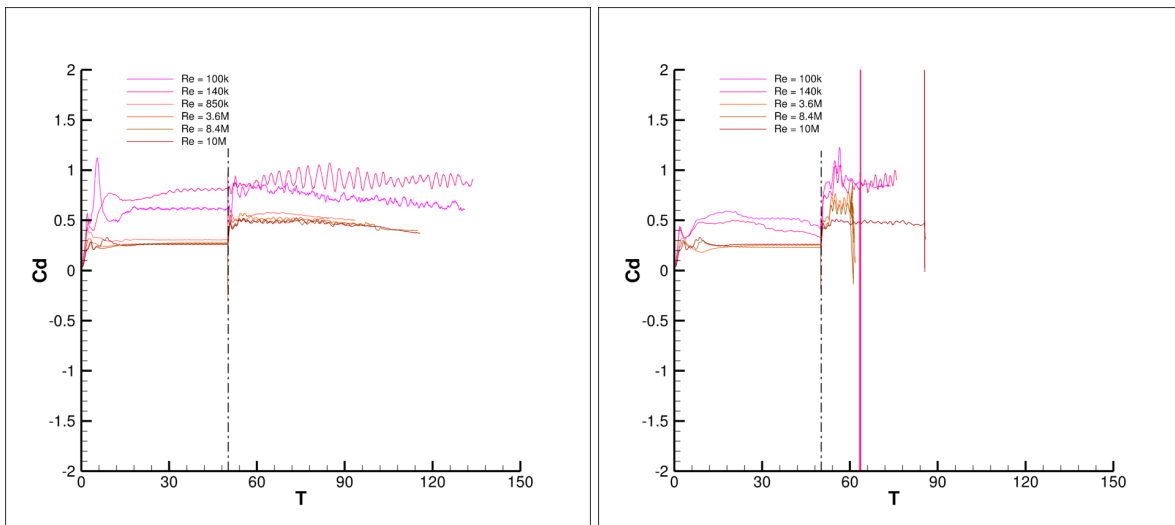
$$\frac{D\tau_{ij}}{\partial Dt} = P_{ij} + \phi_{ij} - \epsilon_{ij} + D_{ij} \quad (41)$$

Where  $\tau_{ij} = \langle u_i u_j \rangle$  is the Reynolds stress tensor,  $P_{ij}$  is the production terms given by:

$$P_{ij} = - \left( \tau_{jk} \frac{\partial U_i}{\partial x_k} + \tau_{ik} \frac{\partial U_j}{\partial x_k} \right) = -2k (b_{ik} S_{kj} + S_{ik} b_{kj}) + 2k \left( b_{ik} W_{kj} - W_{ik} b_{kj} - \frac{4}{3} k S_{ij} \right) \quad (42)$$

[TB et al. \(2000\)](#) and [Gatski et al. \(2002\)](#) provide mathematical background and details on the EASM model. For more information, please refer to the documentation provided by [FineMarine](#)

(2023).



(a) Evolution of avg. coefficient of drag, Cd: EASM (b) Evolution of avg. coefficient of drag, Cd: RSM

Figure 72: Evolution of avg. coefficient of drag, Cd for single cylinder from sub-critical to postcritical flow regime: EASM and RSM

The simulation has been conducted using the EASM and RSM turbulence models in a range spanning from sub-critical to postcritical regime. However, the investigation was not conducted using these turbulence models due to the presence of large fluctuations in the hydrodynamic coefficients and frequent simulation failures. The faults were eventually identified. It is advisable to commence the EASM and RSM turbulence model by utilizing the  $k-\omega$  Shear Stress Transport (SST) model as a starting point. However, in this study, the simulation was conducted from the beginning, resulting in a nearly twofold increase in cell formation compared to the  $k-\omega$  SST model. Additionally, there was a higher level of fluctuations observed in the values of Cd and Cl (see Figure 72). The activation of the AGR is indicated by the presence of a vertical line.

### 1.2.1 DDES

The Delayed Detached Eddy Simulation (DDES) technique is a computational methodology that is derived from the Detached Eddy Simulation (DES) approach. The DES function has been altered in order to mitigate the occurrence of an early transition from DES to LES mode inside

boundary layers. The governing equations of the SST DDES model can be expressed as follows:

$$\begin{aligned} \frac{\partial \rho k}{\partial t} + \nabla \cdot (\rho \bar{U} k) &= \nabla \cdot [(\mu + \sigma_k \mu_t) \nabla k] + P_k - \rho \sqrt{k^3} / l_{DDES} \\ \frac{\partial \rho \omega}{\partial t} + \nabla \cdot (\rho \bar{U} \omega) &= \nabla \cdot [(\mu + \sigma_\omega \mu_t) \nabla \omega] + 2(1 - F_1) \rho \sigma_{\omega 2} \frac{\nabla k \nabla \omega}{\omega} + \alpha \frac{\rho}{\mu_t} P_k - \beta \rho \omega^2 \quad (43) \\ \mu_t &= \rho \frac{a_1 \cdot k}{\max(a_1 \cdot \omega, F_2 \cdot S)} \end{aligned}$$

The SST blending functions are denoted as  $F_1$  and  $F_2$ , and they may be expressed as follows:

$$\begin{aligned} F_1 &= \tanh(\arg_1^4) \\ \arg_1 &= \min \left( \max \left( \frac{\sqrt{k}}{C_\mu \omega d_\omega}, \frac{500\nu}{d_\omega^2 \omega} \right), \frac{4\rho \sigma_{\omega 2} k}{CD_{k\omega} d_\omega^2} \right) \\ CD_{k\omega} &= \max \left( 2\rho \sigma_{\omega 2} \frac{\nabla k \nabla \omega}{\omega}, 10^{-10} \right) \\ F_2 &= \tanh(\arg_2^2) \\ \arg_2 &= \max \left( \frac{2\sqrt{k}}{C_\mu \omega d_\omega}, \frac{500\nu}{d_\omega^2 \omega} \right) \quad (44) \end{aligned}$$

In this context,  $d_\omega$  represents the distance to the closest wall. The production term in equation 43 is expressed as follows:

$$P_k = \min(\mu_t S^2, 10 \cdot C_\mu \rho k \omega) \quad (45)$$

The length scale denoted as DDES in equation 43 is expressed as follows:

$$\begin{aligned} l_{DDES} &= l_{RANSE} - f_d \max(0, l_{RANSE} - l_{LES}) \\ l_{LES} &= C_{DES} h_{max} \\ l_{RANSE} &= \frac{\sqrt{k}}{C_\mu \omega} \quad (46) \end{aligned}$$

$$C_{DES} = C_{DES1} \cdot F_1 + C_{DES2} \cdot (1 - F_1)$$

The symbol  $h_{max}$  represents the maximum edge length of the cell. The computation of the empiric blending function  $f_d$  in equation 46 involves the utilization of the following relations:

$$f_d = 1 - \tanh \left[ (C_{d1} r_d)^{C_{d2}} \right]$$

$$r_d = \frac{\nu_t + \nu}{\kappa^2 d_\omega^2 \sqrt{0.5 \cdot (S^2 + \Omega^2)}} \quad (47)$$

In this context,  $S$  represents the magnitude of the strain rate tensor, whereas  $\Omega$  denotes the magnitude of the vorticity tensor. The model constants are presented as follows:

$$C_\mu = 0.09, \kappa = 0.41, a_1 = 0.31$$

$$C_{DES1} = 0.78, C_{DES2} = 0.61, C_{d1} = 20, C_{d2} = 3 \quad (48)$$

The computation of constants with an index of 3 involves a blend of the equivalent constants from the  $k-\epsilon$  and  $k-\omega$  models.

$$\alpha = \alpha_1 F_1 + \alpha_2 (1 - F_1)$$

$$\alpha_1 = \frac{5}{9}, \beta_1 = 0.075, \sigma_{k1} = 0.85, \sigma_{\omega1} = 0.5$$

$$\alpha_2 = 0.44, \beta_2 = 0.0828, \sigma_{k2} = 1, \sigma_{\omega2} = 0.856 \quad (49)$$

### 1.3 Appendix : Data Compilation: Single Cylinder

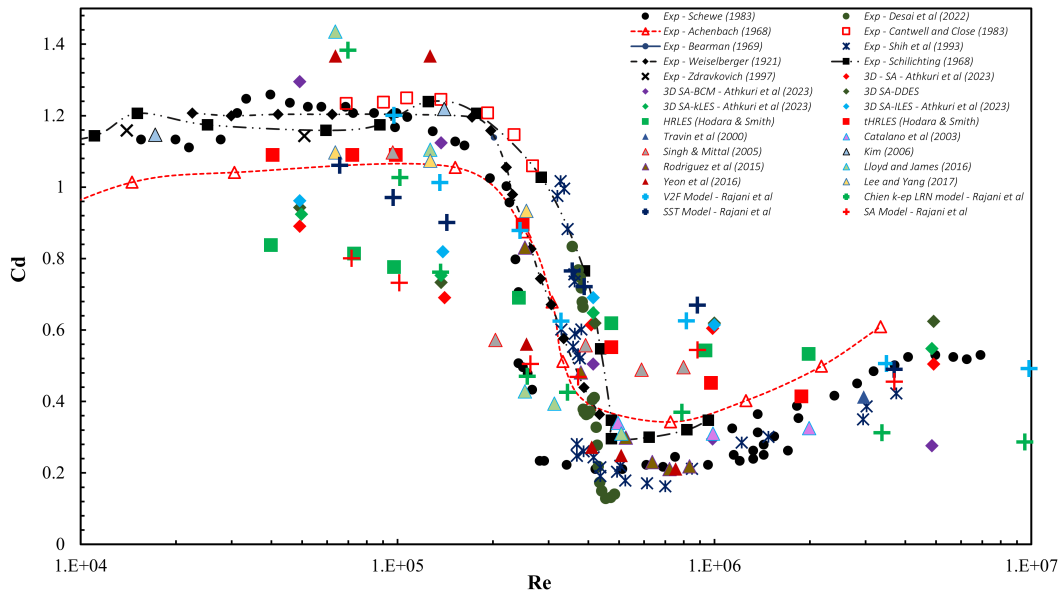


Figure 73: Avg. coefficient of drag,  $C_d$ : Ranging from  $10^4$  to  $10^7$ : Experiment & Simulation Data extracted from literature with the help of [WebplotDigitizer](#)

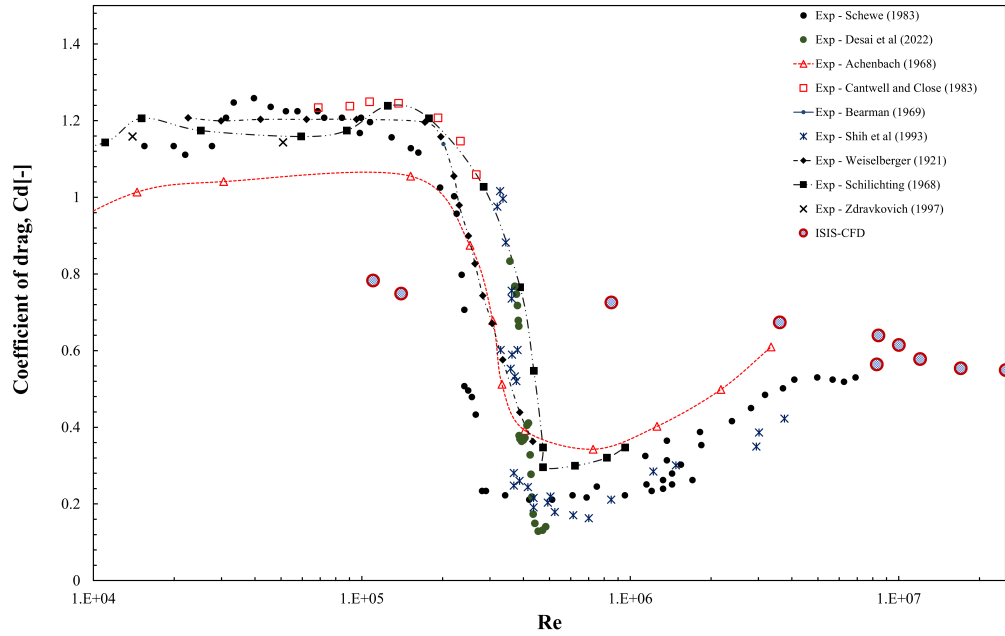


Figure 74: Avg. coefficient of drag,  $C_d$ : Ranging from  $10^4$  to  $10^7$ : Experiment vs ISIS-CFD

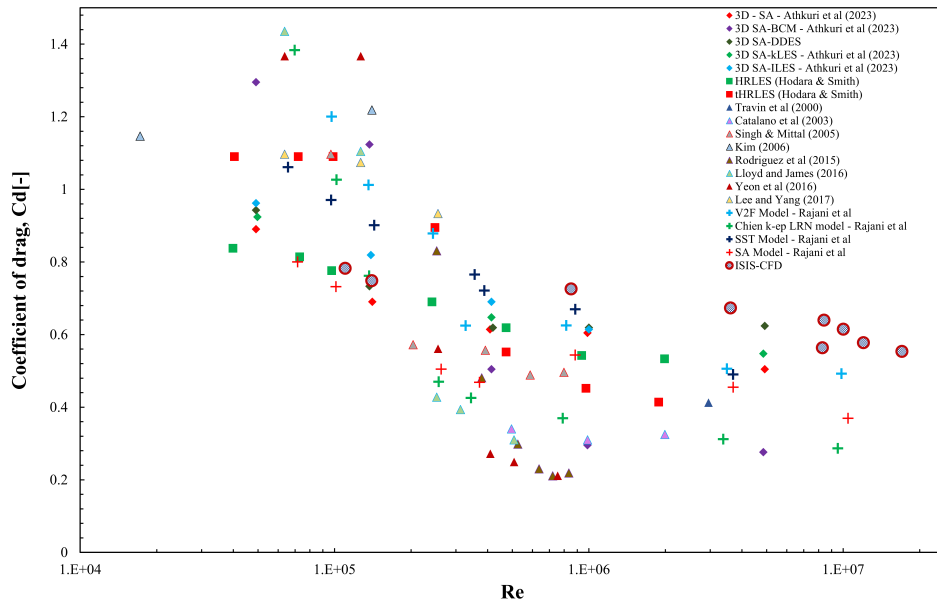


Figure 75: Avg. coefficient of drag,  $C_d$ : Ranging from  $10^4$  to  $10^7$ : Simulation vs ISIS-CFD

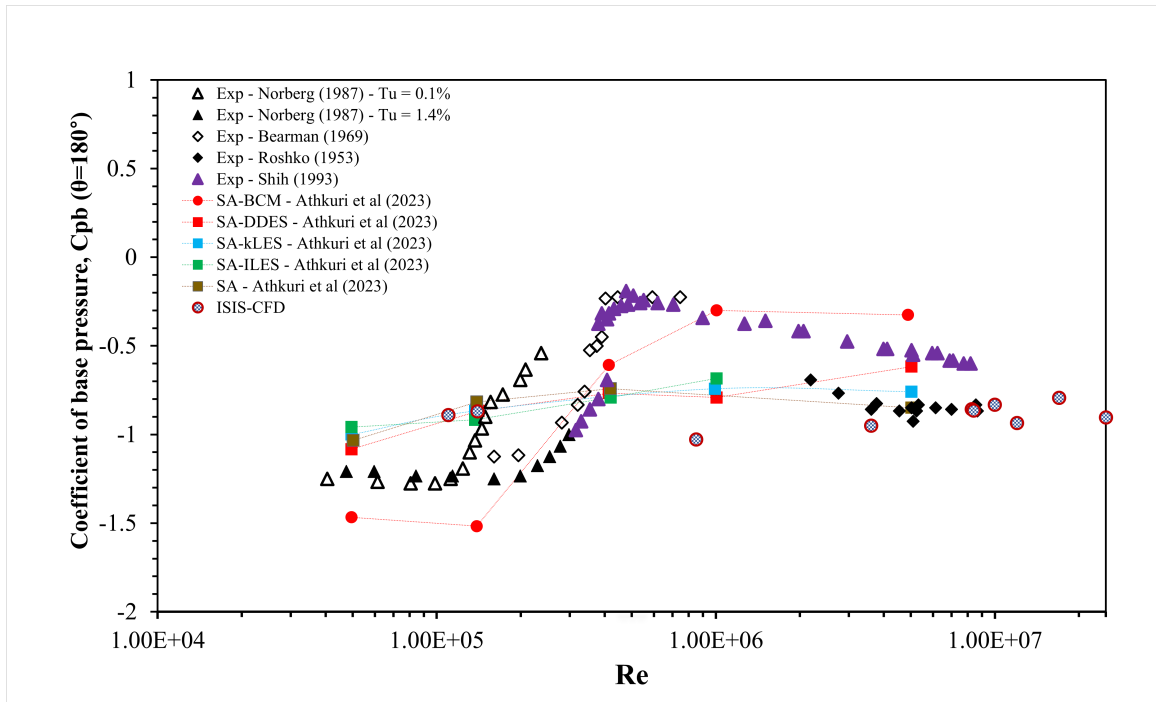


Figure 76: Avg. coefficient of base pressure,  $C_{pb}$ : Ranging from  $10^4$  to  $10^7$ : Experiment, Simulation vs ISIS-CFD

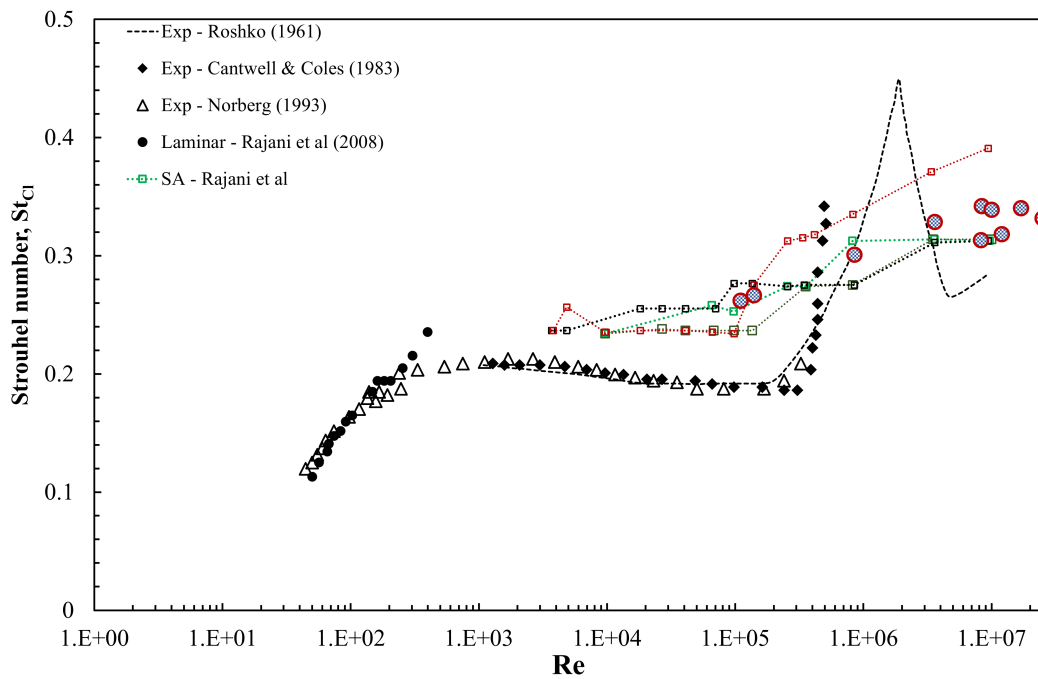


Figure 77: Strouhal number,  $St$ : Ranging from  $10^4$  to  $10^7$

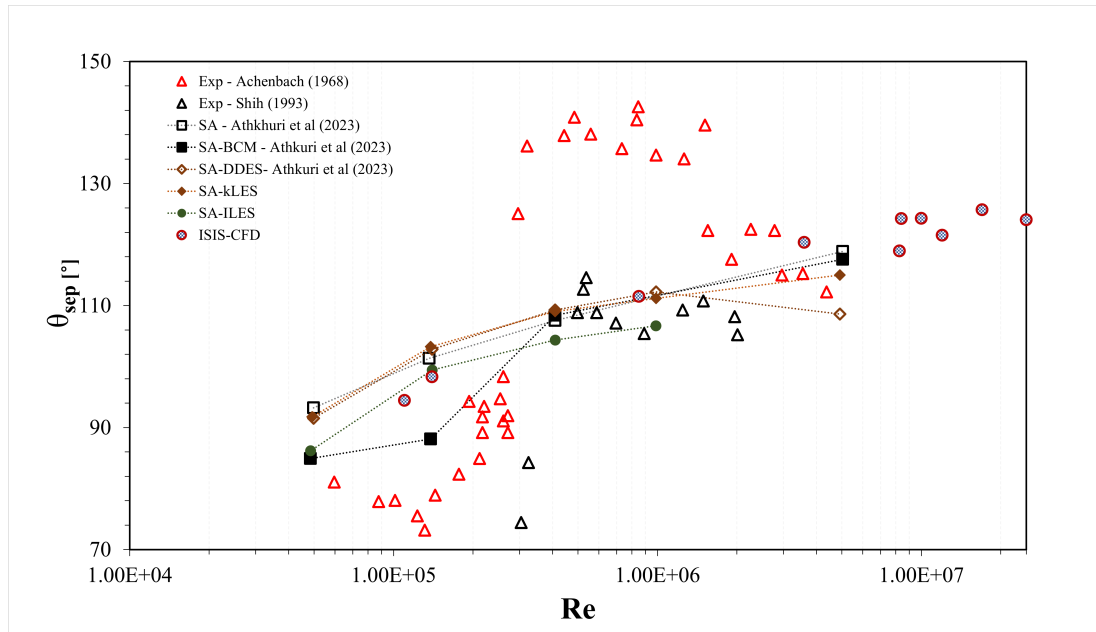


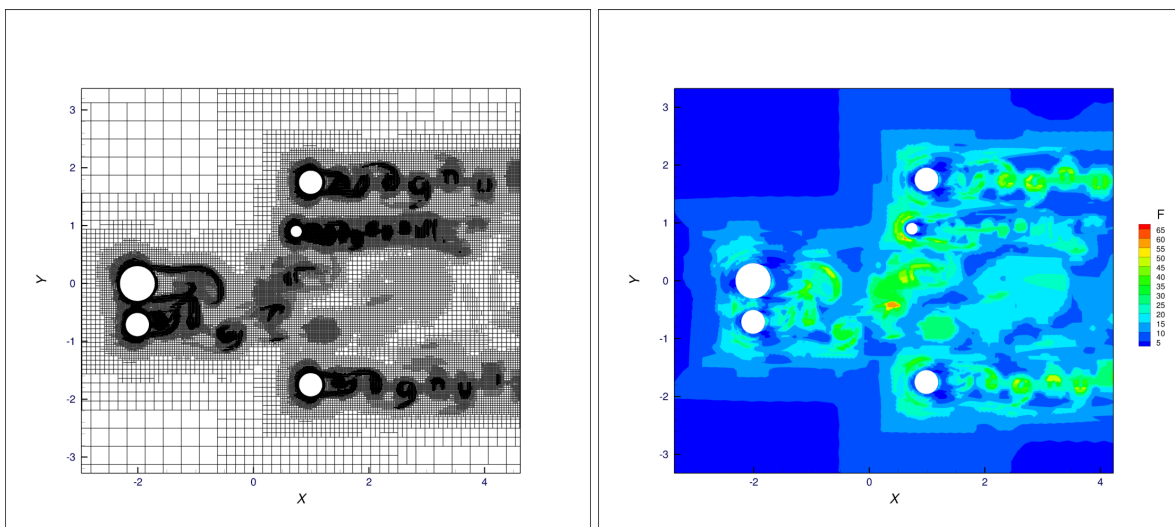
Figure 78: Theta separation,  $\theta_{sep}$ : Ranging from  $10^4$  to  $10^7$  : Experiment, Simulation vs ISIS-CFD



## 1.4 Appendix : 2D URANS $k-\omega$ SST - Six Orientations

### 1.4.1 Orientation: $0^\circ$

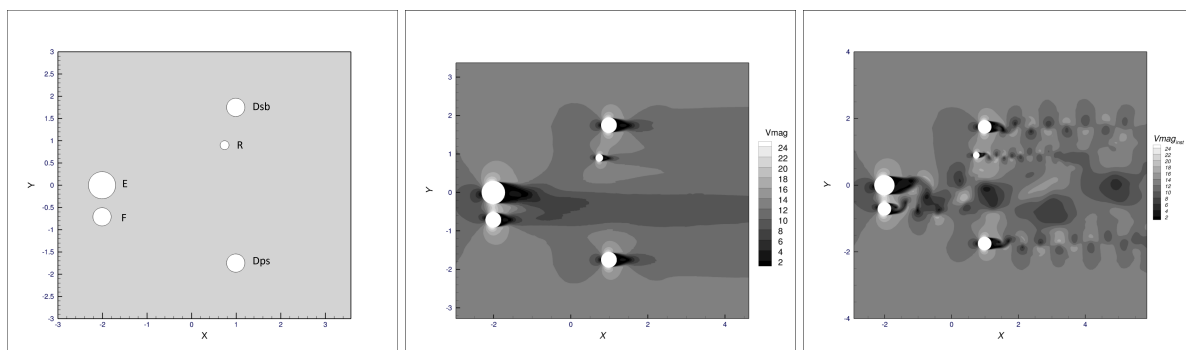
Remarks
<ul style="list-style-type: none"> <li>- Avg. coefficient of drag, <math>C_d</math>, Coefficient of lift <math>C_l</math>, RMS of drag coefficient, <math>Cd_{RMS}</math>, RMS of lift coefficient, <math>Cl_{RMS}</math>, Base pressure coefficient, <math>C_{pb}</math> (<math>\theta = 180^\circ</math>), Flow separation, <math>\theta_{sep}</math>, Vortex length of 2D TMS and single cylinder are shown in Table 31.</li> <li>- The incident angle, <math>\alpha</math>, Pitch distance, P/D are shown in Table 32.</li> </ul>



(a) Mesh : Zoomed view

(b) Contour of function F

Figure 79: Post-processing results,  $\Delta t^* = 0.0025$  New mesh : 2D  $0^\circ$  orientation



(a) TMS:  $0^\circ$

(b) Velocity contour: Average velocity

(c) Velocity contour: Instantaneous velocity

Figure 80: Velocity contour : Orientation  $0^\circ$

### Cylinder E-F

- The interaction between cylinders E and F appears to be biased which suggests that the distance at  $P/D = 1.164$  is in the intermediate range. In this instance, the E-F cylinder arrangement is side-by-side in nature, with incidence angle,  $\alpha = 0$ .
- The two cylinders are clearly shown to be trying to bias each other's flow from the instantaneous velocity contour in Figure 80, however, cylinder E is evidently dominating due to its larger diameter and higher Re number.
- By examining the drag coefficient  $C_d$  and the  $St_{Cl}$  numbers (see Table 27), the statement about biased flow may once more be confirmed. Because the flow biases towards cylinder F, it exhibits larger  $C_d$  and  $St_{Cl}$  values than cylinder E.
- For cylinder E, the base pressure coefficient,  $C_{pb}$ , which is measured at  $180^\circ$  has been raised. For **single cylinder (SC)** simulation with the same Re number exhibits a dip at that location. For cylinder E, however, the dip has disappeared and a concave upward form may be seen in its place (see Figure 81). The cylinder F's base pressure coefficient has been reduced. Additionally, the little shift in the  $C_p$  plot for both cylinders that occurred in the horizontal direction is a sign of proximity interference. In addition, the changes in suction peaks can well be visualized for cylinder F, which gets lowered than the SC. Figure 82 shows the overall distribution of the coefficient of pressure,  $C_p$ .
- The  $C_{d_{RMS}}$  and  $C_{l_{RMS}}$  values, respectively, can be used to observe the unsteadiness of the drag and lift coefficients. Lower values of these variables are desirable in many engineering applications. These values are less impacted for E-F cylinders by the present orientation when compared to SC. Table 31 shows it clearly.
- Tangential wall shear stress can be used to detect flow separation. When compared to the corresponding SC, the advancement of flow separation for E-F cylinders is observed.
- Changes in vortex length may also be seen for E-F cylinders, those are a sign of changes in flow characteristics. For the identical Re values, both of the cylinders display longer vortices than the SC (see Figure 83 & 84). One notable finding is the high sensitivity of the  $Re = 17M$  to the variations in flow parameters. Therefore, for cylinder F, which is operating in an identical Re, a higher rise in vortex length is observed. Furthermore, the vortices of both cylinders have lost their symmetry and have slanted towards the opposite cylinder.

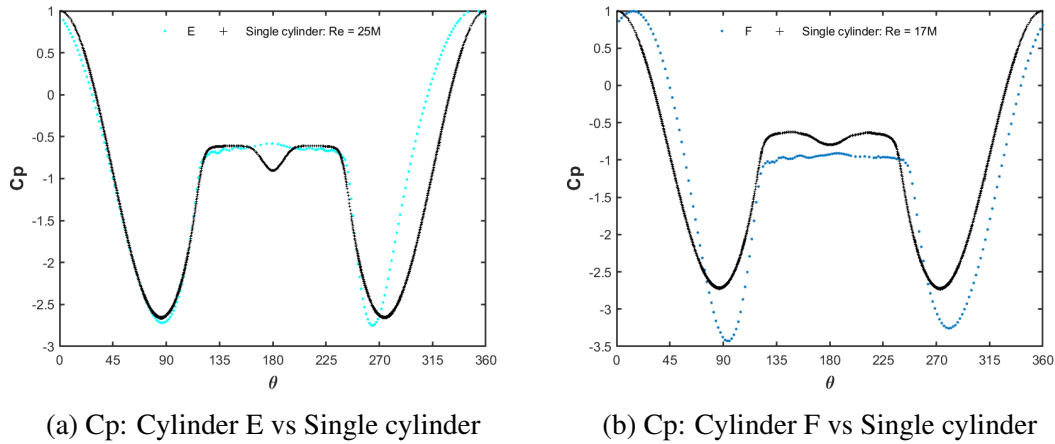


Figure 81: Avg. coefficient of pressure,  $C_p$  : Orientation  $0^\circ$

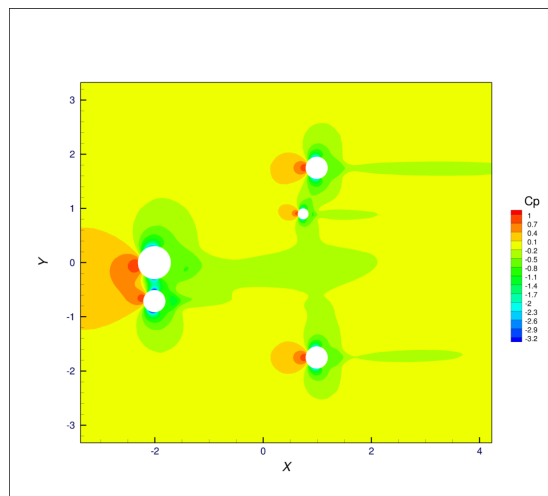


Figure 82: Contour of avg. coefficient of pressure,  $C_p$  : Orientation  $0^\circ$

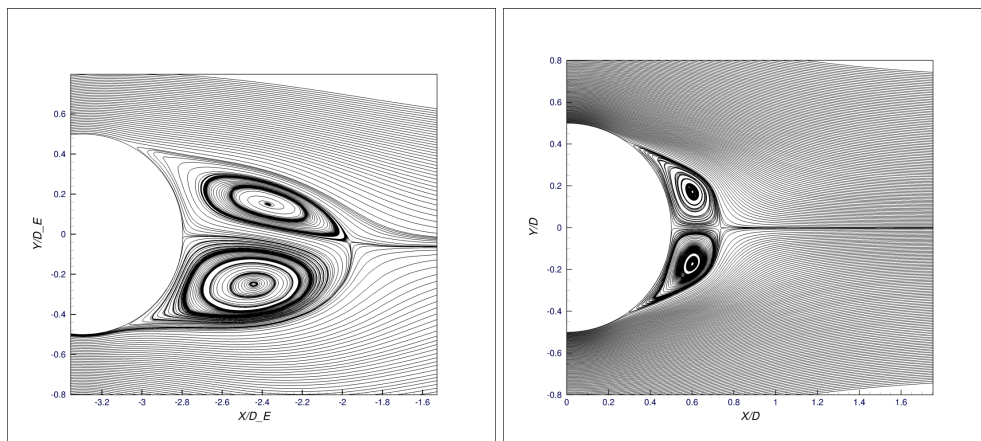


Figure 83: Vortex length : Cylinder E vs Single cylinder : Orientation  $0^\circ$

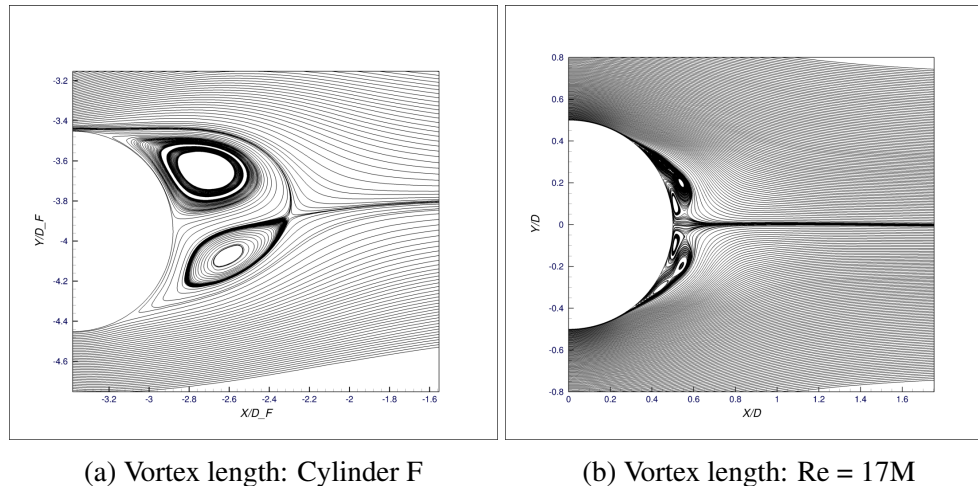


Figure 84: Vortex length : Cylinder F vs Single cylinder : Orientation  $0^\circ$

### Cylinder Dsb-R

-Due to the huge incidence angle  $\alpha = -74^\circ$  and pitch distance,  $P/D = 2.16$ , there is a little interaction between these two cylinders and that is essentially a proximity interference.

-Considering cylinder R stands in front of cylinder Dsb, the influence of Dsb on the incoming flow parameters of cylinder R will be minimal.

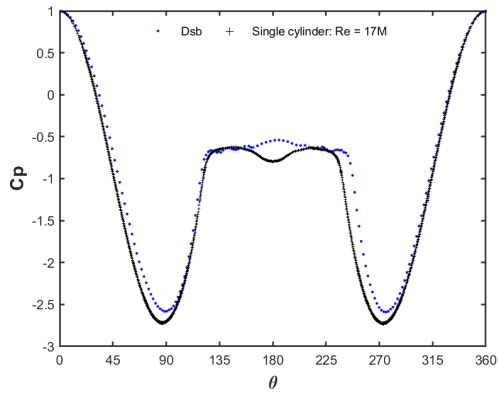
-There is synchronized vortex shedding (SVS): In phase state (see Figure 80c). Both of the cylinders exhibit unique  $St_{Cl}$  due to the larger incidence angle and pitch distance, with the exception that Dsb exhibits a tiny peak before to the dominant one.

-Because of their (Dsb-R) reciprocal interaction, which is anticipated physically, the cylinders' lift coefficients,  $C_l$  have the opposite sign. Additionally, both cylinders' unsteadiness has lessened, which can be seen by looking at  $Cl_{RMS}$  readings. Again, the values of  $C_d$  and  $Cd_{RMS}$  decreased for both cylinders.

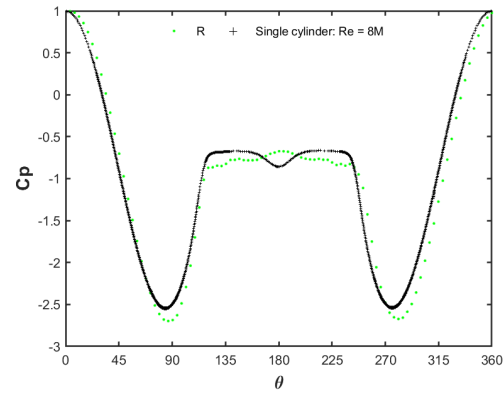
-When compared to the SC, the vortex length for both cylinders shows increases in length, however symmetry in shape is sustained.

-As previously indicated about the minimal interaction, the  $C_p$  plot for both cylinders shows a slight change when compared to an SC. The base pressure coefficient,  $C_{pb}$ , shows a major change at  $180^\circ$  when the dips for both cylinders have changed into concave upward. By looking at the suction peaks and the overall shape of  $C_p$  plots (see Figure 85), an inverse relationship between these two cylinders can be seen.

-Flow separation advanced for cylinder Dsb while it is delayed for cylinder R

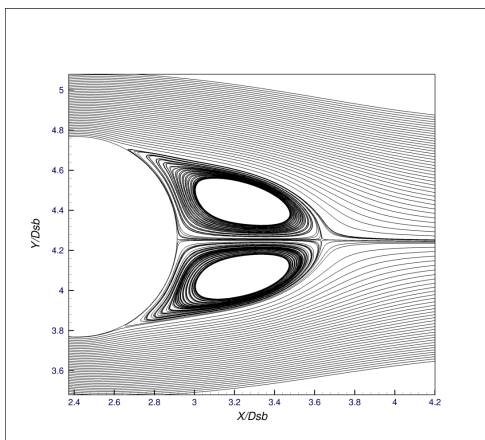


(a) Cp: Cylinder Dsb vs Single cylinder

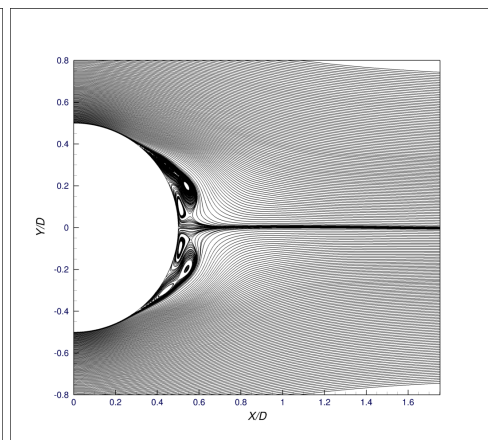


(b) Cp: Cylinder R vs Single cylinder

Figure 85: Avg. coefficient of pressure,  $C_p$  : Orientation  $0^\circ$

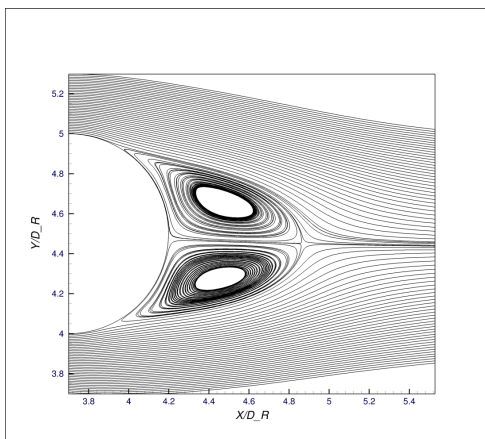


(a) Vortex length: Cylinder Dsb

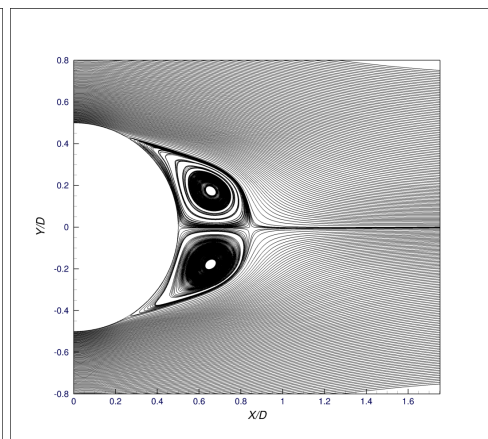


(b) Vortex length:  $Re = 17M$

Figure 86: Vortex length : Cylinder Dsb vs Single cylinder : Orientation  $0^\circ$



(a) Vortex length: Cylinder R



(b) Vortex length:  $Re = 8M$

Figure 87: Vortex length : Cylinder R vs Single cylinder : Orientation  $0^\circ$

## Cylinder Dps

Cylinder Dps is impacted mildly, which altered the shape of the  $C_p$  plot (see Figure 88). The  $180^\circ$  dip transforms into concave upward, which increases the base pressure coefficient,  $C_{pb}$ . The suction points have also been shifted upward. Overall, the symmetry of the flow seems to be maintained. The dominant  $St_{Cl}$  number of the cylinder R is nearly identical to the SC. Also, the changes in the  $C_{pb}$  value influenced the  $C_d$  value, resulting in a lower  $C_d$  value than the SC. The changes in vortex length can be observed in Figure 89.

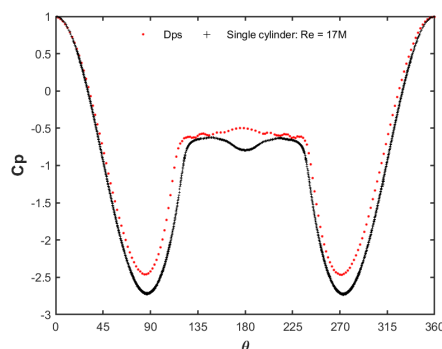
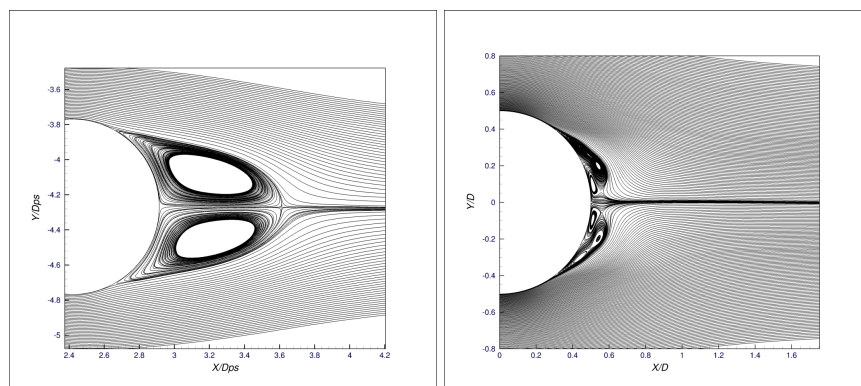


Figure 88:  $C_p$ : Cylinder Dps vs Single cylinder



(a) Vortex length: Cylinder Dps

(b) Vortex length:  $Re = 17M$

Figure 89: Vortex length : Cylinder Dps vs Single cylinder

Table 31: Hydrodynamic parameters:  $0^\circ$  orientation

Re	Cylinder	$C_d$	$C_l$	$C_{d_{RMS}}$	$C_{l_{RMS}}$	$C_{pb} (\theta = 180^\circ)$	$\theta_{sep} [^\circ]$	Vortex length
25M	E	0.5114	0.3817	0.5143	0.4292	-0.5817	121.0976	0.8937
	Single cylinder (SC)	0.5494	-0.0014	0.5508	0.5775	-0.9040	124.0340	0.2392
17M	F	0.6418	-0.3381	0.6443	0.5327	-0.9251	124.0839	0.5564
	Dps	0.4043	-0.0032	0.4044	0.1512	-0.5011	119.4824	0.7414
	Dsb	0.4061	0.0208	0.4061	0.1509	-0.5472	122.9048	0.7657
	SC	0.5541	0.0026	0.5866	0.6470	-0.7939	125.7010	0.0951
8M	R	0.5457	-0.0431	0.5473	0.1965	-0.6748	119.1107	0.6640
	SC	0.5642	0.0007	0.5653	0.5260	-0.8569	118.9370	0.3417



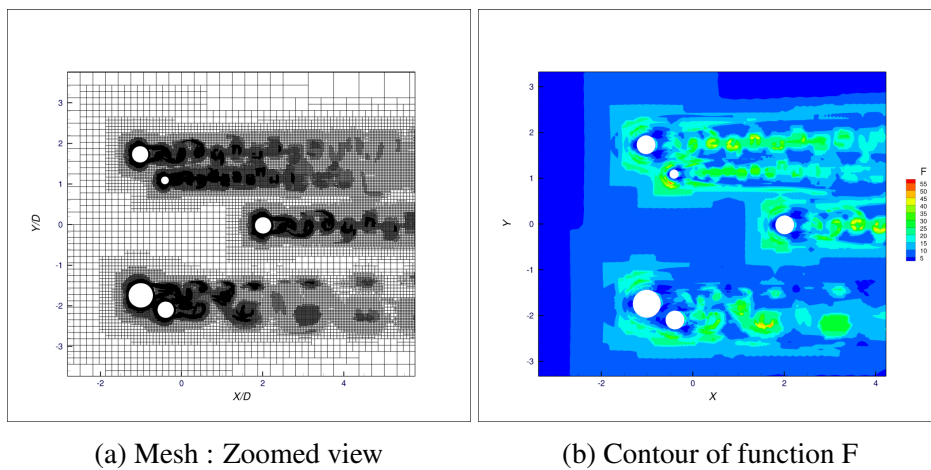
Table 32: Cylinders relative distance and incident angle :  $0^\circ$  orientation

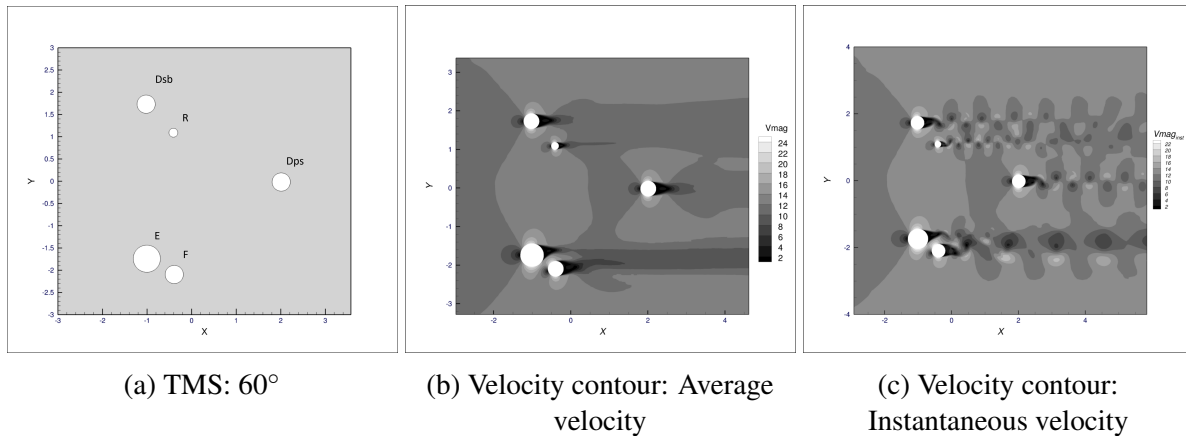
$0^\circ$	Unit	E-F	Dsb-R	F - Dps	E - R
Pitch distance, P	m	0.7100	0.8860	3.1752	2.8935
L	m		0.2500	3.0000	2.7500
T	m		0.8500	1.0400	0.9000
$\alpha$	$^\circ$		-74.0000	-19.0000	18.0000
P/D	-	1.1639	2.1610	7.7444	4.7434
L/D	-		0.6098	7.3171	4.5082
T/D	-		2.0732	2.5366	1.4754

### 1.4.2 Orientation: $60^\circ$

#### Remarks

- Avg. coefficient of drag,  $C_d$ , Coefficient of lift  $C_l$ , RMS of drag coefficient,  $Cd_{RMS}$ , RMS of lift coefficient,  $Cl_{RMS}$ , Base pressure coefficient,  $C_{pb}$  ( $\theta = 180^\circ$ ), Flow separation,  $\theta_{sep}$ , Vortex length of 2D TMS and single cylinder are shown in Table 33.
- The incident angle,  $\alpha$ , Pitch distance, P/D are shown in Table 34.

Figure 90: Post-processing results,  $\Delta t^* = 0.0025$  New mesh : 2D  $60^\circ$  orientation

Figure 91: Velocity contour : Orientation  $60^\circ$ 

### Cylinder E-F

-Both cylinders are acting as a single bluff body (SBB) showing the base bleed behavior due to the small incidence angle  $\alpha = -30^\circ$ , and the pitch ratio,  $P/D = 1.164$ . The  $C_p$  plot also shows that the base pressure coefficient,  $C_{pb}$  for both cylinders has been increased (see Figure 92).  $C_d$  indicates that the drag on both cylinders has been reduced (see Table 33).

-The significant shape variation in the  $C_p$  plot for cylinder E in the range of  $180^\circ$  to  $360^\circ$  caused by the interaction of its 3rd and 4th quadrants with cylinder F's first and second quadrants. Furthermore, Cylinder F functions as a wake stabilizer or drag reducer and is affected by the wake and proximity interference due to cylinder E. Also, cylinder F shows that a  $C_p$  plot in a combination of wake and proximity interference appears to be changed in both (vertical and horizontal) directions (see Figure 92).

-A reverse sign in the lift coefficients for both cylinders is exist. Because of the close proximity and low incident angle,  $\alpha$ , the lift of the two cylinders considerably increases.

-Whereas the  $St_{Cl}$  for cylinder E has grown more than twice that of the SC, the  $St_{Cl}$  for F has been declined. The effect can be seen from the instantaneous velocity contour (see Figure 91c). The vortex shedding is more biased to the cylinder E. Furthermore, the interaction due to close proximity can be realized by looking at the vortex shape for both cylinders (see Figure 95).



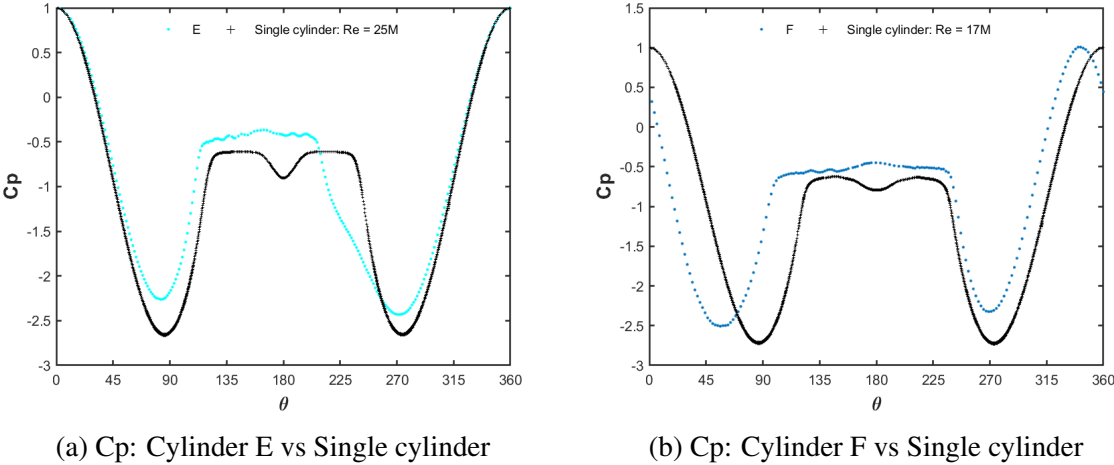


Figure 92: Avg. coefficient of pressure, Cp : Orientation 60 °

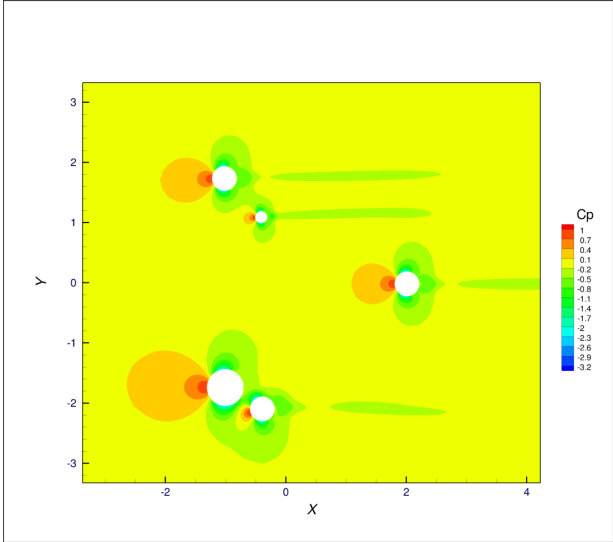
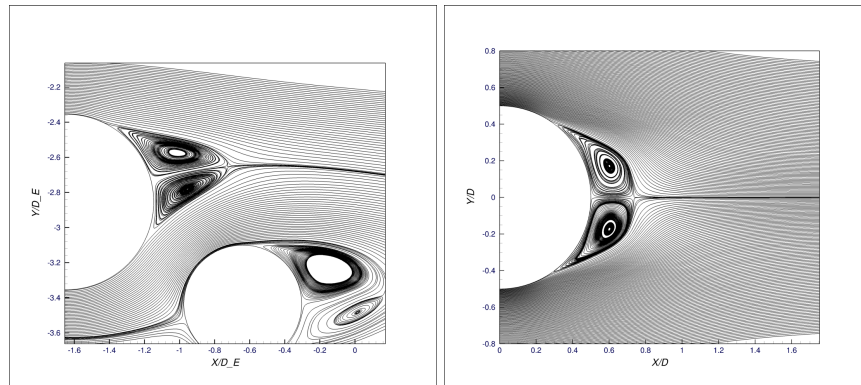


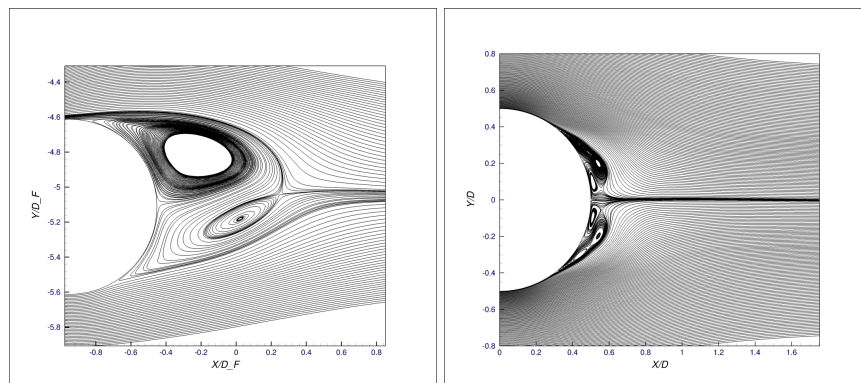
Figure 93: Contour of avg. coefficient of pressure, Cp : Orientation 60 °



(a) Vortex length: Cylinder E

(b) Vortex length: Re = 25M

Figure 94: Vortex length : Cylinder E vs Single cylinder



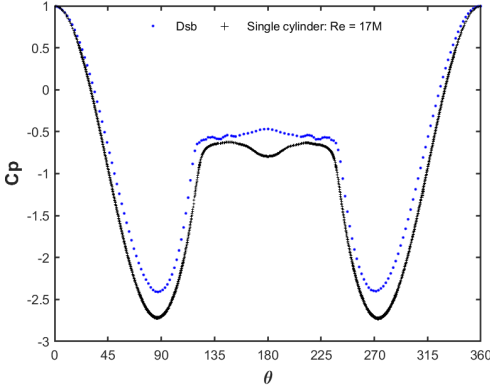
(a) Vortex length: Cylinder F

(b) Vortex length: Re = 17M

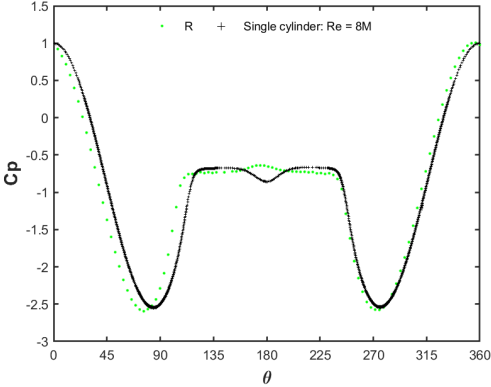
Figure 95: Vortex length : Cylinder F vs Single cylinder

### Cylinder Dsb-R

- Staggered configuration with an incident angle,  $\alpha = -46^\circ$  and pitch distance,  $P/D = 2.16$
- Synchronize vortex shedding can be seen: anti-phase (see Figure 91c)
- Minimal effect in the  $C_p$  plot can be visualized with the transformation of dip at  $180^\circ$  into a concave upward shape (see Figure 96).
- The opposite sign in  $C_l$  is also observed.
- Flow separation advanced for both cylinders (see Table 33).
- Distinct  $St_{C_l}$  can be seen for Dsb and R (see Table 27).

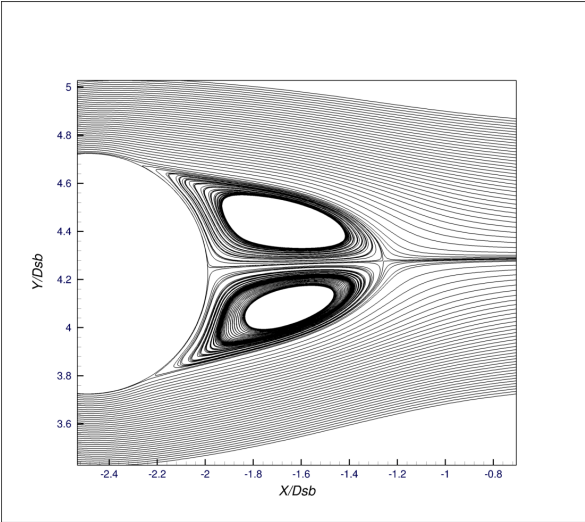


(a) Cp: Cylinder Dsb vs Single cylinder

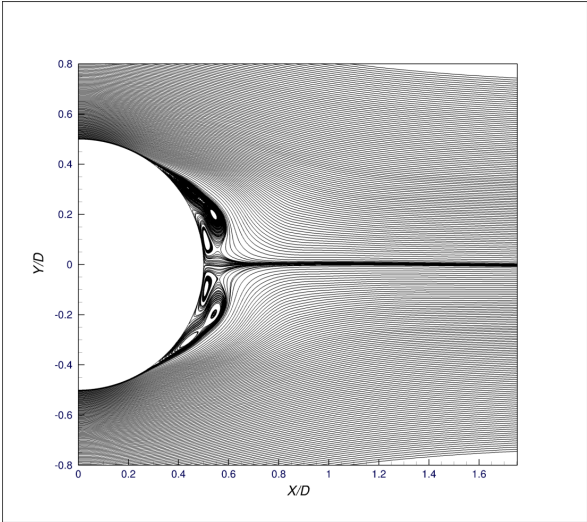


(b) Cp: Cylinder R vs Single cylinder

Figure 96: Avg. coefficient of pressure, Cp : Orientation 60 °

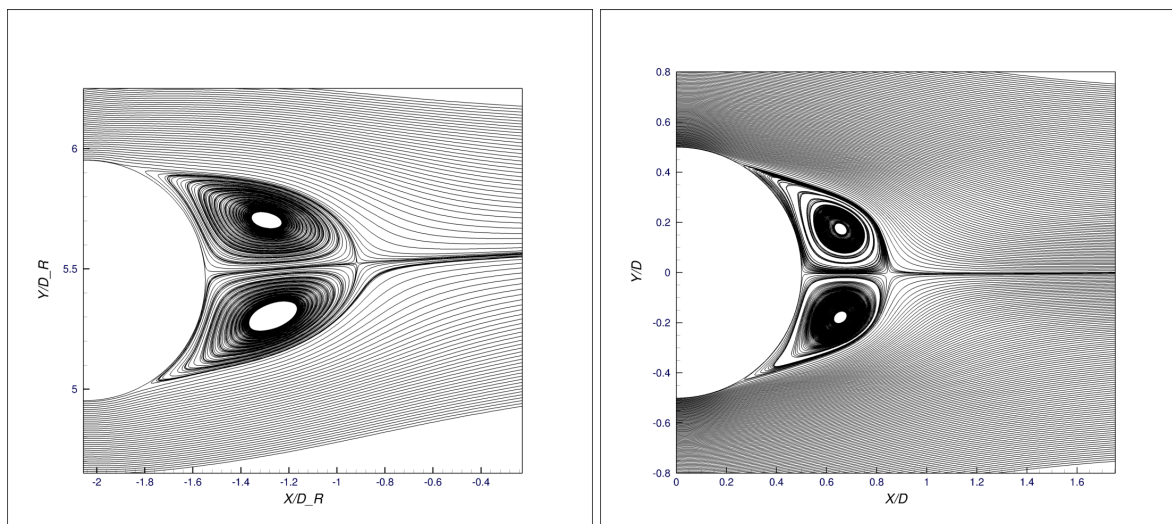


(a) Vortex length: Cylinder Dsb



(b) Vortex length: Re = 17M

Figure 97: Vortex length : Cylinder Dsb vs Single cylinder



(a) Vortex length: Cylinder R

(b) Vortex length: Re = 8M

Figure 98: Vortex length : Cylinder R vs Single cylinder

### Cylinder Dps

While the  $St_{Cl}$  for cylinder E has climbed up more, the  $St_{Cl}$  for cylinder F dropped. Even though the Dps cylinder appears to be isolated from the other 4 cylinders, the free stream has altered as a result of the upstream cylinders, and the effect is apparent. Due to wake interference, the turbulence of incoming flow was enhanced, which caused the Dps cylinder to operate as a drag reduction device explained earlier, resulting in a decrease in the cylinder's drag (see Table 33). However, the flow remained symmetrical, as evidenced by the lift coefficient's closeness to zero.

-For Dps, a distinct  $St_{Cl}$  is detected.

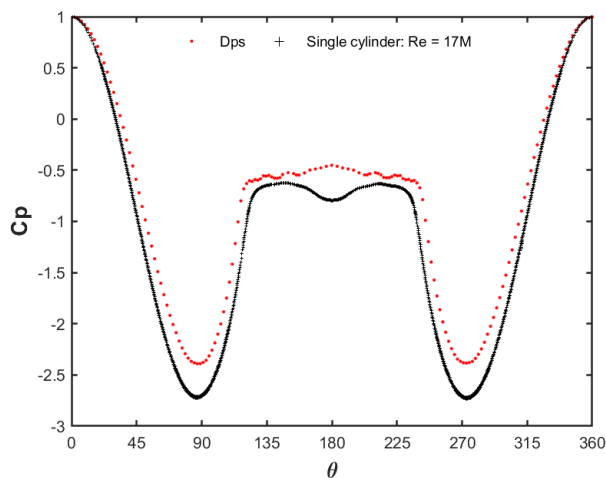
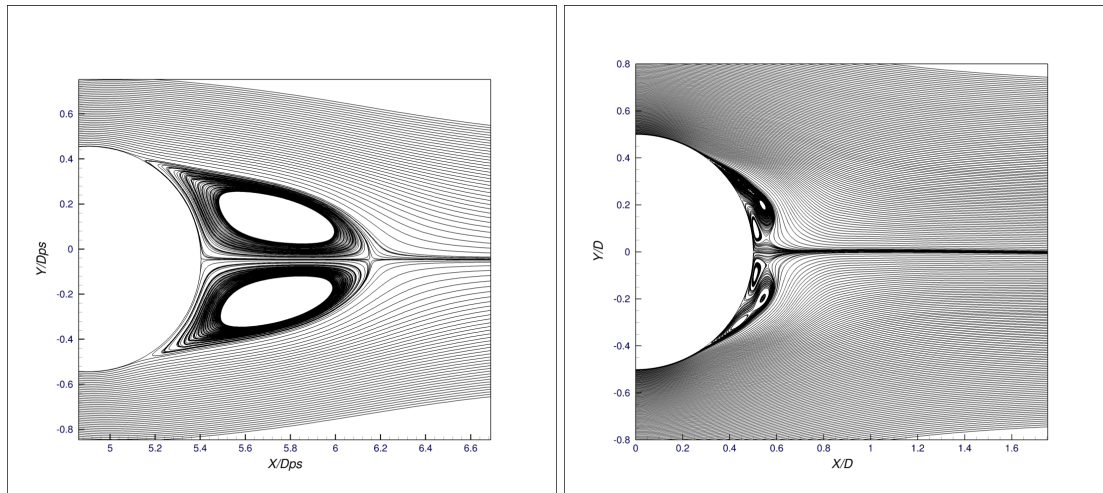


Figure 99: Cp: Cylinder Dps vs Single cylinder



(a) Vortex length: Cylinder Dps

(b) Vortex length: Re = 17M

Figure 100: Vortex length : Cylinder Dps vs Single cylinder

Table 33: Hydrodynamic parameters: 60 ° orientation

Re	Cylinder	$C_d$	$C_l$	$Cd_{RMS}$	$Cl_{RMS}$	$Cpb (\theta = 180^\circ)$	$\theta_{sep} [^\circ]$	Vortex length
25M	E	0.5199	-0.4284	0.5206	0.4309	-0.4221	117.0434	0.4288
	Single cylinder (SC)	0.5494	-0.0014	0.5508	0.5775	-0.9040	124.0340	0.2392
17M	F	-0.0912	0.2346	0.1117	0.3439	-0.4505	102.4792	0.7370
	Dps	0.3909	0.0036	0.3909	0.1104	-0.4522	120.1185	0.8006
	Dsb	0.4180	-0.0029	0.4179	0.0975	-0.4681	120.2940	0.7726
8M	SC	0.5541	0.0026	0.5866	0.6470	-0.7939	125.7010	0.0951
	R	0.4300	0.0349	0.4314	0.2866	-0.6505	108.7768	0.6402
	SC	0.5642	0.0007	0.5653	0.5260	-0.8569	118.9370	0.3417

Table 34: Cylinders relative distance and incident angle : 60 ° orientation

60 °	Unit	E-F	Dsb-R	Dps - R	E - Dps
Pitch distance P	m	0.7100	0.8860	2.6618	3.4731
L	m	0.6149	0.6111	2.4200	3.0155
T	m	0.3550	0.6415	1.1085	1.7231
$\alpha$	°	-30.0000	-46.0000	-25.0000	30.0000
P/D	-	1.1639	2.1610	6.4922	5.6936
L/D	-	1.0080	1.4905	5.9024	4.9434
T/D	-	0.5820	1.5646	2.7037	2.8248

### 1.4.3 Orientation: $90^\circ$

#### Remarks

- Avg. coefficient of drag,  $C_d$ , avg. coefficient of lift  $C_l$ , RMS of drag coefficient,  $Cd_{RMS}$ , RMS of lift coefficient,  $Cl_{RMS}$ , Base pressure coefficient,  $C_{pb}(\theta = 180^\circ)$ , Flow separation,  $\theta_{sep}$ , Vortex length of 2D TMS and single cylinder are shown in Table 35.
- The incident angle,  $\alpha$ , Pitch distance,  $P/D$  are shown in Table 36.

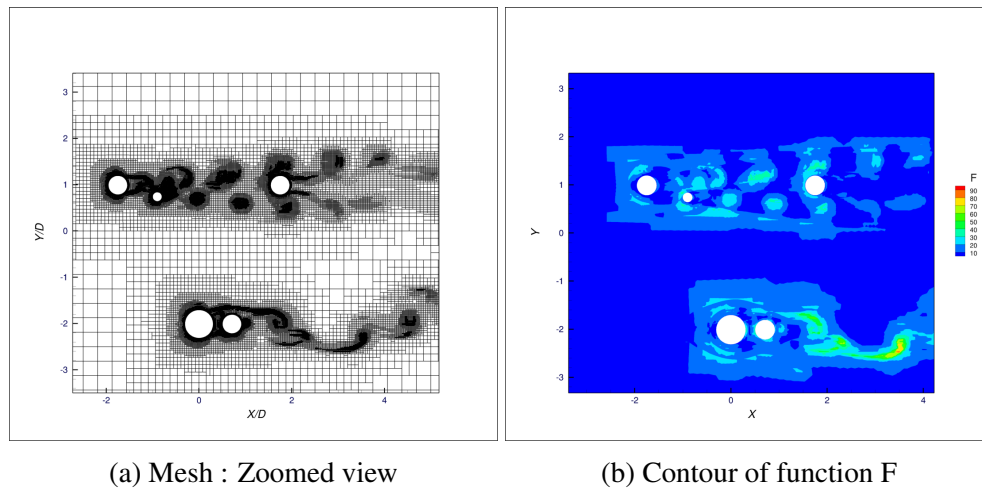


Figure 101: Post-processing results,  $\Delta t^* = 0.0025$  New mesh : 2D  $90^\circ$  orientation

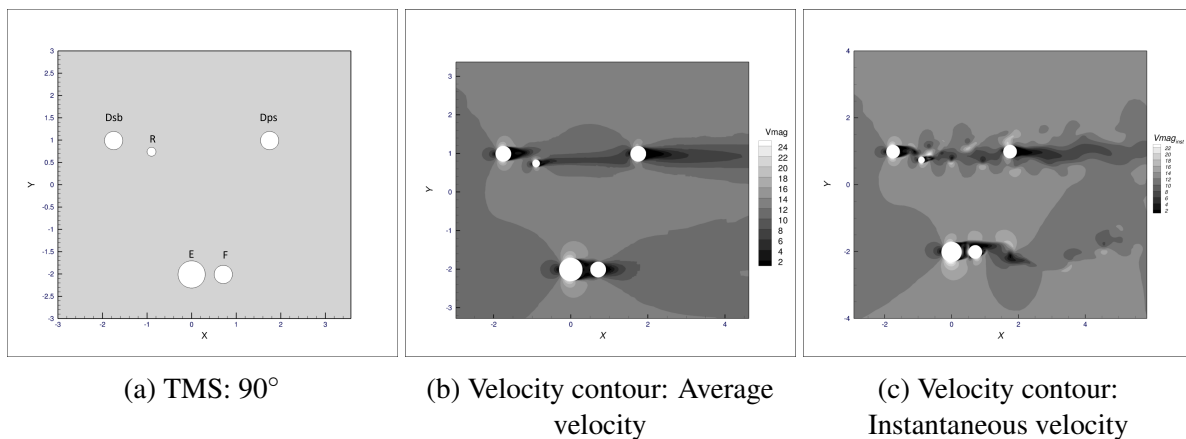


Figure 102: Velocity contour : Orientation  $90^\circ$

#### Cylinder E-F

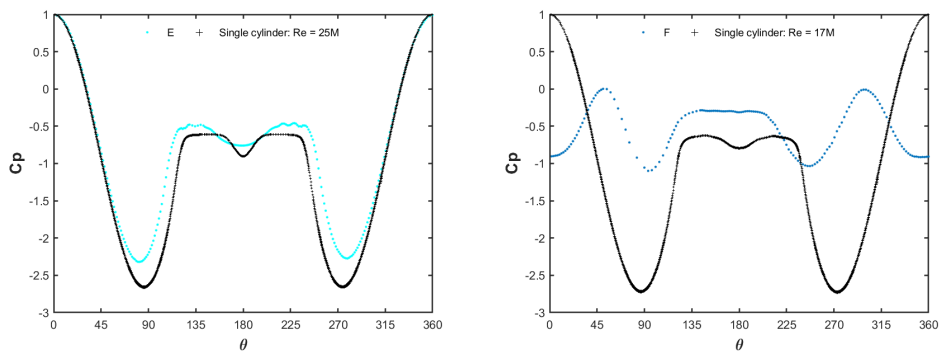
-Due to the compact tandem arrangement, where pitch distance,  $P/D = 1.164$ , wake interference can be observed for cylinder F. The incoming flow is blocked by cylinder E, therefore the reduction in drag for cylinder F is observed (see Figure 102).

-From cylinder E to F, one-sided Shear layer reattachment (SLR) is apparent (see Figure 102c). Additionally, the downstream F cylinder was encircled by the second shear layer from cylinder E without being reattached to its surface. The consequence of this flow arrangement may be observed in the development of a Karman vortex behind the F cylinder, where typically shedding is not formed (see Figure 102). When compared to SC, the  $St_{CI}$  numbers for both cylinders validate the claim. Therefore, the flow pattern for cylinders E to F lies in between the Extended-body (Single bluff body) and Re-attachment regimes.

-Cylinder F has an impact on the vortex's generation of cylinder E, and the length of the vortex E is equal to the distance between the two cylinders. Additionally, the vortex in cylinder F has been suppressed and has an insignificant one-sided length (see Figure 106a).

-Interesting insights can be seen in the  $C_p$  plot. The shift of the  $C_p$  plot and variations in  $C_{pb}$  can clearly be seen for the downstream cylinder F which influences the vortex formation of the upstream cylinder E. Additionally, the stagnation point for cylinder F has moved into around  $45^\circ$ , where the shear layer from cylinder E has been reattached. Overall, it appears that the tandem arrangement has maintained the symmetry of the flow for both cylinders (see Figure 103).

-Flow separation for cylinder E has been advanced, whereas flow separation for cylinder F has been delayed (see Table 35).



(a)  $C_p$ : Cylinder E vs Single cylinder

(b)  $C_p$ : Cylinder F vs Single cylinder

Figure 103: Avg. coefficient of pressure,  $C_p$  : Orientation  $90^\circ$



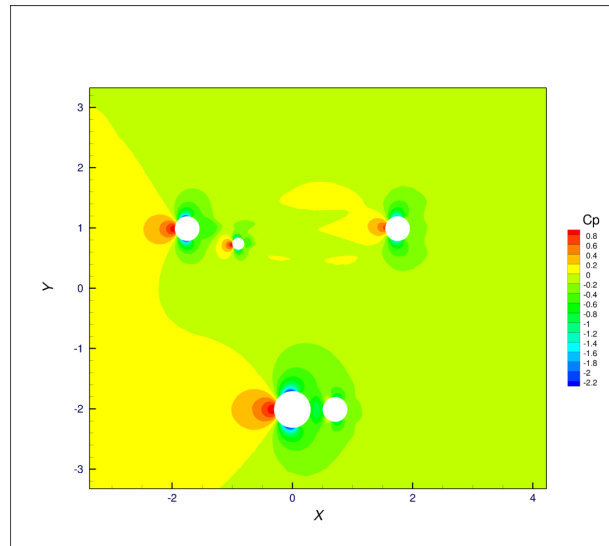
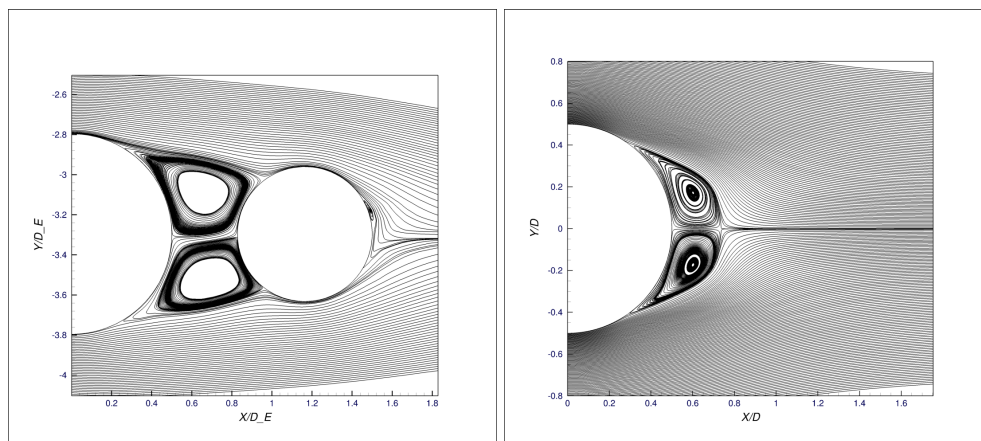


Figure 104: Contour avg. coefficient of pressure,  $C_p$  : Orientation  $90^\circ$



(a) Vortex length: Cylinder E

(b) Vortex length:  $Re = 25M$

Figure 105: Vortex length : Cylinder E vs Single cylinder



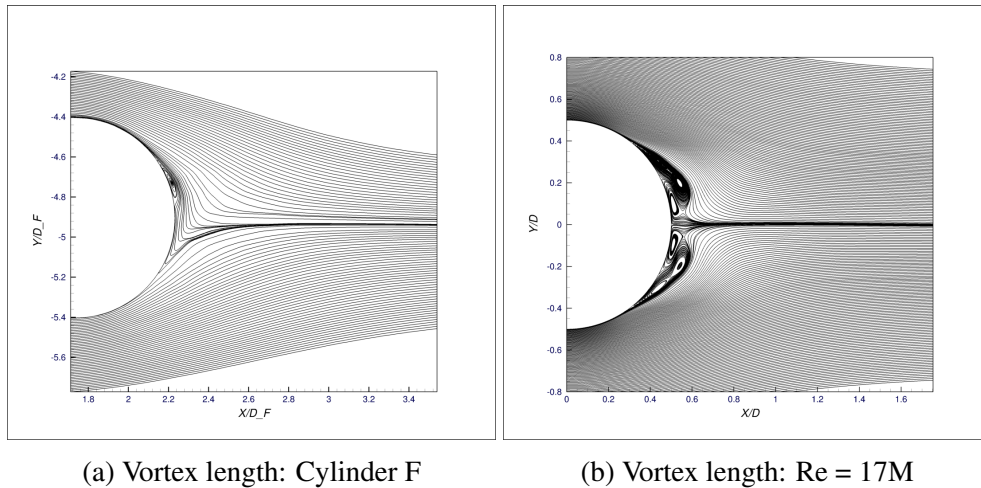


Figure 106: Vortex length : Cylinder F vs Single cylinder

**Cylinder Dsb-R**

-Wake and proximity interference exist due to staggered arrangement with a small incident angle  $\alpha = 16^\circ$ , and pitch distance,  $P/D = 2.161$

-The existence of vortex impingement can be seen which gives rise to a process called **amalgamation** explained earlier. This process ensures the merging of vortex shedding from the upstream cylinder to the downstream one. The vortex in the downstream cylinder is weaker but larger in size due to the distortion of the vortices by its own presence. It can also be verified by checking the  $St_{CI}$  number Dsb-R cylinders in compared to SC.

-Table 35 shows how numerous flow characteristics have changed as a result of the mutual interaction between cylinders Dsb and R. Both cylinders' base pressure coefficients,  $C_{pb}$ , are higher than they are for SC.

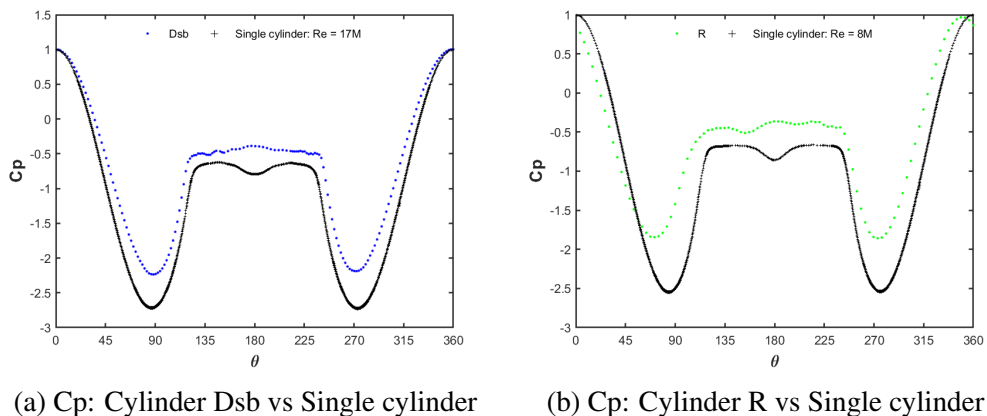


Figure 107: Avg. coefficient of pressure,  $C_p$  : Orientation  $90^\circ$

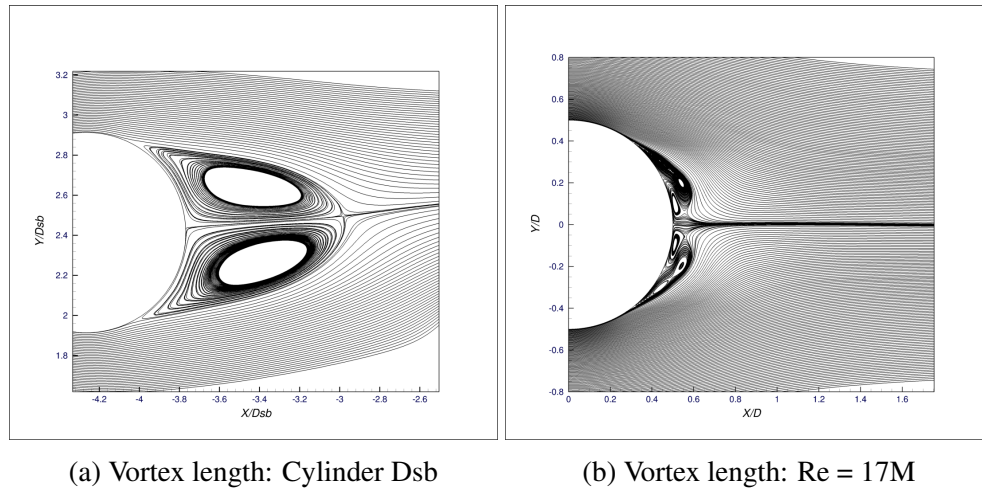


Figure 108: Vortex length : Cylinder Dsb vs Single cylinder

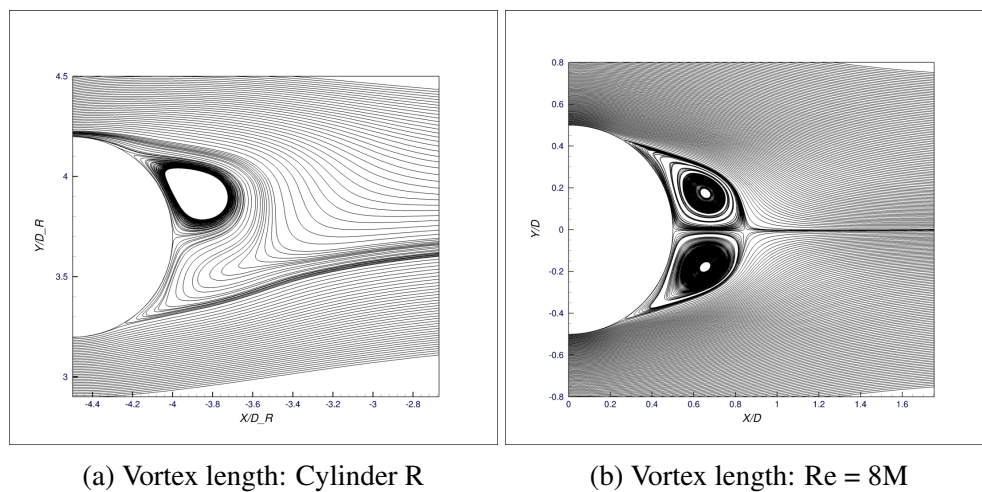


Figure 109: Vortex length : Cylinder R vs Single cylinder

### Cylinder Dps

The effect of the two upstream cylinders, namely Dsb-R, on cylinder Dps is equivalent to the previously mentioned  $30^\circ$  orientation. Nevertheless, the arrangement of Dsb-R has an effect on the incoming flow characteristics of cylinder Dps, resulting in a somewhat greater influence compared to the  $30^\circ$  orientation. As a result,  $C_{pb}$  at  $180^\circ$  and  $St_{Cl}$  have been increased.

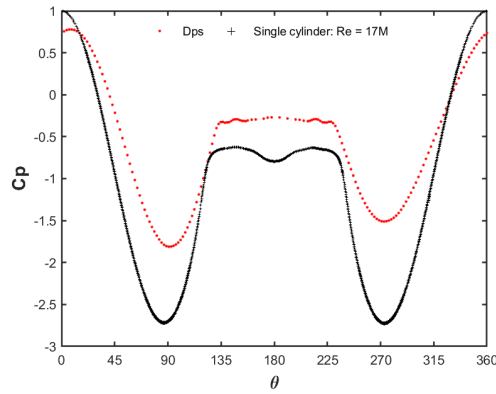
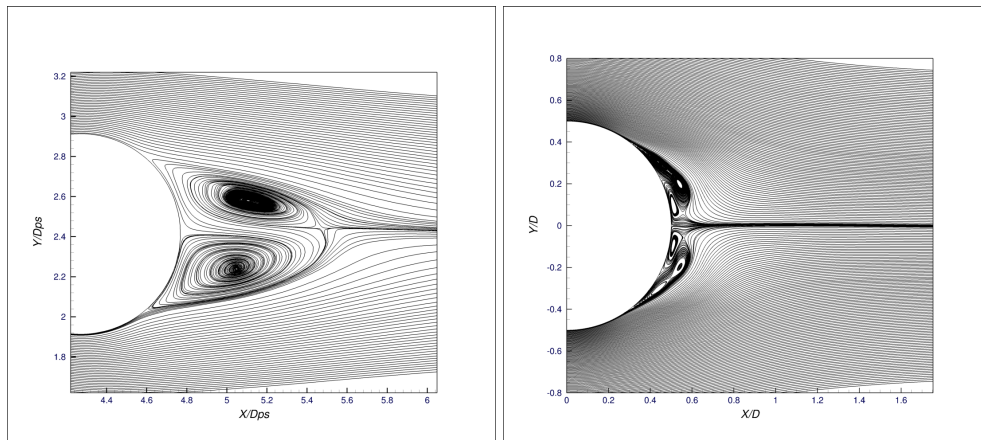


Figure 110: Cp: Cylinder Dps vs SC



(a) Vortex length: Cylinder Dps

(b) Vortex length: Re = 17M

Figure 111: Vortex length : Cylinder Dps vs Single cylinder

Table 35: Hydrodynamic parameters: 90 ° orientation

Re	Cylinder	$C_d$	$C_l$	$Cd_{RMS}$	$Cl_{RMS}$	Cpb ( $\theta = 180^\circ$ )	$\theta_{sep}[^\circ]$	Vortex length
25M	E	0.4442	0.1000	0.4529	0.4537	-0.7594	119.2060	Blocked
	Single cylinder (SC)	0.5494	-0.0014	0.5508	0.5775	-0.9040	124.0340	0.2392
17M	F	-0.1514	0.0442	0.3266	0.5704	-0.3130	137.1880	Insignificant
	Dps	0.3038	0.0680	0.3159	0.1260	-0.2697	133.2218	0.7472
	Dsb	0.3524	0.0055	0.3531	0.1228	-0.3901	121.0826	0.8483
	SC	0.5541	0.0026	0.5866	0.6470	-0.7939	125.7010	0.0951
8M	R	0.3294	0.1515	0.3692	0.6953	-0.3639	121.3156	Single vortex
	SC	0.5642	0.0007	0.5653	0.5260	-0.8569	118.9370	0.3417

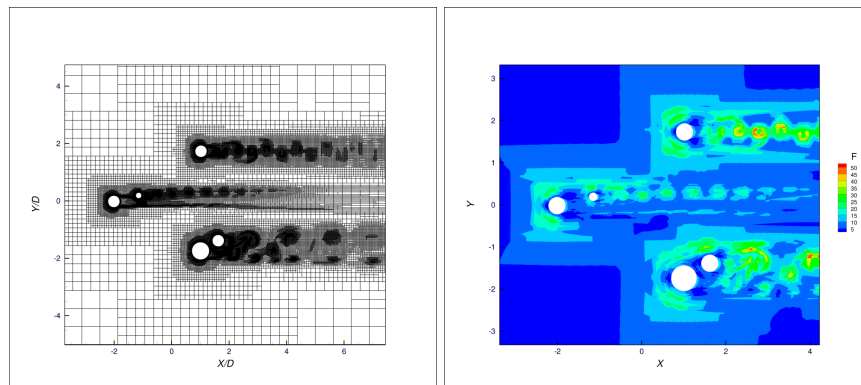
Table 36: Cylinders relative distance and incident angle : 90 ° orientation

90 °	Unit	E-F	Dsb-R	Dsb-Dps	R - Dps
Pitch distance P	m	0.7100	0.8860	3.5316	2.6618
L	m		0.8500		2.6500
T	m		0.2500		0.2500
$\alpha$	°	0.0000	16.0000	0.0000	5.0000
P/D	-	1.1639	2.1610		6.4922
L/D	-		2.0732		6.4634
T/D	-		0.6098		0.6098

1.4.4 Orientation: 120°

**Remarks**

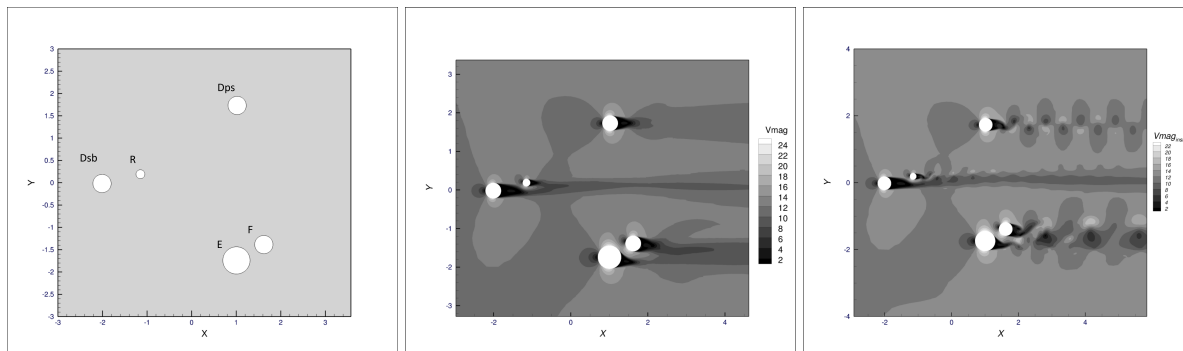
- Avg. coefficient of drag,  $C_d$ , Coefficient of lift  $C_l$ , RMS of drag coefficient,  $Cd_{RMS}$ , RMS of lift coefficient,  $Cl_{RMS}$ , Base pressure coefficient,  $C_{pb}$  ( $\theta = 180^\circ$ ), Flow separation,  $\theta_{sep}$ , Vortex length of 2D TMS and single cylinder are shown in Table 37.
- The incident angle,  $\alpha$ , Pitch distance,  $P/D$  are shown in Table 38.



(a) Mesh : Zoomed view

(b) Contour of function F

Figure 112: Post-processing results,  $\Delta t^* = 0.0025$  New mesh : 2D 120° orientation



(a) TMS: 120°

(b) Velocity contour: Average velocity

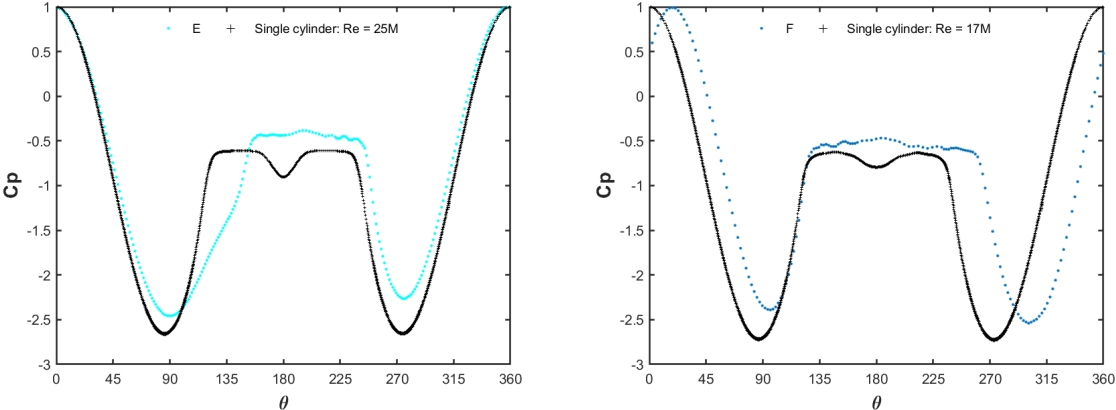
(c) Velocity contour: Instantaneous velocity

Figure 113: Velocity contour : Orientation 120°

**Cylinder E-F**

Staggered arrangement with the incidence  $\alpha = 30^\circ$ , and pitch distance,  $P/D = 1.164$ . Working as a single bluff body (SBB) as described in  $60^\circ$  orientation. The shift of  $C_p$  plot (see Figure 114) for both cylinders are identical to  $60^\circ$  orientation, however in the opposite direction, since the incident angle  $\alpha$  is positive in this case. The rest of the explanations are identical due to similar

flow physics.



(a) Cp: Cylinder E vs Single cylinder

(b) Cp: Cylinder F vs Single cylinder

Figure 114: Avg. coefficient of pressure, Cp : Orientation 120 °

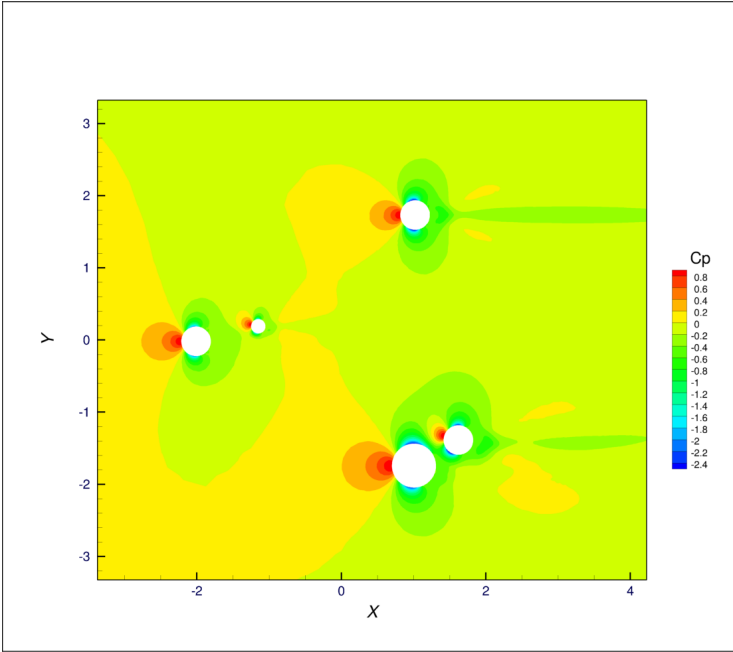


Figure 115: Contour avg. coefficient of pressure, Cp : Orientation 120 °

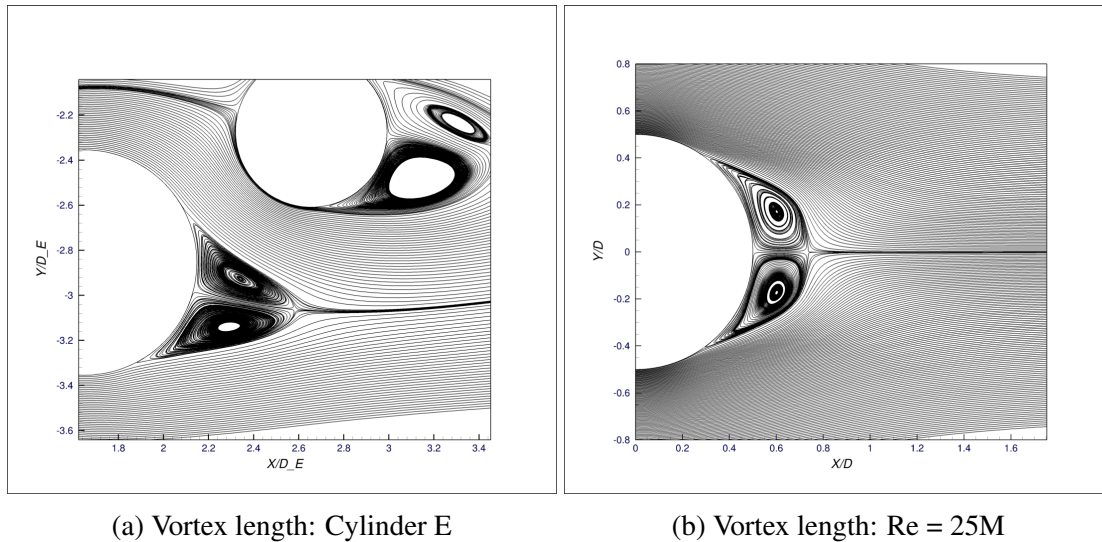


Figure 116: Vortex length : Cylinder E vs Single cylinder

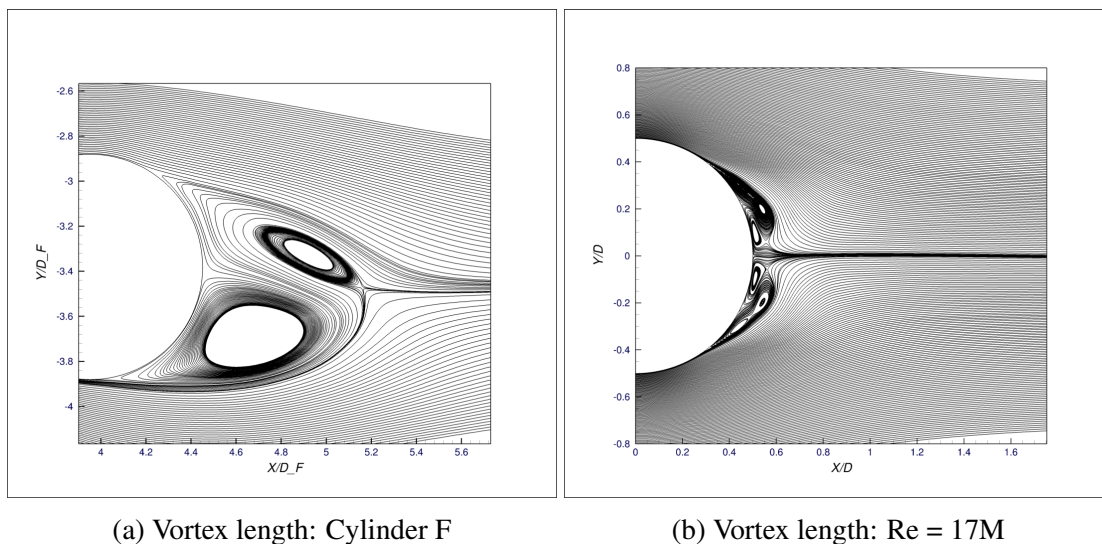
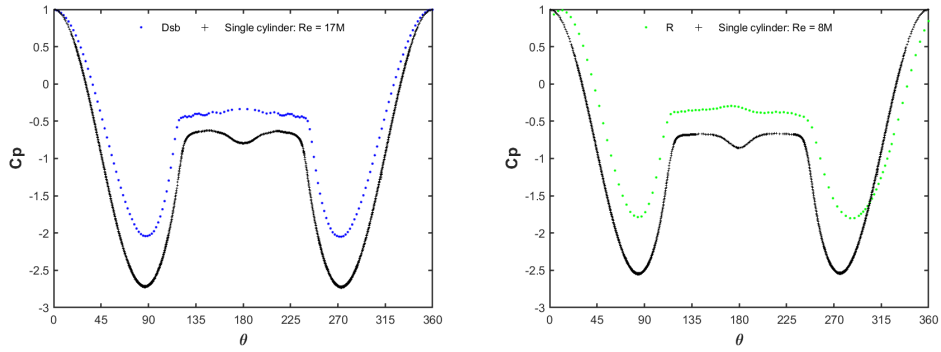


Figure 117: Vortex length : Cylinder F vs Single cylinder

### Cylinder Dsb-R

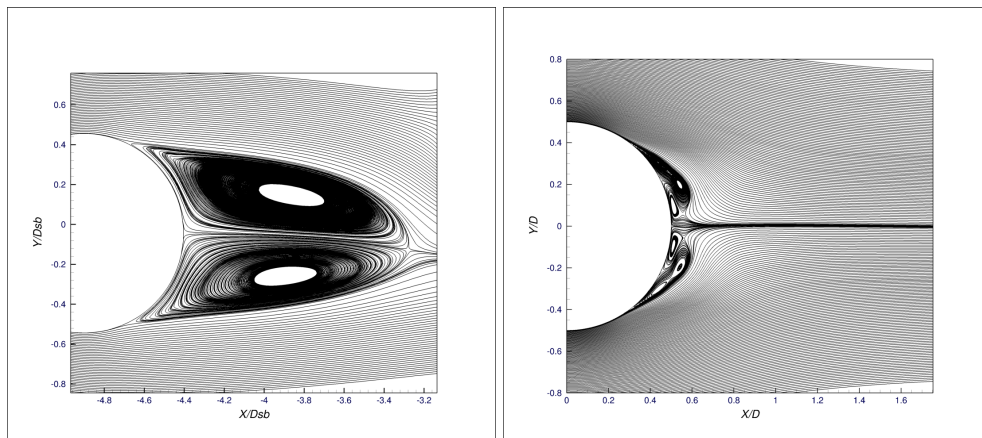
- Staggered arrangement with  $\alpha = 13^\circ$  and pitch distance,  $P/D = 2.161$ .
- Vortex impingement or co-shedding can be seen (see Figure 113 and 32).
- The shift of the  $C_p$  plot is in an upward direction than the SC, which increases the base pressure coefficient,  $C_{pb}$  of both cylinders (see Figure 118).
- Vortex formation of E and F have been mutually affected (see Figure 119).





(a) Cp: Cylinder Dsb vs Single cylinder      (b) Cp: Cylinder R vs Single cylinder

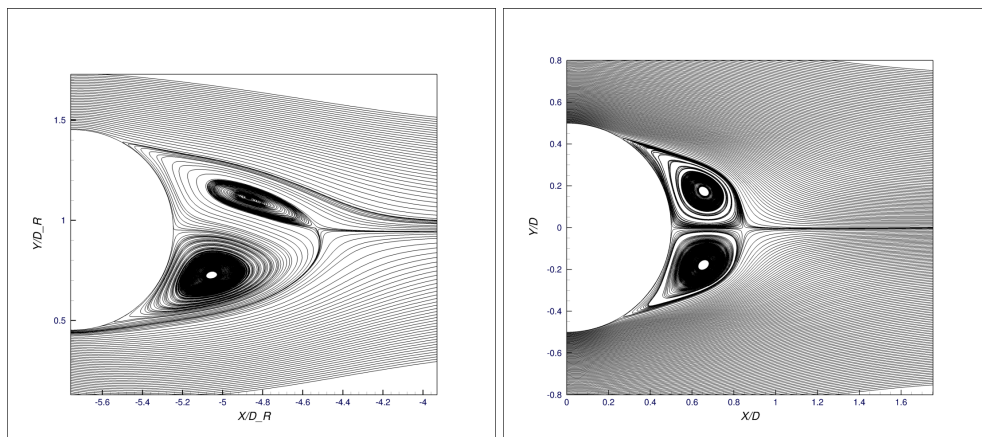
Figure 118: Avg. coefficient of pressure, Cp : Orientation 120 °



(a) Vortex length: Cylinder Dsb

(b) Vortex length: Re = 17M

Figure 119: Vortex length : Cylinder Dsb vs Single cylinder



(a) Vortex length: Cylinder R

(b) Vortex length: Re = 8M

Figure 120: Vortex length : Cylinder R vs Single cylinder

### Cylinder Dps

Cylinder Dps is minimally affected and a distinct  $St_{Cl}$  number can be identified which is close to the SC.

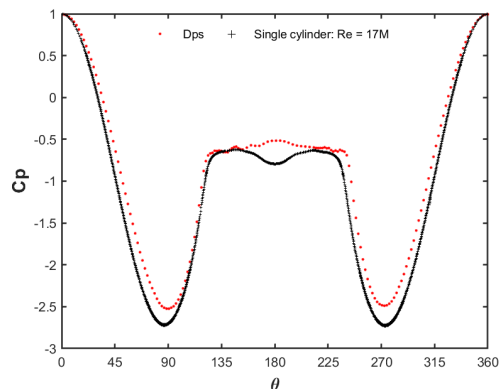
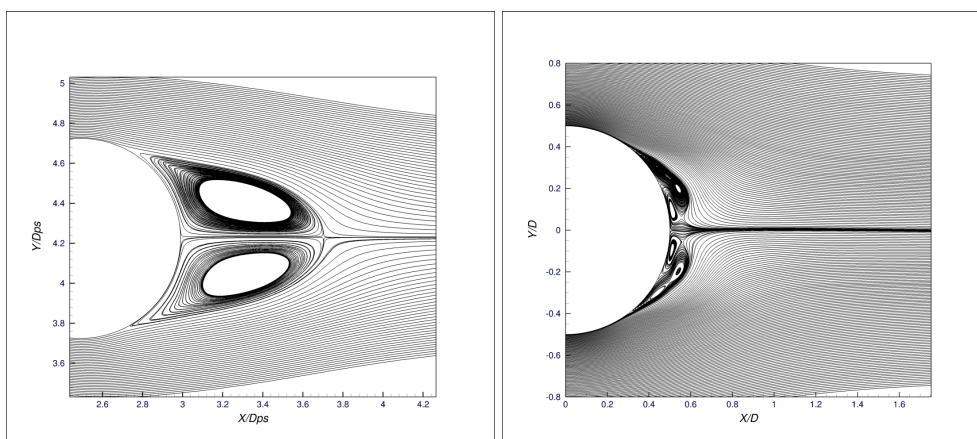


Figure 121: Cp: Cylinder Dps vs Single cylinder



(a) Vortex length: Cylinder Dps

(b) Vortex length: Re = 17M

Figure 122: Vortex length : Cylinder Dps vs Single cylinder

Table 37: Hydrodynamic parameters: 120 ° orientation

Re	Cylinder	$C_d$	$C_l$	$Cd_{RMS}$	$Cl_{RMS}$	$Cpb (\theta = 180^\circ)$	$\theta_{sep} [^\circ]$	Vortex length
25M	E	0.5193	0.4330	0.5206	0.4356	-0.4369	155.2588	0.4619
	Single cylinder (SC)	0.5494	-0.0014	0.5508	0.5775	-0.9040	124.0340	0.2392
17M	F	-0.0808	-0.1965	0.1074	0.3216	-0.4769	127.9093	0.7675
	Dps	0.4117	0.0004	0.4117	0.1273	-0.5170	122.7988	0.7675
	Dsb	0.3048	-0.0010	0.3048	0.0033	-0.3373	119.1755	1.1925
	SC	0.5541	0.0026	0.5866	0.6470	-0.7939	125.7010	0.0951
8M	R	0.1775	-0.2095	0.1776	0.2287	-0.3090	114.1863	0.7319
	SC	0.5642	0.0007	0.5653	0.5260	-0.8569	118.9370	0.3417



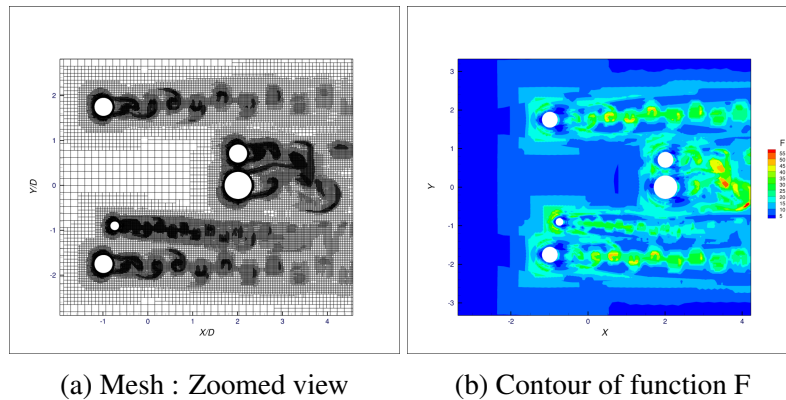
Table 38: Cylinders relative distance and incident angle :  $120^\circ$  orientation

$120^\circ$	Unit	E-F	Dsb-R	R-Dps
Pitch distance, P	m	0.7100	0.8860	2.6618
L	m	0.6149	0.8611	2.1700
T	m	0.3550	0.2085	1.5415
$\alpha$	$^\circ$	30.0000	13.0000	35.0000
P/D	-	1.1639	2.1610	6.4922
L/D	-	1.0080	2.1002	5.2927
T/D	-	0.5820	0.5085	3.7598

### 1.4.5 Orientation: $180^\circ$

#### Remarks

- Avg. coefficient of drag,  $C_d$ , avg. coefficient of lift  $C_l$ , RMS of drag coefficient,  $Cd_{RMS}$ , RMS of lift coefficient,  $Cl_{RMS}$ , Base pressure coefficient,  $C_{pb}$  ( $\theta = 180^\circ$ ), Flow separation,  $\theta_{sep}$ , Vortex length of 2D TMS and single cylinder are shown in Table 39.
- The incident angle,  $\alpha$ , Pitch distance, P/D are shown in Table 40.

Figure 123: Post-processing results,  $\Delta t^* = 0.0025$  New mesh : 2D  $180^\circ$  orientation

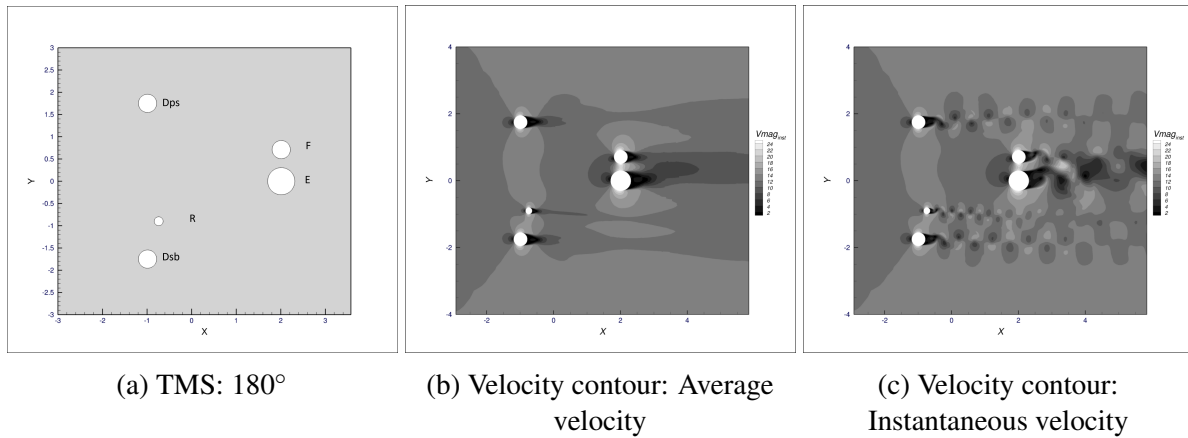


Figure 124: Velocity contour : Orientation 180 °

**Cylinder E-F, Dsb-R, Dps**

The explanation for 180 ° orientation is identical to the previously explained 0 ° orientation. The differences can be realized between these two orientations upon checking Table 31 and 39 mainly emerges from the relative positions of the cylinders which are mirror to each other. For the current orientation, freestream is perturbed by the two three upstream cylinders namely Dps, and Dsb-R which was actually reversed for 0 ° orientation. It can be better realized by looking at the orientations in Figure 124a.

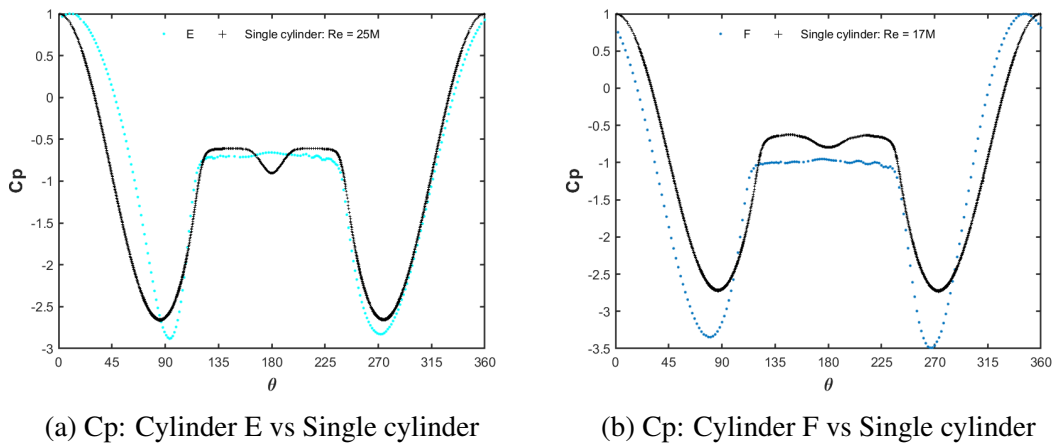


Figure 125: Avg. coefficient of pressure, Cp : Orientation 180 °

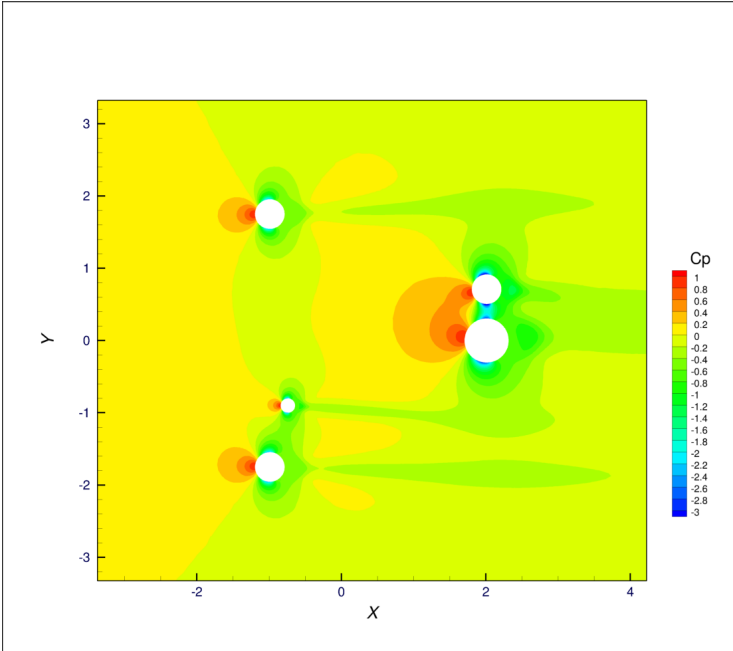
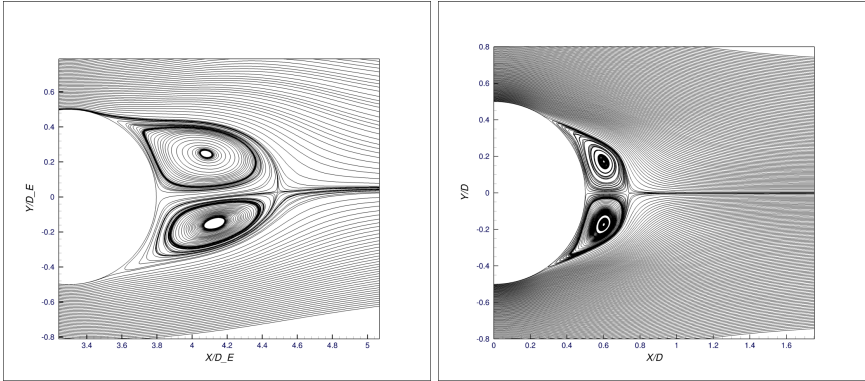
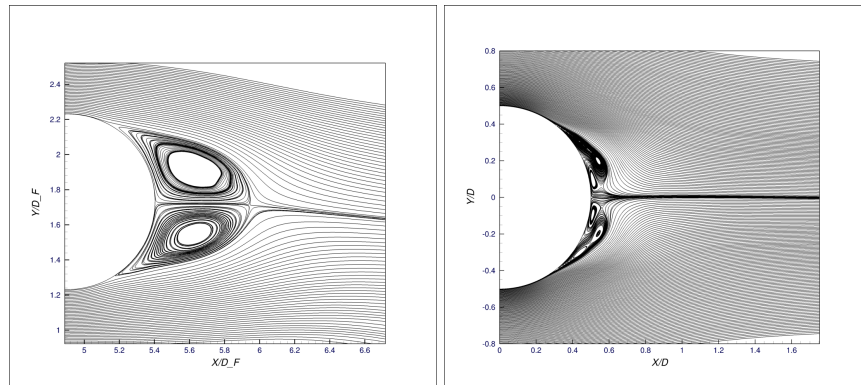


Figure 126: Contour of avg. coefficient of pressure,  $C_p$  : Orientation  $180^\circ$



(a) Vortex length: Cylinder E      (b) Vortex length:  $Re = 25M$

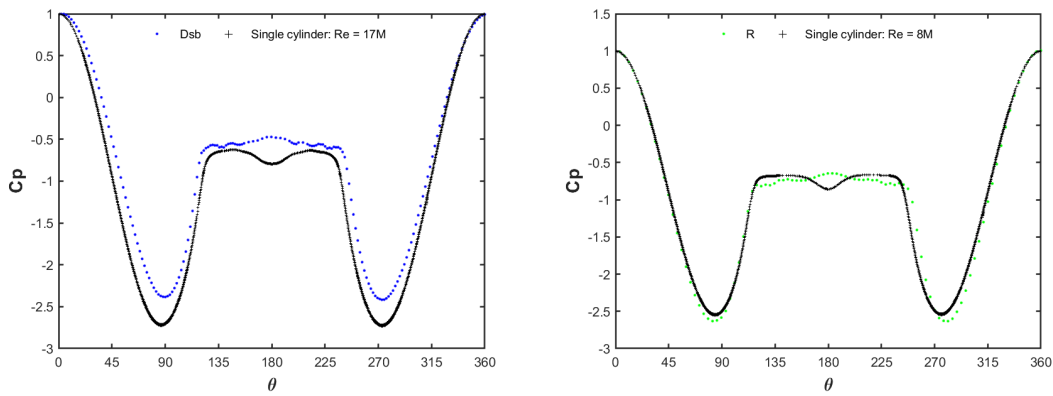
Figure 127: Vortex length : Cylinder E vs Single cylinder



(a) Vortex length: Cylinder F

(b) Vortex length: Re = 17M

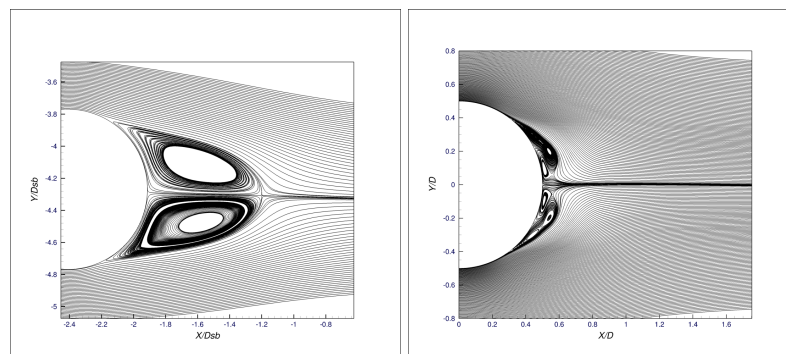
Figure 128: Vortex length : Cylinder F vs Single cylinder



(a) Cp: Cylinder Dsb vs Single cylinder

(b) Cp: Cylinder R vs Single cylinder

Figure 129: Avg. coefficient of pressure, Cp : Orientation 180 °



(a) Vortex length: Cylinder Dsb

(b) Vortex length: Re = 17M

Figure 130: Vortex length : Cylinder Dsb vs Single cylinder

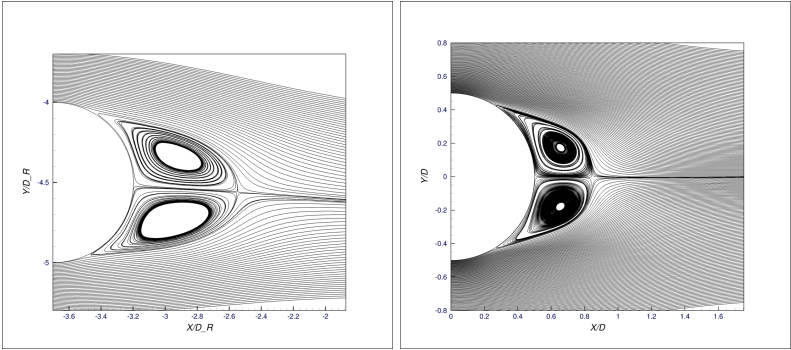


Figure 131: Vortex length : Cylinder R vs Single cylinder

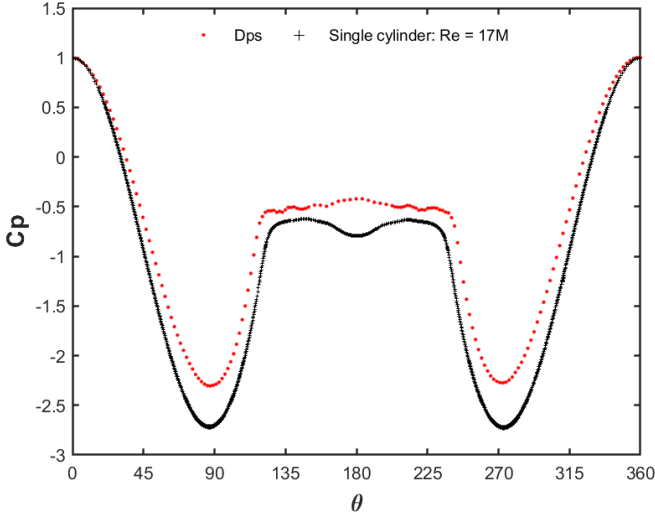


Figure 132: Cp: Cylinder Dps vs Single cylinder

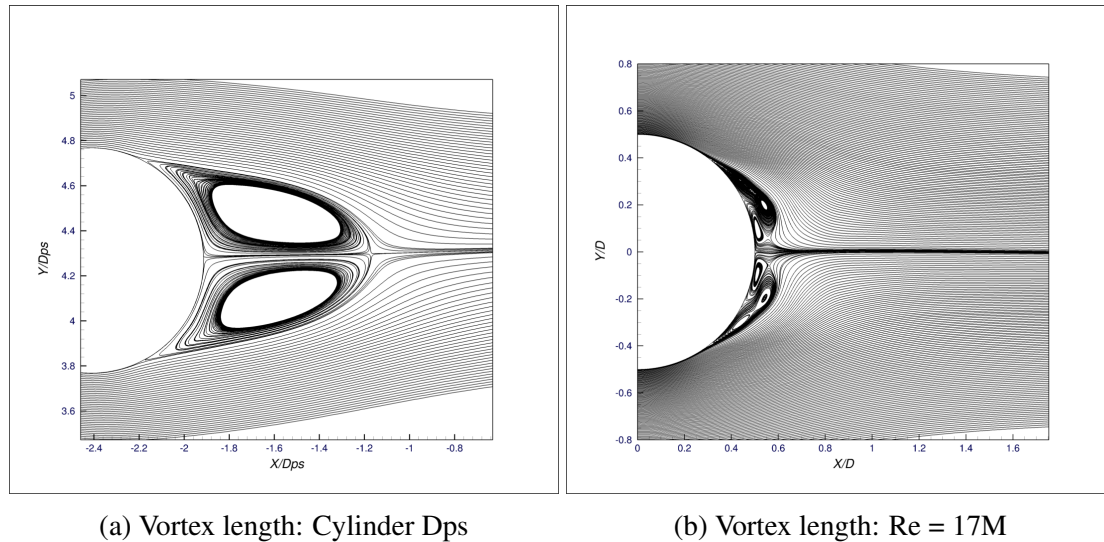


Figure 133: Vortex length : Cylinder Dps vs Single cylinder

Table 39: Hydrodynamic parameters:  $180^\circ$  orientation

Re	Cylinder	$C_d$	$C_l$	$Cd_{RMS}$	$Cl_{RMS}$	$C_{pb} (\theta = 180^\circ)$	$\theta_{sep} [^\circ]$	Vortex length
25M	E	0.5680	-0.3599	0.5705	0.4937	-0.6577	118.7404	0.7472
	Single cylinder (SC)	0.5494	-0.0014	0.5508	0.5775	-0.9040	124.0340	0.2392
17M	F	0.6677	0.3837	0.6782	0.6191	-0.9620	116.6747	0.5536
	Dps	0.3804	0.0114	0.3805	0.1102	-0.4211	120.1372	0.7905
	Dsb	0.4273	-0.0203	0.4271	0.1205	-0.4725	120.4931	0.7523
	SC	0.5541	0.0026	0.5866	0.6470	-0.7939	125.7010	0.0951
8M	R	0.4778	0.0282	0.4779	0.2490	-0.6461	115.6344	0.6580
	SC	0.5642	0.0007	0.5653	0.5260	-0.8569	118.9370	0.3417

Table 40: Cylinders relative distance and incident angle :  $180^\circ$  orientation

$180^\circ$	Unit	E-F	Dsb-R	Dps - F	Dsb - E	R - E
Pitch distance, P	m	0.7100	0.8860	3.1752	3.4731	2.8935
L	m		0.2500	3.0610	3.0000	2.7500
T	m		0.8500	1.0400	1.7500	0.7100
$\alpha$	$^\circ$	0.0000	74.0000	-19.0000	30.0000	18.0000
P/D	-	1.1639	2.1610	7.7444	5.6936	4.7434
L/D	-		0.6098	7.4659	4.9180	4.5082
T/D	-		2.0732	2.5366	2.8689	1.1639

1.4.6 Orientation: 270°

**Remarks**

- Avg. coefficient of drag,  $C_d$ , avg. coefficient of lift  $C_l$ , RMS of drag coefficient,  $Cd_{RMS}$ , RMS of lift coefficient,  $Cl_{RMS}$ , Base pressure coefficient,  $C_{pb} (\theta = 180^\circ)$ , Flow separation,  $\theta_{sep}$ , Vortex length of 2D TMS and single cylinder are shown in Table 41.
- The incident angle,  $\alpha$ , Pitch distance,  $P/D$  are shown in Table 42.

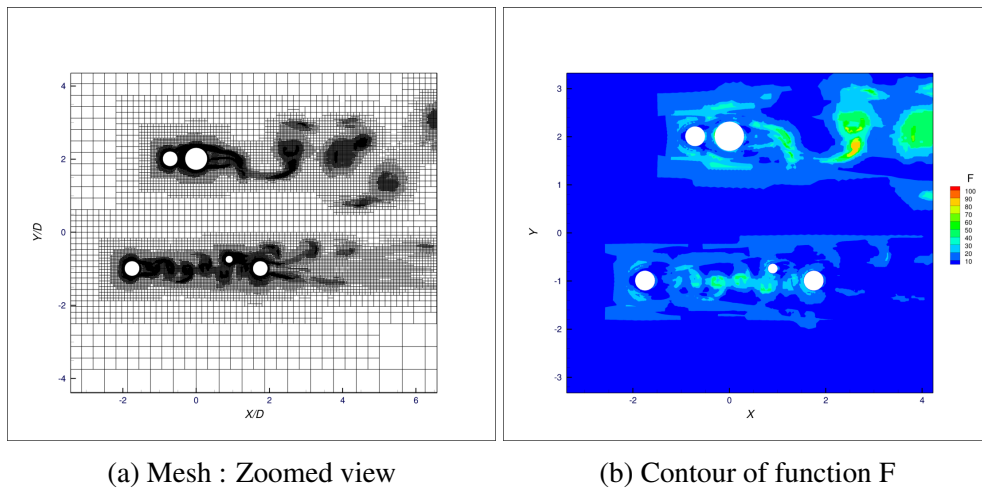


Figure 134: Post-processing results,  $\Delta t^* = 0.0025$  New mesh : 2D 270° orientation

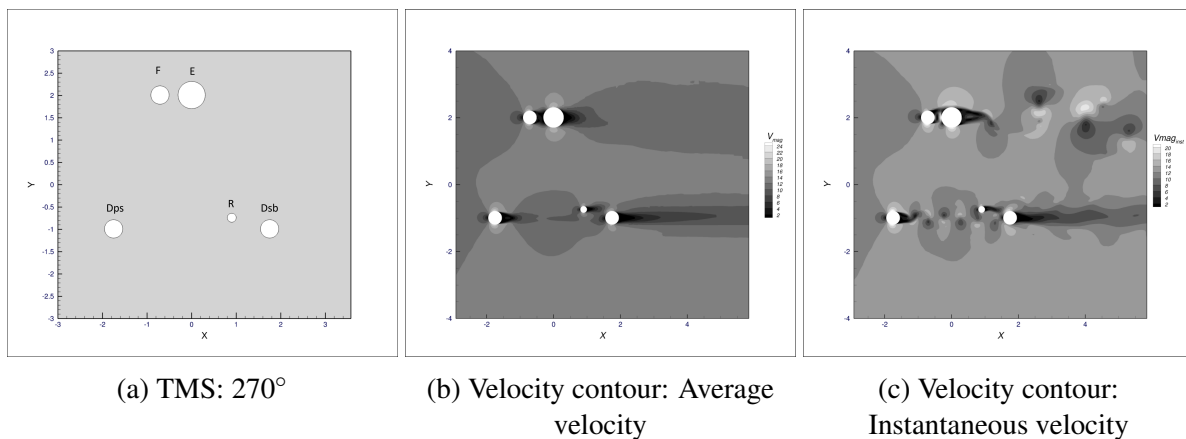


Figure 135: Velocity contour : Orientation 270°

**Cylinder E-F**

- Tandem arrangement with pitch distance,  $P/D = 1.164$
- Same analogy can be drawn from the 90° orientation, however, the relative position has been reversed, therefore, differences in hydrodynamic parameters can be seen when compared to the

90 ° orientation.

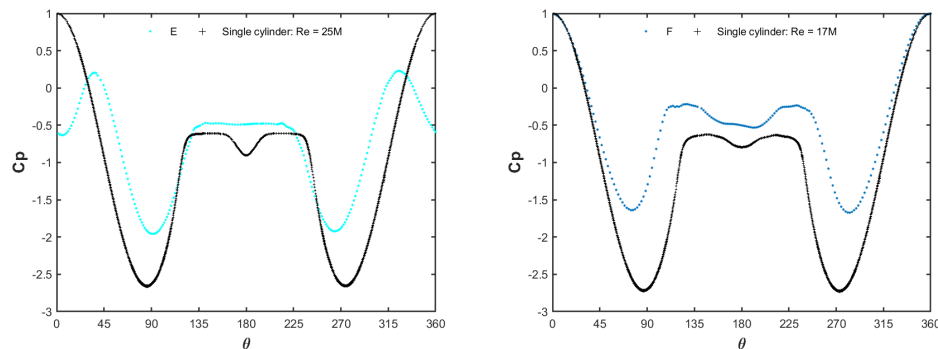
-One of the distinctions is the formation of the Karman vortex in a usual manner which was not present for 90 ° orientation.

-Since cylinder F (upstream) is smaller than the cylinder E (downstream), therefore, the stagnation point in the  $C_p$  plot is advanced (before 45 °) for the downstream cylinder E (see Figure 136).

-The vortex formation of cylinder E has been affected and declined in length, however, not insignificant to the previous case (90° orientation). Also, two distinct vortices exist for cylinder E (see Figure 139).

-Flat base pressure coefficient can be seen in the  $C_p$  plot for cylinder E, which was seen for cylinder F in 90° orientation (see Figure 136).

-The drag of cylinder E has been reduced remarkably which was expected based on the explanation that has been presented in previous cases (see Table 41).



(a)  $C_p$ : Cylinder E vs Single cylinder

(b)  $C_p$ : Cylinder F vs Single cylinder

Figure 136: Contour of avg. coefficient of pressure,  $C_p$  : Orientation 270 °



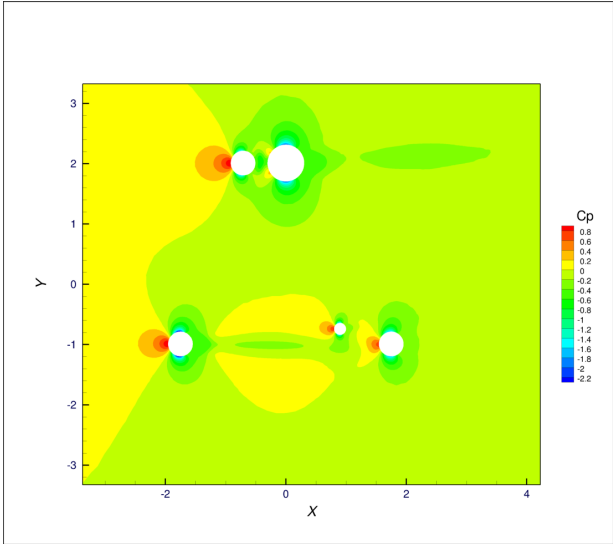
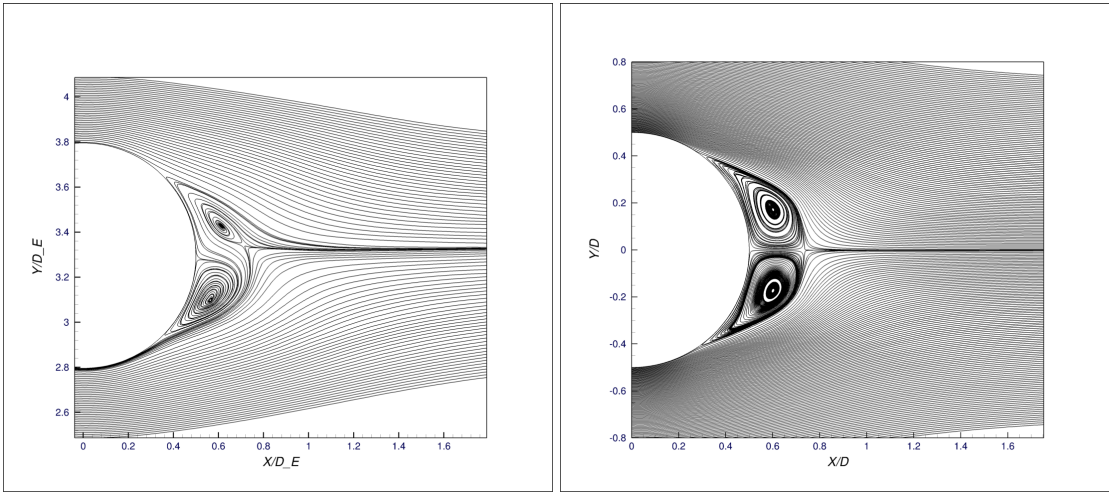


Figure 137: Contour avg. coefficient of pressure,  $C_p$  : Orientation  $270^\circ$



(a) Vortex length: Cylinder E

(b) Vortex length:  $Re = 25M$

Figure 138: Vortex length : Cylinder E vs Single cylinder

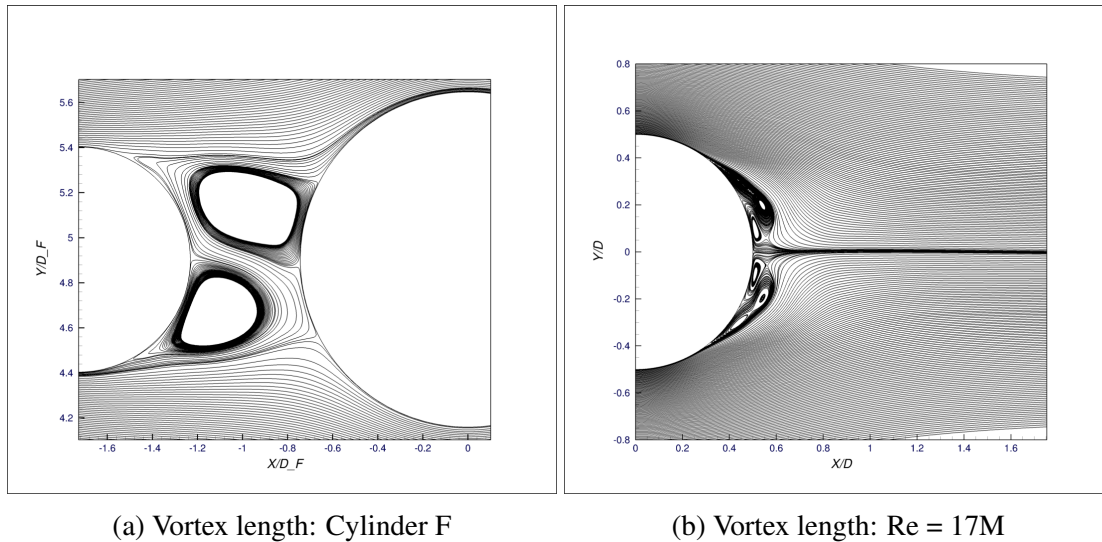


Figure 139: Vortex length : Cylinder F vs Single cylinder

**Cylinder Dsb-R**

- The incident flow has been changed due to cylinder Dps (see Figure 135c).
- For cylinder Dsb, the upstream flow is shaped by both cylinder Dps and R.
- The wake interference effect was dominant for cylinder Dsb than the cylinder R which can be seen in Cp plot (see Figure 140). The stagnation point of cylinder Dsb is reduced from the unity which was also seen in 60° orientation for cylinder F. This is a classical phenomenon of cylinders being tandem arrangement or staggered arrangement with little incident angle  $\alpha$ . Here,  $\alpha = -16^\circ$ , and pitch distance,  $P/D = 2.161$ .

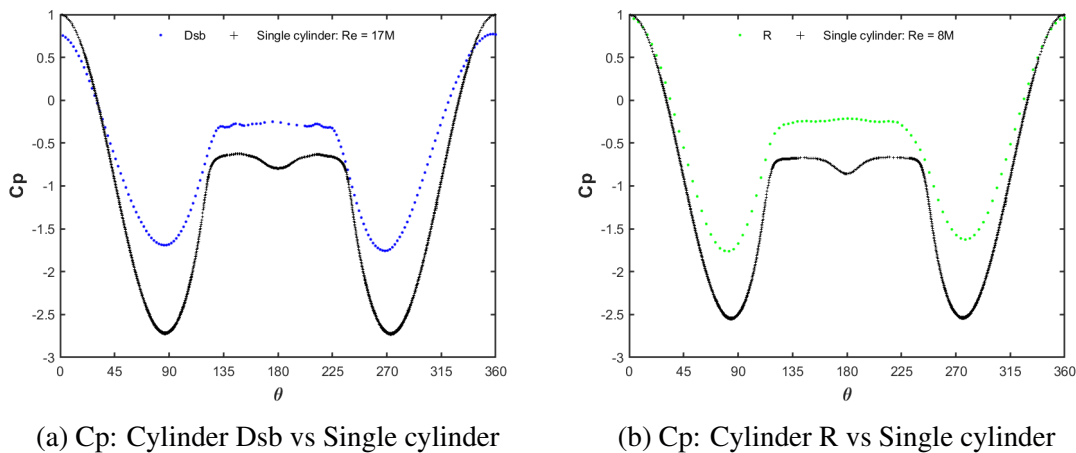
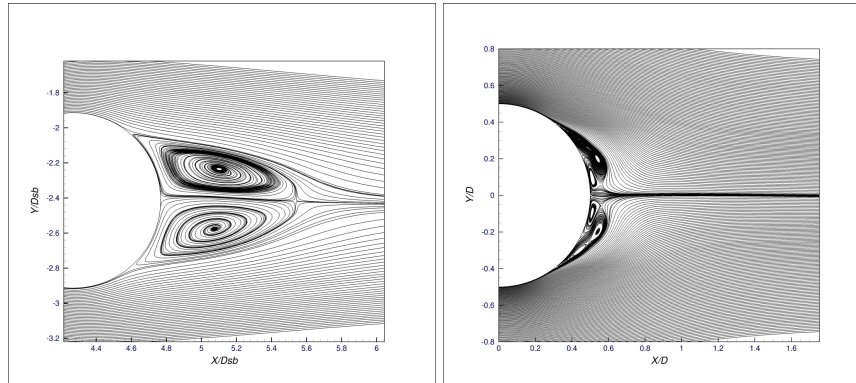


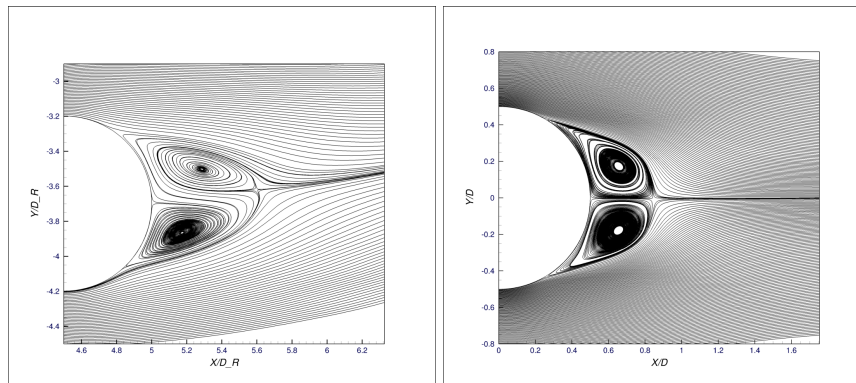
Figure 140: Avg. coefficient of pressure, Cp : Orientation 270 °



(a) Vortex length: Cylinder Dsb

(b) Vortex length: Re = 17M

Figure 141: Vortex length : Cylinder Dsb vs Single cylinder



(a) Vortex length: Cylinder R

(b) Vortex length: Re = 8M

Figure 142: Vortex length : Cylinder R vs Single cylinder

### Cylinder Dps

-Distinct  $St_{Cl}$  value can be seen in Table 27 which is expected since it is isolated from the other cylinders. However, the other cylinders have influenced in the flow regime in a way that the effect of it can be seen in cylinder Dps for its various parameters (see Table 41).

-Cylinder Dps is acting as a turbulence generator for downstream cylinders namely Dsb – R.

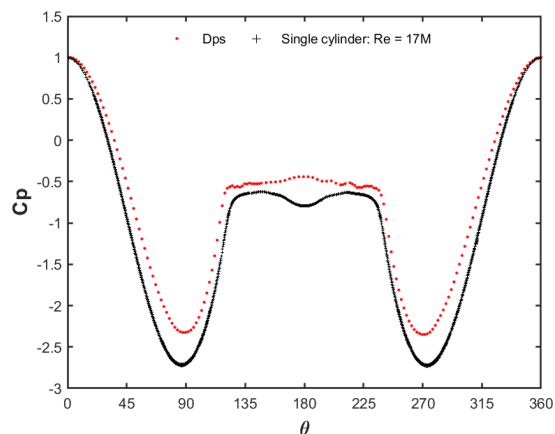
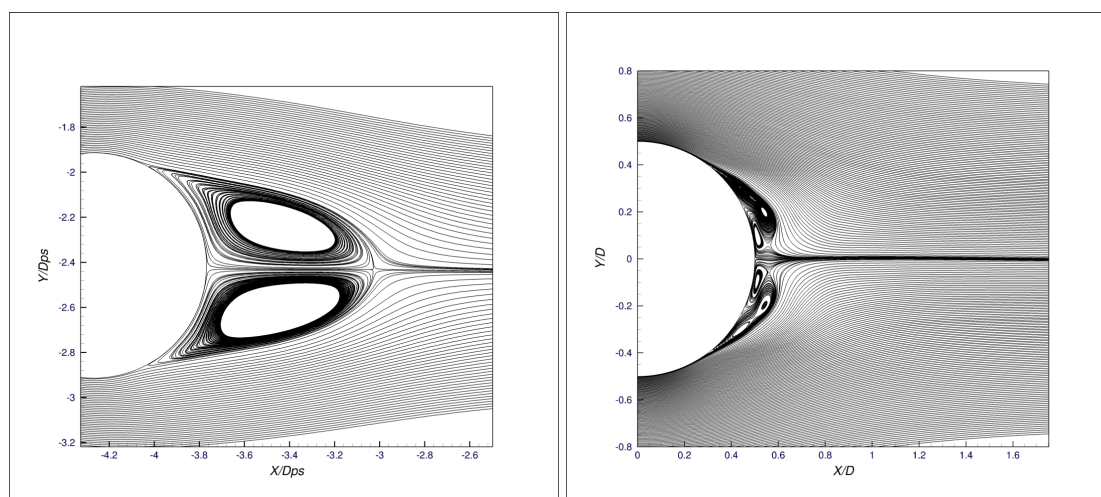


Figure 143: Cp: Cylinder Dps vs Single cylinder



(a) Vortex length: Cylinder Dps

(b) Vortex length: Re = 17M

Figure 144: Vortex length : Cylinder Dps vs Single cylinder

Table 41: Hydrodynamic parameters: 270 ° orientation

Re	Cylinder	$C_d$	$C_l$	$Cd_{RMS}$	$Cl_{RMS}$	$C_{pb} (\theta = 180^\circ)$	$\theta_{sep} [^\circ]$	Vortex length
25M	E	0.2833	0.0511	0.3912	0.6930	-0.4876	132.8458	0.2760
	Single cylinder (SC)	0.5494	-0.0014	0.5508	0.5775	-0.9040	124.0340	0.2392
17M	F	0.3777	-0.0464	0.4265	0.6010	-0.5016	116.5148	Blocked
	Dps	0.3877	0.0006	0.3878	0.1125	-0.4413	120.6345	0.7981
	Dsb	0.2363	0.0392	0.2537	0.3351	-0.2567	130.8199	0.8272
8M	SC	0.5541	0.0026	0.5866	0.6470	-0.7939	125.7010	0.0951
	R	0.3203	0.0327	0.3251	0.3623	-0.2139	123.0258	0.6096
	SC	0.5642	0.0007	0.5653	0.5260	-0.8569	118.9370	0.3417

Table 42: Cylinders relative distance and incident angle : 270° orientation

270°		Unit	E-F	Dsb-R	Dps - Dsb	Dps - R
Pitch distance P	m		0.7100	0.8860	3.5000	2.6618
L	m			0.8500		2.6500
T	m			0.2500		0.2500
$\alpha$	°		0.0000	-16.0000	0.0000	5.0000
P/D	-		1.1639	2.1610		6.4922
L/D	-			2.0732		6.4634
T/D	-			0.6098		0.6098

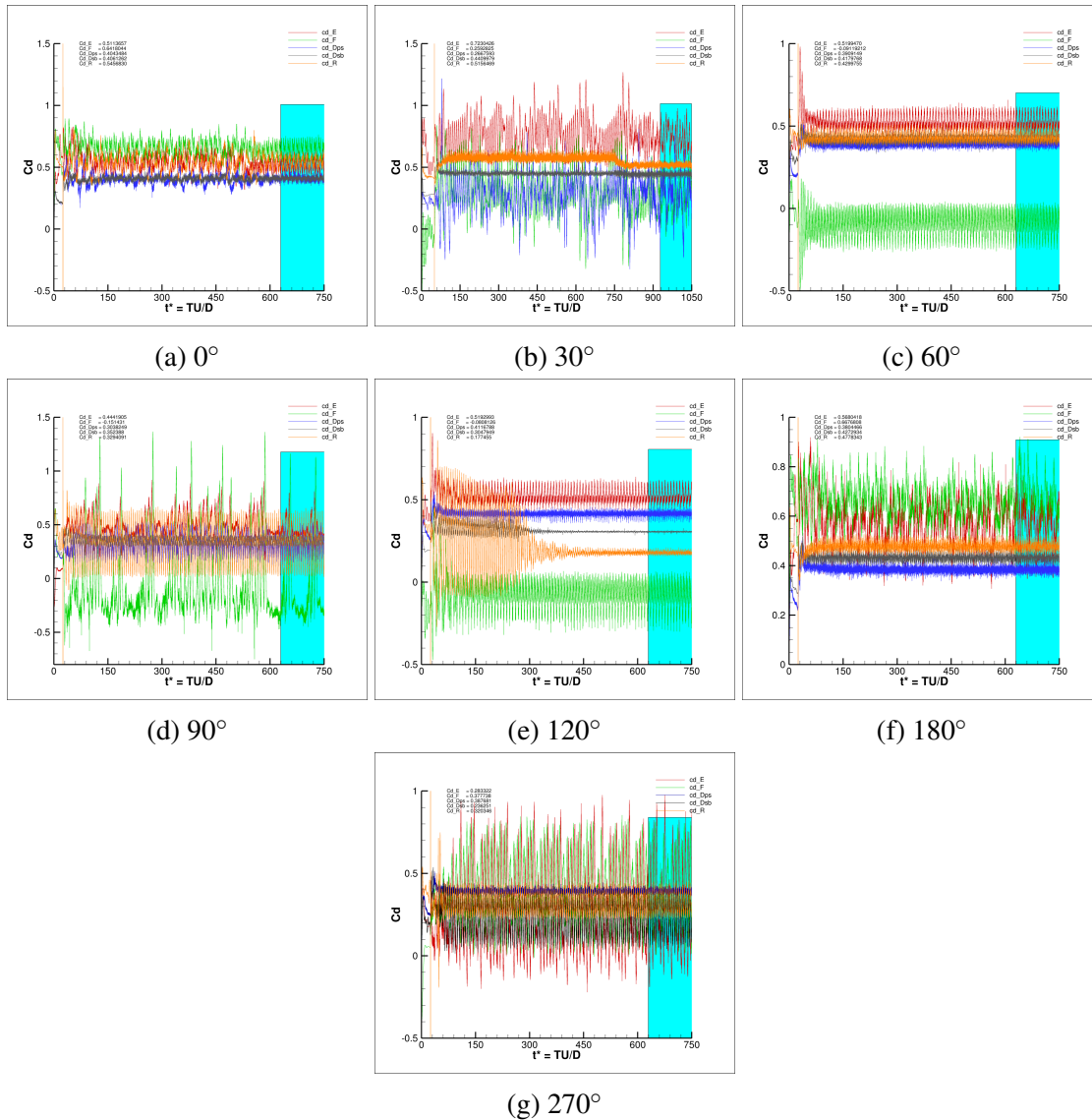


Figure 145: Evolution of avg. coefficient of drag, Cd : Seven orientations

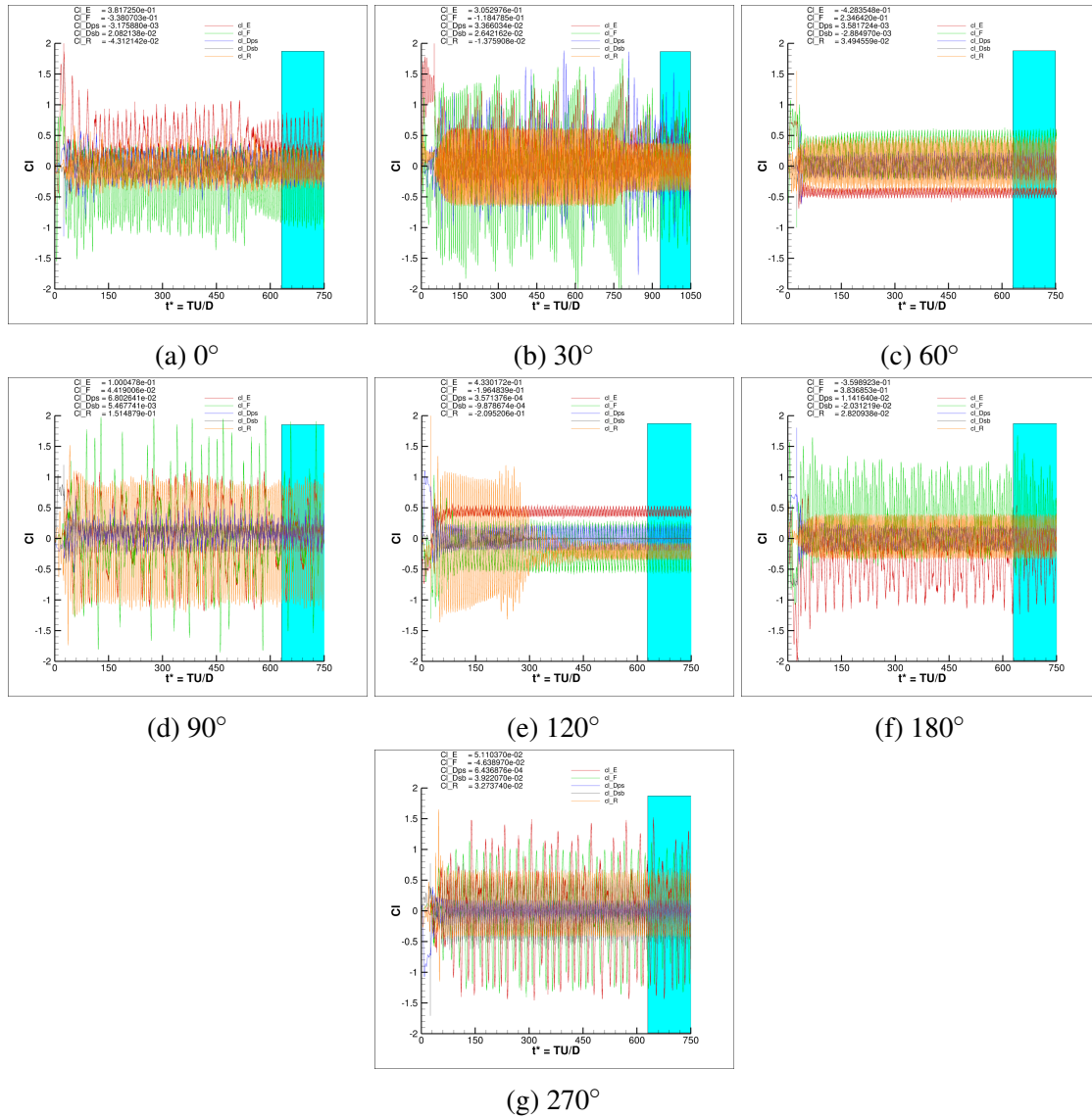


Figure 146: Evolution of avg. coefficient of lift,  $C_l$  : Seven orientations



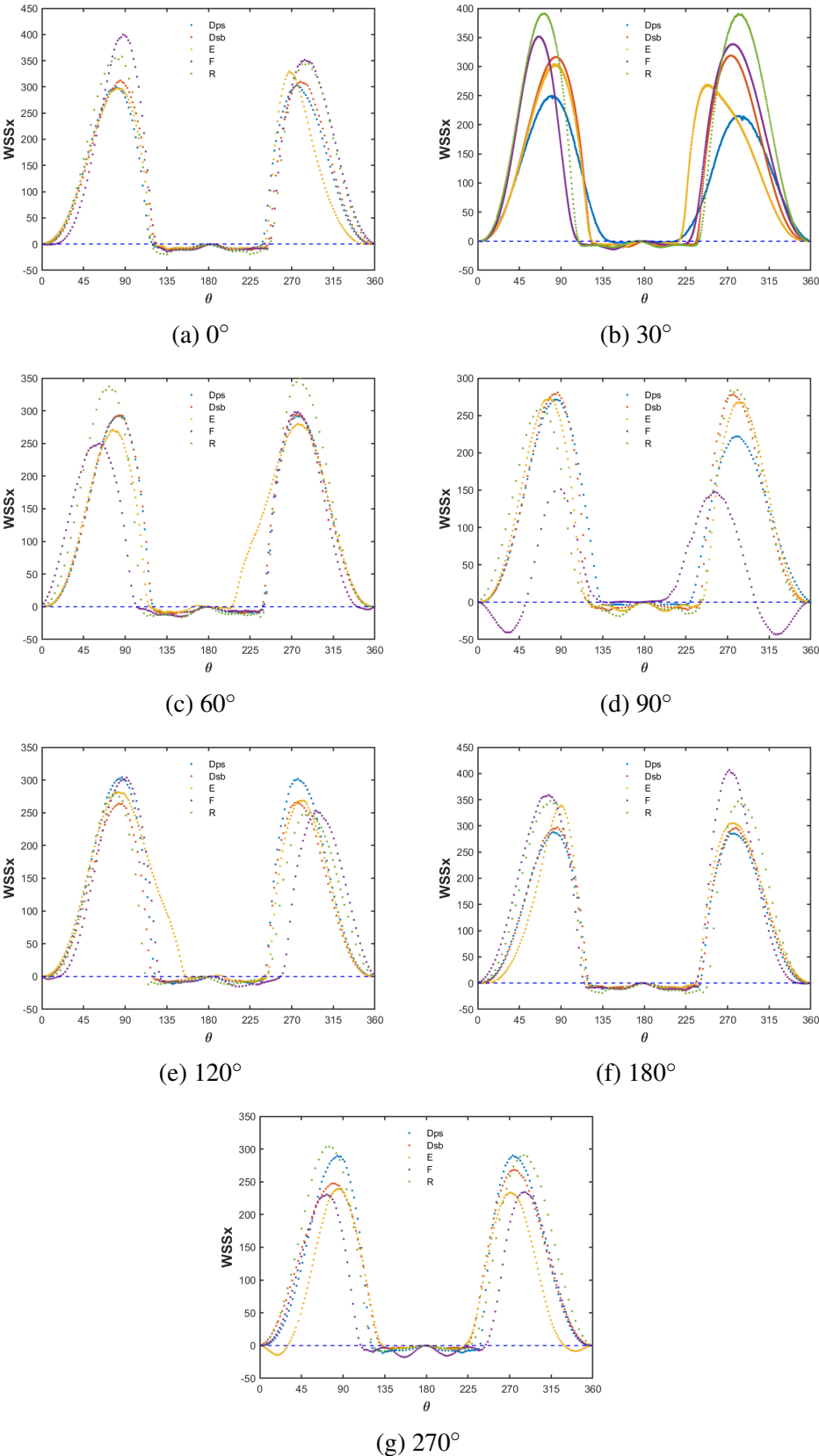


Figure 147: Avg. tangential wall shear stress (WSSx) vs  $\theta$ : Seven orientations

### 1.5 Delayed Detached Eddy Simulation (DDES)

The simulation utilizing Detached Eddy Simulation (DDES) has exhibited nonphysical variations in the flow field (see Figure 64a), which may be attributable to the excessive refining in the AGR box settings. Therefore, the simulation was terminated. Approximately 150 million cells were created in the simulation. The illustration presented in Figure 148 depicts a mesh that has been excessively refined in DDES simulation.

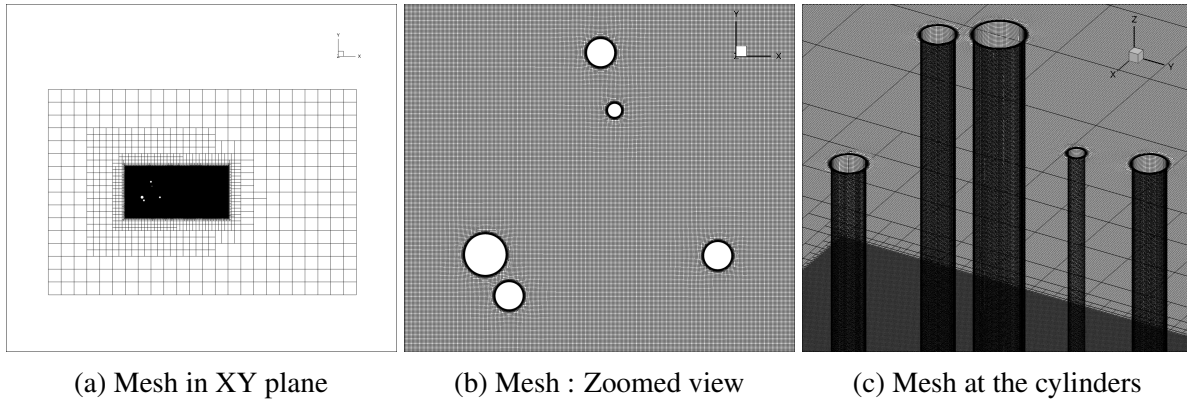


Figure 148: DDES simulation: Excessive mesh refinement

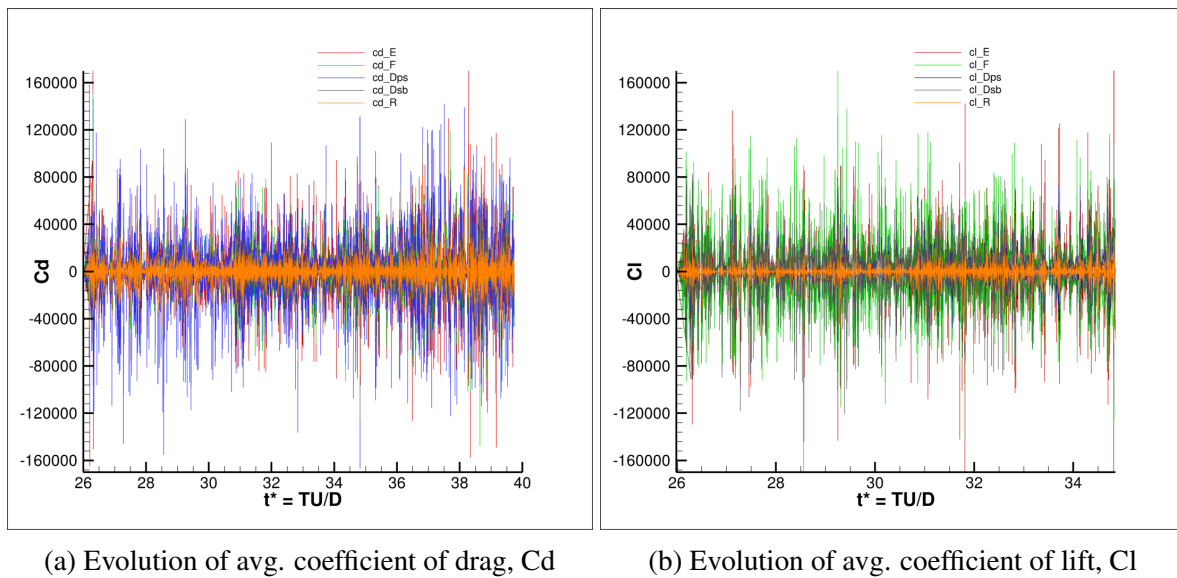


Figure 149: Evolution of avg. Cd, and Cl: DDES simulation